TECHNISCHE UNIVERSITÄT WIEN
Vienna University of Technology

DISSERTATION

Development of a detector for the simultaneous measurement and for the study of uranium-233 capture and fission yields at the CERN n_TOF neutron source

ausgeführt zum Zwecke der Erlangung des akademischen Grades eines Doktors der technischen Wissenschaften unter der Leitung von

Ao.Univ.Prof.i.R. Univ.Prof. Dipl.-Ing. Dr.techn. Helmut Leeb
Atominstitut der Österreichischen Universitäten (E141)
Technische Universität Wien

Dr. Frank Gunsing
Universite Paris Saclay

eingereicht an der Technischen Universität Wien
Fakultät für Physik
von

Michael Bacak
0926776
Neuburgerstraße 10, A-2512 Oeynhausen

Wien, 22. September 2019

Michael Bacak

Declaration

I declare that I have developed and written this thesis completely by myself, and have not used sources or means without declaration in the text. Any thoughts from others or literal quotations are clearly marked. This thesis was not used, in whole or in part, to achieve an academic degree.

Vienna, 22. September 2019

Michael Bacak

Abstract

A low-carbon energy outlook to mitigate the impact of the climate change requires the progressive replacement of fossil fuel technologies by sources with low CO_2 emissions. In this context, nuclear energy can play a relevant role. Ensuring the long-term sustainability of nuclear energy points to the use of innovative nuclear systems, such as Accelerator Driven Systems and Generation-IV reactors and new fuel compositions. One of the options discussed in the Gen-IV International Forum dedicated to the next generation of nuclear reactors is to use a fuel based on the thorium cycle. This cycle being little used in the world, the associated basic data are of relatively poor quality at present. The fissile isotope ^{233}U is among the most important isotopes in the thorium cycle and directly responsible for the neutron economy and all subsequent quantities for the operation of such a nuclear system. One of the particularities of this nucleus is to have a capture cross section which is on average one order of magnitude lower than its fission cross section in the whole energy range. This circumstance makes the measurement of the ^{233}U capture cross section very challenging as indicated by only two high resolution data sets available since the 1960s which in addition are discrepant. The n_TOF collaboration performs measurements of neutron capture cross sections associated with nuclear technology. A first series of measurements have been carried out since 2004 using the n_TOF Total Absorption Calorimeter (TAC), with the main difficulty of these measurements being the lack of a fission detector to identify the fission events in the calorimeter, making capture-fission discrimination very difficult to perform in the case of fissile isotopes.

In this manuscript, a new measurement at the n_TOF facility is discussed where the gamma calorimeter was equipped with a new specifically designed fission chamber hosting several ^{233}U targets with the aim of improving the accuracy of the capture cross section of ^{233}U significantly while providing additional information on the fission reaction. The fission chamber is custom tailored to this capture measurement and its performance is discussed in detail. A fission veto, or fission tagging, technique is used to identify the prompt fission gamma-rays, allowing for an efficient capture-fission discrimination. This technique is also used to study the properties of the prompt fission gamma-rays in ^{233}U. A detailed discussion of the experimental setup and the performance of the novel fission chamber and the TAC is given in this manuscript. The analysis procedure applied to the experimental data estimates the sources of background, experimental biases, and is complemented with simulations to estimate dead time and geometrical effects in the measurement.

Finally the so-called alpha-ratio, the ratio between the capture and fission cross section, is determined and shows a reasonable agreement with evaluated nuclear data libraries. In summary, the measurement presented in this work improves the knowledge on the ^{233}U fission

process and capture cross section, thus contributing to the global effort to narrow the gap between the current status of nuclear data and the target accuracies required to design and operate innovative nuclear systems.

Kurzfassung

Um den Einfluss des Klimawandels abzumildern muss die Energiezerzeugung mit fossilen Brennstoffe progressiv durch Technologien mit geringen CO_2 Emissionen ersetzt werden. In diesem Zusammenhang, kann Kernenergie eine relevante Rolle spielen. Die Langzeitnachhaltigkeit der Kernenergie kann durch Verwendung von neuen und innovativen Systemen zur Kernenergieerzeugung, wie zum Beispiel Generation-IV Reaktoren oder beschleunigergetriebene Systeme (Accelerator-driven system ADS), sowie die Nutzung neuer Kernbrennstoffe verbessert werden. Das sogenannte internationale Gen-IV Forum widmet sich der Erforschung und Entwicklung dieser Systeme. Eine mögliche Option für die Zukunft stellt der sogenannte Thorium-Uran Brennstoffkreislauf dar. Dieser Kreislauf ist derzeit kaum in Verwendung und die damit verbundenen Grundlagen sind wenig erforscht oder von geringer Qualität. Im Thorium-Uran Brennstoffkreislauf nimmt ^{233}U die wichtige Rolle des spaltbaren Isotops ein. Eine Besonderheit von ^{233}U ist der geringe Neutroneneinfangwirkungsquerschnitt, der im Durchschnitt um eine Grössenordnung kleiner ist als der Spaltwirkungsquerschnitt. Dieser Umstand macht die Messung des Einfangwirkungsquerschnitts zu einer Herausforderung was sich in der Tatsache widerspiegelt, dass es nur zwei Datensätze mit hoher Auflösung und weitem Energiebereich seit 1960 gibt, welche wiederum signifikante Unterschiede aufweisen. Die n_TOF Collaboration führt Messungen zur Bestimmung des Einfangwirkugsquerschnitts von spaltbaren Isotopen durch. Seit 2004 wurden mehrere Versuche zur Messung des ^{233}U Einfangwirkungsquerschnitts durchgeführt, jedoch ohne einen zusätzlichen Detektor zur Charakterisierung des durch die Spaltreaktion verursachten Untergrunds was zu grossen Unsicherheiten in den Ergebnissen führte.

In diesem Manuskript wird eine neue Messung des Einfangwirkungsquerschnitts von ^{233}U diskutiert, die zusätzlich zu einem γ-Kalorimeter einen neu und eigens für diese Messung entwickelten Spaltdetektor verwendet. Die Spaltkammer ist genau auf diese Anwendung zugeschnitten worden und sowohl der Aufbau als auch die Charakterisierung dieses Detektors werden genau diskutiert. Die Verwendung beider Systeme in Koinzidenz erlaubt es die Signale der Spaltreaktion im Kalorimeter zu identifizieren und so den Untergrund genau zu charakterisieren, damit dieser mittels Veto aus allen Signalen im Kalorimeter herausgefiltert wird. Weiters erlaubt diese Methode die Spaltsignale zu charkterisieren. Eine genaue Beschreibung des Experimentaufbaus, sowie die Verfahren zur Datenreduktion und Analyse werden genau beschrieben. Die Analyse wird durch Simulationen im Bereich der Totzeit und bei der Charakterisierung diverser geometrischer Effekte im Experimentaufbau unterstützt. Schlussendlich wird aus den Daten das Verhältnis von Einfang- und Spaltquerschnitt bestimmt und mit bestehenden Daten und Evaluationen verglichen. Zusammenfassend verbessert diese Messung das Wissen über den Einfangwirkungsquerschnitt und den Spaltprozess von ^{233}U.

Abstract

Une perspective énergétique à faible émission de carbone pour atténuer l'impact du changement climatique nécessite le remplacement progressif des combustibles fossiles par des sources à faibles émissions de CO_2. Dans ce contexte, l'énergie nucléaire peut jouer un rôle important. Assurer la viabilité à long terme de l'énergie nucléaire passe par l'utilisation de systèmes nucléaires innovants, tels que les systèmes pilotés par accélérateurs, les réacteurs de Génération IV et les nouveaux combustibles. L'une des options discutées lors du Forum international Gen-IV consacré à la prochaine génération de réacteurs nucléaires est d'utiliser un combustible basé sur le cycle du thorium. Ce cycle étant peu utilisé dans le monde, les données de base associées sont actuellement de qualité relativement médiocre. L'isotope fissile uranium-233 est l'un des isotopes les plus importants du cycle du thorium et directement responsable du bilan neutronique et de toutes les quantités qui en découlent pour assurer le fonctionnement d'un tel système nucléaire. Une des particularités de ce noyau est d'avoir une section efficace de capture en moyenne inférieure d'un ordre de grandeur à sa section efficace de fission dans toute la gamme énergétique. Cette circonstance rend la mesure de la capture de l'uranium-233 très difficile, comme l'atteste les deux seuls jeux de données à haute résolution disponibles depuis les années 1960 qui, en outre, sont contradictoires. La Collaboration n_TOF effectue des mesures de sections efficaces de capture neutronique associées aux technologies nucléaires. Une première série de mesures a été effectuée depuis 2004 à l'aide du Calorimètre gamma (TAC) de n_TOF , la principale difficulté de ces mesures étant l'absence d'un détecteur de fission pour identifier les événements de fission dans le calorimètre, rendant très difficile la discrimination capture-fission dans le cas des isotopes fissiles. Dans ce manuscrit, il est question d'une nouvelle mesure à l'installation n_TOF où le calorimètre gamma a été équipé d'une nouvelle chambre à fission spécialement conçue contenant plusieurs cibles d'uranium-233 dans le but d'améliorer de manière significative la précision de la section de capture de l'uranium-233 tout en fournissant des informations supplémentaires sur la réaction de fission. La chambre à fission est adaptée à cette mesure de capture et sa performance est discutée en détail. Une technique de veto de fission, ou de marquage de fission, est utilisée pour identifier les rayons gamma prompts de fission, ce qui permet une discrimination capture-fission efficace. Cette technique est également utilisée pour étudier les propriétés des rayons gamma prompts de fission de l'uranium-233. Ce manuscrit présente une discussion détaillée du montage expérimental et de la performance de la nouvelle chambre à fission et du TAC. La procédure d'analyse appliquée aux données expérimentales permet d'estimer les sources de bruit de fond, les biais expérimentaux et est complétée par des simulations pour estimer le temps mort et les effets géométriques de la mesure. Enfin, on détermine ce qu'on appelle le rapport alpha, c'est-à-dire le rapport entre la section efficace de capture et la section efficace

de fission, qui est en accord avec les bibliothèques de données nucléaires évaluées. En résumé, la mesure présentée dans ce travail améliore les connaissances sur le processus de fission et la section efficace de capture de l'uranium-233, contribuant ainsi à l'effort mondial visant à réduire l'écart entre l'état actuel des données nucléaires et les précisions cibles requises pour concevoir et exploiter des systèmes nucléaires innovants.

Contents

1 Nuclear energy and nuclear data **5**

1.1 Nuclear reactors . . . 5

1.1.1 Proliferation risks . . . 7

1.1.2 Radioactive waste . . . 7

1.1.3 Th-U fuel cycle . . . 9

1.1.3.1 Proliferation resistance . . . 10

1.1.3.2 Challenges . . . 11

1.1.4 Conversion of nuclear waste . . . 12

1.1.5 Accelerator Driven System (ADS) . . . 14

1.1.6 Generation IV reactors . . . 14

1.2 The role of nuclear data . . . 15

1.2.1 Present status on the ^{233}U(n,γ) reaction . . . 16

2 Neutron-induced Nuclear Reactions **21**

2.1 Neutron cross section . . . 21

2.1.1 The Compound Nucleus: neutron resonances . . . 23

2.1.2 Radiative capture . . . 23

2.1.3 Fission . . . 25

2.2 Measurements of cross-sections . . . 27

2.2.1 Time-of-Flight method . . . 27

2.2.1.1 Resonance Broadening . . . 28

2.2.2 Measurement of capture cross-sections in fissile isotopes . . . 28

3 Experimental Setup **33**

3.1 The n_TOF facility at CERN . . . 33

3.1.1 Neutron fluence . . . 35

3.1.2 Neutron beam profile . . . 36

3.1.3 Resolution function . . . 37

3.1.4 Data Acquisition . . . 38

3.1.5 Neutron beam monitors . . . 39

3.1.5.1 Stability . . . 40

3.2 The n_TOF Total Absorption Calorimeter . . . 40

3.2.1 Neutron sensitivity and absorber . . . 41

3.2.2 Pulse shape analysis and particle discrimination . . . 42

3.3 A novel fast Fission Chamber . . . 43

3.3.1 Technical description . . . 44
3.3.2 Choice of gas and gas system . . . 45
3.3.3 Dedicated electronics . . . 47
3.3.4 Pulse shape analysis . . . 47
3.4 The ^{233}U samples . . . 48
3.5 Geometry model of the experimental setup for Monte Carlo simulations . . . 50
3.5.1 Event reconstruction . . . 51
3.5.2 Validation of the simulation process . . . 51

4 Detector performance and Fission Tagging 55
4.1 Performance of the TAC . . . 55
4.1.1 Energy calibration . . . 55
4.1.1.1 α/γ/noise discrimination . . . 55
4.1.1.2 Response to standard γ-ray calibration sources . . . 57
4.1.1.3 Gain monitoring and correction . . . 58
4.1.2 Energy resolution . . . 61
4.1.3 Time calibration and coincidence window . . . 63
4.1.4 Count rate, dead-time and pile-up . . . 66
4.2 Performance of the FICH . . . 67
4.2.1 Pulse height spectra and particle discrimination . . . 67
4.2.2 Gain monitoring . . . 74
4.2.3 Count rate and comparison of the ^{233}U(n,f) cross-section with evaluated libraries . . . 77
4.3 Fission Tagging . . . 79
4.3.1 Event reconstruction . . . 79
4.3.1.1 Time calibration and coincidence window . . . 79
4.3.1.2 Event selection . . . 80
4.3.2 Pulse-height spectra . . . 83
4.3.2.1 Monte Carlo simulations of the FICH response to fission fragments . . . 83
4.3.3 Prompt fission γ-ray spectra . . . 91
4.3.3.1 Comparison with Monte Carlo simulations . . . 91

5 Data reduction for the determination of the experimental ^{233}U α-ratio 101
5.1 Time independent background . . . 102
5.2 Neutron beam induced background unrelated to the ^{233}U samples . . . 103
5.3 Neutron beam induced background related to the ^{233}U samples . . . 104
5.3.1 Elastic scattering . . . 104
5.3.2 Delayed γ-rays from the decay of the fission products . . . 105
5.3.3 Prompt fission background . . . 106
5.3.4 Background induced by prompt fission neutrons . . . 110
5.3.4.1 Fission neutrons and neutron scattering . . . 115
5.3.5 Determination of the fission tagging efficiency . . . 116

5.3.5.1 Correlations between TAC and FICH event detection 119
5.3.5.2 Experimental correction to the FICH efficiency 121
5.4 Simulated response to ^{233}U(n,γ) events 123
5.4.1 The ^{233}U(n,γ) cascade generator 124
5.4.2 Simulated response to the ^{233}U capture cascades 127
5.4.3 Final TAC efficiency and uncertainty estimation 129
5.5 Summary 130

6 The experimental ^{233}U α-ratio **133**
6.1 Analysis conditions 133
6.2 Dead time corrections 135
6.3 Comparison with evaluated libraries and other experimental data 136
6.3.1 Comparison with evaluated libraries 137
6.3.2 Comparison with other experimental data 140

7 Summary and Conclusions **149**
7.1 Improvements for future measurements 151

Bibliography **155**

Context and Introduction

The world's increasing demand for energy and the challenge to find a sustainable carbon emission free source of energy have been a dominant topic in society and politics over the past years. The 2016 source mix of the total primary energy supply and of electricity production in the world is shown in the left and right panel of Figure 1 respectively. The increasing global demand for energy brings up questions regarding climate change, energy security and uncertainty about fossil fuel supplies which have contributed to an increased interest in nuclear energy. Nuclear energy continues to play an important role in global electricity

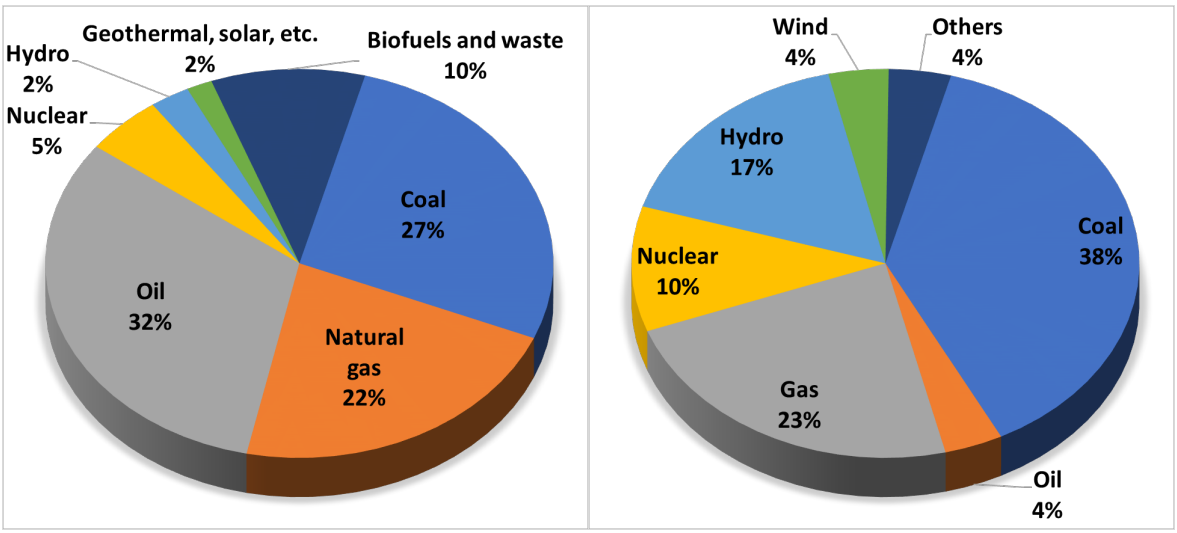

Figure 1: Total primary energy supply by source (left) and total electricity supply by source (right) for 2016 from [1, 2]

production. At the end of 2017 a total of 448 nuclear power reactors were in operation according to the International Atomic Energy Agency (IAEA) [3]. This includes 4 reactors newly connected to the grid, while construction started on 4 reactors, with a total of 59 reactors under construction around the world. The trend in the annual generation of nuclear power over the past 25 years can be seen in Figure 2. Since 2007 there is a slight downward trend in the annual generation of nuclear power, which was accelerated due to the accident at Fukushima Daiichi nuclear power plant (NPP) in 2011 and the subsequent decisions from Japan to decrease the dependence on nuclear energy or even phase out of nuclear energy as in the case of Germany. Despite this downwards trend, many countries have re-assured the continuation of their nuclear programs.

The installation of renewables like wind and solar has increased above all predictions but is far away from replacing fossil fuel power sources like coal, gas and oil in the near future.

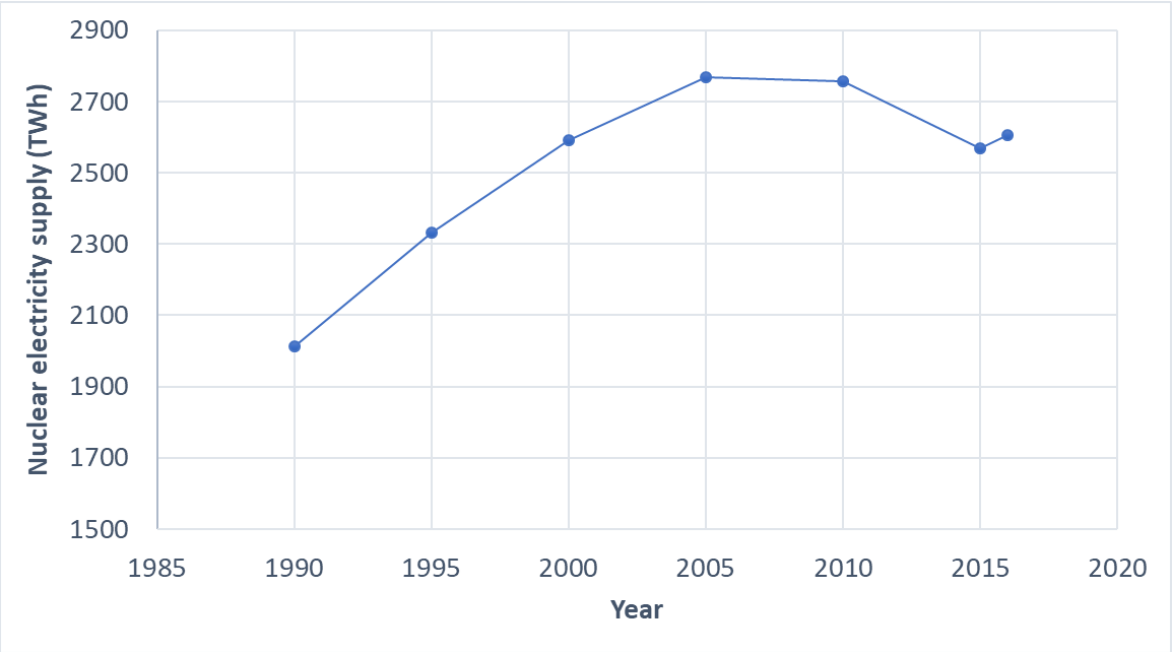

Figure 2: Development of installed nuclear electricity supply worldwide from [2].

Nuclear fusion might become a potent candidate for clean energy in the future, if the ITER facility [4] are successful. A sustainable and economical decarbonization of electricity and energy production can only be achieved with a mix of renewables, nuclear and also fossil fuel power plants that capture and store their emissions [5]. The IAEA projects an increase in the global installed nuclear power capacity of 42 % by 2030, 83 % by 2040 and 123 % by 2050 in the high case scenario. The low case scenario projects a capacity dip of 12 % by 2030 and 15 % by 2040, before a return to 2016 levels by 2050. While the expansion of the nuclear power programs is driven especially by China, Russia and India, having a total of 24 new reactor units under construction, in many countries nuclear power is being replaced by renewables. Apart from concerns related to safety the main problems in the use and further expansion of nuclear energy are:

- The production of radioactive waste, in particular long-lived radioactive isotopes such as plutonium, americium, neptunium and curium. Their associated radio-toxicity is a major long-term concern for the disposal of radioactive nuclear waste.
- Potential diversion of nuclear material for military purposes, i.e. plutonium.

Those issues must be addressed if nuclear is going to play a significant role in the energy mix of the future. The international community is considering innovative nuclear systems that improve the situation regarding the production of radioactive waste and proliferation risk. At the moment two families of options are investigated on a national and international level, namely:

- Advanced Minor Actinide Burners, designed to transmute transuranic elements. An example is the Accelerator Driven System (ADS) proposed by Carlo Rubbia [6] with a European demonstrator *MYRRHA* [7] under construction.

- Generation IV [8] reactors mainly based on a fast neutron spectrum.

Such new systems could be the answer to the challenges of nuclear energy in terms of waste minimization, availability of fuel, safety, economic and non-proliferation issues. However, the design and optimization of such innovative nuclear systems requires improved knowledge in many different fields, for example new materials for fuels, fuel treatment and new development in the field of reactor and basic nuclear physics. In addition to design and optimization of new nuclear systems, improvements in those fields will also increase the safety margins of currently operating nuclear reactors and are necessary for planning a safe and cost effective dismantling of old reactors and storage of medium and high level radioactive waste. Furthermore, within the Generation IV designs new fuel cycles like the Thorium-Uranium fuel cycle are investigated as they offer several advantages compared to the Uranium-Plutonium fuel cycle. On the other hand the Th-U fuel cycle imposes new challenges that have to be dealt with, foremost the lack of accurate nuclear data. In the light of all these points, the role of nuclear data is essential as it provides the basis for all calculations. These data, in particular neutron-induced reaction cross sections, are available in evaluated data libraries [9–11], as well as in experimental databases like *EXFOR* [12] and are the results of national and international efforts for several decades. Nevertheless, in some cases the data still lack the needed accuracy and/or neutron energy range [13].
Within this context the work done in this thesis aims to contribute to the world effort towards the improvement of the knowledge needed in the development of advanced nuclear technologies using the Th/U fuel cycle. This manuscript is divided in several chapters:

- The first chapter introduces the motivation and the objective of the work done in this thesis and the current state of the relevant nuclear data regarding ^{233}U is discussed.
- The necessary theory is discussed in the second chapter which also gives a brief introduction of the neutron induced fission and capture reaction channels and the challenges that come along with a measurement of the neutron capture cross section in fissile isotopes.
- In the third chapter the experimental setup for the measurement of the ^{233}U α-ratio is introduced.
- The performance of the detectors and the technique used to determined the prompt fission background is discussed in the fourth chapter.
- The fifth chapter describes the data reduction and analysis routines used to extract the detector's response to the ^{233}U(n,γ) reaction.
- In the sixth chapter the final analysis conditions for the extraction of the ^{233}U α-ratio from the experimental data are discussed and a comparison of the obtained ^{233}U α-ratio with evaluated libraries and experimental data is done.
- In the last chapter a summary of the work done is given and an outlook and improvements for future measurements are discussed.

Chapter 1

Nuclear energy and nuclear data

In this section, a brief introduction to nuclear power generation and its related problems concerning the fuel cycle and nuclear waste is given. Within this context, the role of nuclear data is discussed, in particular in the light of the Th-U fuel cycle and projects of nuclear waste transmutation in advanced systems, such as Accelerator Driven Systems and Generation IV fast reactors. Furthermore, the current status of the experimental data and of the most commonly used nuclear data libraries for the ^{233}U(n,γ) reaction is discussed.

1.1 Nuclear reactors

The idea of producing electricity with a sustained neutron chain reaction is known since the end of the 1930s. In order to sustain a chain reaction one of the neutrons emitted in a nuclear fission event must produce another fission event on average. This can quantitatively be described by the effective multiplication factor k_{eff}, defined as the ration between the number of fissions in one generation divided by the number of fissions in the preceding generation. The steady state situation, also called critical condition, of a reactor is reached when $k_{eff} = 1$, meaning that the neutron population in the system is constant. Subcritical ($k_{eff} < 1$) or critical ($k_{eff} \approx 1$) states in a standard reactor describe transitions between steady states or shut downs of the system. k_{eff} strongly depends on the neutron energy distribution in the system, the composition of the fuel, and the geometrical assembly of the fuel and moderator. This dependence can be expressed in the so-called criticality equation [14]

$$k_{eff} = f\eta\varepsilon p P_{NL} = k_{\infty} P_{NL}. \tag{1.1}$$

In equation (1.1) the so-called thermal utilization factor f describes the fraction of thermal neutrons absorbed in the fuel with respect to the total number of absorbed thermal neutrons, η is the number of fission neutrons per neutron absorbed in the fuel, ε is the fast fission factor and p is called the resonance escape probability, accounting for neutrons captured in (n,γ) reactions during moderation to thermal neutron energies. The product of these factors are defined as criticality of an ideal and infinite system (k_{∞}), while the last remaining factor P_{NL} is the non-leakage probability which is linked to the probability of a neutron escaping a realistic finite fuel and moderator assembly.
Natural uranium contains only 0.72 % of ^{235}U, the only fissile isotope existing in nature. Most reactors nowadays use enriched uranium, usually 2-3 % to increase f. In thermal reactors

the energy of the neutrons emitted in fission is in the MeV region and has to be reduced to thermal energies, where cross sections are larger, by a so-called moderation process, i.e. elastic collisions with low-mass nuclei, for example hydrogen in the light-water.
The most important neutron reactions occurring in the reactor fuel are fission and capture. Therefore, an important parameter in reactor physics is the ratio of the capture to fission cross section of a given isotope, also called α-ratio, defined as:

$$\alpha = \frac{\sigma_\gamma(E_n)}{\sigma_f(E_n)} \tag{1.2}$$

The convolution of this parameter for all the isotopes contained in the reactor fuel is a key parameter for assessing the neutron economy of a nuclear reactor core. Another important parameter is the conversion or breeding ratio, defined as the ratio between the rate of production of fissile nuclei to the rate of their destruction at any given time.
Reactors can be classified, from a physics point of view, in two categories, thermal and fast reactors. The neutron spectrum in a reactor is essentially defined by the moderator material, which is very often also used as the coolant. Most of today's commercial power reactors are designed as thermal reactors and use light water, either pressurized or boiling. Currently operating Pressurized Water Reactors (PWR) are Generation II reactors, using light water both as coolant and neutron moderator, which is kept at high pressure (superheated water) to prevent it from boiling when flowing into the reactor core. Another commonly used reactor is the Pressurized Heavy Water Reactor (PHWR) which uses D_2O as coolant, and is mostly used in countries without enrichment capabilities, since natural uranium can be used in that case, because heavy water captures less neutrons compared to light water. On the other hand, Boiling Water Reactors (BWR) are characterized by two-phase mixed fluid flow (water and steam) in the upper part of the reactor core. In thermal reactors the neutron spectrum is thermalized, thanks to the good moderating properties of hydrogen.
In fast reactors fission occurs at relatively high energies. In the case of the U-Pu fuel cycle, ^{239}Pu is the fissile fuel which is produced from the fertile ^{238}U. At neutron energies in the MeV region, breeding conditions are optimal as neutron-induced fission of ^{239}Pu dominates ($\alpha = 0.03$). The most prominent example of a fast power reactor is the liquid-metal reactor (LMR) such as the 250 MWe reactor PHENIX and the 1200 MWe SUPERPHENIX in France, both cooled with liquid sodium. The majority of fast reactors are designed as breeder reactors, meaning that more fissionable material is produced than consumed. Furthermore, a gas can also be used as a coolant for fast reactors, as well as for thermal ones, if a moderator such as graphite is employed. Mainly two types exist, the Advanced Gas Reactors (AGR) and the High-Temperature Gas Cooled Reactors (HTGR) cooled with CO_2 and He respectively. More advanced reactor types, from the Generation IV, are introduced in § 1.1.6 and are more thoroughly described in Ref. [8].
Since the discovery of the possibility to exploit nuclear reactions for energy production and the construction of the first nuclear power plant in 1956, vast progress has been made in the field of nuclear energy up to the conceptual designs of innovative systems such as Generation IV reactors and Accelerator Driven Systems. Nevertheless, problems with nuclear energy

Table 1.1: Inventory of a 1 GWe PWR reactor at loading and at discharge (1 year), values taken from [15].

	Initial loading (mass in kg)	After discharge (mass in kg)
^{235}U	954	200
^{236}U		111
^{238}U	26328	26047
^{239}Pu		156
Total Pu		266
Minor Actinides		20
^{90}Sr		13
^{137}Cs		30
LLFFs		63
Total FFs		946
Total	27282	27279

production still have to be investigated and current research addresses issues affecting the fuel availability, safety, costs, non-proliferation, etc. Apart from safety concerns, the most important problem of nuclear energy regards the production and management of radioactive waste, which is also one of the most critical parts in public acceptance of nuclear energy.

1.1.1 Proliferation risks

The minimization of the proliferation risk has been a major concern for a sustainable exploitation of the nuclear energy source. Since the early 1950s, the fear of diversion of civil nuclear material towards military use has always been present. This concern is characteristic for nuclear energy and has motivated the implementation of measures to avoid that sensitive materials, such as enriched uranium and plutonium, or technologies developed for civilian purposes, such as those involved in enrichment or reprocessing, could be diverted for military and/or terroristic use. Therefore, advanced nuclear energy systems must be very unattractive and the least desirable route for diversion or theft of weapons-usable materials, and provide increased physical protection against acts of terrorism.

1.1.2 Radioactive waste

Radioactive waste is generated in sizeable amounts, see Table 1.1, due to irradiation with neutrons when operating a nuclear reactor. While unstable fission fragments are created in the fission reaction, neutron capture leads to the creation of TRansUranic elements (TRUs). Fission fragments decay mainly by beta emission and the transuranic elements decay via alpha and beta radioactivity, some with relative long half lives. There are many national classifications of radioactive waste and also the International Atomic Energy Agency (IAEA) distinguishes several classes of waste [16], as described in Table 1.2.
High level waste (HLW) is composed of highly radioactive fission and neutron capture byproducts of the nuclear fuel cycle in the form of either spent fuel or liquid and solid products from

Table 1.2: Radioactive waste classification according to the IAEA [16].

Waste class	Characteristics	Disposal options
Exempt Waste (EW)	meets the criteria for clearance [17], exemption or exclusion from regulatory control for radiation protection purposes	no radiological restrictions
Very short lived waste (VSLW)	very short half-lives often used for research and medical purposes	short term storage, subsequently cleared from regulatory control for disposal
Very low level waste (VLLW)	not exactly EW; no need for high level of containment and isolation	disposal in near surface landfill type facilities with limited regulatory control
Low level waste (LLW)	above clearance levels, but with limited amounts of long lived radionuclides	requires robust isolation and containment for periods of up to a few hundred years and is suitable for disposal in engineered near surface facilities
Intermediate level waste (ILW)	contains higher concentrations of long lived radionuclides; requires a greater degree of containment and isolation than that provided by near surface disposal	no/limited provision for heat dissipation during its storage and disposal below 10s of meters
High level waste (HLW)	activity concentration high enough to generate significant quantities of heat or waste with large amounts of long lived radionuclides	disposal in deep, stable geological formations

the post-irradiation reprocessing of fuel. Its major component are long-lived fission products (LLFP). Activated machine parts, structural materials and protective clothing make most of the low level waste. The long term hazard of spent fuel and HLW is associated with minor actinides (MA), particularly the TRUs, while the short and long term risks are due to the mobility of fission products in the geosphere and the possibility of their entering the biosphere. The evolution of the radiotoxicity, indicating the dose resulting from the ingestion of a certain mass of radioactive material, of spent fuel depends on the type of fuel and the attained burnup. The example of the evolution of the radiotoxicity in spent fuel is shown in Figure 1.1. The radiotoxicity of plutonium and other MA decay to the natural level of the uranium ore required to produce the fuel after several 10 thousand to 100 thousand years. The reference level of the natural uranium required to produce 1 ton of enriched U-nuclear fuel is a horizontal line at 1.47×10^5 Sv/t heavy metal. At present, most spent fuel is planned to be disposed in deep geological repositories but the waste can also be reprocessed, also called partitioning and transmutation (P&T) to reduce the radiotoxicity significantly, see § 1.1.4.

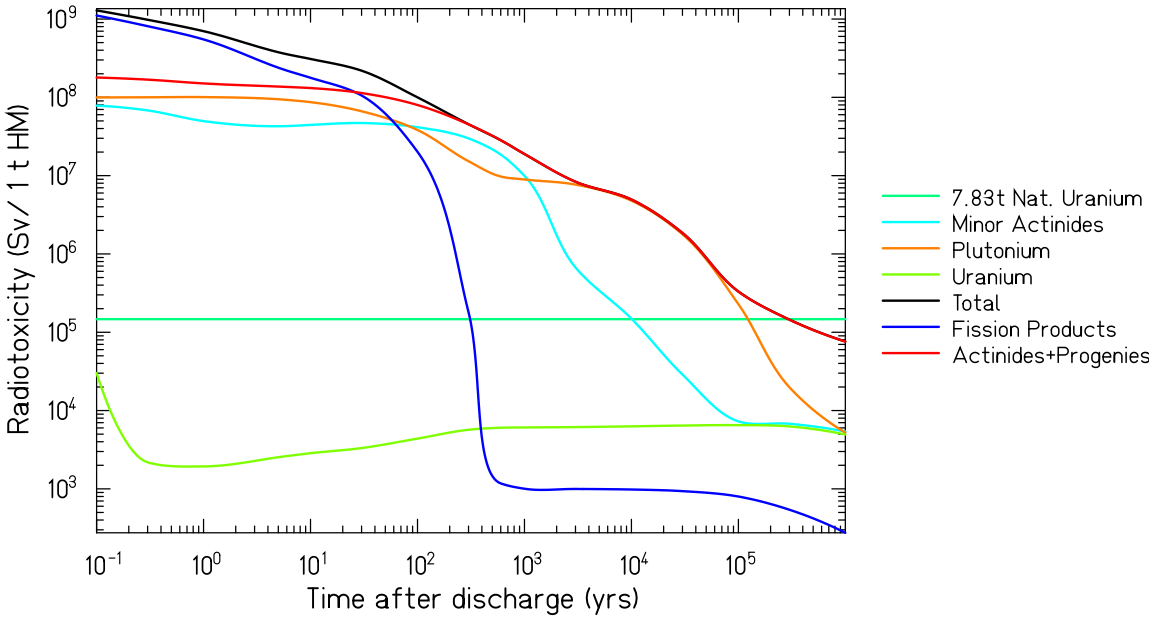

Figure 1.1: Radiotoxicity of spent nuclear fuel in Sv per 1 ton of heavy metal as a function of time after discharge from the reactor, taken from [18].

1.1.3 Th-U fuel cycle

While the most exploited cycle is the U-Pu cycle, the Th-U fuel cycle, shown in Figure 1.2, starts from the fertile material ^{232}Th. This process is similar compared to the breeding process of the fertile ^{238}U to the fissile ^{239}Pu in fast breeder reactors or thermal reactors using a graphite moderator. The basis of the Th-U fuel cycle is the following reaction:

$$^{232}\mathrm{Th}(n,\gamma)^{233}\mathrm{Th} \xrightarrow{\beta^-,\ 22\ m} {}^{233}\mathrm{Pa} \xrightarrow{\beta^-,\ 27\ d} {}^{233}\mathrm{U} \tag{1.3}$$

The Th-U cycle offers some advantages compared to the U-Pu:

- Thorium is 3-4 times more abundant than uranium.
- Due to the lower atomic number of thorium the amount of produced transuranic waste, in particular plutonium, neptunium, americium and curium, is significantly reduced.
- ^{232}Th is a better fertile material compared to ^{238}U in thermal reactors, due to its higher thermal capture cross section, 7.4 b and 2.7 b in the case of ^{232}Th and ^{238}U respectively.
- The average number of neutrons emitted per absorbed neutron in the fission reaction of ^{233}U is above 2 over a wide energy range, contrary to ^{235}U and ^{239}Pu, making the Th-U cycle less sensitive to the type of reactor and providing more neutrons for breeding.
- While the thermal fission cross section is similar for all isotopes, ^{233}U(525 b), ^{235}U(577 b) and ^{239}Pu(742 b), the thermal capture cross section is much smaller for ^{233}U(46 b) compared to ^{235}U(101 b) and ^{239}Pu(271 b). The smaller α-ratio thus reduces the amount of transuranic waste per energy unit produced even more. In Figure 1.3 the ratio of the fission to capture cross section, or inverse α-ratio is shown for ^{233}U, ^{235}U and ^{239}Pu.

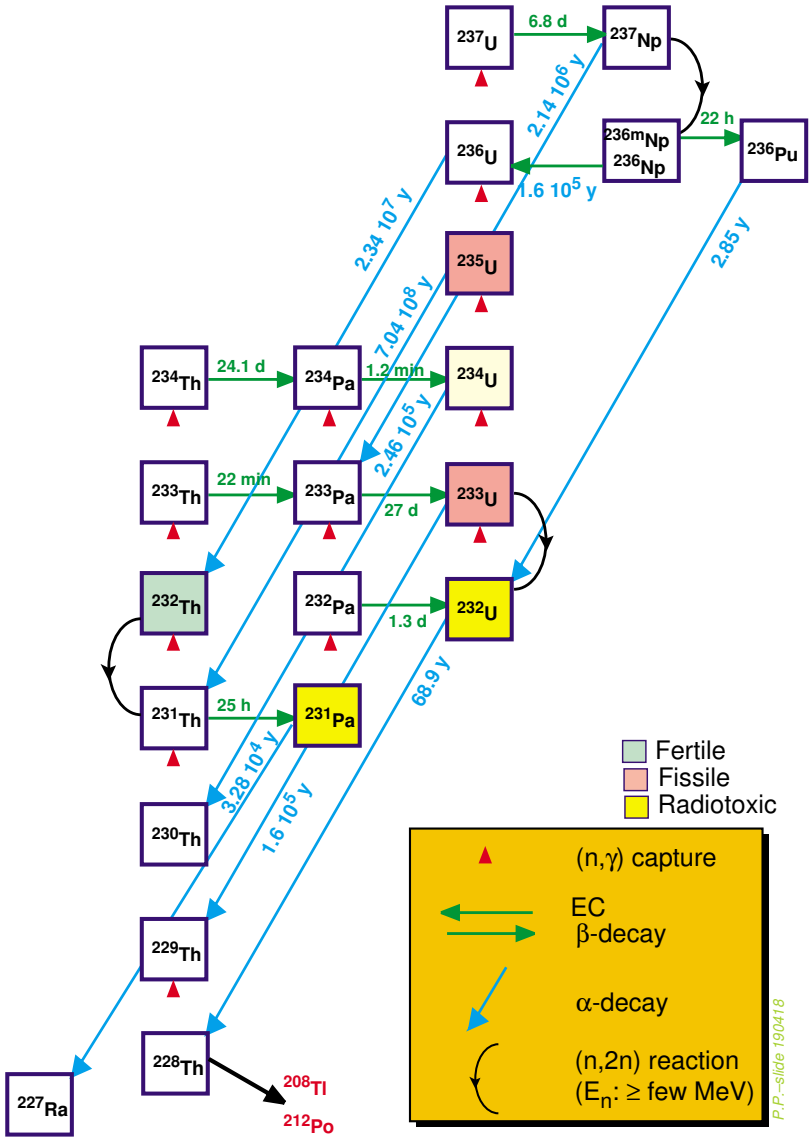

Figure 1.2: Schematic view of the Th-U fuel cycle [19].

- Th-U fuel in the form of ThO_2 is chemically more stable and radiation harder compared to UO_2 which allows direct disposal in permanent repositories.

There was a worldwide interest in the development of the Th-U fuel cycle during the developing years of nuclear energy in order to increase the fissile reserves. This interest decreased later, as new uranium reserves were discovered and the efficiency in the use of nuclear fuel increased. Nevertheless some reactors have operated with the Th/U cycle. In recent years, the interest in thorium based fuels has arised again, due to the need to find proliferation resistant and longer fuel cycles with higher burnup and improved waste characteristics.

1.1.3.1 Proliferation resistance

The best way to avoid proliferation is always based on inherent passive properties of the fuel cycle itself. Fuel cycles based on the Th-U cycle have intrinsic proliferation resistance, due to

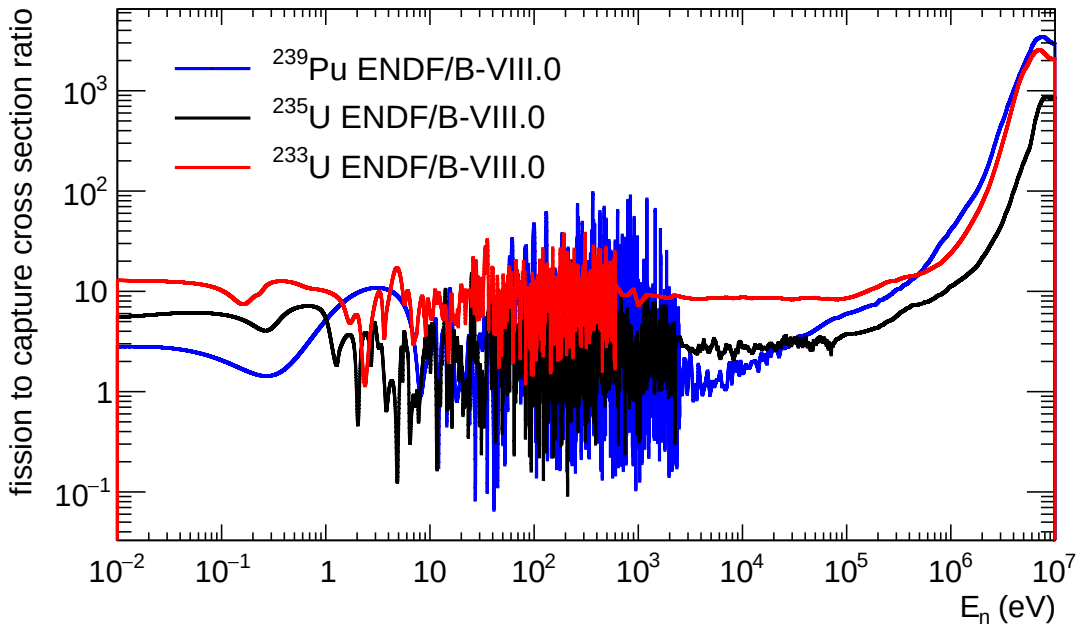

Figure 1.3: Inverse α-ratio for ^{233}U, ^{235}U and ^{239}Pu. ^{233}U has the largest inverse α-ratio leading to a reduction in the amount of transuranic waste per energy unit produced.

the production of ^{232}U by means of (n, 2n) reactions on ^{233}U and (indirectly) on ^{232}Th and by neutron capture on ^{230}Th. In the latter two cases ^{231}Th is produced which subsequently proceeds through the chain $^{231}\text{Th} \xrightarrow{\beta^-,\ 25\ h} {}^{231}\text{Pa(n,}\gamma\text{)}^{232}\text{Pa} \xrightarrow{\beta^-,\ 1.3\ d} {}^{232}\text{U}$.
^{232}U has a half life of 68.9 a and its daughter products with very short half lives emit strong gamma radiation, with energies in the order of MeV. This makes the material itself difficult to handle, for example when trying to produce nuclear weapons, and also easy to trace. Furthermore, this fuel can be mixed with weapon-grade or reactor-grade plutonium for burning in fast reactors going through a cycle once as plutonium cannot be produced by breeding in the thorium based fuel, while the produced ^{232}U makes the fuel proliferation resistant.

1.1.3.2 Challenges

Of course several challenges have to be faced in the Th-U fuel cycle before industrial scale use can be employed. Apart from the presence of ^{232}U in the fuel which makes reprocessing and handling of spent fuel difficult and costly, some issues remain unsolved:

- In the intermediate step of the conversion chain, the role of ^{239}Np with a half life of 2.35 d in the U-Pu fuel cycle is taken by ^{233}Pa with the longer half life of 26.96 d in the Th-U fuel cycle. The long half life of ^{233}Pa leads to a decrease in the breeding efficiency.
- The reprocessing technology is by far not as developed as for the U-Pu cycle.
- Minimization of the ^{232}U content in the fuel, as it creates difficulties in handling spent fuel. This can be achieved by keeping the thorium breeding blanket in a region in the reactor where it is only exposed to a well moderated neutron flux, hence threshold reactions like (n,2n), responsible for the ^{232}U production, are much less likely.

- The acquired experience with this cycle is very limited compared to the U-Pu cycle and the knowledge and behaviour of reactors has to be studied intensely.
- The nuclear data concerning this cycle is not as well known as in the U-Pu cycle.

Most of the scientific attention was given to the isotopes of the U-Pu fuel cycle in the past, resulting in the lack of accurate nuclear data for the isotopes concerned in the Th-U fuel cycle which is a major issue. The experimental data is incomplete and sometimes solely based on theoretical models and nuclear systematics [20]. A significant part of the experimental data have been generated and evaluated in the 1960s to mid 1980s and lack in terms of neutron energy range or do not fulfill the necessary accuracy requirements.

1.1.4 Conversion of nuclear waste

The long term hazard of nuclear waste comes from a limited number of radionuclides. Currently, the only available option is the disposal in geological repositories. However, those isotopes can be converted into nuclides with significantly decreased radiotoxicity by exposing them to a high flux of fast neutrons. This is the basis of P&T, eventually the residual waste would still need to be put in a geological repository, but the problems related to finding a suitable repository would be reduced. There are two types of nuclear reactions that can be exploited for waste conversion:

- **Transmutation** - the isotope is converted into a stable one by neutron capture reactions. This method is suitable for few LLFPs, for example ^{99}Tc and ^{129}I.
- **Incineration** - neutron induced fission of transuranic elements allows to reduce especially the inventory of minor actinides. Fission can obviously be used for energy production. In several countries some of the plutonium inventory is already treated and used in this way in mixed oxide fuel (MOX).

Before converting the waste, it has to be chemically separated, isolating the different elements. This procedure, also called partitioning, is well developed for many isotopes in countries like France and England and is adapted from the technology pioneered to extract plutonium for nuclear weapons. Afterwards the different elements can be reprocessed into minor actinide enriched fuels and eventually be exposed to high neutron fluxes. A good example is ^{99}Tc, with a long half life of $t_{1/2} = 2.11 \times 10^5$ y, which can be transmuted into ^{100}Tc which beta decays with a half life of $t_{1/2} = 16$ s to the stable ^{100}Ru. The ^{100}Ru can capture neutrons again but produce only stable isotopes.
An example for the reduction in radiotoxicity is given in Figure 1.4 showing the evolution of the radiotoxicity of 1 t LWR (UO_2) fuel at a burnup of 50 GWd/t of heavy metal [21, 22]. Without any waste transmutation, the radiotoxicity decreases to the level of natural radioactivity of 7.83 t uranium needed for the production of 1 t fuel after 130 000 y. Partitioning with different efficiencies for different elements, as indicated in the figure, leads to the decrease of the radiotoxicity to the level of 7.83 t uranium after less than 1000 y. Clearly

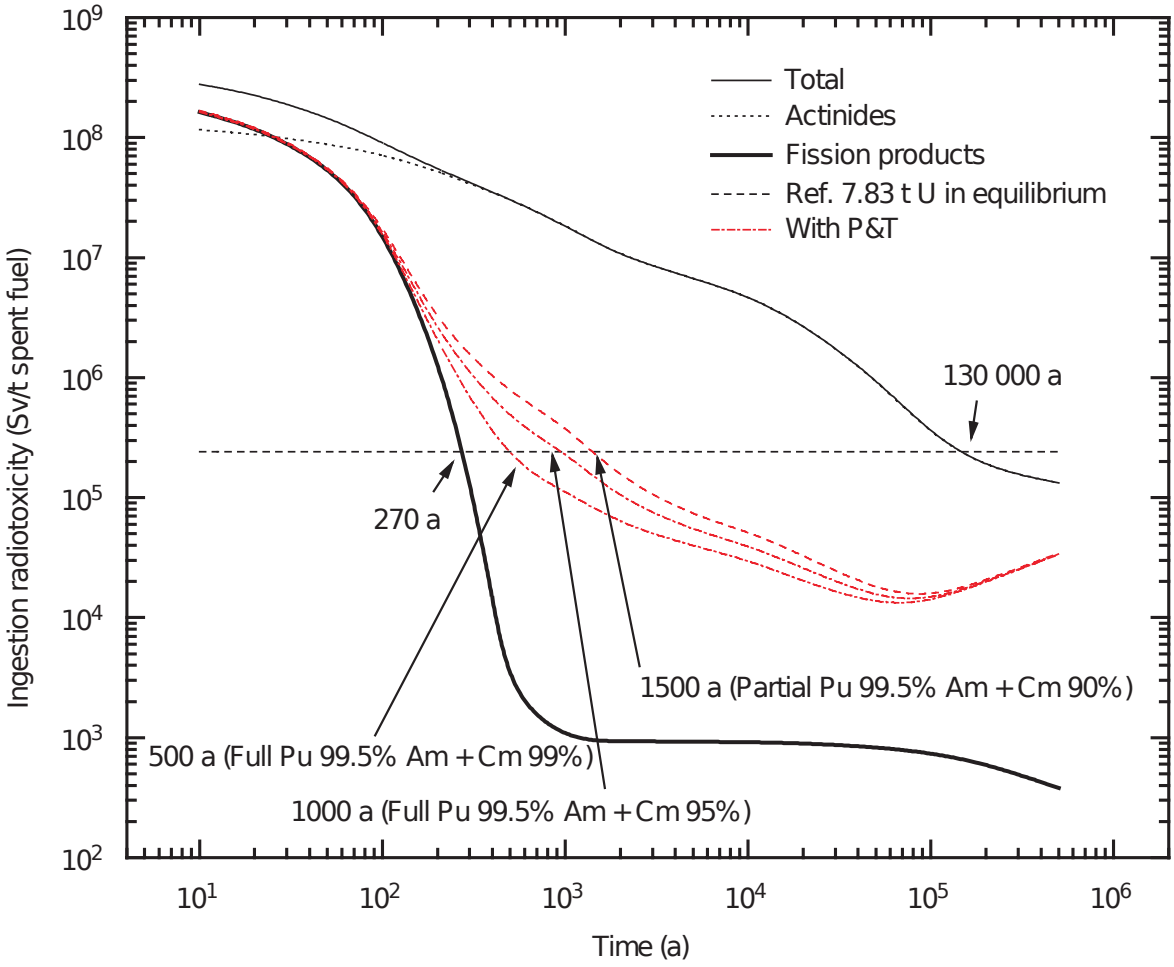

Figure 1.4: Ingestion radiotoxicity of 1 t of spent nuclear fuel, taken from [23].

the timescale of the necessary confinement and the requirements for their storage would be drastically reduced.

This leads to the question which type of device is the most efficient and suited one for transmutation purposes. The existing technology, i.e. LWR, is sufficient to stabilize and slowly decrease the inventory of ^{239}Pu, but MAs show low fission cross sections at thermal neutron energies and high α-ratios, eventually leading to an even larger buildup of minor actinides. As the fission to capture cross section ratio increases drastically for neutron energies above 100 keV the incineration of minor actinides requires fast reactors. Fast reactors could be used to close the fuel cycle by reducing MAs through fission while minimizing their production by neutron capture. The issue of using MAs in reactors regards the safe operation of the reactor, as the fraction of delayed neutrons emitted in minor actinides is smaller compared to that of ^{235}U, which reduces the reactor period. One potential solution for incinerating MAs could be a subcritical accelerator driven system (ADS) directly using high energy spallation neutrons.

1.1.5 Accelerator Driven System (ADS)

The idea and concept of an Accelerator Driven System (ADS) consists of a subcritical (k_{eff} <1) nuclear reactor core combined with an independant/additional neutron source. Most concepts include a continuous wave proton accelerator, either a linear accelerator (LINAC) or a cyclotron, with an energy of around 1 GeV. Those protons are directed onto a spallation target to produce neutrons in nuclear cascade reactions. The neutrons from the spallation neutron source allow to achieve criticality (k_{eff} =1) in the reactor core. This has the immediate advantage that this system is less prone to nuclear accidents because as soon as the proton beam is turned off, the reactor becomes subcritical and the chain reaction stops. The dynamical behaviour of the system is governed by the accelerator operation and the total thermal power output is linked to the proton beam current. Furthermore, more flexibility with respect to the reactor core design and fuel management is achieved as the core itself does not need to be critical on its own (k_{eff} <1). This in particular allows transmuters to be designed as pure MAs or TRUs burners. Mainly technical challenges oppose those advantages. For example, a steadily high proton beam current delivered by a highly reliable accelerator is required for operation. Beam trips or rapid current changes could cause transient events, especially for MA cores. The need for installing a spallation target in the center of a reactor core leads to issues with containment.
At present there are only a few such facilities, exclusively demonstrators. The Energy amplifier Demonstration Facility (EADF) [24] is an example of an advanced design for a 80 MWth subcritical transmuter system, consisting of a core immersed in a lead-bismuth fluid coolant and spallation target coupled with $ThPuO_2$ fuel mixed with MAs. The MYRRHA (Multipurpose hYbrid Research Reactor for High-tech Applications) facility [7] is currently under construction in Belgium with a planned reactor power of 100 MWth. Part of its purpose is to demonstrate the ADS concept on adequate power levels and to study the efficient transmutation of radioactive waste.

1.1.6 Generation IV reactors

The first generation of nuclear reactor prototypes were constructed in the 1950s and 60s and culminated in the construction of the first series of civil nuclear power reactors. Since then the reactor technology has evolved and several generations [25] of nuclear power reactors have been developed. In recent years a new impulse for the development of critical systems for electricity production has been given with the focus being more attractive than present reactors in terms of sustainability, economy, safety and proliferation resistance. Such new systems are referred to as Generation IV reactors and their development is coordinated by the so-called Gen-IV International Forum (GIF) [8, 25].
In general Generation IV reactors can again be classified in thermal and fast reactors, but contrary to the commonly used designs of previous generations the focus is more on fast breeder reactors and closed fuel cycles. The GIF selected six reactor technologies for further research and development. These include the: Gas-cooled Fast Reactor (GFR), Lead-cooled Fast Reactor (LFR), Molten Salt Reactor (MSR), Supercritical Water-cooled Reactor

Table 1.3: Overview of the Generation IV nuclear reactors. The DFR is not an official design but is supposed to meet Gen-IV design criteria.

System	Neutron spectrum	Coolant	Temperature (°C)	Fuel Cycle
VHTR	Thermal	Helium	900–1000	Open
SFR	Fast	Sodium	550	Closed
SCWR	Thermal or fast	Water	510–625	Open or Closed
GFR	Fast	Helium	850	Closed
LFR	Fast	Lead	480–800	Closed
MSR	Fast or thermal	Fluoride or chloride salts	700–800	Closed
DFR	Fast	Lead	1000	Closed

(SCWR), Sodium-cooled Fast Reactor (SFR) and Very High Temperature Reactor (VHTR). An overview of six designs is given in Table 1.3, with one additional system, the Dual fluid reactor (DFR) that recently emerged and is supposed to reach the Gen-IV standards.
Some of these reactor designs could be demonstrated within the next decade, with commercial deployment foreseen by 2020-2040 with the world's first Generation IV power reactor, the HTR-PM in China, expected to start operation in 2019 [26]. Although still considered a prototype, the HTR-PM is a significant step towards the development of the VHTR. Russia is developing advanced sodium-fast reactor designs for near-term demonstration.

1.2 The role of nuclear data

The accurate knowledge of neutron cross-sections is of major relevance in the design and exploitation of critical and subcritical nuclear systems, especially new systems where the operational experience is limited. Simulations and calculating the behavior of reactor cores depend strongly on capture and fission cross-sections data. In particular, parameters such as the multiplication factor k_{eff}, the Doppler and coolant void reactivity coefficient (see [27]), the reactivity loss during irradiation and the variation of the concentration of isotopes due to transmutation strongly depend on nuclear data.
Nuclear data are compiled into several libraries, so-called evaluated nuclear data libraries. There is no consense in the international community about the best neutron cross section values, thus the validation and accuracy of the few main libraries are still of major concern in the field. It is worth noticing that accurate nuclear data are not only important for future reactors, but also for the current ones. The improved knowledge and accuracy of nuclear data (namely cross-sections, neutron multiplicities, fission neutron spectra) has been essential in improving the efficiency of reactors, since it has allowed, for example, to relax some safety constraints on reactor operation, that were previously required to take into account uncertainties on several basic nuclear parameters.

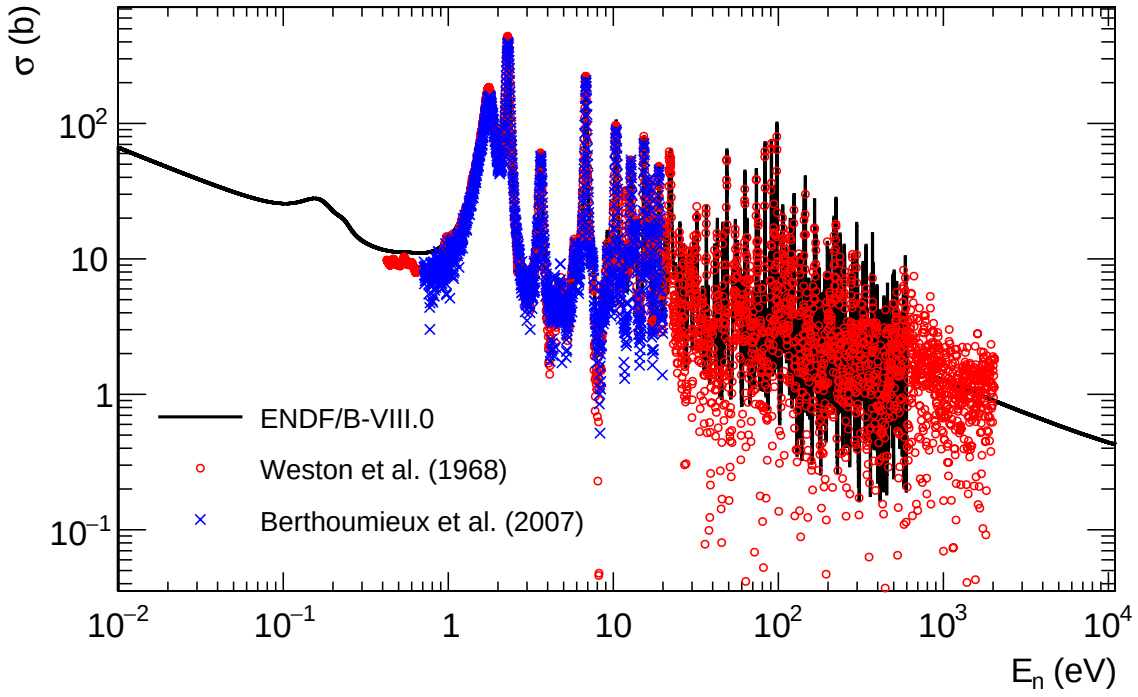

Figure 1.5: The two data sets of ^{233}U(n,γ) from EXFOR compared to the ENDF/B-VIII.0 evaluation.

1.2.1 Present status on the ^{233}U(n,γ) reaction

Regarding the specific case of ^{233}U, the isotope plays the essential role of the fissile nucleus in the Th-U fuel cycle. To understand the reason why the available capture cross sections on ^{233}U are not sufficient for the optimization of a transmutation device and for Generation IV nuclear reactors, one has to consider the two steps previous to the release of the corresponding evaluated files:

- The available data sets are not accurate enough and incompatible with each other. They do not cover the necessary energy range and the resolution provided is not sufficient.
- The available evaluated libraries do not agree between themselves either, due to evaluators being forced to question and re-investigate the accuracy of specific data sets in order to reach a self-consistent result in their evaluation for all the reaction channels.

Thus, the result on the evaluation depends strongly on the decisions adopted by the evaluators but more accurate measurements are necessary to help them constrain the parameters of the physics models applied in the evaluation.
Apart from several thermal cross section values there are only few point wise cross section data available for the ^{233}U(n,γ) reaction. Several experiments have been performed in the past, the first one being from 1966 [28] and several new experiments have been performed, for example at Los Alamos Neutron Science Center (LANSCE) using Detector for Advanced Neutron Capture Experiments (DANCE) [29, 30] or at GELINA [31] at Geel, Belgium, but no results have been presented yet. There are only two, one from 1968 [32] and a more recent one from n_TOF [33], point wise data sets available covering a wider energy range. The two

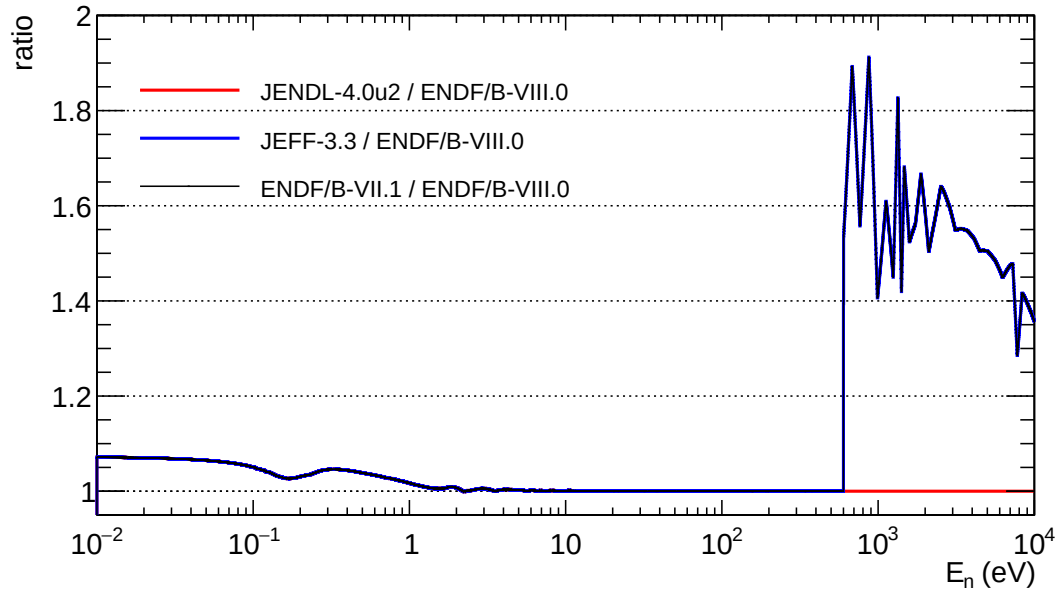

Figure 1.6: Comparison of the ^{233}U(n,γ) cross section ratios between several evaluated libraries and the ENDF/B-VIII.0 library. Significant discrepancies can be seen in the URR above 600 eV while deviations within 8 % are observed for neutron energies below 10 eV.

data sets are shown in Figure 1.5 and are compared to the current ENDF/B-VIII.0 evaluation. The 1968 measurement done by Weston et al. has an energy range up to 2 keV using the fission veto technique while the n_TOF experiment measured the fission and capture cross section simultaneously and provides a better energy resolution. It has to be noted that the 2007 n_TOF data released to the experimental nuclear reaction database (EXFOR) [12, 34]

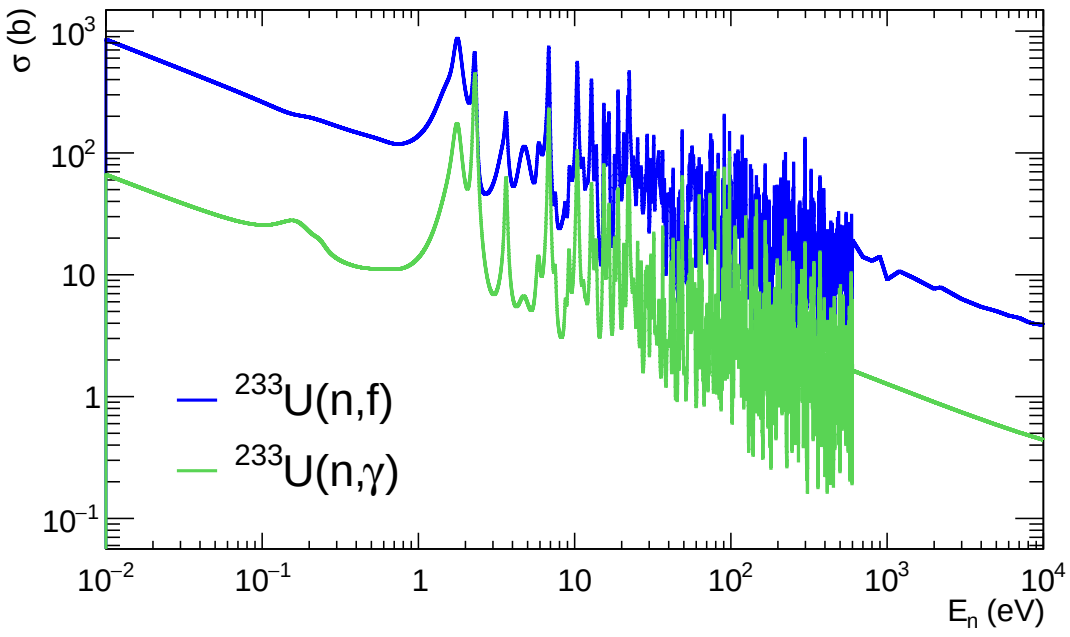

Figure 1.7: Capture and fission cross section of ^{233}U in the ENDF/B-VIII.0 evaluated library. Note the end of the resolved resonance region at 600 eV.

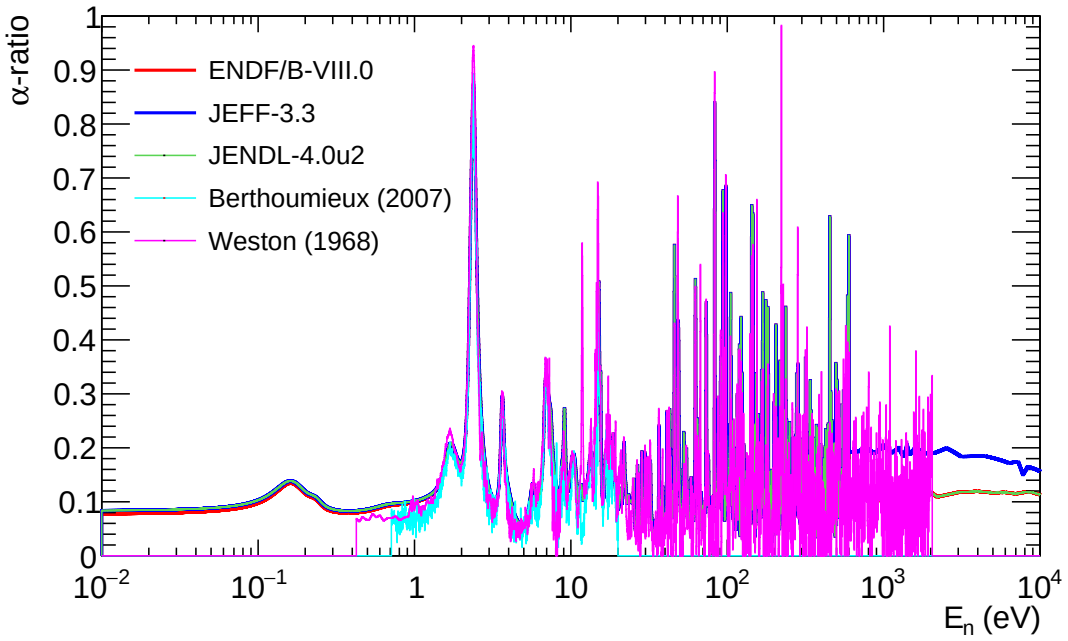

Figure 1.8: Comparison of the ^{233}U α-ratio for different evaluated libraries and previous measurements.

suffer from some experimental effects that were not correctly treated at that time while the fission events could not be tagged reliably. Nevertheless, the Weston data shows a resonance at 11.8 eV which is not present in the n_TOF data nor considered in the evaluations. The origin of this resonance is not clear and is most likely related to a contamination of the sample. The evaluation seems to overestimate the cross section below the first resonance at 1.7 eV where the Weston and n_TOF data clearly show deeper valleys compared to the evaluation. The differences between the two data sets could be attributed to the different energy resolution of the used spectrometers, the n_TOF facility compared to the Rensselaer Polytechnic Institute (RPI) facility.

But not only these two data sets show discrepancies. Figure 1.6 shows the ratio of the ^{233}U(n,γ) cross section for different evaluated libraries to ENDF/B-VIII.0. All evaluations show a deviation within 8 % for neutron energies below 10 eV with respect to ENDF/B-VIII.0. While being in good agreement in the resolved resonance region (RRR), JEFF-3.3 and ENDF/B-VII.1 show significant deviations with respect to ENDF/B-VIII.0 in the unresolved resonance region (URR). In general it must be noted that these evaluations show a systematic dependency between each other because they have been adopted from one another. Regarding comparison of experimental data with evaluations, it is therefore sufficient to compare to one of the evaluated libraries in the RRR.

The reason for the lack of data regarding the ^{233}U(n,γ) measurement is the challenge in the measurement itself. ^{233}U possesses the smallest α-ratio from the fissile isotopes, see Figure 1.3. In Figure 1.7 the ^{233}U fission and capture cross sections are shown from thermal neutron energies up to 10 keV. In all current evaluations the RRR ends at a neutron energy of 600 eV. Comparing the fission and capture cross section the ^{233}U α-ratio is on average close to 0.1, meaning that for each capture event in the experiment the gamma detector

will register around 10 events related to the ^{233}U(n,f) reaction. This dominating background component proves to be the major challenge in the measurement of the ^{233}U(n,γ) or ^{233}U α-ratio . In Figure 1.8 the ^{233}U α-ratio is shown for different evaluations and existing data sets. While the ENDF/B-VIII.0 and JENDL-4.0u2 evaluations show an identical ^{233}U α-ratio , a difference in the ^{233}U α-ratio between ENDF/B-VIII.0 and JEFF-3.3 can be seen, which can only be explained by different values of the capture cross section. All evaluations seem to overestimate the ^{233}U α-ratio below 1 eV while in the RRR a reasonable agreement can be observed. The two data sets are also not in perfect agreement and clear differences can be observed in the peaks of the ^{233}U α-ratio , for example at 1.8 eV.

For the work presented in this thesis the yields of the ^{233}U(n,γ) and ^{233}U(n,f) reactions will be measured relative to each other in order to obtain the ^{233}U α-ratio with the aim to fulfill the targeted goals related to uncertainties of less than 5 % as expressed in entry 9G in the High Priority Request List (HPRL) [35] of the Nuclear Energy Agency.

Chapter 2

Neutron-induced Nuclear Reactions

There is a variety of nuclear reactions which can occur when neutrons interact with nuclei. In this chapter an overview of the theoretical background and basic principles necessary to understand neutron-induced nuclear reactions are described and the needed quantities and techniques used in the measurement of cross section or the α-ratio in fissile isotopes are introduced.

2.1 Neutron cross section

The so-called interaction cross section σ is used to quantify the probability of neutron-induced nuclear reactions. When a neutron beam hits a thin layer of a given isotope, the reaction rate R (1/s) is proportional to the intensity of the neutron beam I ($\mathrm{cm}^{-2}\mathrm{s}^{-1}$) and the number of target nuclei N

$$R = IN\sigma \tag{2.1}$$

assuming that the neutron beam is practically not attenuated by the layer [36]. The proportionality constant σ is known as the cross-section and has the dimension of an area, usually given in barn (barn = $10^{-24}\mathrm{cm}^2$).
A large variety of neutron-induced reactions can occur and for each of these reactions a partial cross section σ_i can be defined. The sum of all σ_i is called the total cross section σ_{tot}

$$\sigma_{tot} = \sum_i \sigma_i = \sigma_{el} + \sigma_\gamma + \sigma_f + \sigma_{inel} + ... \tag{2.2}$$

where the subscript indicates the corresponding reactions, in the listed order: elastic scattering, radiative neutron capture, neutron-induced fission and inelastic scattering. The partial cross sections are very different depending on the specific reaction and the energy of the incident neutron. Furthermore, neutron cross sections are completely different from one isotope to another because they are related to the nuclear structure of the nucleus.
An example cross section is shown in Figure 2.1 showing the neutron capture (n,γ) and fission (n,f) cross section of ^{233}U for a neutron energy range spanning nine orders of magnitude. It can be observed that there is a very wide range of more than six orders of magnitude between the smallest and largest cross section values. Furthermore, within small energy intervals there

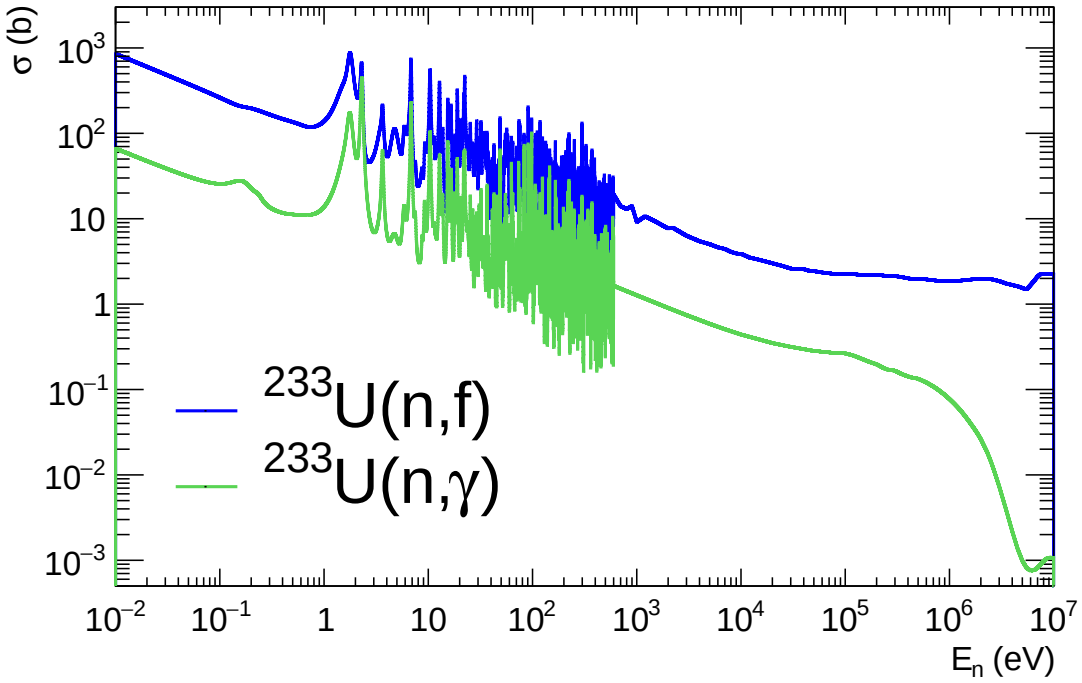

Figure 2.1: Capture and fission cross section of ^{233}U in the ENDF/B-VIII.0 evaluated library.

are strong resonant structures with peak to valley ratios as large as two orders of magnitude for this particular isotope which is not an extreme case.
Four regions can be identified in Figure 2.1:

- For low E_n, thermal and epithermal energies, σ is proportional to the time the neutrons spend in the vicinity of the nucleus ($\sigma \propto 1/\sqrt{E_n} \propto 1/v_n$).
- The resolved resonance region (RRR), between a few eV and a few keV, depending on the isotope, the cross section shows well resolved resonances, with large peak to valley ratios. The nature of these resonant structures is related to the existence of quasi-stationary levels of the *Compound Nucleus* ($n + {}^{A}X \rightarrow {}^{A+1}X^{*}$) and is discussed in the next section.
- The unresolved resonance region (URR) is where the individual resonances start to overlap, meaning that their intrinsic widths become comparable to the distance between neighbouring resonances.
- At higher neutron energies the distances between resonances is much smaller compared to their intrinsic widths and resonant structures cannot be observed anymore. In addition, more and more reaction channels corresponding to threshold reactions open up.

The point wise cross sections displayed in Figure 2.1 correspond to the ENDF/B-VIII.0 evaluated data library and consist of 14994 and 19128 data points for (n,f) and (n,γ), respectively. At low energy the cross sections are usually not provided in a point-wise basis but instead are parameterized in the appropriate theoretical formalisms. This offers the advantage, among

others, of only having to store a few parameters per resonances instead of thousands of points. In the case of single well separated resonances the resonant structures are usually described using the $R-matrix$ formalism in which the shape of each resonance is given by its energy and spin as well as several partial widths Γ_i related to each opened reaction channel. In this way a large number of data points is reduced to a few parameters per resonance. The R-matrix formalism can be extended to the URR and also the $1/v$ region can be described using "negative energy" resonances (corresponding to compound nucleus levels below the neutron separation energy). The *Optical Potential* model provides detailed information on the elastic channel, while the non-elastic ones are treated globally. At higher energies the concept of the nuclear statistical model is relevant. For these models the optical potential yields only the transmission coefficients.

2.1.1 The Compound Nucleus: neutron resonances

The Compound Nucleus theory [37] allows to understand the resonant structures observed in neutron induced reaction cross sections. The basic idea is the that neutron induced reactions take place in two steps:

- In a first step the compound nucleus is formed with a high excitation energy $E^* = S_n + \frac{A}{A+1}E_n$, with the neutron separation energy S_n. At some specific neutron energies, the excitation energy gives rise to a complex configuration of the nucleons corresponding to a quasi-stationary level or resonance defined by its half-life τ, spin and parity.

- In a second step, the excitation energy is released by any open channel, such as emission of γ-radiation (n,γ), the emission of a neutron with equal or lower energy (n,n'), the fission of the nucleus (n,f), etc.

A schematic illustration of the resonances to nuclear levels of the compound nucleus is given in Figure 2.2. The shape of the resonances is in good approximation described by a Breit-Wigner form [38], which is determined by the resonance energy E_0 and a set of partial widths Γ_i , each related to the decay probability of the compound nucleus into the different exit channels (Γ_n ,Γ_γ, etc.). The sum of all widths Γ_{tot} is related to the life-time of the quasi-stationary level of the compound nucleus state by the Heisenberg uncertainty principle $\tau = \hbar/\Gamma_{tot}$ [39]. In the actinide region the observed values of Γ_{tot} are of the order of millielectron volts, thus the expected half-life of 10^{-15} s is several orders of magnitude larger than the typical time needed by a neutron to cross a nucleus without interaction. The physical foundation of this theory is given by the R-matrix theory [40–43].

2.1.2 Radiative capture

In case of the radiative neutron capture reaction (n,γ) the compound nucleus emits γ-rays to de-excite back to the ground or a meta stable (isomeric) state of the compound nucleus. In the context of the analysis of experimental data an accurate reproduction of those electromagnetic (EM) cascades is necessary in order to determine the efficiency of the detection

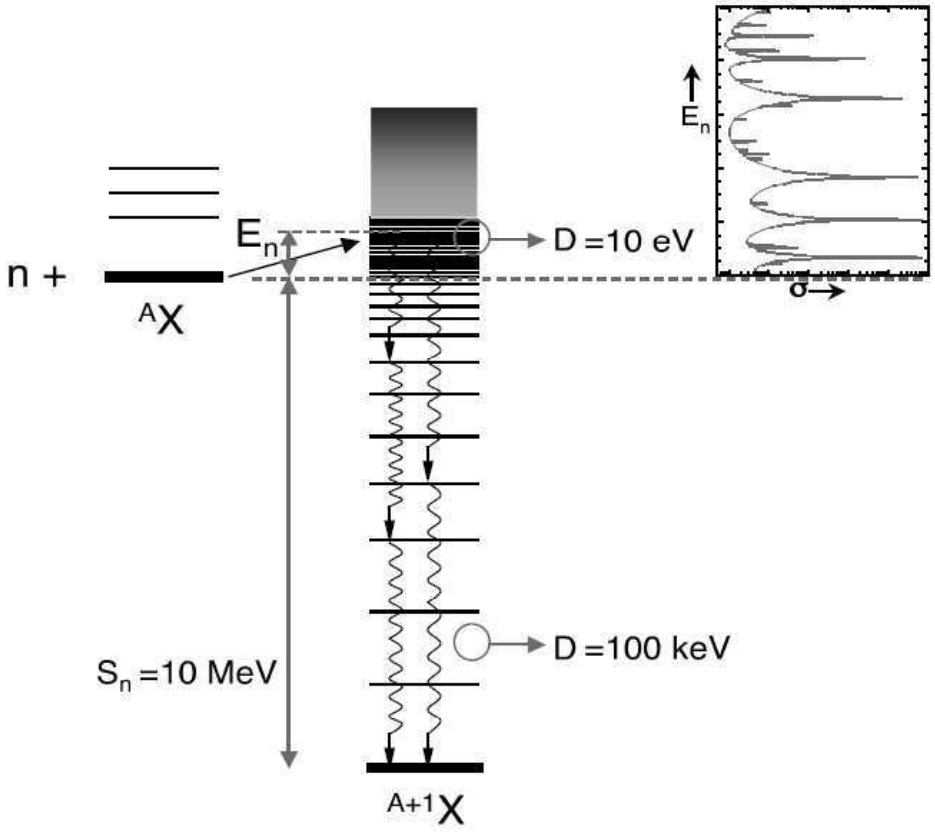

Figure 2.2: Schematic view of the formation a compound nucleus $^{A+1}$X followed by the emission of γ-rays, corresponding to the radiative capture process. Typical values of the average level spacing D at different excitation energies are given as well as the neutron separation energy S_n.

system. For this purpose, it is necessary to know the exact nuclear level scheme of the compound nucleus up to and above the excitation energy as well as all the branching ratios and information related to the conversion electrons for each possible decay path. This is impossible from a practical point of view due to experimental limitations. Therefore the experimental nuclear level scheme measured at low excitation energy must be completed by a statistical model from a specific excitation energy up to the excitation energy of the resonance.
The radiation width $\Gamma_{a\gamma b}$ is translated in the probability of a γ-ray decay from a level with energy E_a to another with excitation energy E_b in most statistical models [44, 45] for the generation of EM cascades. The expectation value of $\Gamma_{a\gamma b}$ for a a given radiation type X (E or M) and multipolarity L is following Fermi's golden rule:

$$\Gamma_{a\gamma b} = f^{(XL)}(E_\gamma) E_\gamma^{2L+1} / \rho(E_a, J_a^{\pi_a}) \tag{2.3}$$

where $\rho(E_a, J_a^{\pi_a})$ is the nuclear level density for states with J^π and $f^{(XL)}(E_\gamma)$ is the so-called Photon Strength Function (PSF) which is assumed to be dependent on the γ-ray energy only and not the property of the initial or final state. There exist several models for the calculation of the nuclear level density, like the Back Shifted Fermi Gas model or Constant Temperature model. The PSF functions are usually parameterized as one or a combination of Standard Lorentzian or Enhanced Generalized Lorentzian (EGLO) functions. These shape functions

are described by three parameters, the Lorentzian energy E_r, the width Γ_r and the cross section σ_r. More details can be found in Refs. [46–49].

2.1.3 Fission

The first extensive theoretical description of fission was given by Bohr and Wheeler [50] and is based on the Liquid Drop Model (LDM) according to which the binding energy E_b of a nucleus depends on its volume (E_V), surface (E_S), electrostatic (or Coulomb) repulsion between its protons (E_C) and its specific composition of nucleons ($E_A, \delta(A,Z)$))

$$E_b = E_V - E_S - E_C + E_A + \delta(A,Z). \tag{2.4}$$

In a heavy nucleus a nucleon in the center of the nucleus is in constant motion due to the attraction of the rest of the nucleons. Since it is completely surrounded the net force is zero. For a nucleon on the surface of the nucleus this is not the case. The net force applied to such a nucleon is directed towards the center, thus the nucleon is pulled inwards and repelled starts to oscillate due to the repulsion of the inner nucleons. As a consequence the nucleus in the classical picture has a spherical shape with a vibrating surface. The amplitude of those oscillations and the probability of a nucleus fissioning increases as energy is added from outside, like by formation of a compound nucleus. In the simple picture, fission will happen once the amplitude of the vibration or deformation has reached a critical energy, or threshold. The energy threshold corresponds to a so-called fission barrier height, characteristic for the nucleus involved. Below this threshold it is very unlikely to de-excite via fission but instead the nucleus will de-excite via emission of γ-rays. The LDM alone is not sufficient to describe the fission process properly. It has been shown [50] that the nuclear radius of the compound nucleus can be expanded in Legendre polynomials leading to the quadrupole and octupole deformations describing the shape of the nucleus with an ellipsoid. Including quantum-mechanical corrections, namely shell corrections [51], in the calculations results in a model of the fission process sufficient to describe many observables in the fission process and leads to the so-called double-humped fission potential. In Figure 2.3 a schematic view of the fission process is given with the double-humped fission potential. Just after the neutron reaches the target nucleus, the compound nucleus is formed at a nuclear level with excitation energy E^*. If this energy is above the fission threshold (barrier) the fission reaction is energetically possible and the reaction channel is open. If E^* is smaller than the fission threshold fission is still possible, even if strongly suppressed, via tunneling through the barrier. In some nuclei the excitation energy of the compound nucleus is larger than the fission barrier no matter what the neutron energy. This is the case in ^{233}U, ^{235}U and ^{239}Pu, thus those nuclei are called fissile. In the fission process the compound nucleus is split into two highly excited fragments. The fission fragments de-excite from states with high angular momenta and excitation energies via emission of prompt neutrons and a prompt γ-ray cascade. The total released energy during fission can be derived from the conservation of energy law and is on average about 200 MeV considering thermal fission of ^{235}U. This energy is distributed between the excitation and kinetic energy of the fission fragments. The fission

Table 2.1: Average total released energy ΔE, total kinetic energy TKE of the fission fragments, average number of prompt neutrons and γ-rays emitted in thermal fission from ENDF/B-VIII.0.

Reaction	ΔE (MeV)	TKE (MeV)	$\overline{\nu}$	m_γ
$^{233}U + n_{th}$	198	168	2.479	8.0
$^{235}U + n_{th}$	203	169	2.414	8.6
$^{239}Pu + n_{th}$	206	175	2.870	7.6

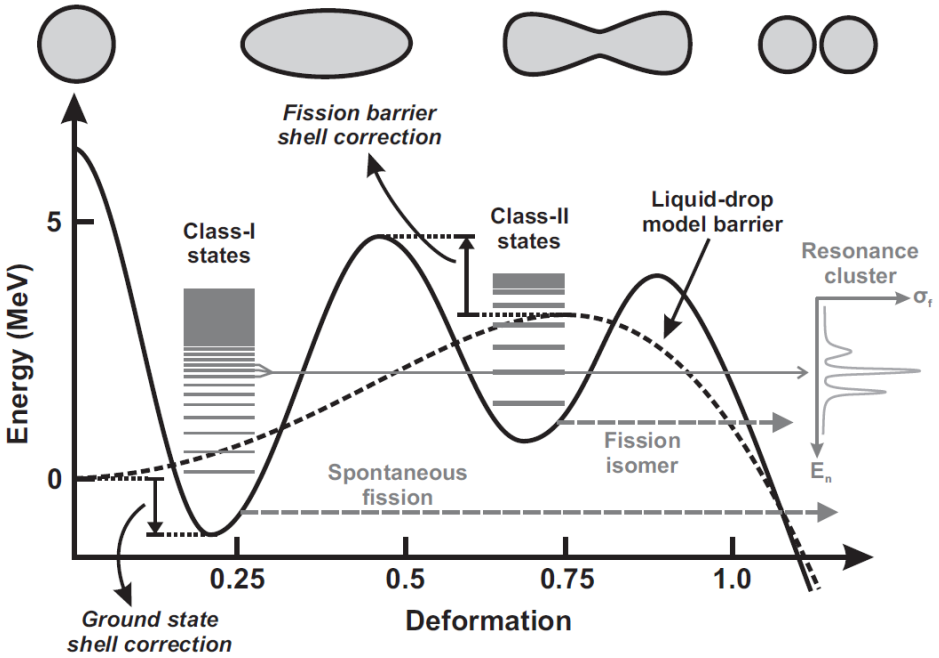

Figure 2.3: Schematic illustration of the double-humped fission potential, taken from [54]

fragments de-excite by emitting fission neutrons, with kinetic energies in the MeV range) and the prompt γ-rays. In fissile isotopes the fission cross section is typically larger than the capture cross section. In the measurement of capture cross sections in fissile isotopes this fact combined with the large amount of prompt γ-rays and fission neutrons emitted, see Table 2.1 leads to an overwhelming amount of background that must be accurately subtracted in the analysis.

Furthermore, the fission potential consists of two wells: one in small deformations and another in larger ones. Each well is occupied by states which are designated as class-I and class-II ones for small and large deformations, respectively. Class-I states are denser and lie in a narrower well, while class-II ones are more sparsely spaced and reside in a much wider well, hence their larger lifetime that can explain the existence of fission (or shape) isomers. Fission isomers are excited nuclear states which decay by spontaneous fission or γ de-excitation to the ground state after population in a nuclear reaction. The half lives depend on the height and width of the potential barriers. The nuclei caught in the second minimum can either tunnel through the outer barrier (isomeric fission), or can decay back to the first minimum (isomeric γ-decay). For ^{233}U fission isomeric states with a half life of 30.4(49) ns [52, 53] have been reported.

2.2 Measurements of cross-sections

Cross sections are experimentally measured by determining the reaction yield $Y(E_n)$ which gives the fraction of the beam that undergoes a certain nuclear reaction x of interest and can be expressed by

$$Y(E_n) = (1 - e^{-n\sigma_{tot}(E_n)})\frac{\sigma_x(E_n)}{\sigma_{tot}(E_n)} + \text{multiple scattering corrections}, \tag{2.5}$$

where n is the surface density of the sample. The first term in equation (2.5) corresponds to self shielding (neutron beam attenuation through the sample and is important in the case of thick samples. If only thin samples are used an approximation can be made, the so-called thin sample approximation, where $lim\ n\sigma_{tot} \rightarrow 0$ and the multiple scattering corrections are negligible, thus the reaction yield becomes directly proportional to the cross section of interest σ_x

$$Y(E_n) = n\sigma_x(E_n). \tag{2.6}$$

In the experiment the number of the reaction products $c(E_n)$ is measured together with the neutron fluence at sample position $\Phi(E_n)$, the efficiency for detecting these reaction products ε. After the subtraction of the background $b(E_n)$ the reaction yield can be determined to

$$Y(E_n) = \frac{c(E_n) - b(E_n)}{\Phi(E_n)\varepsilon(E_n)} \tag{2.7}$$

assuming no dead time or pile-up corrections, which can be considered in the efficiency ε if necessary. The reaction cross section of interest can then be calculated combining equations 2.6 and 2.7 to

$$n\sigma_x(E_n) = \frac{c(E_n) - b(E_n)}{\Phi(E_n)\varepsilon}. \tag{2.8}$$

Several experimental methods exist to measure neutron cross sections. All of them require a neutron source and a sample as isotopically pure as possible. If neutron energy dependent cross sections are needed a Time-of-Flight (TOF) spectrometer is usually the choice.

2.2.1 Time-of-Flight method

In a Time-of-Flight experiment, the kinetic energy of the neutrons E_n is determined by their required time TOF to travel a given distance L.
Typically, in this type of measurement the neutrons are produced by a pulsed neutron source at time t_0. They travel towards the sample at the measuring station at a distance L with respect to the point of creation. Depending on the facility L can range from centimeters to hundreds of meters. The neutrons interact with the nuclei of the sample and the reaction

products are measured at the time t_n. The times t_n are directly related to the energy of the incident neutron via

$$E_n = E_{tot} - mc^2 = \frac{mc^2}{\sqrt{1 - v^2/c^2}} - mc^2, \tag{2.9}$$

where c is the speed of light. The classical expression for the neutron kinetic energy can be obtained from the first term of the series expansion

$$E_n(eV) = \frac{1}{2} m_n v^2 = \left(\frac{72.2983 \cdot L(m)}{t_n(\mu s) - t_0(\mu s)} \right)^2 . \tag{2.10}$$

The immediate consequence is that the resolution of a TOF spectrometer is given by the flight path length and its uncertainty, the time resolution of the detection system and the so-called Resolution Function of the facility. The Resolution Function describes the additional time neutrons spend in the neutron producing target before travelling to the sample, resulting in a spread in time-of-flight. It is characteristic for the production mechanism and the geometry of the target and is described in section 3.1.3 for the used TOF spectrometer.

2.2.1.1 Resonance Broadening

In addition to the broadening from the resolution function of the facility a thermal broadening effect has to be considered. Usually experiments take place at a non-zero temperature which results in a vibration of the nuclei of the sample. This causes a broadening in the resonances as the energy at which a reaction occurs is thus not only given by the incident's neutron energy anymore but also by the motion of the nuclei. This effect is commonly referred to as Doppler broadening (DB) and the most common model to describe this effect is the free gas model. In good approximation, the expression of the FWHM of the Gaussian broadening of the resonances Δ_{DB} can be written as

$$\Delta_{DB} = 2\sqrt{ln2}\sqrt{\frac{4E_n k_B T m_n}{M}}, \tag{2.11}$$

where k_B is the Boltzmann constant, E_n the neutron energy, T the effective temperature ($\approx$ ambient temperature [55]) and m_n and M the masses of the neutron and the target nucleus, respectively. This effect is later illustrated together with the resolution function of the used TOF spectrometer in section 3.1.3. Below neutron energies of a few electronvolt the free gas model using an effective temperature is usually not valid anymore and a crystal lattice model [56] should be used instead.

2.2.2 Measurement of capture cross-sections in fissile isotopes

The measurement of a neutron capture cross section $\sigma_\gamma(E_n)$ is usually performed by detecting the outgoing γ-ray cascades after the formation of the compound nucleus. In fissile nuclei the probability of undergoing a fission reaction is on average higher compared to the capture reaction, this is expressed in the so-called α-ratio which is the ratio between the capture and fission cross section. Furthermore, since the capture and fission reaction are de-excitations

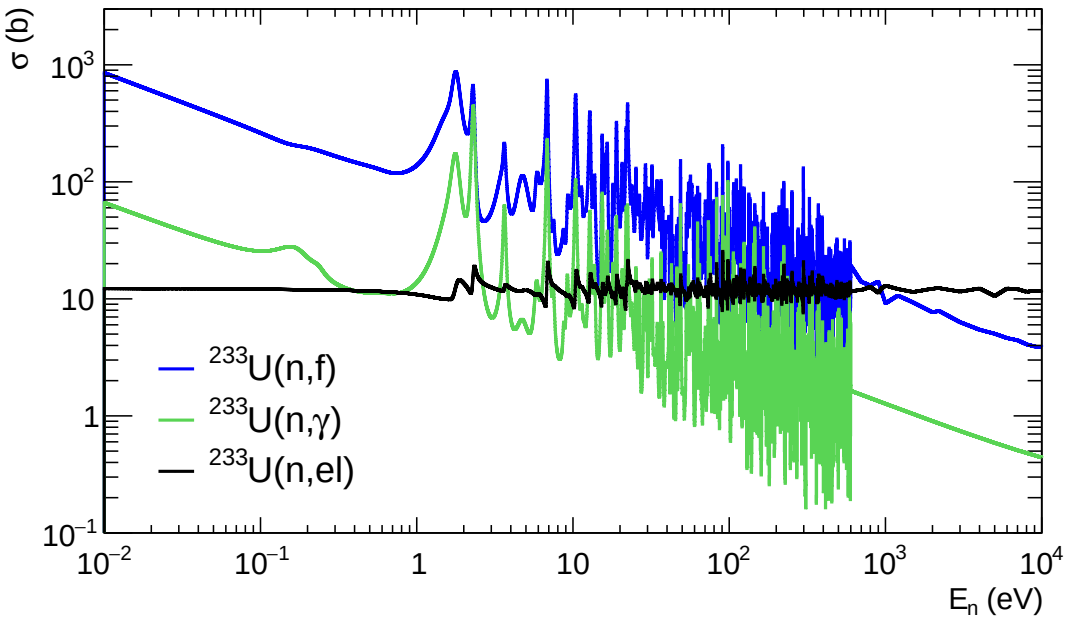

Figure 2.4: ^{233}U(n,γ) , ^{233}U(n,γ) and ^{233}U(n,n) cross sections from ENDF/B-VIII.0.

of the compound nucleus, the capture and fission cross section will show a similar resonant behaviour, as can be seen in Figure 2.4. The energy released in a fission reaction via γ-rays and their multiplicity is on average higher than in a capture reaction. Thus, measuring (n,γ) cross sections in fissile isotopes is challenging due to the competing stronger fission reaction producing large amounts of background.

A careful and precise subtraction of the fission reaction induced background has to be performed. In order to accomplish this the so-called *fission tagging technique* [29, 30, 57–61] is applied. The key idea of the technique is to employ a fission detector to detect the fission fragments in addition to the γ-rays from the capture or fission reaction measured by γ-ray detectors. Considering time coincidences between both detection systems, the fission γ-ray cascades can be tagged and then subtracted knowing the efficiency of both detection systems. Since the idea came up [57, 58] it has been modified and improved at the n_TOF [59, 61] and DANCE [29, 30] facility in recent years. Nevertheless the technique also has some inherent difficulties:

- Employing a fission tagging detector into the neutron beam will lead to a large amount of material intercepting the neutron beam. This material produces a significant amount of background in the γ-detector coming from (n,γ) reactions.
- Determining the fission detector efficiency has to be done very carefully as it will directly lead to a systematic uncertainty in the determination of the ^{233}U(n,γ) cross section or ^{233}U α-ratio .
- In order to reduce the tagging uncertainty a high efficiency is desired for the fission detector. This can be achieved by using thin targets with a very low mass. This leads

to a lower capture to background ratio compared to thicker samples and longer periods of measurement are required to obtain sufficient counting statistics.

Due to those constraints, not all fission and γ-ray detectors are suitable for this technique which requires:

- High detection efficiency γ-ray detectors for (n,γ) cascades like the n_TOF Total Absorption Calorimeter (TAC) [62].
- Compact, high detection efficiency fission detectors for the (n,f) reaction with low mass, which has been developed for this measurement [63].

Both detection systems will be described in section 3.2 and 3.3.

As described the cross section cannot be measured directly. The experimental observable is the reaction yield $Y_x(E_n)$ (compare equation (2.7)):

$$Y_x(E_n) = \frac{C_x(E_n)}{\Phi(E_n)} \tag{2.12}$$

where $C_x(E_n)$ is the total number of reactions produced in the targets and $\Phi(E_n)$ is the number of neutrons impinging on the sample. The total number of reactions is obtained from the difference of the total number of detected reactions $c_{tot}(E_n)$ and the background $b(E_n)$ and has to be corrected for the efficiency $\varepsilon_x(E_n)$ for detecting the specific reaction products

$$C_x(E_n) = \frac{c_{tot}(E_n) - b(E_n)}{\varepsilon_x(E_n)}. \tag{2.13}$$

In equation (2.13) dead time corrections are implicitly assumed in the efficiency $\varepsilon_x(E_n)$. Usually the higher the reaction rate the larger those dead time corrections and the smaller the efficiency. In the case of this measurement dead time corrections are negligible below count rates of 0.1 μs^{-1} and will be discussed in section 4. The background in the measurement can be written as the sum of the background induced by fission, the prompt fission γ-ray cascade $b_{FissPrompt}$ and other sources of background b_{other}, i.e. the material intersecting the neutron beam

$$b(E_n) = b_{FissPrompt} + b_{other}. \tag{2.14}$$

The prompt fission γ-ray background $b_{FissPrompt}$ is determined with the fission tagging technique and can be calculated by using the counts in coincidence between the fission and γ-ray detectors, $b_{tagg}(E_n)$ divided by the tagging efficiency ε^f_{TAC}, which takes into account that not all fission events are tagged by the fission detection system

$$b_{FissPrompt} = \frac{b_{tagg}(E_n)}{\varepsilon^f_{TAC}}. \tag{2.15}$$

The tagging detection efficiency ε^f_{TAC}, and the fission detection efficiency ε_{FICH} are the same quantity only in the particular case that the probability of detecting a fission reaction

with one of the detectors does not depend on whether it has been detected by the other. Resubstituting equations 2.13, 2.14 and 2.15 into 2.12 the reaction yield for the neutron capture reaction can be written as

$$Y_\gamma(E_n) = \frac{c_{tot}(E_n) - \frac{1}{\varepsilon^f_{TAC}} b_{tagg}(E_n) - b_{other}(E_n)}{\Phi(E_n)\varepsilon^\gamma_{TAC}} \tag{2.16}$$

with the TAC detection efficiency ε^γ_{TAC} for capture events. The experiment requires the simultaneous measurement of the neutron capture and neutron-induced fission reaction yields. Thus the measurement provides the ratio between both reaction yields which can be expressed for small neutron energy intervals

$$\frac{Y_\gamma(E_n)}{Y_f(E_n)} = \frac{\frac{\sigma_\gamma(E_n)}{\sigma_{tot}(E_n)}(1 - e^{-n\sigma_{tot}(E_n)})}{\frac{\sigma_f(E_n)}{\sigma_{tot}(E_n)}(1 - e^{-n\sigma_{tot}(E_n)})} = \frac{\sigma_\gamma(E_n)}{\sigma_f(E_n)} = \alpha(E_n). \tag{2.17}$$

With the number of fission reactions $c_f(E_n)$ and related background from the natural α-decay of the ^{233}U $b_f(E_n)$ detected by the fission detector, the experimental α-ratio can be calculated as

$$\alpha(E_n) = \frac{Y_\gamma(E_n)}{Y_f(E_n)} = \frac{\varepsilon_{FICH}}{\varepsilon^\gamma_{TAC}} \frac{c_{tot}(E_n) - \frac{1}{\varepsilon^f_{TAC}} b_{tagg}(E_n) - b_{other}(E_n)}{c_f(E_n) - b_f(E_n)}. \tag{2.18}$$

Measuring the α-ratio, as in equation (2.18), is an absolute measurement of the ratio between both reaction channels and minimizes systematic uncertainties since:

- Cancellation of errors in the determination of the shape and absolute value of the neutron fluence.
- The measurement does not depend on the actual mass of the sample and thus related uncertainties in the measurement or determination of the mass do not enter in the calculation.

In this way systematic uncertainties associated with the sample thickness and inhomogeneities as well as the absolute value of the neutron fluence are removed from the calculation.
The α-ratio's sensitivity related to the fission tagging efficiency ε^f_{TAC} can be estimated by propagating its uncertainty to the α-ratio under the following assumptions:

- The probability of detecting γ-ray cascades from (n,γ) or (n,f) reactions is similar.
- The (n,f) events are detected independently by both detection systems. Thus the fission tagging efficiency and the fission detection efficiency are the same quantity $\varepsilon^f_{TAC} = \varepsilon_{FICH}$.

With those assumptions the α-ratio sensitivity with respect to ε^f_{TAC} can be expressed as

$$\frac{\Delta_{\varepsilon^f_{TAC}}(\alpha(E_n))}{\alpha(E_n)} = \left(1 + \varepsilon^\gamma_{TAC}\frac{\sigma_f(E_n)}{\sigma_\gamma(E_n)}\right)\frac{\Delta(\varepsilon^f_{TAC})}{\varepsilon^f_{TAC}}. \tag{2.19}$$

It has to be noted that in the case of ^{233}U the fission to capture cross section ratio σ_f/σ_γ is about 10 on average, meaning that an uncertainty of 1 % in the tagging detection efficiency will introduce a systematic uncertainty of 10 % in the α-ratio. Thus, an accurate determination of this parameter is crucial for the calculation of the ^{233}U α-ratio .
In summary, the measurement of an α-ratio offers the advantage of reducing the systematic uncertainties compared to a standard cross section measurement due to the cancellation of errors in the determination of the shape and absolute value of the neutron fluence as well as independence of the actual sample mass or normalization. In order to ensure a high quality measurement the key quantities in the fission tagging method are accurately determined values of the efficiencies of the γ-ray and fission detectors.

Chapter 3

Experimental Setup

The measurements of the ^{233}U α-ratio presented here were performed at the n_TOF facility at CERN employing two detection systems, namely n_TOF 's Total Absorption Calorimeter and a novel fission chamber optimized for this measurement to allow tagging of the prompt fission γ-ray spectra. The aim of this chapter is to describe the n_TOF facility, the two detection systems and the Data Acquisition System as well as the ^{233}U samples used in the measurements.

3.1 The n_TOF facility at CERN

The n_TOF facility was proposed by Rubbia et al. [64] in 1998 and built at CERN from 2000 to 2001. The facility provides the nuclear scientific community with a powerful tool for the measurement of energy dependent neutron cross-sections in an energy range from thermal up to GeV. The measurements primarily focus on satisfying data needs from nuclear astrophysics, nuclear technology, medical physics and basic nuclear research. Recently the activities at n_TOF have expanded and now include also detector and electronics development as well as using n_TOF as a neutron imaging facility [65].

At n_TOF neutrons are produced in a spallation reaction in lead induced by protons. The schematic layout of the facility is given in Figure 3.1 together with the accelerator complex of CERN. A full CAD model of the n_TOF facility is shown in Figure 3.2. The facility comprises of the spallation target area, the neutron beam lines with their respective collimators and magnets and the experimental areas.

300 neutrons per 20 GeV/c proton are created on average via spallation of lead induced by proton beams delivered by CERN's Proton Synchrotron (PS). The average proton beam intensity is $7 \cdot 10^{12}$ or $4 \cdot 10^{12}$ protons per bunch which depends on the beam type, dedicated or parasitic respectively. The proton beams exhibit a width (RMS) of 7 ns for both pulses types [67]. Thus the average time structure of the two beam types is not identical but the effect on the resolution function or TOF introduced by the different widths is negligible in the neutron energy region of interest below 10 keV. CERN's accelerator complex is able to deliver proton beams to n_TOF with a maximum repetition rate of 0.8 Hz, the average being lower though. The high intensity pulsed proton beam results in a high instantaneous neutron flux. This allows measurements of highly radioactive samples or low mass samples due to

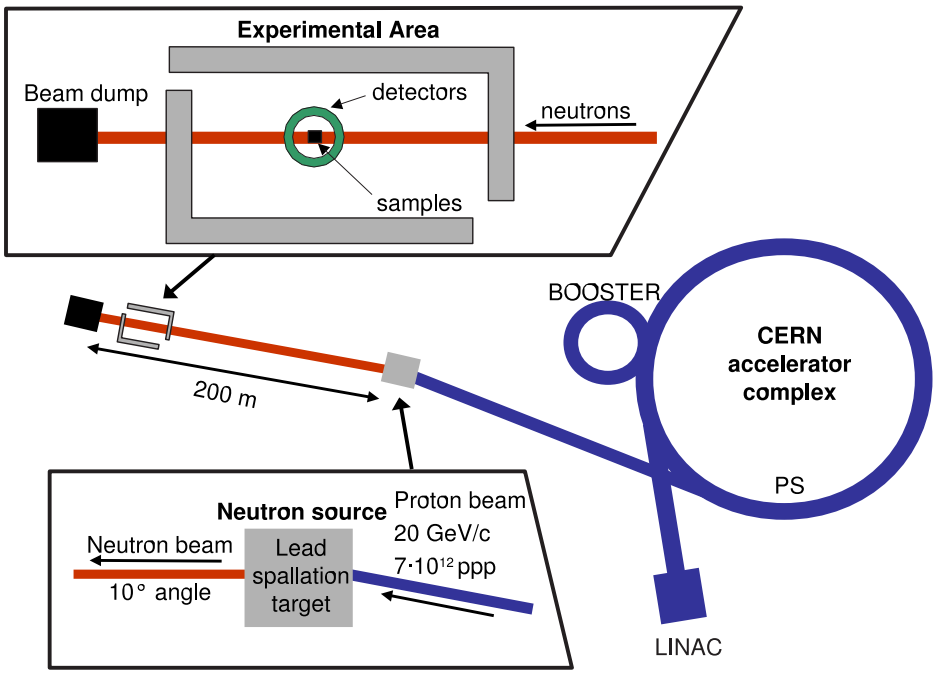

Figure 3.1: Schematical overview of the n_TOF facility at CERN, only showing experimental area 1, picture taken from [66].

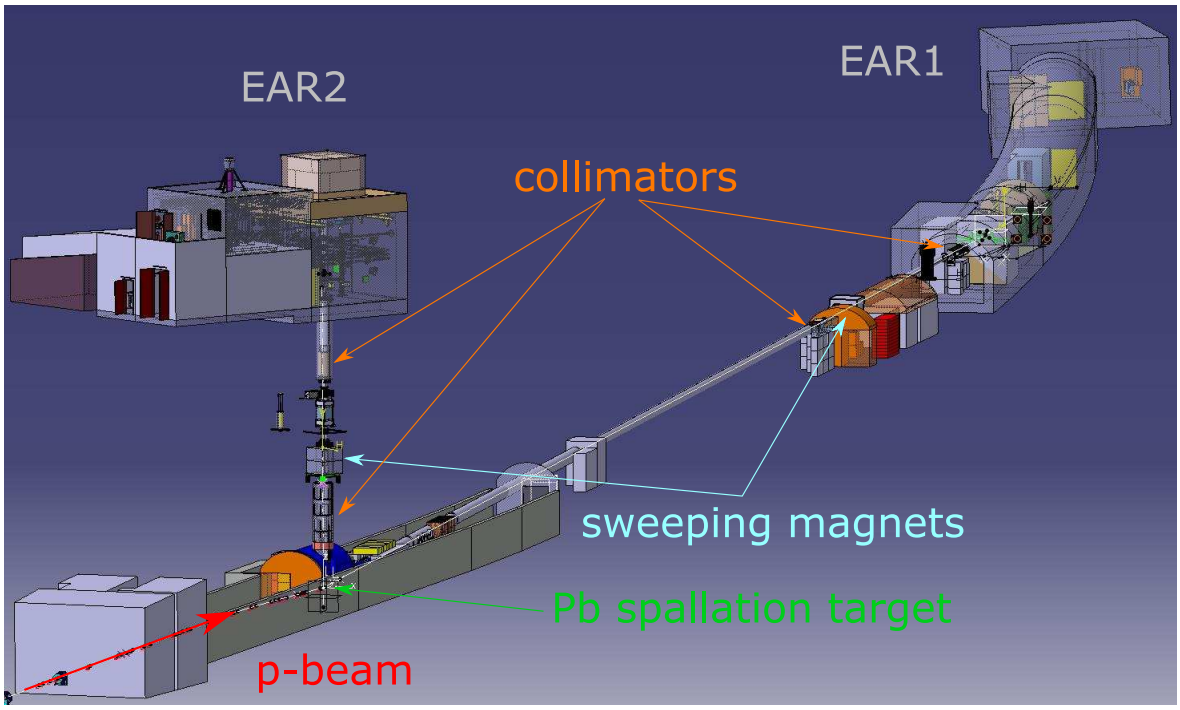

Figure 3.2: CAD model of the full n_TOF facility. Indicated are both experimental areas, the spallation target, sweeping magnets and collimators.

an improved signal to background ratio, compared to other facilities at similar flight paths length.

The proton beam impinges on the lead spallation target under an angle of 10° with respect to the EAR1 neutron beam line , in order to reduce the amount of charged particles and γ-rays which are strongly forward directed. The lead is immersed in demineralized water used as coolant as well as for moderating the initially fast neutrons into a white neutron spectrum down to thermal energies. For EAR1, an additional layer of borated water intercepts the neutron beam to suppress and shift the 2.2 MeV γ-rays from neutron capture in hydrogen to 0.48 MeV γ-rays from ^{10}B(n,α), at the same time also reducing the thermal and epithermal neutron flux. The neutrons travel inside evacuated beam lines towards the experimental areas. Strong magnets eventually sweep charged particles from the beam and the neutron beam itself is shaped with massive collimators made out of iron, concrete and borated polyethylene.

n_TOF simultaneously operates two experimental areas with complementary features, with the second experimental area built in 2014 [68]. While experimental area 1 (*EAR1*) provides a flight path length of roughly 180 m and therefore exhibits an excellent energy resolution, experimental area 2 (*EAR2*) at 20 m flight path length trades energy resolution for a roughly 40 times larger instantaneous neutron flux, which allows measuring highly radioactive and low mass samples [69].

3.1.1 Neutron fluence

The entrance of the neutron beam to the experimental area (EAR1) is located 182 m from the spallation target. The shape of the neutron fluence at EAR1 was determined during the commissioning phase of the Phase-II target in 2009. Two calibrated fission chambers from PTB (Physikalisch-Technische Bundesanstalt) [70] were used to determine the absolute value of the neutron fluence. In addition to those fission chambers other auxiliary detection systems such as a silicon detector using a ^{6}Li foil, C6D6 γ-ray detectors and Parallel Plate Avalanche Counters (PPAC) were employed to investigate certain energy regions in more detail. The full details of the determination of the neutron fluence in EAR1 are given in [71].

Complementary to the measurements, calculations of the production and moderation of the neutrons have been performed with the Monte-Carlo code FLUKA [72] and MCNP [73]. In Figure 3.3 the FLUKA simulation of the neutron fluence in EAR1 is shown. Concerning the shape of the fluence four different regions can be identified. The bump at a neutron energy of about 100 MeV correspond to spallation neutrons. The high neutron energy (MeV region) shape corresponds to a typical evaporation spectrum, while the region from 1 eV to 10 keV corresponds to partially moderated neutrons. The low energy region below 1 eV originates from fully thermalized neutrons but is strongly suppressed by the borated water intercepting the neutron beam at the level of the target, as described before. There are several dips in the otherwise smooth shape of the neutron fluence. Those dips, especially in the 100 eV to 100 keV region, correspond to resonances of aluminum of the pipes and flanges of the neutron beam line. The dip at roughly 300 eV corresponds to a resonance of manganese also present in the aluminium alloy of the pipes and flanges.

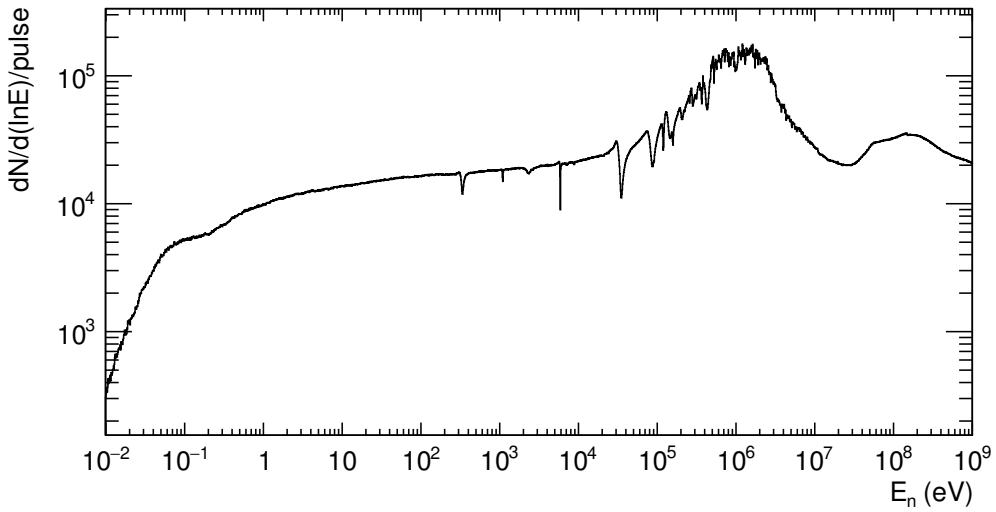

Figure 3.3: Neutron fluence in EAR1 from FLUKA simulations in isolethargic units.

3.1.2 Neutron beam profile

Two collimators are installed along the 182 m flight path towards EAR1. The first one with an inner diameter of 11.5 cm is located at 136.7 m and consists of 2 m of concrete and steel. The second collimator is the beam shaping collimator which is located immediately before the experimental area at 178 m and consists of 2.5 m iron and 5 % borated polyethylene. Two versions of the second collimator are available, e.g. a big collimator opening mainly devoted to neutron induced charged particle reactions, and a small collimator aperture devoted to capture measurements. For the ^{233}U α-ratio measurement the small collimator, standard for capture measurements at n_TOF , with an aperture diameter of 18 mm was installed.
The spatial distribution of the neutron beam was measured with a stripped MicroMegas detector [74] for the Phase-I spallation target at n_TOF . The spatial neutron beam profile of the Phase-II target has been measured with a newly developed 2D pixelated MicroMegas detector [75] which provided results compatible with the Phase-I target [66]. The profile has been simulated as well with FLUKA and the profile of the neutron fluence at a flight path of 185 m is shown in Figure 3.4. The neutron beam profile has a flat top Gaussian like shape with a width of $\sigma = 0.77$ cm, corresponding to a FWHM of roughly 16 mm and a total width of less than 40 mm which varies slightly with neutron energy. The alignment of samples with respect to the neutron beam can usually not be done insitu. At n_TOF samples are aligned with finite precision to a hair cross given by lasers which are calibrated with the center of the beam. This adds an uncertainty to the position of the samples. Depending on the size of the samples this can introduce an uncertainty on the so-called beam interception factor, defined by the fraction of neutrons hitting the sample divided by the total number of incoming neutrons. The FLUKA simulations allow to estimate the uncertainty on this beam interception factor.

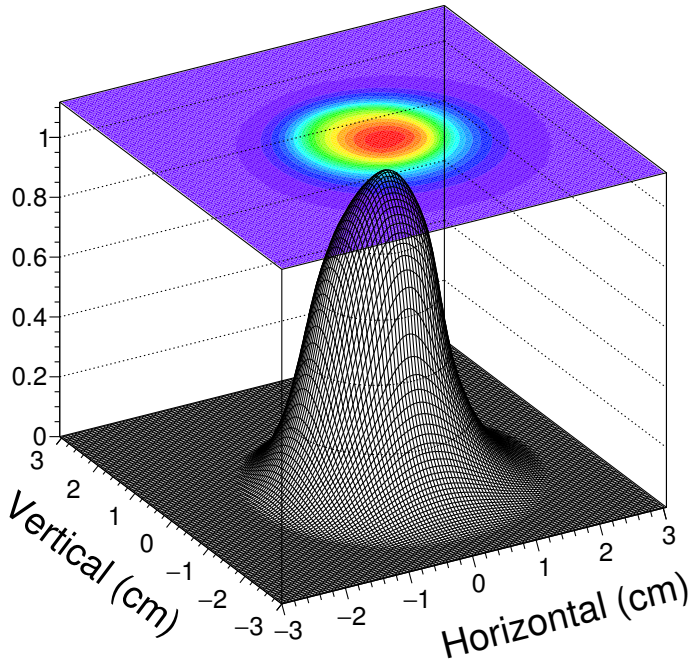

Figure 3.4: Spatial profile of the neutron beam in EAR1 at 185 m taken from FLUKA simulations for the full energy range of n_TOF .

3.1.3 Resolution function

Neutrons arriving at a given time-of-flight at the sample position can have different neutron energies due different amounts of time spent inside the spallation target-moderator assembly. Hence, the relation between neutron energy and time of flight is not unambiguously defined, but is influenced by a distribution called Resolution Function (RF). The resolution function is given by the initially produced neutrons, the target-moderator assembly and the flight path length and is therefore unique to the facility and experimental area.

The n_TOF resolution function has been calculated with FLUKA and MCNP. The results of the simulations were validated by measuring narrow p- and d-wave capture resonances like in iron as they are very sensitive to the shape of the RF.

The RF introduces a broadening of the resonances in the measurements of neutron cross-sections because they are measured as a function of time-of-flight. Another additional broadening effect known as Doppler broadening is caused by thermal motion of the nuclei, as described in section 2.2.1.1. Both broadening effects depend on the neutron energy and their respective effect on the resolution are shown in Figure 3.5. While Doppler broadening is dominating the low energy region the RF starts to dominate above a few keV in EAR1. The widths Γ_γ of the ^{233}U(n,γ) resonances are shown as well and below 100 eV its resonances can be resolved by the n_TOF spectrometer. Resonances are analyzed with specialized R-Matrix codes which are able to correct for effects like Doppler broadening and the resolution function.

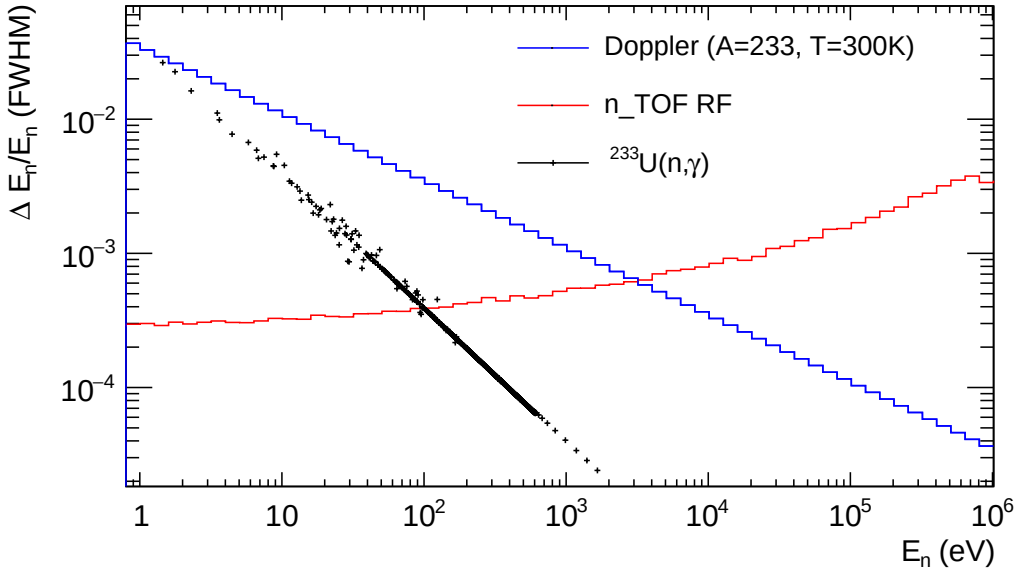

Figure 3.5: Comparison of the effects of Doppler Broadening ($T = 297\,\mathrm{K}$) for ^{233}U and of the n_TOF resolution function on the resolution of the ^{233}U α-ratio measurement. The resonance widths Γ_γ of the ^{233}U(n,γ) resonances according to ENDF/B-VIII.0 are plotted.

3.1.4 Data Acquisition

The n_TOF facility provides the advantage of using its fully digital Data Acquisition system (DAQ), fully described in Ref. [76]. The advantage of such a system is that it allows to analyze the data offline by *pulse shape analysis* (PSA) routines optimized for every individual detector. The read-out of all detector channels is done via high performance digitizers, ADQ412 or ADQ414 [77], with 12 or 14 bit resolution respectively which are operated at 500 MSamples/s. The flash-ADCs are triggered with a common external clock to avoid time drifts between different modules. A data buffer corresponding to a time-of-flight window of 100 ms, triggered by the PS, is digitized for every proton bunch hitting the spallation target. This allows to reconstruct neutron energies from 20 meV up to 20 GeV. To reduce the data size a zero suppression algorithm is applied to select and store only part of the buffer containing true detector signals with an amplitude larger than a certain threshold individual for each flash-ADC. The data of all detectors are merged into segments, transferred to and stored on tapes. The required tapes and the infrastructure behind is provided by the *CERN Advanced STORage manager* (CASTOR) [78].

The first particles arriving in the experimental area are relativistic charged particles and γ-rays produced in the spallation reaction. The response to those particles in the detectors is referred to as the γ-flash. This response varies from detector to detector and with the proton beam intensity. Due to those particles a detector can saturate and remain *blind* for a certain period of time, shown in Figure 3.6 where a BaF_2 detector is saturated for several microseconds after the γ-flash. The recovery time of a detector determines the upper limit for the neutron energy range that can be analyzed.

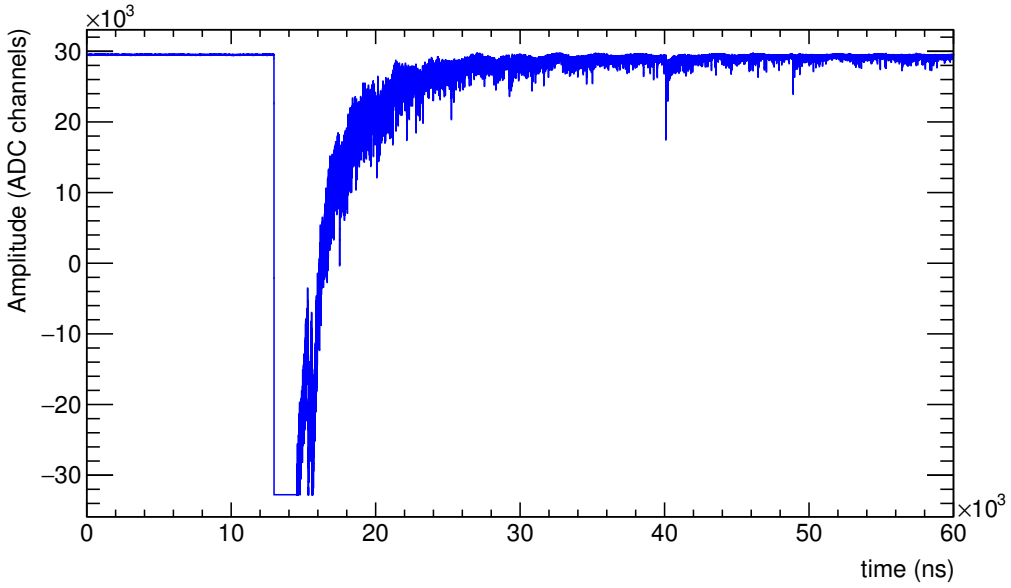

Figure 3.6: Example of the response of a BaF_2 module to the γ-flash.

3.1.5 Neutron beam monitors

The neutron beam intensity in EAR1 is constantly monitored with four out-of-beam silicon detectors (SiMon) [79] looking at a lithium foil measuring the outgoing particles of the standard reaction ^{6}Li(n,t)^{4}He reaction, which has a large, smooth and well known cross-section. The SiMon detector was designed to interfere as little as possible with the neutron beam. It consists of a thin Mylar foil with a 600 µm/cm^2 thick ^{6}LiF deposit surrounded by four off-beam silicon detectors as shown in the scheme in the left panel of Figure 3.7.

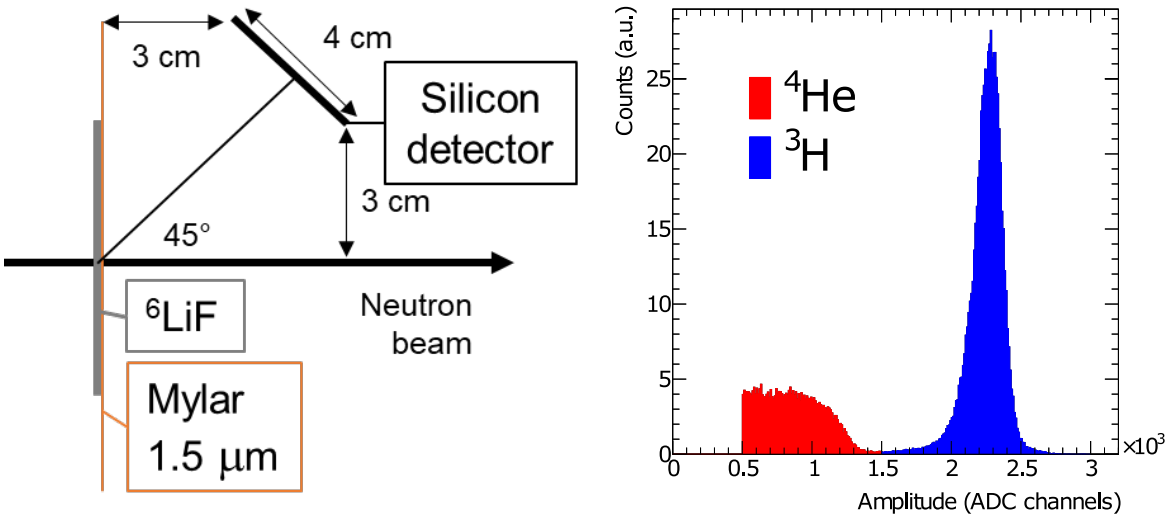

Figure 3.7: Scheme of the SiMon detector (left, from [80]) and the pulse height spectrum (right), where the alpha region and the triton peak are nicely separated.

The kinetic energies of the alpha and triton particle emitted in the ^{6}Li(n,t)^{4}He reaction are roughly 2 MeV and 2.7 MeV respectively, if the incident neutron energy is neglected. In a pulse height spectrum those two particles will correspond to two different regions and can clearly be separated as shown in the right panel of Figure 3.7. The lower charge of the tritons allows them to escape the deposit, which is not always the case for alpha particles. Therefore, only the tritons are used to determine the beam intensity.

3.1.5.1 Stability

The stability of the proton beam and subsequently the neutron beam can be monitored with the *SiMon* detector. The average number of triton counts per standard proton pulse (i.e. $7 \cdot 10^{12}$) basically gives the ratio between neutrons arriving in the experimental area and the number of protons. This quantity can be influenced by the point of impact of the proton beam on the spallation target or wrong number of protons communicated between the operators of CERN's accelerator complex and the DAQ. The point of impact of the proton beam on the spallation target can changed due to requirements from radio protection and spallation target safety.

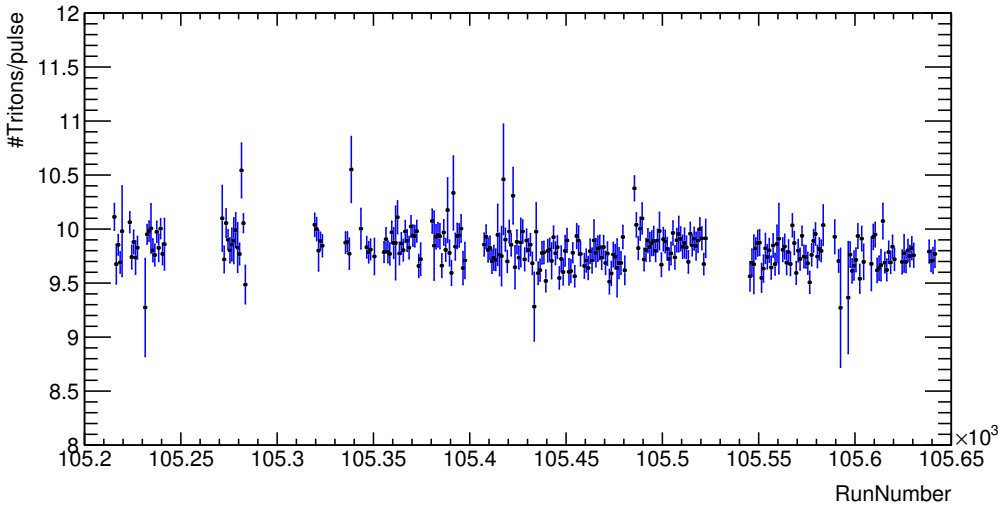

Figure 3.8: Averaged number of tritons per standard proton pulse per run during the whole experimental campaign.

Figure 3.8 shows the average number of tritons per proton pulse for each run of the experimental campaign. Apart from statistical fluctuations a steady number of tritons per pulse is observed indicating that the beam was stable during the whole campaign of about 48 days.

3.2 The n_TOF Total Absorption Calorimeter

The γ-ray cascades emitted in the capture reaction are detected by n_TOF 's Total Absorption Calorimeter *TAC* [62]. The TAC is a segmented 4π scintillator array made out of 40 individual BaF_2 crystals and based on the design from the former Karlsruhe TAC [81].

Each crystal is encapsulated by 0.2 mm thick layers of teflon and polished aluminum foil and a 1 mm thick borated carbon fiber shell to reduce the neutron sensitivity. The crystals are coupled to 5 inch Photonis XP4508B photomultipliers and attached to an aluminum housing mounted in a honeycomb structure which holds the full spherical detector shell as shown in Figure 3.9. The entire spherical BaF_2 shell has a 20 cm and 50 cm inner and outer diameter respectively, covering 95 % solid angle.

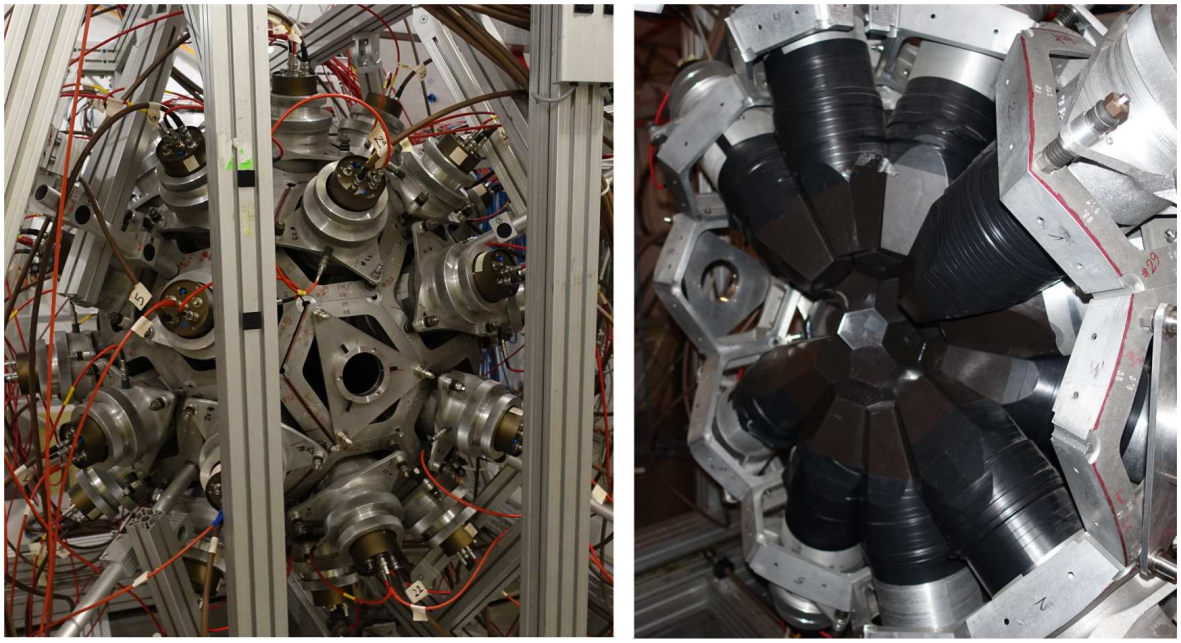

Figure 3.9: Pictures of the fully assembled (left) and open (right) TAC.

The TAC is designed to detect in coincidence the γ-rays from the EM cascade following a neutron capture event. The efficiency of detecting at least one γ-ray from a cascade is close to 100 %. This high detection efficiency is usually brought down to 60-70 % with the final cuts applied in the analysis in order to improve the signal-to-background ratio and can be calculated with simulations.

3.2.1 Neutron sensitivity and absorber

Neutron scattering describes the effect that neutrons from the beam are scattered by any material intersecting the beam. The probability of detecting those scattered neutrons is usually referred to as the neutron sensitivity of the detector.

In order to minimize the neutron sensitivity and therefore its related background contribution for the TAC set-up, a combination of neutron moderator and absorber material surrounds the sample. A so-called neutron absorber made out of moderating material loaded with neutron absorbers is employed. The absorber is made of polyethylene loaded with 7.56 w% natural lithium with a total density of 1.06 g/cm^3 which shows good performance for moderating and absorbing neutrons having the advantage of a very low γ-ray attenuation due to its low effective atomic number Z. The inside of the absorber is void in order to leave space for the neutron beam and the fission chamber containing the samples. Figure 3.10 shows a

Figure 3.10: CAD drawing (left) and pictures (middle and right) of the neutron absorber used in the measurement.

CAD drawing of the spherical absorber used in the ^{233}U α-ratio measurement with an outer diameter of 20 cm. The middle of the inner cylinder is shifted by 2 mm with respect to center of the sphere.

3.2.2 Pulse shape analysis and particle discrimination

The BaF_2 signals are recorded with the n_TOF DAQ and analyzed offline with a dedicated pulse shape routine [82]. A typical signal and the performance of the pulse shape analysis routine can be seen in Figure 3.11. After individual signals have been identified an algorithm, described in section 4.1.3, takes care of reconstructing the event depending on a certain coincidence time window.

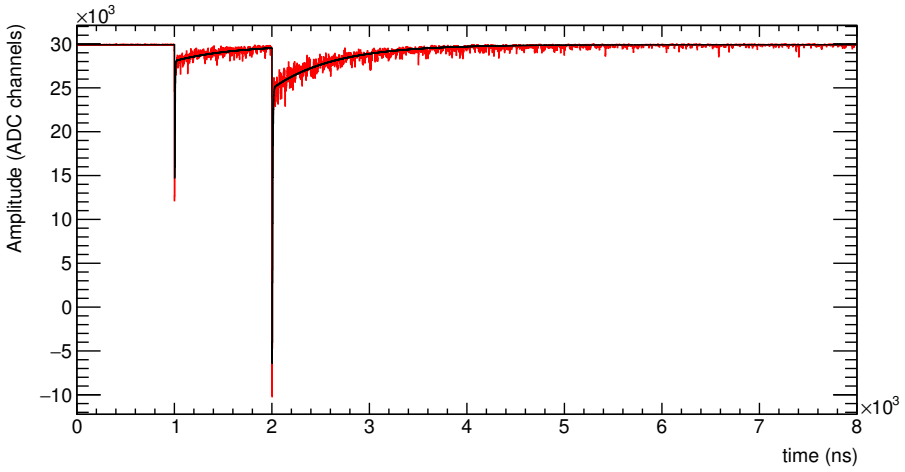

Figure 3.11: Digitized data buffer (red) and result of the pulse shape analysis routine (black). The negative units in ADC are due to the internal range of the 14 bit flash ADCs which are internally mapped on a 16 bit like scale with a total of 65536 possible values ranging from -32768 to +32767. The resolution is 14 bit though.

3.3 A novel fast Fission Chamber

In order to properly tag and remove the prompt γ-ray cascades of the fission reaction of ^{233}U from the total measured spectra a fast fission chamber (*FICH*) has been developed. The main design criteria for the chamber are:

- Compact size
- Maximize the amount of ^{233}U
- Good timing performance
- Minimum amount of dead material in and in the vicinity of the neutron beam

The first constraint originates in the limited amount of space available inside the n_TOF Total Absorption Calorimeter, namely a sphere of 20 cm diameter. This space is further reduced by the neutron absorber, therefore the goal is to design a compact chamber which has to be balanced against the second criteria to allow a sufficient amount of statistics to be collected in a reasonable beam time.
The timing performance is important for the time resolution and affects the possibility to resolve alpha particle pile up as well as the tagging performance. The intrinsic timing performance of the detector depends on the drift velocity of the electrons produced by the ionizing fission fragments and is therefore a function of the gas, the pressure and the applied electric field. On top of that the electronics have to be optimized to the gas and the detector geometry.
The last criteria originates from background considerations. In general the smaller the amount of dead material in the neutron beam the less background can be expected in the TAC. A

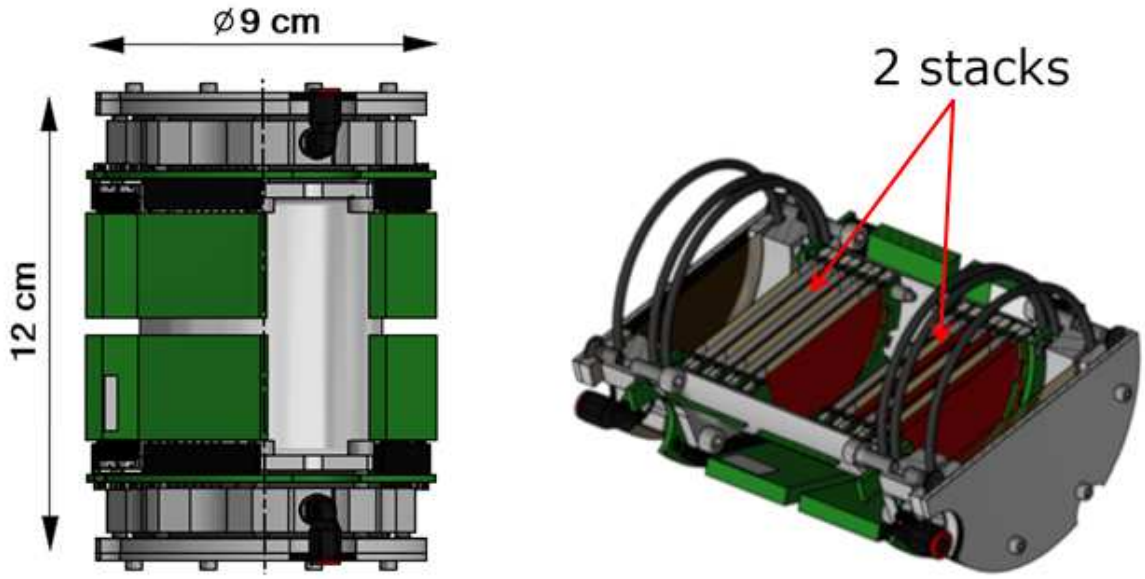

Figure 3.12: 3D-CAD drawing of the fission chamber and a sectional view. The green blocks around the chamber represent the preamplifiers.

similar measurement [61] using MicroMegas (MGAS) detectors showed a dominating background contribution above several 100 eV coming from the copper mesh and anode of the amplification stage of the MGAS. This basically leaves the choice of a simple ionization cell design without amplification stage, which is anyway not necessary for fission fragments.

3.3.1 Technical description

As a result the FICH is designed as multi-plate ionization chamber containing two stacks of axial ionization cells. Figures 3.12 and 3.13 show CAD drawings and pictures of the chamber. The housing is made of a 1.5 mm thick aluminum tube with an outer diameter of 66 mm and a length of 78 mm. The maximum outer diameter of 90 mm and the total length of 123 mm, including all flanges, fits nicely in the TAC leaving sufficient space for the absorber and the connecting pipes. Two stacks of seven ionization cells are mounted directly on their respective motherboards and are inserted from each end of the chamber. The stacks have a minimum inner diameter of 50 mm leaving enough space for the beam with a FWHM of roughly 16 mm and a total width of less than 40 mm. In total 8 anodes are collecting signals from 14 ^{233}U targets deposited on the cathodes. The chamber is closed with aluminized 25 µm Kapton windows to provide a Faraday cage.
The arrangement of the cathodes, anodes and deposits can be seen in Figure 3.14. The ionization cells are separated by 20 µm aluminium, either one 20 µm anode or two 10 µm cathodes, resulting to a total of 300 µm aluminium in beam.
Additionally, a second fission chamber was produced identical to the first one but the ^{233}U deposits. The purpose of this dummy chamber is to measure the background induced by the material of the chamber in order to subtract its contribution from the total measured spectra in the analysis.

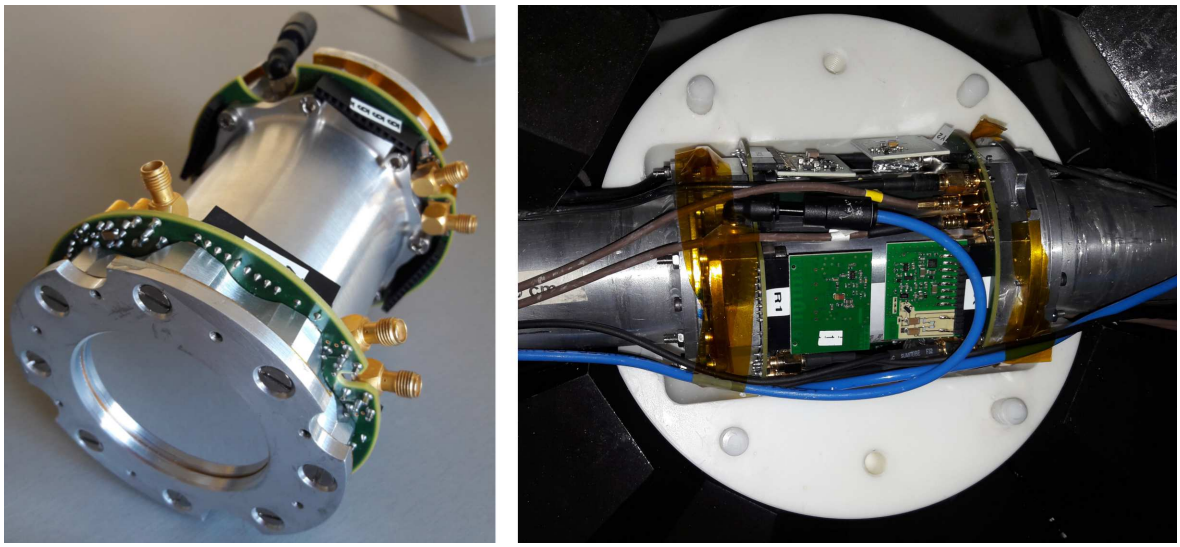

Figure 3.13: Pictures of the dummy fission chamber in the lab (left) and the ^{233}U loaded fission chamber with electronics and gas connected and embedded in one half of the absorber inside the TAC (right).

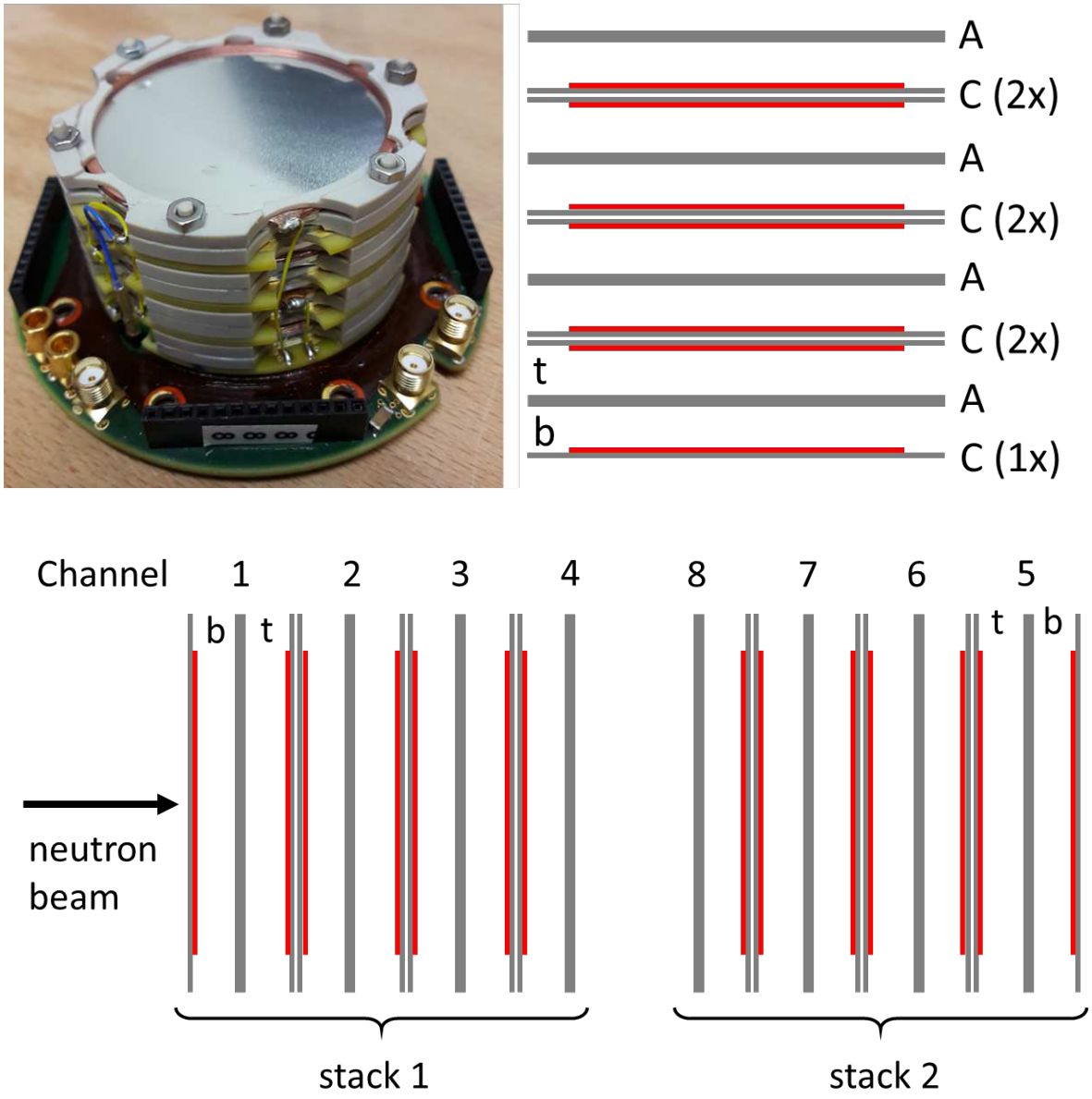

Figure 3.14: Photo of one stack of ionization cells mounted on the motherboard (top left). Arrangement (top right) of the cathodes (C) and anodes (A) of one stack, ^{233}U deposits are indicated in red. There is one anode that reads only from 1 deposit while the others read signals from two deposits. In the case of two deposits the two ionization cells per anode are labeled top (t) and bottom (b). Mounting of the FICH DAQ channels in the chamber with respect to the neutron beam in the experiment (bottom).

3.3.2 Choice of gas and gas system

The choice of the gas is of high importance for the very specific requirements of this measurement. It has to exhibit a high drift velocity and provide a good alpha-fission fragment separation.

Several standard experimental gases have been investigated with Monte Carlo simulations using GARFIELD [83], see Figure 3.15 taken from Ref. [84]. In general high purity tetrafluoromethane CF_4 is a very fast gas but has the drawback of being electro-negative. This

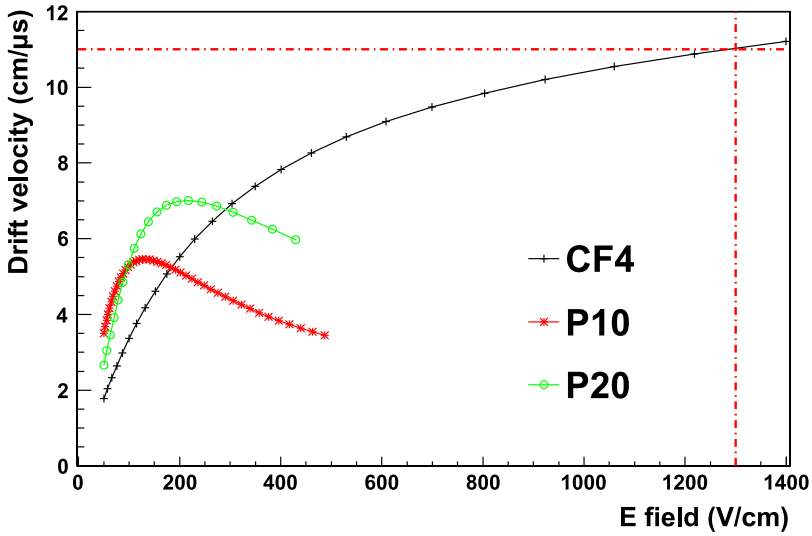

Figure 3.15: GARFIELD simulations of the electron drift velocities for different experimental gases at atmospheric pressure as a function of the applied electric field taken from Ref. [84].

causes electron attachment which worsens the energy resolution. Nevertheless, the advantage it offers due to its higher drift velocity compared to other gases outweigh the disadvantages and make it a good choice for this measurement. At the applied electric field of 1400 V/cm the drift velocity is roughly 11 cm/µs at a gas pressure of 1100 mbar.

In order to guarantee stable conditions throughout the measurement period of several weeks a gas pressure and flow regulation system was employed and is schematically shown in Figure 3.16. The fission chamber was operated at an absolute pressure of 1100 mbar with a constant gas flow of 0.1 l/min to allow for thin windows of the fission chamber, hence reduce background in the TAC.

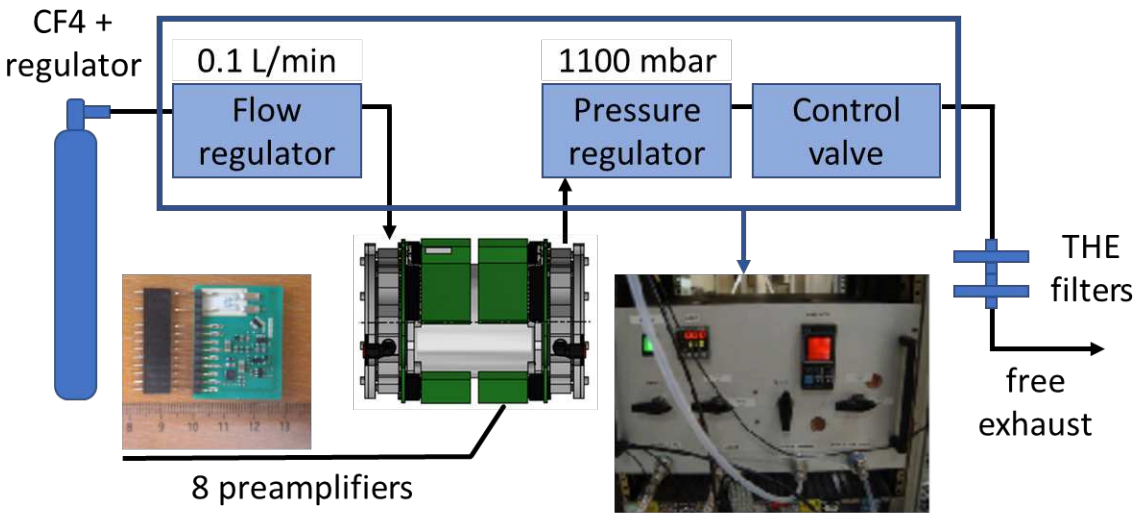

Figure 3.16: Schematic illustration of the full FICH setup including the chamber, a schematic drawing of the gas system, a picture of one preamplifier-filter PCB and a picture of the gas regulation system.

3.3.3 Dedicated electronics

In order to allow good signal recognition and to reduce potential α-particle pile up fast and low-noise electronics have been developed, optimized to the geometry of the detector and the gas. A dedicated card combining a preamplifier and a fast timing filter amplifier was developed at CEA Bruyères-le-Châtel to meet the requirements of this fission chamber. A photo of those cards can be seen in the lower left part of Figure 3.16. Per stack, four of these cards are directly mounted on the specifically designed motherboards. Low voltage for the electronics is supplied via Lemo connectors, a 420 V bias voltage is supplied through SMA connectors and the signals are taken via SMA connectors as well. The electronics themselves are not shielded which is problematic due to the γ-flash in the n_TOF EAR1. One part of the γ-flash is an electromagnetic wave which induces an oscillation in the unshielded electronics and hence in the output voltage, see Figure 3.17. This limits the maximum neutron energy that can be analyzed. Nevertheless, that maximum neutron energy is about 7 MeV which is much higher than what can be achieved with the TAC itself.

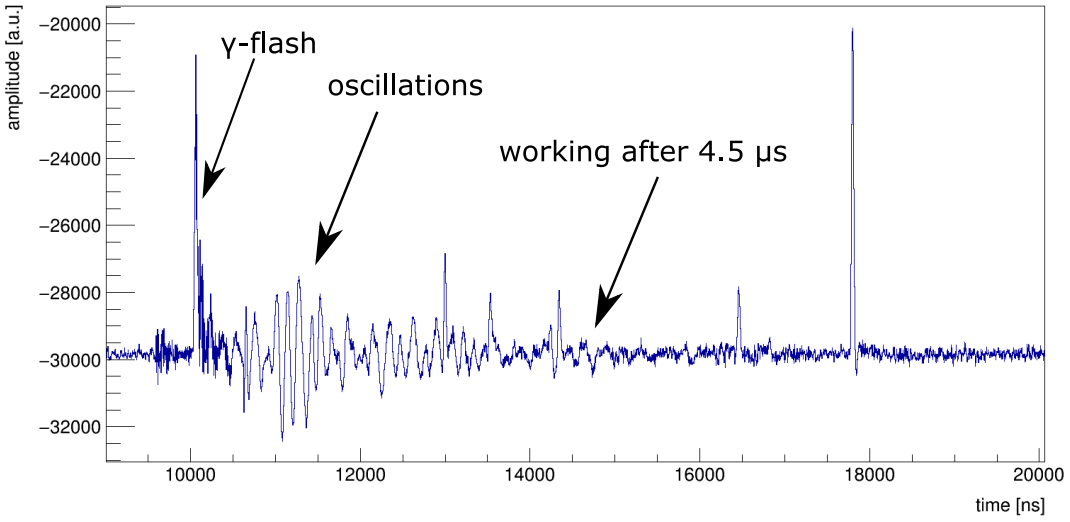

Figure 3.17: Reponse of the FICH to the γ-flash. A time-of-flight of 4.5 µs corresponds to a neutron energy of roughly 7 MeV.

3.3.4 Pulse shape analysis

The signals recorded by the data acquisition system were processed offline using the pulse shape analysis routine provided by the n_TOF collaboration [85] based on the calculation of the first derivative of each recorded waveform. Among other quantities, the amplitude and arrival time of each signal were stored for further processing. An example of a typical signal of a fission fragment is shown in Figure 3.18 with a full width at half maximum FWHM of 34 ns and a rise time RT of 16 ns measured from 10-90 % of the maximum amplitude.

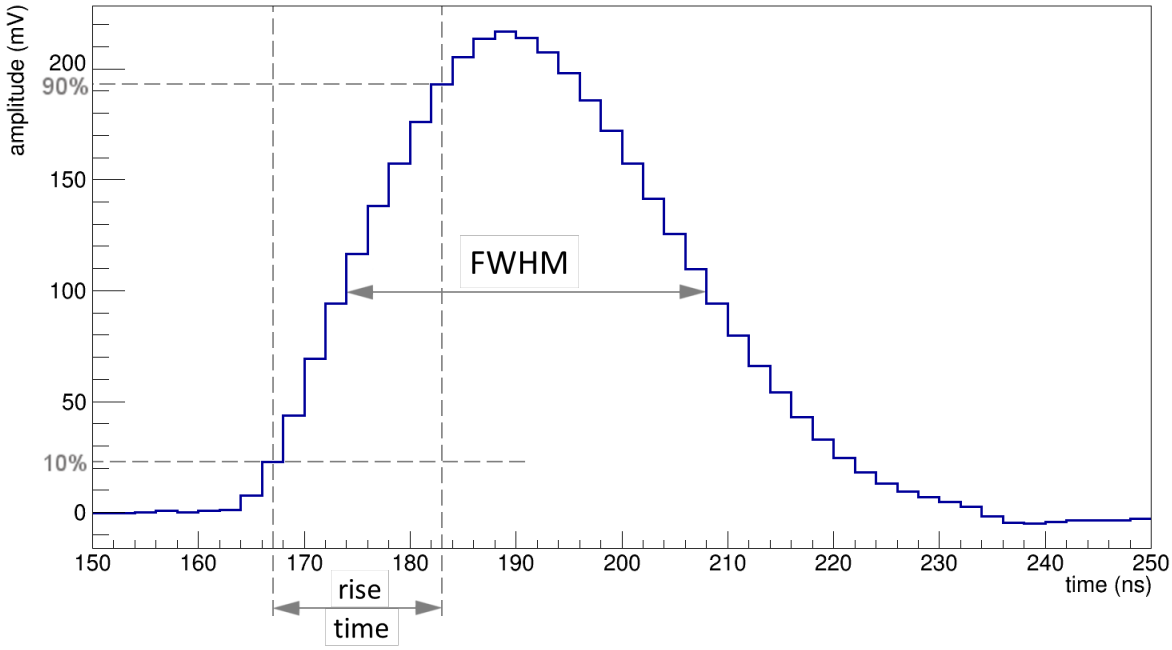

Figure 3.18: Average shape of a fission fragment signal from the FICH.

3.4 The ^{233}U samples

The uranium oxide targets, highly enriched in ^{233}U, used in the measurement of the ^{233}U α-ratio have been prepared by JRC-Geel. Thin uranium oxide layers were deposited on 10 µm thick aluminium foils, acting as cathode, by molecular plating in a polycetal molecular plating cell with a rotating platinum anode. The diameter of the mask used for the preparation of the ^{233}U samples was 40.00 ± 0.02 mm which also defines the active area of the samples. The aluminium foils were glued on 3 mm thick aluminium rings with an inner and outer diameter of 50 mm and 54.8 mm respectively. In total 14 samples were used in the measurement. The activity of each sample has been determined by defined solid angle α-particle counting and amounts to an average α-activity of about 1.16 MBq per sample. The mass and areal density of each sample are derived from the activity. The samples have an average areal density of 264.5 µg/cm^2, which permits fission fragments to escape the samples. Table 3.1 provides a summary of the activity, mass and areal density in atoms/barn of the individual samples used in the measurement.

The base material was 99.936 % enriched in ^{233}U with the largest contaminant being 0.0496 % ^{234}U. The isotopic composition has been measured by mass spectrometry and the full isotopic composition is given in Table 3.2. Due to concentration/enrichment ratios and the relative capture cross sections of ^{233}U and ^{234}U it can be expected to see the tip of the large resonance of ^{234}U with a cross-section of 23 kbarn at an incident neutron energy of $E_n = 5.16$ eV in the data. The expected contribution from this resonance is shown in Figure 3.19.

In Ref. [86] a morphological and compositional study is performed on ^{238}U thin film targets for nuclear experiments. It was shown that there are discrepancies between the uranium mass derived by alpha-particle counting at a defined solid angle and by direct weighting. The ^{238}U

Table 3.1: Summary of the ^{233}U targets used in the experiment. The characterization of the samples was performed on 5 February 2016. The areal density and the mass are inferred from the measured activity of each sample.

FICH chan.	ion. cell	areal density (μg/cm^2)	mass (mg)	n_{at} ($\cdot 10^{-7}$) (at/barn)	Activity (MBq)	ID (TP2015-#)
1	b	219.6 ± 3.1	2.76 ± 0.02	5.67 ± 0.04	0.97 ± 0.01	13
1	t	298.0 ± 5.7	3.74 ± 0.02	7.70 ± 0.05	1.31 ± 0.01	8
2	b	253.6 ± 4.3	3.19 ± 0.02	6.55 ± 0.04	1.12 ± 0.01	3
2	t	270.6 ± 4.9	3.40 ± 0.02	6.99 ± 0.05	1.19 ± 0.01	2
3	b	281.1 ± 5.1	3.53 ± 0.02	7.26 ± 0.05	1.24 ± 0.01	5
3	t	226.9 ± 3.4	2.85 ± 0.02	5.86 ± 0.04	1.00 ± 0.01	17
4	-	305.1 ± 6.1	3.83 ± 0.03	7.88 ± 0.05	1.34 ± 0.01	4
5	b	223.6 ± 3.1	2.81 ± 0.02	5.78 ± 0.04	0.98 ± 0.02	15
5	t	291.8 ± 5.5	3.67 ± 0.02	7.54 ± 0.05	1.28 ± 0.01	10
6	b	276.4 ± 5.0	3.47 ± 0.02	7.14 ± 0.05	1.22 ± 0.01	9
6	t	235.2 ± 3.5	2.96 ± 0.02	6.08 ± 0.04	1.04 ± 0.01	11
7	b	241.5 ± 3.9	3.03 ± 0.02	6.24 ± 0.04	1.06 ± 0.01	19
7	t	273.3 ± 4.9	3.43 ± 0.02	7.06 ± 0.05	1.20 ± 0.01	7
8	-	306.7 ± 6.1	3.85 ± 0.03	7.93 ± 0.05	1.35 ± 0.01	6
TOTAL			46.54 ± 0.30	95.70 ± 0.62	16.30 ± 0.11	

Table 3.2: Isotopic composition of the base material, characterized on 12 March 2012 (Lot 2146, TP2015-10).

Isotope	mass fraction m(^{x}U)/m(U) (%)
^{233}U	99.9361
^{234}U	0.04965
^{235}U	0.00124
^{236}U	0.00025
^{238}U	0.0128

mass measured by direct weighting was up to 40 % higher than the mass derived by alpha-particle counting for molecular plated ^{238}U deposits. This indicates that there was something about the elemental compositions of the deposited films produced via molecular plating that was not well understood. The study showed the only elements that could significantly contribute to this discrepancy are carbon and oxygen, with about 10-14 wt% and 21-31 wt% respectively. Furthermore, the use of isopropanol as a plating solvent in addition with a fast drying process on at hotplate of 100 °C and the roughness of the aluminium substrate lead to a maze like cracking pattern of the surface of the deposit, as can be seen in the Scanning Electron Microscopy (SEM) images in the left and middle panel of Figure 3.20. In the right panel of Figure 3.20 a table of the elemental composition measured with X-ray photo-electron spectroscopy (XPS) at the regions indicated in the middle panel is given in wt%. One can expect that there would not be much difference between a ^{238}U and a ^{233}U layer, therefore the additional amount of carbon and oxygen and the inhomogeneity have to be taken into account in Monte Carlo simulations of the fission chamber pulse height spectra, as it will

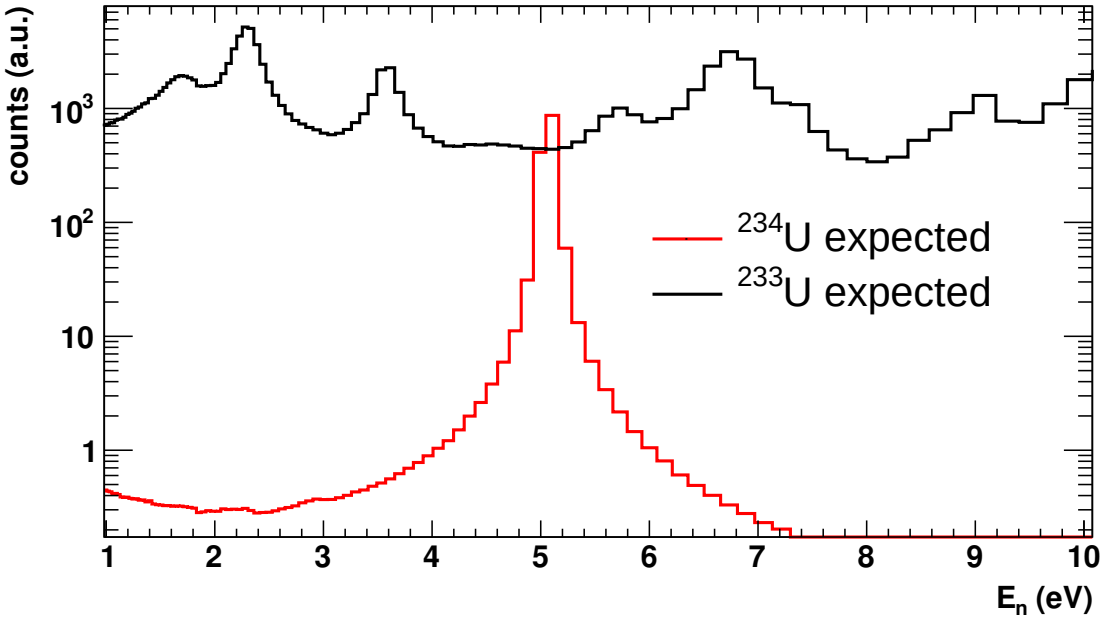

Figure 3.19: Expected counts from ^{233}U and ^{234}U according to the isotopic composition using the capture cross-sections from ENDF/B-VIII.0.

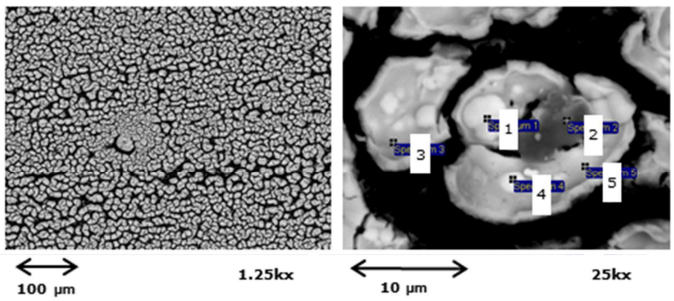

Point	U	O	Al	C
1	68.30	20.57	1.24	9.88
2	43.39	30.66	5.26	13.62
3	45.74	31.04	9.39	13.83
4	56.81	27.46	3.27	12.46
5	51.53	31.63	5.26	11.58

Figure 3.20: SEM image of a molecular plated ^{238}U layer (left and middle). Elemental composition in wt% measured with XPS at different regions of the layer (right) as indicated in the middle panel. Image taken from [86].

significantly change the energy loss by the fission fragments when exiting the deposit.

3.5 Geometry model of the experimental setup for Monte Carlo simulations

The geometry of the TAC has already been implemented in previous works [80, 87, 88] into the simulation toolkit GEANT4 [89, 90]. It contains the BaF_2 crystals with their encapsulation, the photomultipliers and the honeycomb structure supporting the detector array as shown in the left panel of Figure 3.21. In addition to this geometry the fission chamber and its electronics, Kapton windows as well as the absorber and the beam pipes are added, as can be seen in the right panel of Figure 3.21.

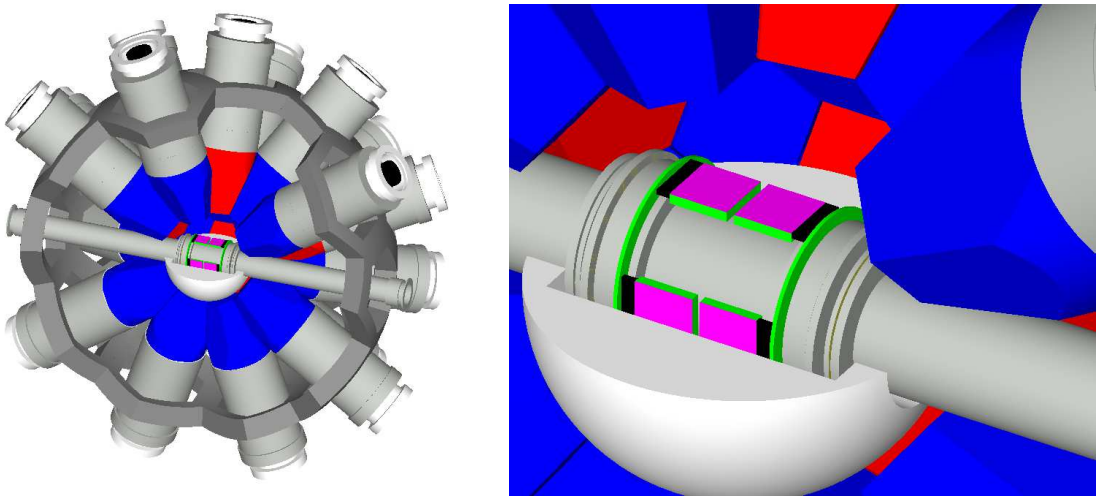

Figure 3.21: Image of the model (left) of the experimental set-up in GEANT4. Only one hemisphere is displayed for visual purposes. The hexagonal and pentagonal crystals are colored in red and blue respectively. For better visibility the zoom (right) shows the housing, the PCB parts (green) and connectors (black) of the fission chamber embedded in one half of the neutron absorber and connected to the beam pipes.

3.5.1 Event reconstruction

The results of the GEANT4 simulation are processed on an event by event basis, similar to the experimental data:

- All hits in the BaF_2 detectors are read from the output of the simulations.
- The deposited energy in each crystal is sampled according to the energy resolution of that crystal applying an additional broadening of 17 % ($1.17\Delta E$) obtained by comparison with the experimental spectra (see Figure 3.22 and section 4.1.2, taking into account errors committed during the energy calibration of the detectors.
- The time between two consecutive events is sampled according to a predefined reaction rate while the time between individual hits in detectors is given by the Monte Carlo simulation.
- The coincidence time window between the crystals applied to the simulated data is the same as in the experimental data.
- Application of dead time and pile-up
- The result is a list of events characterized by their total deposited energy in the TAC and detected crystal multiplicity.

3.5.2 Validation of the simulation process

The geometry model is validated by comparing simulated and experimental sum energy spectra of standard calibration sources like ^{137}Cs and ^{88}Y for different multiplicity conditions.

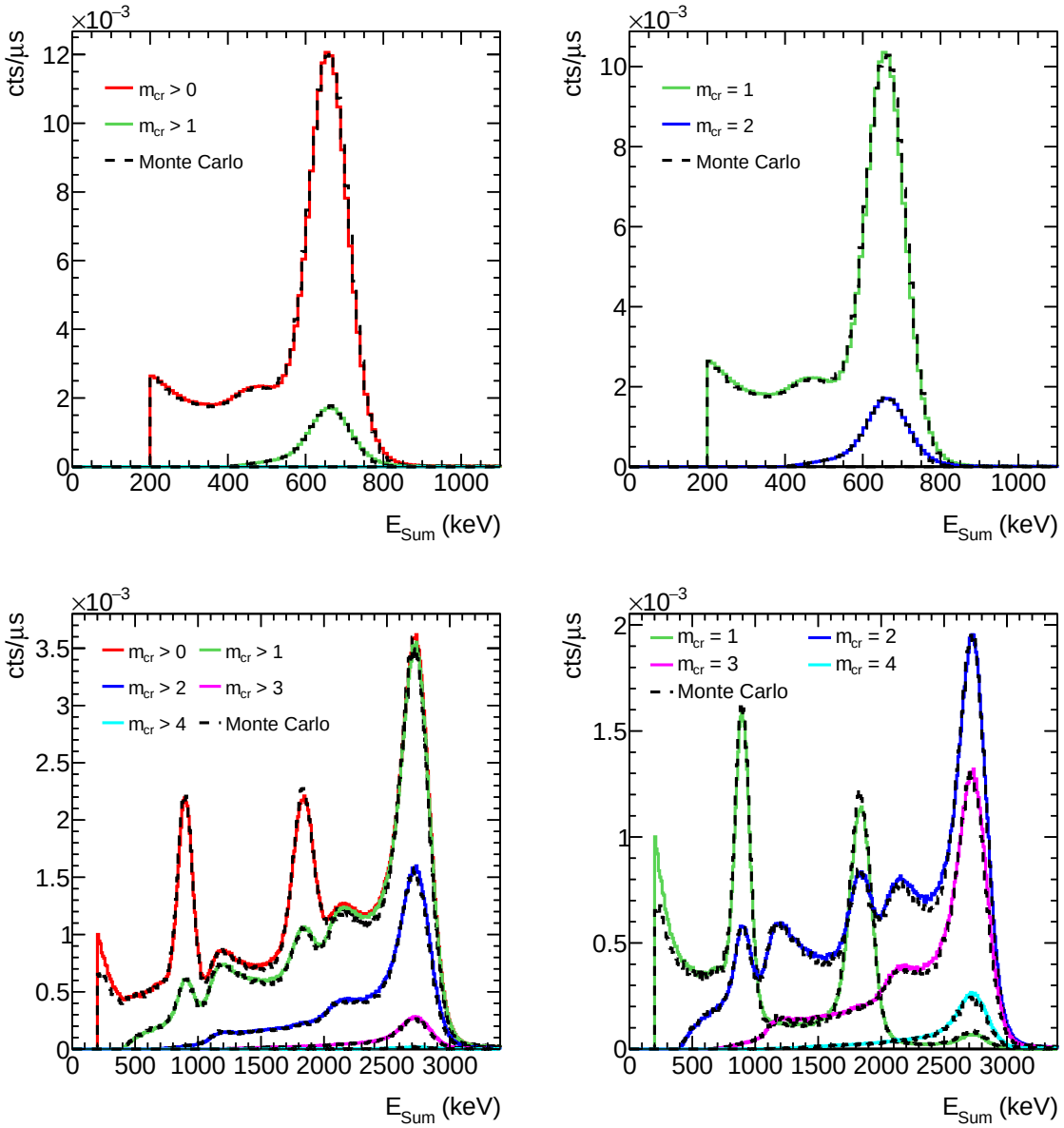

Figure 3.22: Comparison between simulated results (dashed lines) and experimental data (solid/colored lines) for the ^{137}Cs (top) ^{88}Y (bottom) calibration source including the absorber.

The comparison between the simulated results and the experimental data can be found in the top and bottom panels of Figure 3.22 for ^{137}Cs and ^{88}Y respectively. The coloured solid lines represent the experimental data while the dashed black lines are the results from the Monte Carlo simulation. There is no direct normalization applied between the two spectra, but instead the γ-ray source's activity was used to calculate the count rate for the post processing of the simulated data. A good agreement is found between the simulations and the experimental data and permits the adjustment of two essential parameters, summarized in Table 3.3, for the simulations and further analysis:

- The experimental BaF_2 detection threshold E_{thresh} defines the low energy γ-threshold and is chosen via software for the post processing of the experimental data. The simulations are used to verify that the applied threshold is not too low causing noise in the

Table 3.3: Summary of the low energy detection threshold for the individual BaF_2 crystals and the inner geometrical radius of the TAC.

E_{thresh} (keV)	R_{TAC} (cm)
200	10.56

data or too high causing real count loss.

- The inner radius of the TAC (R_{TAC}) strongly influences the sum energy spectra. This parameter was varied within a few mm until the experimental data was reproduced by the Monte Carlo results. This adjustment is done by trial and error and judged by eye (not fitting).

Chapter 4

Detector performance and Fission Tagging

This chapter is organized in three main parts and describes the performance of the TAC and FICH detectors and introduces the tagging technique used to determine the prompt fission γ-ray spectra for the background subtraction.

4.1 Performance of the TAC

This section describes the analysis of data from the Total Absorption Calorimeter (TAC). The analysis is summarized as follows:

- The energy calibration and energy resolution for each crystal is obtained using standard γ-ray calibration sources.
- The gain drift of the TAC can be monitored using the intrinsic α-particle background in each crystal.
- The time calibration of the BaF_2 detectors needed for the TAC reconstruction.

4.1.1 Energy calibration

The process of calibrating the BaF_2 modules has been done for each module individually and is comprised of three well defined parts:

- The α/γ/noise discrimination using the pulse shape of the signals.
- The response of the individual crystals to standard γ-ray sources.
- The gain control of the different detectors during the measurement.

The energy calibration of all detectors affects the quality of the TAC event discrimination and allows to compare the experimental data with Monte Carlo simulations easily.

4.1.1.1 α/γ/noise discrimination

The BaF_2 crystals contain a certain amount of radium which undergoes α-decay. The response of the scintillation material BaF_2 provides a convenient method to discriminate between γ-rays, α-particles from the natural decay of radium as well as noise. The signal

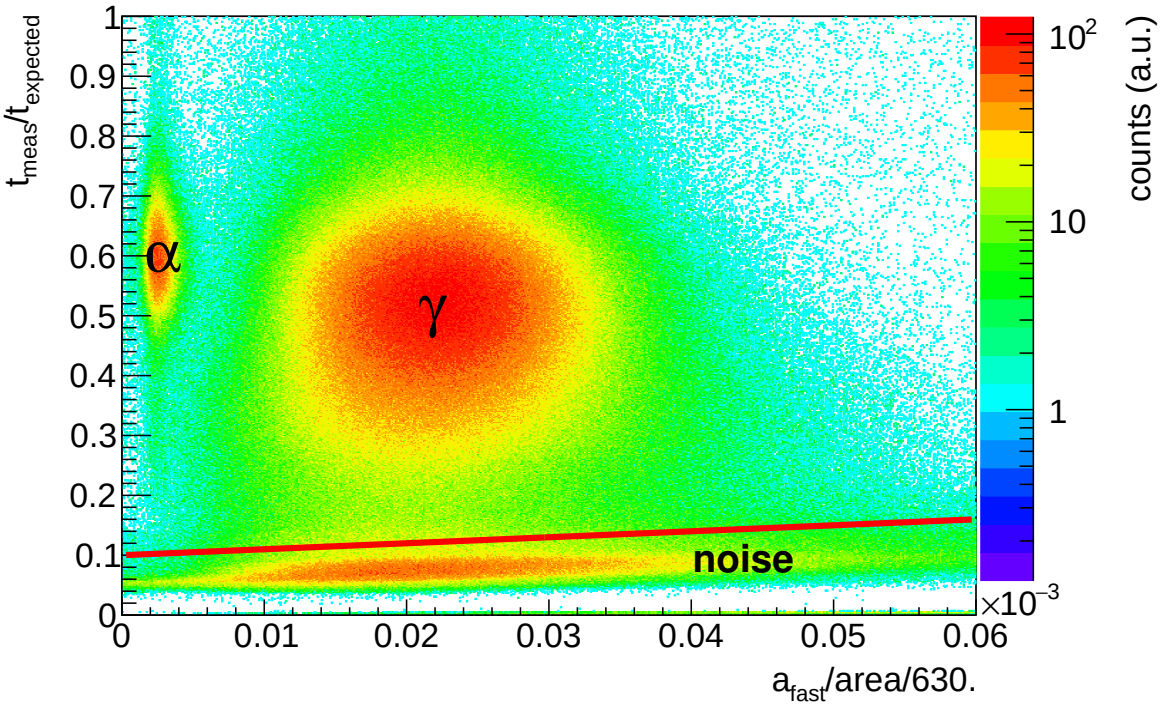

Figure 4.1: Particle discrimination in BaF_2 . The region below the red line corresponds to noise. The upper left hotspot corresponds to α-particles while the central region corresponds to γ-rays.

reconstruction is based on fitting two (expected) exponentials, a fast and a slow one, to the recorded (measured) shape. The two exponential components are:

- The first component, labeled fast, due to the short decay constant of $\tau_{fast} \sim 0.7\,\text{ns}$. This component allows for excellent determination of the timing of the signal.
- The second component, labeled slow, due to the long decay constant of $\tau_{slow} \sim 630\,\text{ns}$. This component contains most of the information regarding the deposited energy in a crystal.

In Figure 4.1 the ratio of the actual to expected signal duration t_{meas}/t_{expec} versus the ratio of the fast component to the signal integral is plotted. Three regions can be identified:

- Noise: short signals, hence they will populate a region with a small ratio of the measured to the expected signal duration.
- α-particles: do not show a fast component in the signal, which in turn means that the region for low ratios of the fast component to the signal integral corresponds to α-particles.
- γ-rays: the rest.

For α-particles this way of discrimination can be further improved for some crystals. In the left panel of Figure 4.2 the ratio of the fast and slow component is shown against the deposited energy in a crystal providing an alternative cut for α-particles. All events within the red frame of the left panel of Figure 4.2 correspond to α-particles using a similar argument

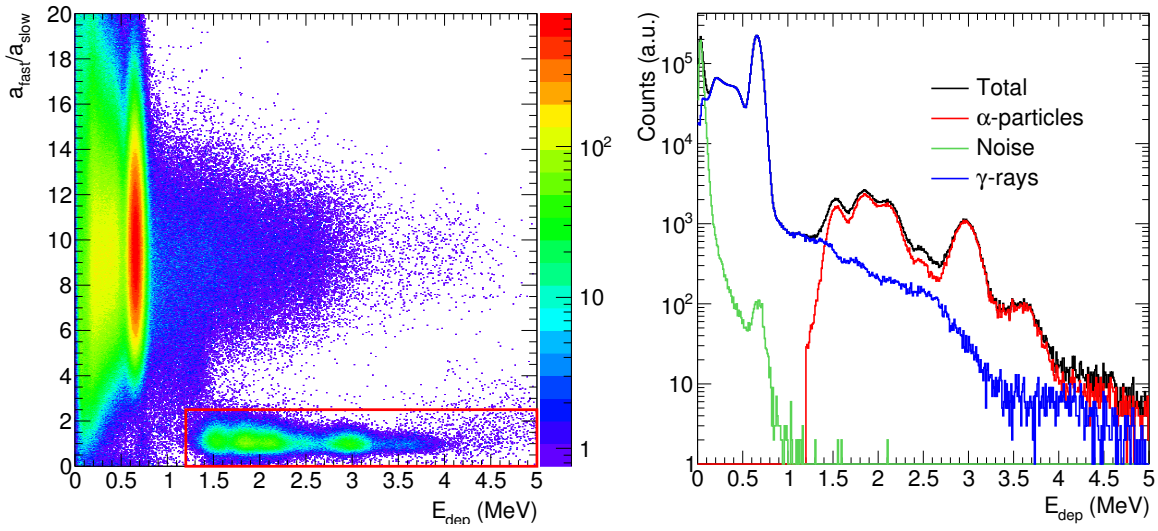

Figure 4.2: Particle discrimination of α-particles in a BaF_2 crystal with improved α-particle cut indicated by the red framed region (left). Contributions to the total spectrum in a crystal (right) measured with a ^{137}Cs calibration source (approx. 340 kBq).

described in the above mentioned method. The α-particles show a clear signature in deposited energy E_{dep} which allows improved discrimination. In the right panel of Figure 4.2 the different contributions to the total spectrum from γ-rays, α-particles and noise is shown. This discrimination procedure for noise and α-particles has been applied to all 40 TAC modules individually.

4.1.1.2 Response to standard γ-ray calibration sources

Throughout the experiment calibration measurements have been performed with standard γ-ray calibration sources listed in Table 4.1. The deposited energy in the crystal is proportional to the integrated area of the signal. Hence, an energy calibration can be done by linking the signal area and the known γ-ray energies E_γ of the calibration sources.
Figure 4.3 shows the response of BaF_2 module 7 to the calibration sources. In order to obtain the centroid of the fits, a Gaussian function plus an assumed exponential background were used in the fits. In case of the AmBe and the CmC source two Gaussian functions plus an assumed exponential shape of the background were used to fit the full energy deposition and first escape peak of the spectra. In this way the deposited energy calibration of the detectors

Table 4.1: γ-ray sources used to calibrate the detectors and the energy E_γ of the emitted γ-ray(s).

source	E_γ (MeV)
^{137}Cs	0.662
^{88}Y	0.898 and 1.836
AmBe	4.438
CmC	6.130

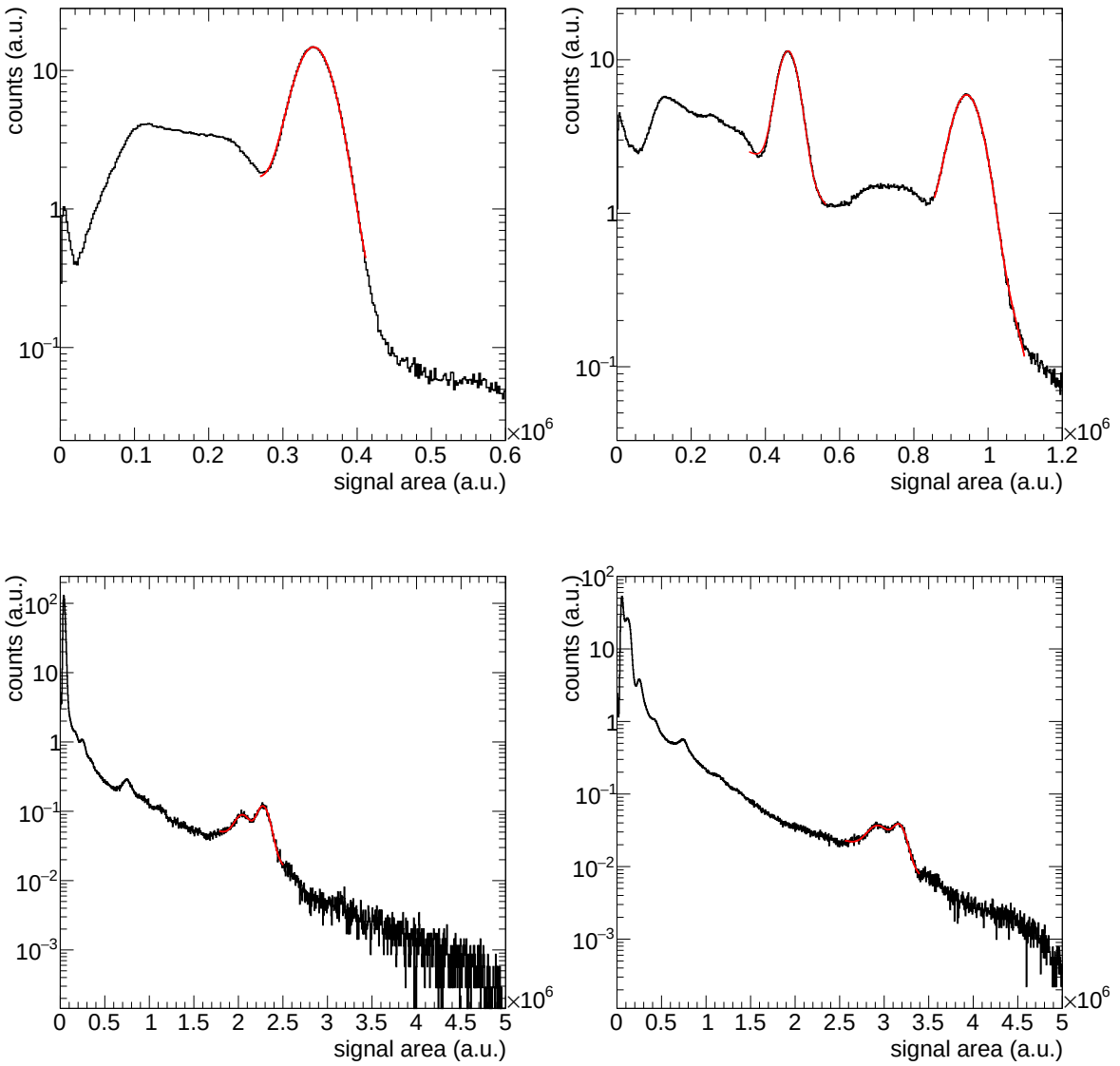

Figure 4.3: Response of BaF_2 module 7 to the standard calibration sources - ^{137}Cs (top left), ^{88}Y (top right), AmBe (bottom left), CmC (bottom right). Fits to the experimental data in red using different fitting functions.

is obtained by a linear fit

$$centroid = k \cdot E_\gamma[MeV] + d \tag{4.1}$$

of the corresponding centroids and γ-ray energy shown for module 7 in Figure 4.4.

4.1.1.3 Gain monitoring and correction

The gain of each module has been monitored on a run by run basis using the intrinsic α-decay of the radioactive isotopes in the BaF_2 crystals. The methodology is based on the comparison of the deposited energy spectra (= *signal area*) from the intrinsic α-decay of the crystals from a reference run and all other runs. From this comparison a correction factor is

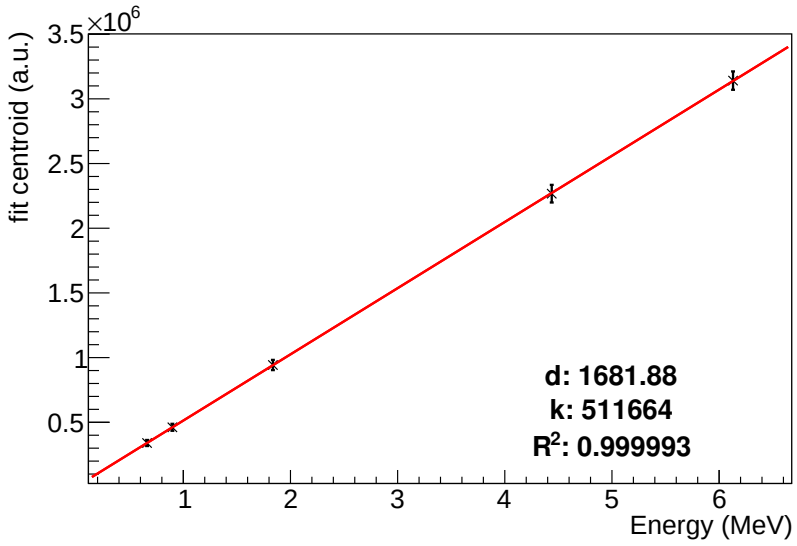

Figure 4.4: Calibration curve for BaF_2 module 7.

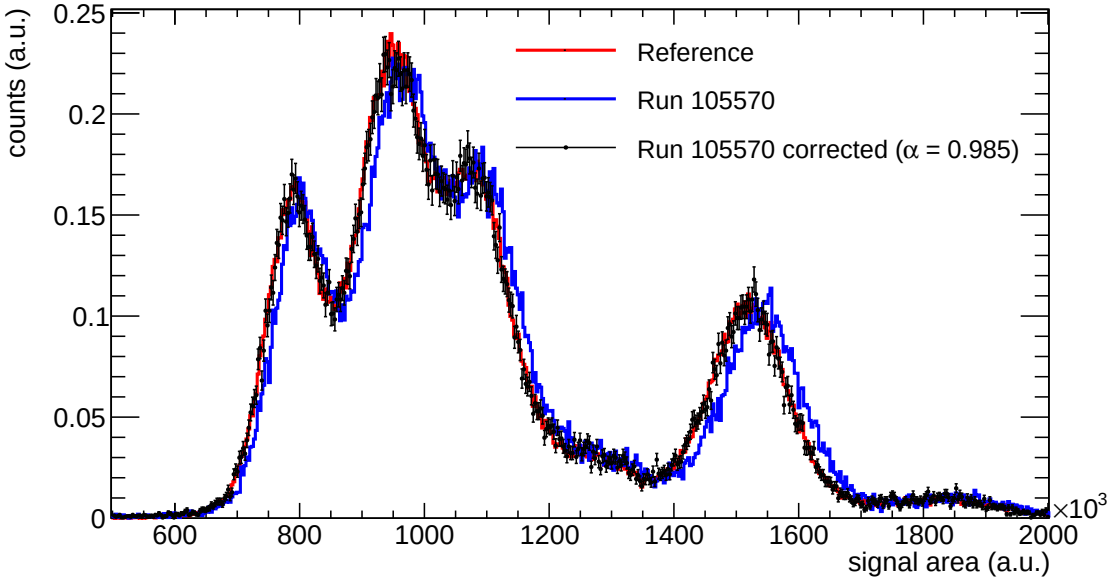

Figure 4.5: Illustration of the gain correction method for BaF_2 module 7.

calculated and applied to the deposited energy of each signal in the corresponding run. The procedure can be summarized as follows:

1. Choose a reference run with high statistics and prepare a reference histogram h^{ref} of the deposited energy *signal area* spectrum and define the gain factor $\alpha \equiv 1$ for this run.
2. The gain factor of every other run i is determined in the following way:
   (a) Define a grid with n steps for which the gain factor α_i shall be investigated, i.e. the range $\alpha_i \in [0.7, 1.3]$ and the step size $\alpha_{i+1} - \alpha_i = 0.01$.
   (b) Fill n deposited energy histograms h^i with $signal\ area \cdot \alpha_i$.

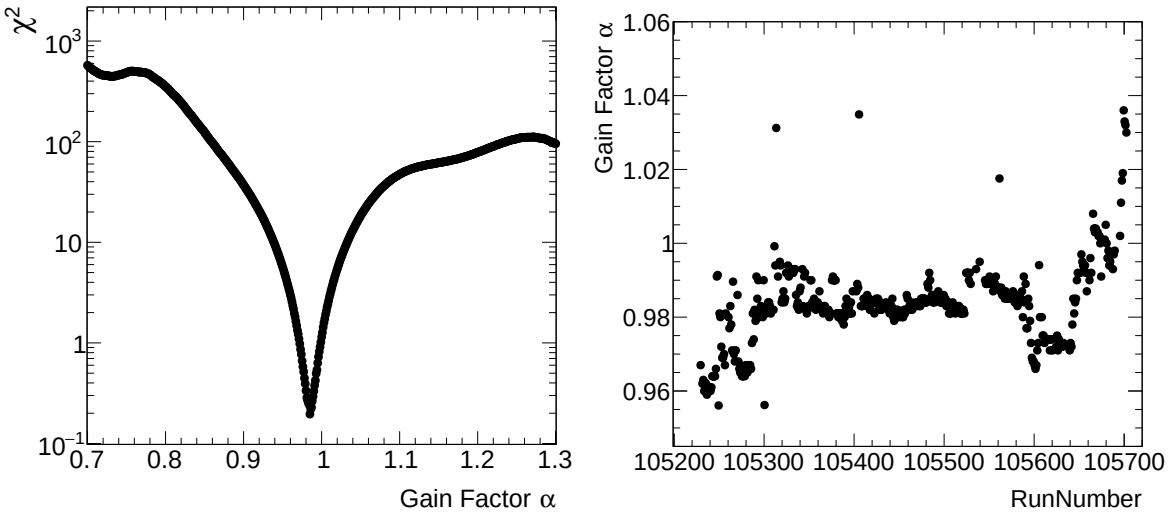

Figure 4.6: χ^2 for various gain factors α for BaF_2 module 7 and Runnumber 105570 (left). Gain variation over time for BaF_2 module 7 (right).

(c) Compare all h^i with the reference histogram h^{ref} using a χ^2 method summing up the bin by bin squared difference, i.e.

$$\chi_i^2 = \sum_{j=1}^{nbins} (h_j^i - h_j^{ref})^2 \tag{4.2}$$

(d) The smallest χ_i^2 will fit the reference histogram best and the corresponding α_i is the correction factor to be applied to the deposited energy of a certain detector for this run i.

Figure 4.5 shows the reference histogram h^{ref} in red, the original and corrected deposited energy spectrum of run 105570 in blue and black respectively for BaF_2 module 7. In this case the smallest χ_i^2 was found for an α_i of 0.985. In the left panel of Figure 4.6 χ_i^2 as a function of α_i is shown. A rapid convergence towards the minimum is visible towards the optimal

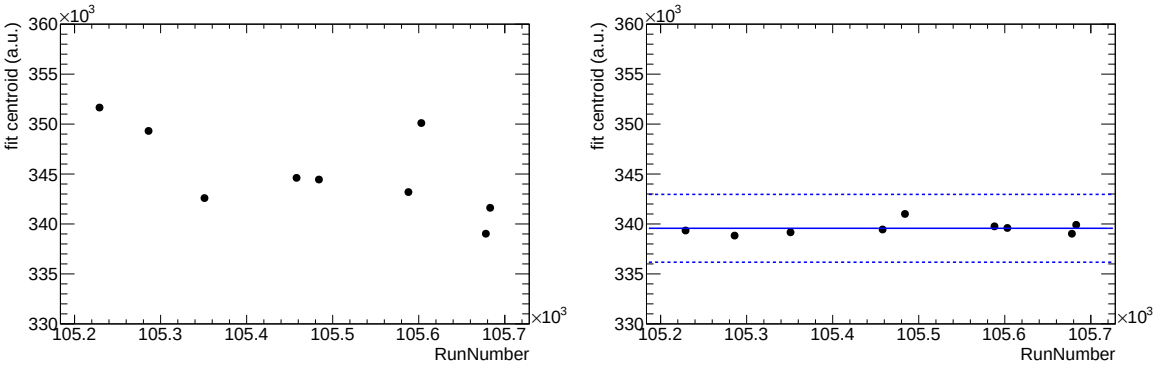

Figure 4.7: Fit centroid of the ^{137}Cs standard calibration source over time before (left) and after (right) gain correction for BaF_2 module 7. The blue solid line corresponds to the average and the dashed line to its error.

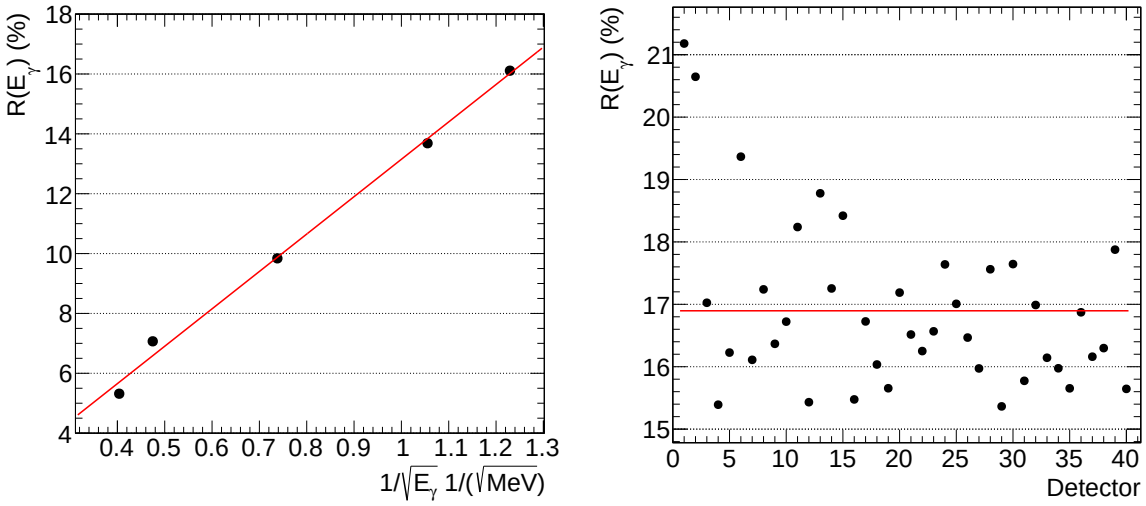

Figure 4.8: Energy resolution for BaF_2 module 7 - smaller E_γ are on the upper end of the x-axis (left). Energy resolution of all detectors at $E_\gamma = 0.662\,\text{MeV}$ from ^{137}Cs. The average (red line) of all crystals is calculated to $R(E_\gamma = 0.662\ MeV) \approx 16.9\,\%$ (right).

$\alpha = 0.985$. Applying this technique to all runs yields all gain (correction) factors α for all detectors and all runs. An example for detector 7 is shown in the right panel of Figure 4.6. To validate the method the centroids of all ^{137}Cs measurements throughout the duration of the experiment are shown in Figure 4.7 before and after the application of the gain correction. The centroids of the fits to the ^{137}Cs source before the gain correction are scattered several percent from the average of all the measurements. After the gain correction the spread between the points is reduced to less than 1 % indicated by the dashed blue lines, surrounding the average fit of the data points shown as solid blue line.

4.1.2 Energy resolution

The characterization of the energy resolution of the BaF_2 crystals as a function of the deposited energy E_γ is necessary for accurate Monte Carlo simulations of the TAC response to γ-rays and subsequently for the calculation of the detection efficiency. The resolution $R(E_\gamma)$ has been calculated by fitting equation (4.3) [91]

$$R(E_\gamma) = \frac{\Delta(E_\gamma)}{E_\gamma} = \frac{FWHM}{E_\gamma} = \alpha + \beta/\sqrt{E_\gamma} \tag{4.3}$$

to the experimental energy resolution, namely the full width at half maximum ($FWHM$) of the fits to the experimental response of the calibration sources. The parameters α and β obtained from the fit can be used to calculate the energy resolution for any deposited energy in a crystal in the Monte Carlo simulations.

In the left panel of Figure 4.8 the energy resolution for all E_γ and the fit according to equation (4.3) in red is shown. In the right panel of Figure 4.8 the energy resolution for all detectors at $E_\gamma = 0.662\,\text{MeV}$ is shown and the average of all detectors is drawn as red solid line. In Figure 4.9 the energy resolution for all detectors is shown at various E_γ corresponding

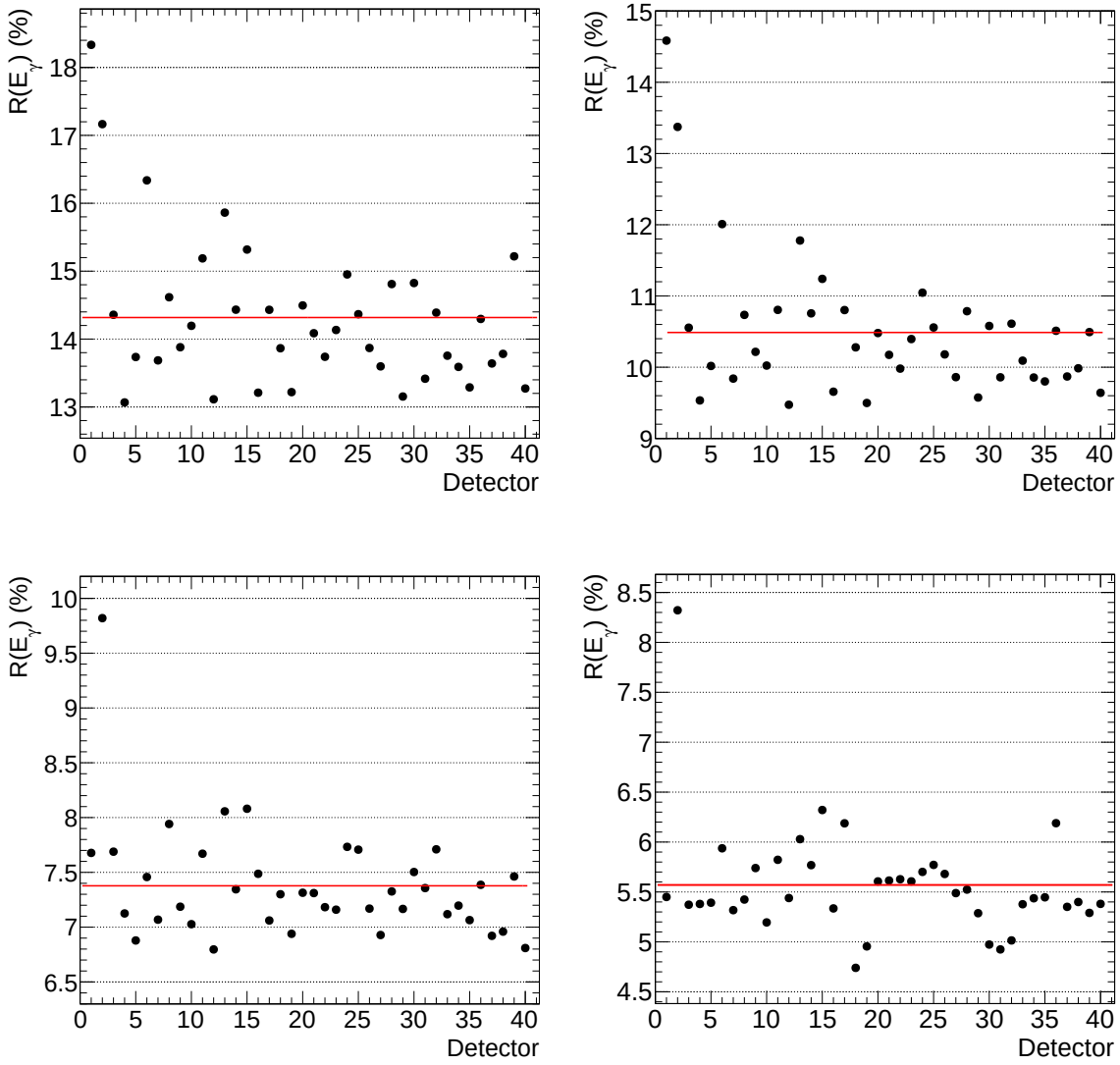

Figure 4.9: Energy resolution of all detectors at various E_γ: 0.898 MeV (top left), 1.836 MeV (top right), 4.438 MeV (bottom left), 6.130 MeV (bottom right). The average values are indicated in red and summarized in Table 4.2.

to all calibration sources but ^{137}Cs. The average energy resolution for all E_γ is summarized in Table 4.2. The obtained fitted values are slightly better than what can be obtained from the E_{Sum} spectra. For example, the interpolated energy resolution for the TAC at the sum energy peak of the ^{88}Y source at $E_{Sum} = 2.734$ MeV is 8.7 % while fitting the experimental spectra a value of 9.3 % is obtained. This mismatch is partially responsible for the additional broadening of the simulated data that has to be applied to match the experimental spectra, see section 3.5.2. The detectors with the worst energy resolution, 1 and 2, correspond to BaF_2 modules with a poor pulse shape, hence the worse behaviour in energy resolution. This could be attributed to badly adjusted settings of the voltage divider, issues in the optical coupling between crystal and photo multiplier tube or defects in the crystals themselves, i.e. detector 1 has never been working satisfactory since the installation of the TAC.

Table 4.2: Average energy resolution of the TAC at various E_γ.

	E_γ (MeV)	TAC $R(E_\gamma)$ (%)
^{137}Cs	0.662	16.9
^{88}Y	0.898	14.3
^{88}Y	1.836	10.5
AmBe	4.438	7.4
CmC	6.130	5.6

4.1.3 Time calibration and coincidence window

The event reconstruction in the TAC is based on a simple time coincidence between the signals detected by all the BaF_2 detectors. Using a time coincidence method two effects have been observed in the past and have to be checked:

- A time offset can be expected between different flash-ADC cards and even between channels within the same flash-ADC card due to slightly different electronic chains, for example cable lengths.
- A time drift due to different chronometers in each flash-ADC card. This issue should be addressed by the common chronometer originating from a master trigger, but remains to be verified.

Therefore a time calibration has to be done for each detector. For determining the time offset as well as the time drift, a radioactive source emitting two γ-rays simultaneously like ^{88}Y with a released energy of $E_{Sum} \approx 2.7\,\text{MeV}$ is used. The method used is explained as follows:

- Choose a reference detector.
- Choose a large coincidence window to make sure not to lose events.
- Calculate the time difference δT between signals in all detectors with respect to the reference detector where the sum energy of this coincidence event corresponds to the sum energy peak of the ^{88}Y source.
- These differences should correspond to a Gaussian distribution from which the time offset can be calculated.

The time difference between the reference detector (29) and detector 7 are shown in the left panel of Figure 4.10 together with a gaussian fit as red solid line using a large coincidence time window of 100 ns. The gaussian behaviour is sufficiently good to determine the time offset of $-12.4\,\text{ns}$ between the detector 7 and the reference detector.
Correcting for this offset yields the distribution shown in the right panel of Figure 4.10. One can observe two contributions to this distribution: an exponential for $\|\delta T\| < 10\,\text{ns}$ and a constant shape for $\|\delta T\| > 10\,\text{ns}$. The exponential shape corresponds to the coincidences from the ^{88}Y calibration source and the constant background correspond to random coincidences. To study the effect of the coincidence window one can look at the sum energy spectra from the ^{88}Y source for different coincidence windows shown in the left and right panel of Figure 4.11

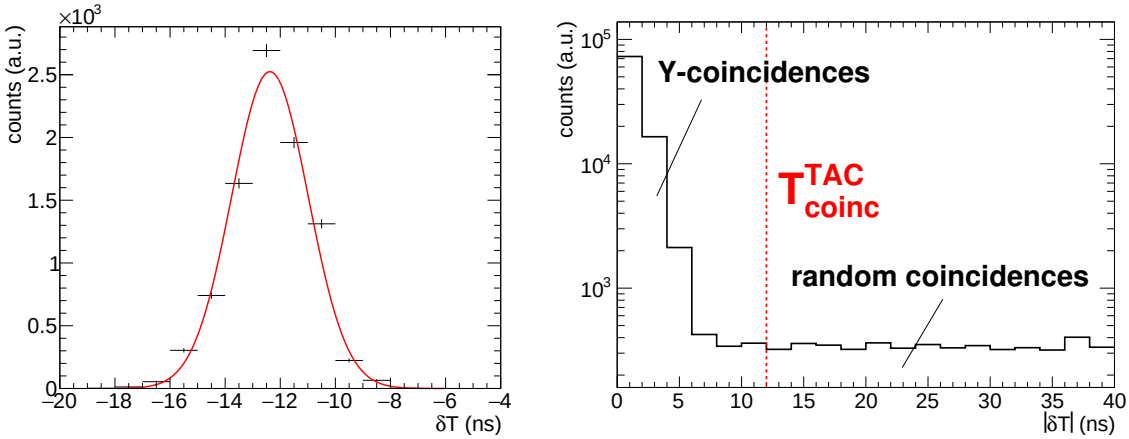

Figure 4.10: Time differences between signals from the reference detector and detector 7 where $E_{Sum} \approx 2.7\,\text{MeV}$. The timing offset between those two detectors equals the centroid of the Gaussian fit of $-12.4\,\text{ns}$ (left). Time offset corrected time differences - the optimal coincidence window T^{TAC}_{coinc} is indicated at 12 ns (right).

in linear and logarithmic scale respectively. A T^{TAC}_{coinc} of 3 ns is too small, hence events in the sum peak around 2.7 MeV are lost and the shape of the spectrum changes, favouring lower sum energies. On the other hand a $T^{TAC}_{coinc} > 10\,\text{ns}$ seems sufficient to catch all the TAC events but at the same time a coincidence window larger than 15 ns leads to pile-up of individual events resulting in a growing peak at 5.4 MeV which corresponds to twice the sum energy of the calibration source. Choosing the optimal time window for the further analysis is a compromise between a sufficiently large window to avoid splitting γ-ray cascades from capture events and to avoid random coincidences or pile-up. The optimal coincidence window for the TAC T^{TAC}_{coinc} for the measurement has been determined in a conservative approach to 12 ns as indicated in the right panel of Figure 4.10.

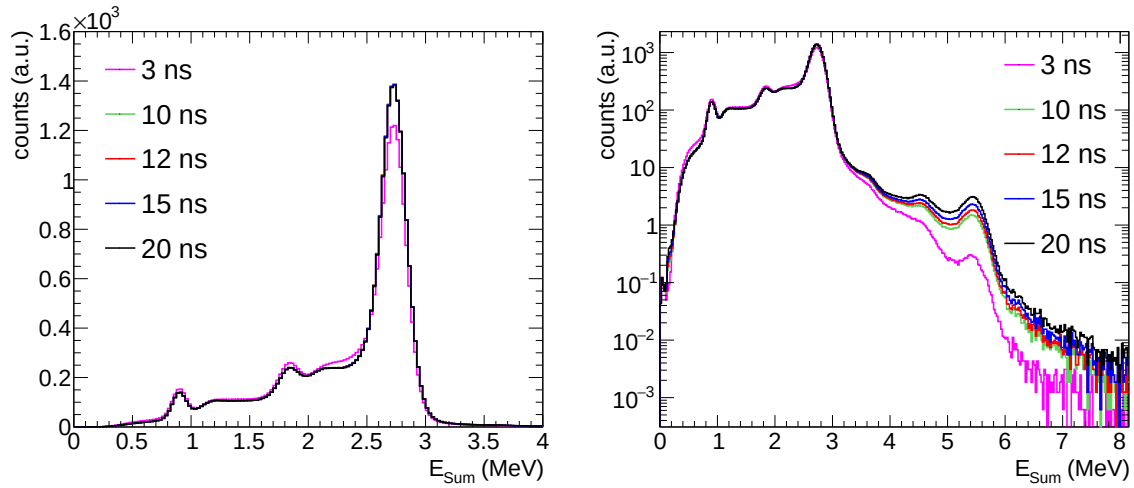

Figure 4.11: Sum energy spectra of the ^{88}Y calibration source using different time coincidence windows in linear (left) and logarithmic (right) scale.

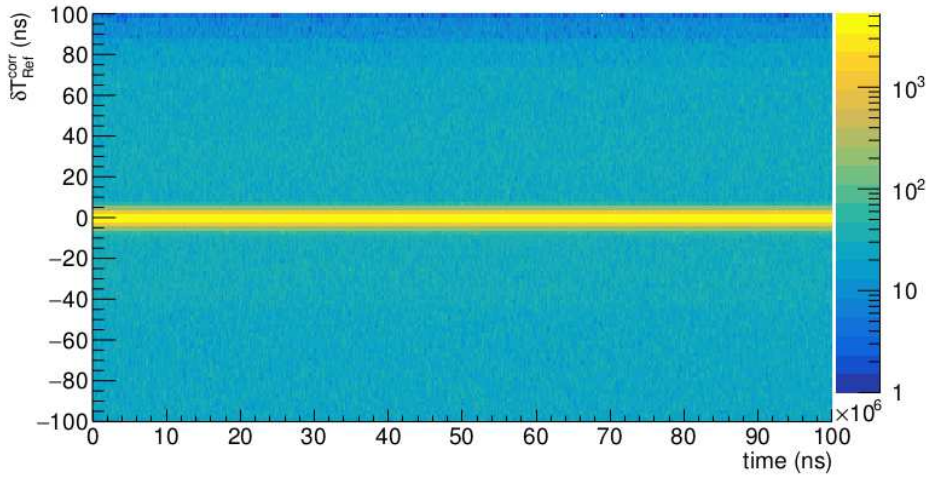

Figure 4.12: Time stability of the time differences (corrected for the constant time offset) δT^{corr}_{Ref} between all detectors and the reference detector. This nicely shows that there is no drift of the time window over the DAQ time window or time-of-flight.

The time drift is easily addressed by looking at the evolution of δT with time, namely time-of-flight. This evolution is shown in Figure 4.12 where the corrected δT is plotted against TOF for events with $E_{Sum} \approx 2.7\,\text{MeV}$. The histogram is split in 10 µs bins in time-of-flight. The maximum allowed time coincidence window is 100 ns and most of the coincidences are found within the chosen optimal coincidence window T^{TAC}_{coinc} of 12 ns. No drift of the centroid can be observed outside of statistical limits resulting in the conclusion that a further time calibration with time-of-flight is not necessary and the common chronometer is working as intended.

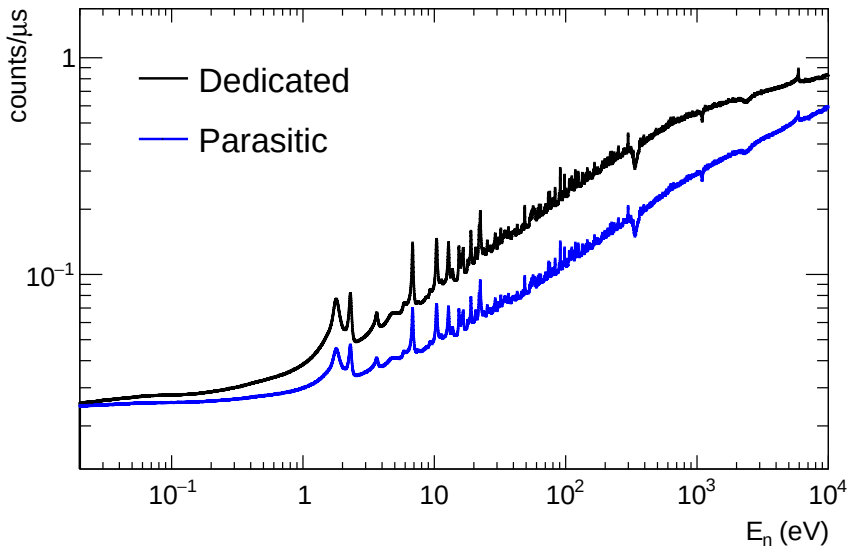

Figure 4.13: Count rate in the TAC for dedicated and parasitic beam types.

4.1.4 Count rate, dead-time and pile-up

As mentioned before the decay time of the BaF_2 scintillation light is rather long ($\tau \approx 630\,ns$). For high count rates this slow decay can cause two effects:

- Pile-up effect: If two uncorrelated events are detected as a single event in the TAC which leads to wrong summing of cascades.
- Dead-time effect: If the time between two consecutive signals in a BaF_2 crystal is too short a signal can be lost. This is enhanced if the deposited energy of the signals is very different.

Both effects depend on the incident γ-ray energies and the time difference between the γ-rays hitting the BaF_2 crystal, namely the count rate. The count rate of TAC events is shown in Figure 4.13 for dedicated and parasitic pulses. For low neutron energies the count rate is dominated by time constant background caused by the environment, cosmic radiation and events related to the α-activity of the uranium, thus the count rates approach the same value. The difference between the count rates for the two different beam types is the number of neutrons, hence the signal to background ratio. Above a few 100 eV the count rate for dedicated pulses decreases and approaches the parasitic one. This can have two causes:

- A higher rate of reactions leading to classic dead-time and pile-up effects in the TAC
- Some TAC modules have not yet recovered from the γ-flash, thus signals are either lost or wrongly reconstructed

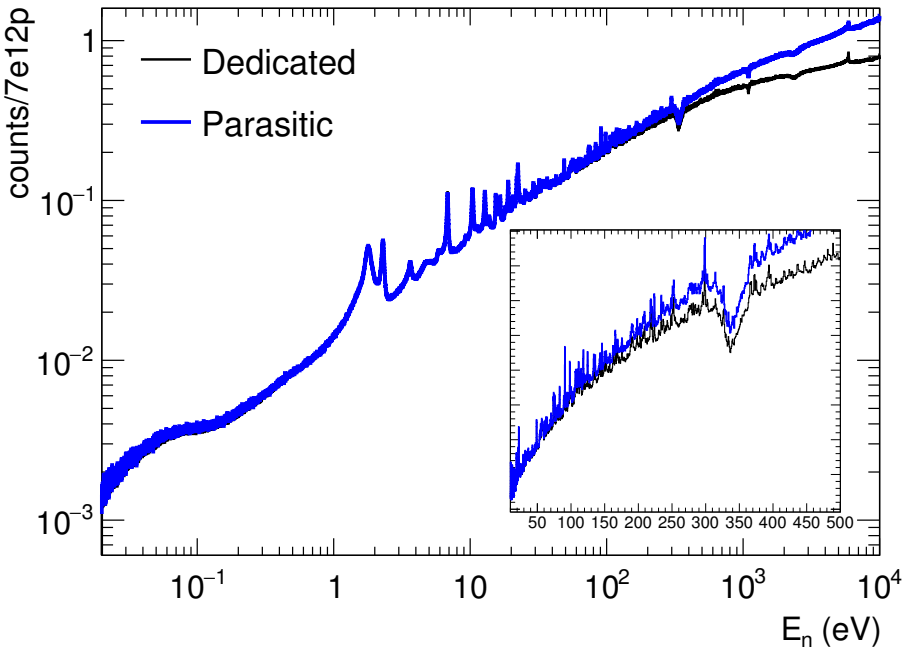

Figure 4.14: Comparison of the shape of the TAC count rate for dedicated and parasitic beam types normalized to a standard proton pulse. A deviation can be seen starting at 100 eV, indicating that pile-up or dead-time effects have to be taken into account for neutron energies higher than that. The time constant background has been subtracted for both curves.

The recovery after the γ-flash, namely the fast in beam γ-rays, depends on the crystal volume, distance to the center of the beam line and the applied high voltage. The effect caused by the γ-flash effectively limits the maximum neutron energy of the measurement, while models to correct for higher count rates in the TAC have been modelled and well characterized [92, 93]. If the detector would work in perfect conditions the dedicated and parasitic count rates (or counts) normalized to the neutron flux (or number of protons) must be equal if the time constant background can be neglected or is subtracted. The proton-normalized count rates for the two different beam types are shown in Figure 4.14. The two shapes start to divert at around 100 eV which corresponds to a count rate of 0.2-0.3 μs^{-1} (from Figure 4.13). At those rates dead-time and pile-up effects have a significant effect in the TAC and have to be corrected for. The method used will be described later.

4.2 Performance of the FICH

In this chapter the following properties and characteristics of the fission chamber relevant to the experiment are discussed:

- Pulse height spectrum: the pulse height spectrum of the fission chamber is composed of the α-particle background originating from the natural decay of ^{233}U and the fission fragments emitted in the fission process. Due to the optimization of the detector for fast timing neither fission fragments nor α-particles are stopped in the gas which results in a mediocre particle discrimination. Ways to improve the separation will be discussed. Furthermore, parameters of the pulse shapes will be used to look at specific regions in the pulse height spectra.
- Gain monitoring: among other things the gain of gaseous detectors depends on the thermodynamic conditions of the gas. Changes in the temperature, outside air pressure and humidity cause the gain to drift over time. The gain was monitored throughout the experiment and the results will be briefly discussed.
- The count rate will be briefly discussed and eventually a scaled fission cross-section will be extracted from the FICH data.

4.2.1 Pulse height spectra and particle discrimination

The use of thin ^{233}U samples allows reaction products to escape from the layer with a probability close to 100 %. However, absorption of the reaction products in the sample layers can occur if the reaction products get emitted close to parallel with respect to the layer. In this case the products lose a significant amount of their kinetic energy before escaping the sample and will be registered as low energy tail in the pulse height spectrum. This low energy tail overlaps with signals corresponding to ^{233}U α-particles emitted by the natural decay of ^{233}U. The discrimination between fission fragments and α-particles depends on the characteristics of the detector, the thickness of the samples and the kinetic energy of the α-particles. The discrimination is done with a cut in signal amplitude or pulse height. The choice of this threshold is based on a compromise between the fission detection efficiency and the exclusion

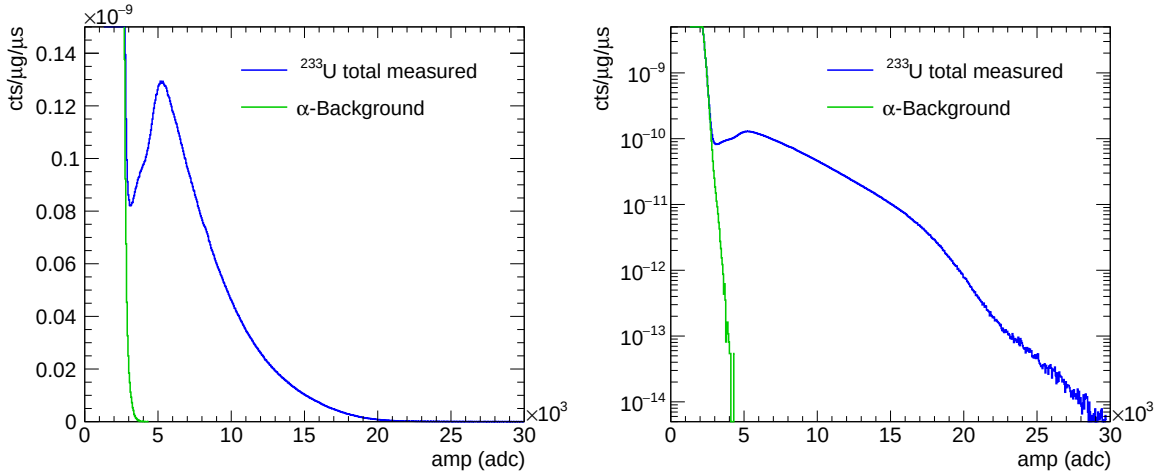

Figure 4.15: Pulse height spectra of the events in the fission chamber with and without beam in linear (left) and logarithmic (right) scale. Only events with $E_n < 10\,\text{keV}$ are considered.

of the α-particles.

In the left and right panels of Figure 4.15 the pulse height spectra of the events in all channels of the fission chamber with and without neutron beam is shown in linear and logarithmic scale respectively. The blue line corresponds to events recorded with the neutron beam while the events without neutron beam, the green line, correspond to the α-particle background of the ^{233}U samples and electronic noise, and have been recorded during dedicated beam-off measurements. The low pulse height part is cut with a software threshold at 1300 adc units in order to save disk space. The mediocre separation of fission fragments and α-particle background is not surprising considering the high count rate per anode caused by the natural activity of the samples of roughly 1 MBq in 2π per anode. The spectra show events with incident neutron energies smaller than 10 keV which corresponds to almost the full time

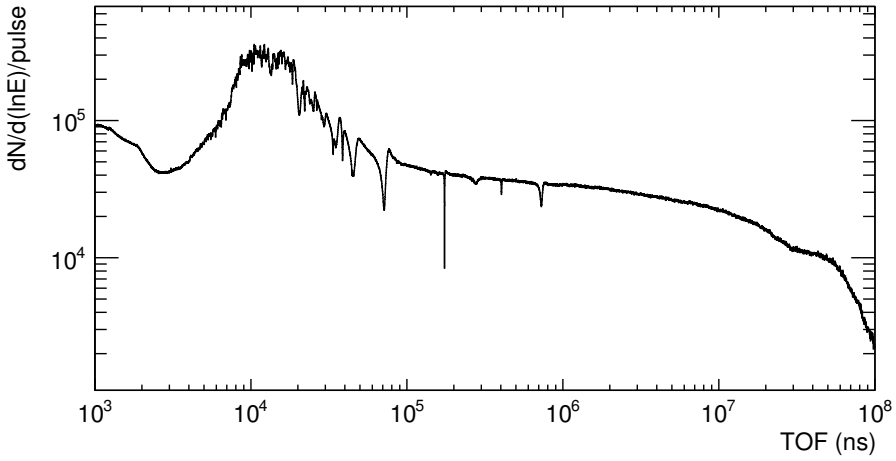

Figure 4.16: Neutron fluence in EAR1 at 185 m flight path from FLUKA simulations in isolethargic units. Note the increased fluence in the region $5\,\mu\text{s} < TOF < 15\,\mu\text{s}$.

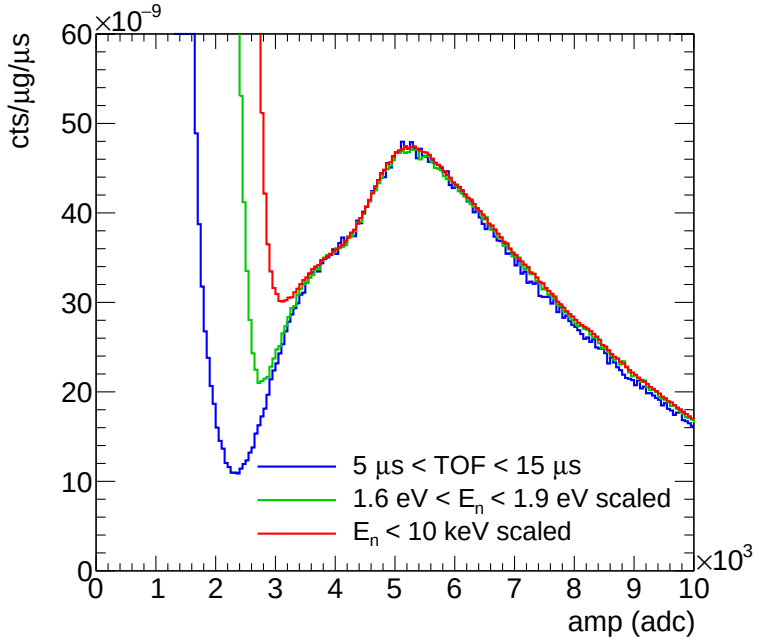

Figure 4.17: Pulse-height spectra of the events in the fission chamber for different TOF/E_n regions corresponding to different fission fragment to α-particle ratios (see text).

window of the digitizers of 100 ms. The resulting fission fragment to α-particle ratio in this time-of-flight region is not suited for a more detailed investigation of the amplitude threshold of the FICH.

In order to investigate the response to fission fragments below 3000 adc units one can look at specific regions in the TOF spectra. Firstly, the cross-section of the fission reaction can be used to enhance the fission fragment to α-particle ratio. Gating on the first resonance at 1.6 eV$< E_n <$1.9 eV greatly improves this ratio and allows to see the response to fission fragments well below 3000 adc units. Secondly, characteristics of the shape of the neutron fluence at n_TOF EAR1 can also be used to enhance the fission rate. Figure 4.16 shows the neutron fluence of n_TOF EAR1. The fluence is flat in most parts of the spectrum but shows a large plateau in the region around 5-15 µs. Due to the higher fluence in this region the fission fragment to α-particle ratio is increased.

In Figure 4.17 the pulse height spectra is shown again for three different neutron energy or TOF regions. It can be seen that the valley between fission fragments and α-particles has widened for the two aforementioned cases compared to the total measured spectrum for neutron energies below 10 keV. Obviously, fission tagging can be used in every TOF region and will significantly improve the α-FF separation and push the threshold even lower, as will be discussed in section 4.3. Note that the threshold obtained from the fission tagged pulse height spectra can not be used in order to extract the proper TOF response of the FICH alone.

With an inter-electrode gap of 3 mm in the ionization cells fission fragments are almost never stopped in the gas itself. Hence, the interpretation of the amplitude spectrum is not straight forward. In the blue curve (5 µs $< TOF <$ 15 µs) in Figure 4.17 a central peak at

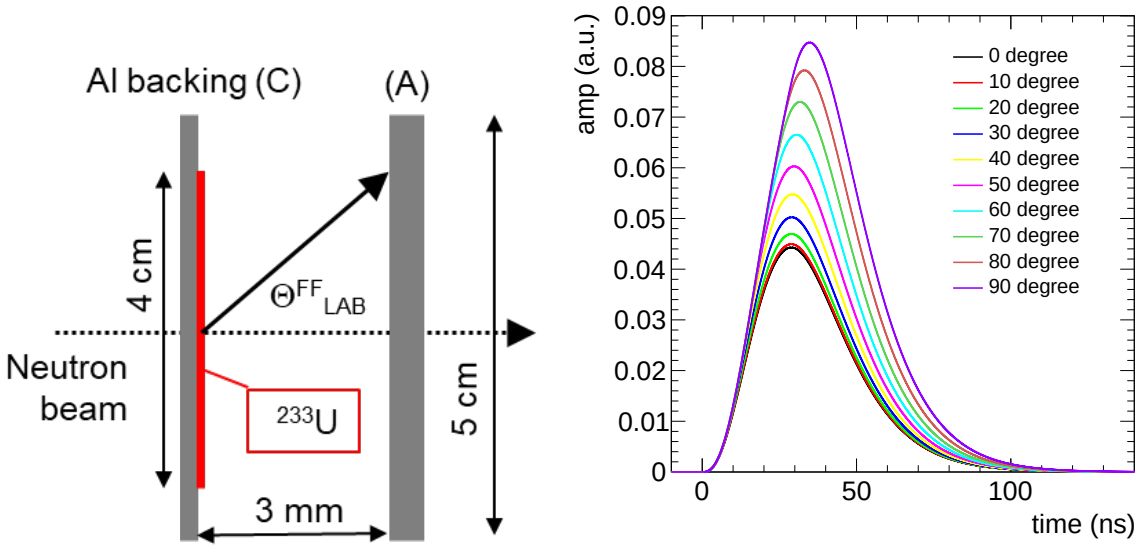

Figure 4.18: Definition of some quantities in the FICH simulations (left). Pulse shapes depending on the fission fragment's angle of emission θ^{FF}_{LAB} in the lab frame simulated using GARFIELD++. In the simulations an equal amount of electrons was used (= same deposited energy) to calculate the signals.

5200 adc units and on its left a shoulder at 3800 adc units are visible, corresponding to the light and heavy fission fragments respectively. Those two peaks can be separated under certain conditions, namely the direction of emission of the fission fragment. In an ionization cell the rise time of a signal depends, among others, on the angle of emission of the fission fragment. With the specific characteristics of the FICH and the electronics used to form the signals, signals with the shortest rise time are related to fission fragments emitted perpendicular to the electrodes and parallel to the neutron beam. On the contrary the longest rise times

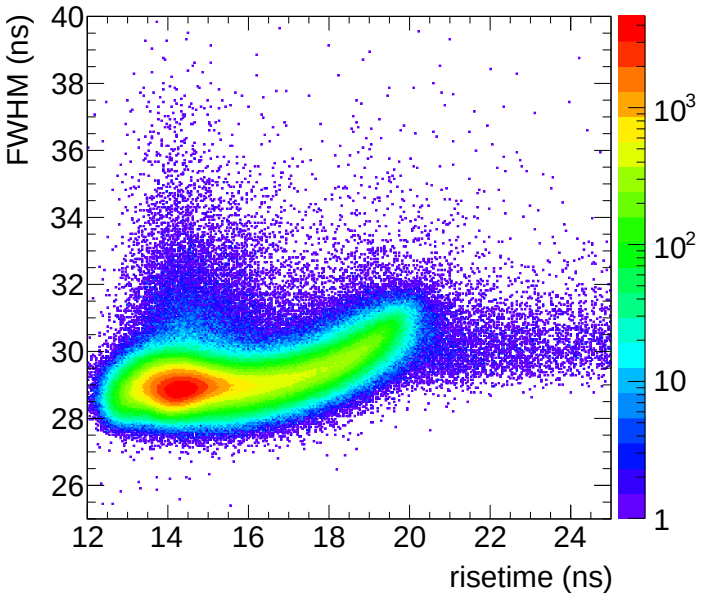

Figure 4.19: Fission fragment (amp>3000) signal shape parameters from FICH channel 4 reading only from a single ^{233}U deposit.

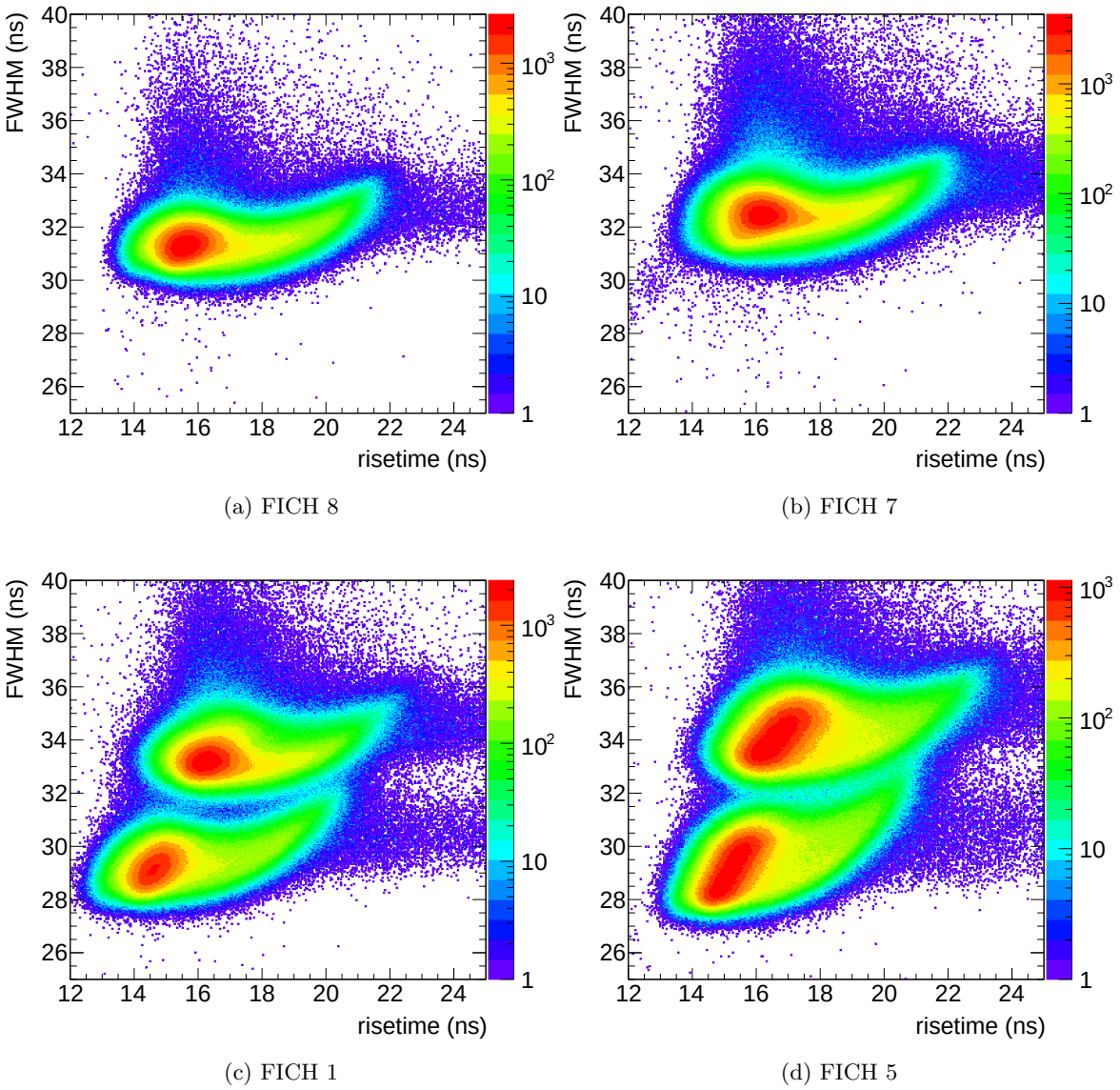

(a) FICH 8

(b) FICH 7

(c) FICH 1

(d) FICH 5

Figure 4.20: Fission fragment signal shape parameters from different FICH channels. For FICH channel 1 and 5 their two ionization cells show a different behaviour in the signal shape.

are related to fission fragments emitted parallel to the electrodes, thus perpendicular to the neutron beam. In the left panel of Figure 4.18 key quantities to simulate the signals in the FICH are defined and the right panel shows simulated signal shapes for different fission fragment emission angles using GARFIELD++[83]. It is obvious that the angle of emission θ^{FF}_{LAB} has a large influence on the signal amplitude and area.

Furthermore the full width at half maximum ($FWHM$) of the signals is related to the signal formation in the detector, namely the gap distance between the electrodes and the electron drift velocity. In Figure 4.19 the FWHM and rise time of fission fragment signals in FICH channel 4 (only one ^{233}U deposit) is shown. A clear peak in the 2D distribution is visible and a slightly curved behaviour for rise times larger than 16 ns can be observed. No difference between the light and heavy fragments can be seen, showing that the different ionization densities of the various fragments dE/dx do not pose a significant difference.

Table 4.3: Gates on FWHM and rise time of the FICH signals. The FWHM is important for FICH channel 1 and 5 as can be seen in Figure 4.20, while the rise time intervals can be used to select fission fragments emitted perpendicular to the deposits in order to visualize the light and heavy FF peaks as illustrated in Figure 4.21 and 4.22.

Detector	FWHM (ns)		rise time RT (ns)	
	min	max	min	max
1	25	31.5	12	13.5
	31.5	40	12	15.1
2	25	40	12	13.8
3	25	40	12	13.8
4	25	40	12	13.25
5	25	32	12	14.2
	32	40	12	15.2
6	25	40	12	14.7
7	25	40	12	14.8
8	25	40	12	14.5

Figure 4.20 shows the same plot for four other FICH channels. FICH channel 8 has the same position as channel 4 in their respective stacks and also posses only one ionization cell or one ^{233}U deposit. FICH channel 7 reads fission fragment signals from two ionization cells but shows no difference between the two different cells, thus it works as expected with respect to this criteria. Surprisingly, FICH channel 1 and 5 exhibit two clearly distinguishable distributions suggesting that their respective two ionization cells can be separated from each other. The bent drop like shape appears again for all individual distributions. Only FICH channel 1 and 5 show this behaviour so clearly.

Eventually, to see the dependence of the fission fragment signal amplitude on the angle of emission the signal amplitudes are shown in dependence of their rise time in Figure 4.21 for several FICH channels. Two banana like shapes can be identified in each plot. The respective peaks of the bananas for small rise times are the light and heavy fission fragments emitted perpendicular to the deposits. In case of FICH channels 1 and 5 the two different ionization

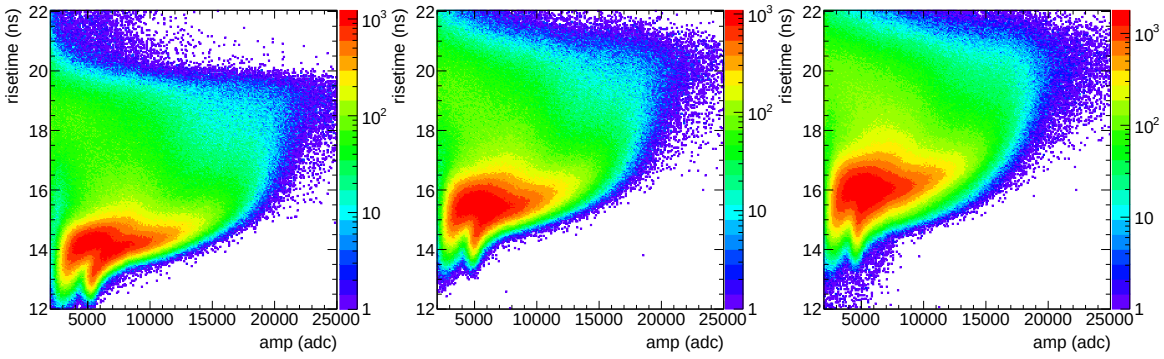

Figure 4.21: Rise time versus amplitude of FICH signals from the two single ^{233}U deposit FICH channels 4 (left) and 8 (middle) and FICH channel 7 (right) reading signals from two ionization cells. For short rise times (i.e. $cos\theta^{FF}_{LAB} \approx 1$) the light and heavy fission fragment peaks become visible.

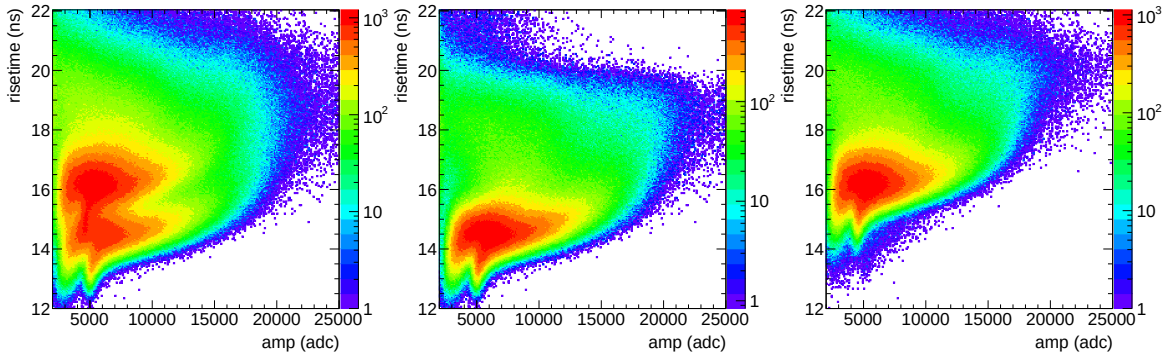

Figure 4.22: Rise time versus amplitude of FICH signals from FICH channel 1. As mentioned in the text the total (left) signals can be split with cuts on the FWHM of the signals according to the values in Table 4.3 to separate the signals from the two different deposits or ionization cells (middle, right) read out by FICH channel 1.

cells of each channel have to be separated to avoid summing effects as shown in Figure 4.22 with the separation for the FWHM given in Table 4.3.

As the amplitude spectrum is rather smooth a good calibration of simulation data could be problematic. Luckily the light and heavy fission fragment peak offer two points in the calibration curve and thus can be used to get an idea of the calibration. The extracted peaks are shown in Figure 4.23 for various detectors using the rise time gates from Table 4.3.

The strong influence of the angle of emission and energy loss in the sample due to the unknown thickness or homogeneity makes a final conclusion on the differences in the signal parameters between the channels difficult but in general it can be said that these parameters are influenced by the uniformity and strength of the applied electric field as well as the electronic read out chain. The field is by definition not uniform because of the finite geometry of the detector but should be inhomogeneous in the same way for all cells, if electrostatic forces can be neglected. The strength of the electric field depends on the applied voltage and the geometry, namely the gap distance, of the ionization cells. Several effects could cause different electric field in the different cells. Voltage drops on imperfect electrical connections as well as uncertainties in the production of the machined parts of the FICH could be responsible for the different behaviour of the individual cells.

Because the two ionization cells in each of FICH channel 1 and 5 are read out by their respective electronic chain at least for those channels an influence from the electronic chain can be ruled out. Both channels are at the same position in their respective stacks. Both show a similar behaviour, namely the bottom cell contains the smaller mass deposit out of the two cells and exhibits the shorter rise times and FWHM. This suggests that there might be a systematic error in the manufacturing or mounting of the related cells in the stacks. In any case this does not influence the further analysis but offers a nice feature for calibrating simulation data and also offers a way to monitor the gain, see section 4.2.2

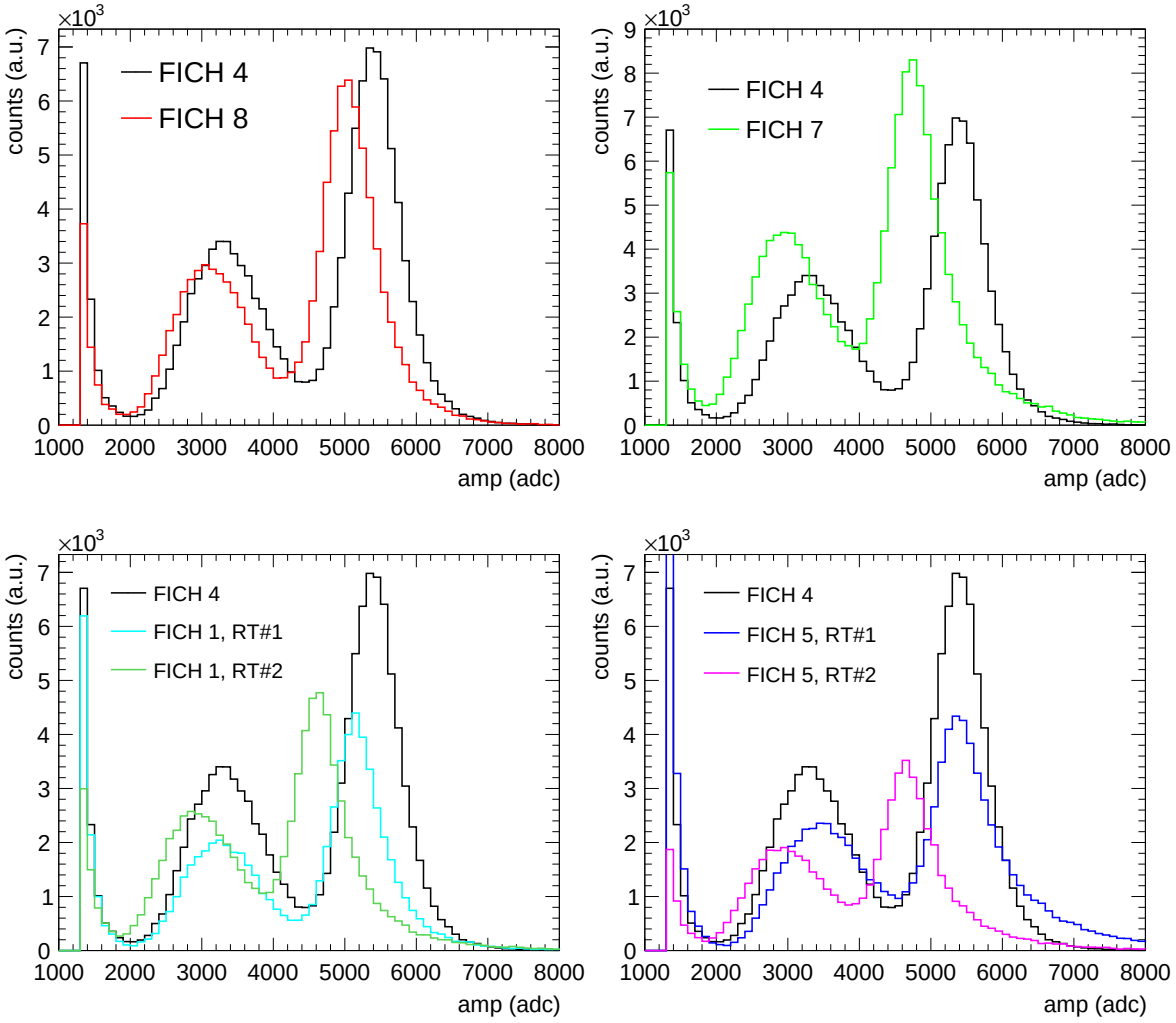

Figure 4.23: Pulse height spectra of different FICH channels with respective gates on the FWHM and rise time - values given in Table 4.3

4.2.2 Gain monitoring

As any gaseous detector the gain of the fission chamber depends on two variables: the bias voltage applied between the electrodes and the density of the gas in the ionization cells. The applied bias voltage is well controlled within 1 V by a high voltage power supply. However, the gas density is subject to various other variables, namely thermodynamic conditions like temperature and pressure as well as the outside air pressure at the exhaust of the gas system and the humidity amongst others. This can cause changes in the drift velocity of the electrons and subsequently the gain to drift over time. The gains of the individual detectors have been monitored throughout the measurement by counting the number of events above a certain threshold of $amp > 3500$ adc units normalized to the number of protons impinging the spallation target. Figure 4.24 shows the gain drift of detector 4 over time for the full duration of the experiment, indicated in *RunNumbers*.

Thanks to the excellently working gas regulation system, the gain variations were kept small throughout the whole measurement within statistical fluctuations. A general decrease of the

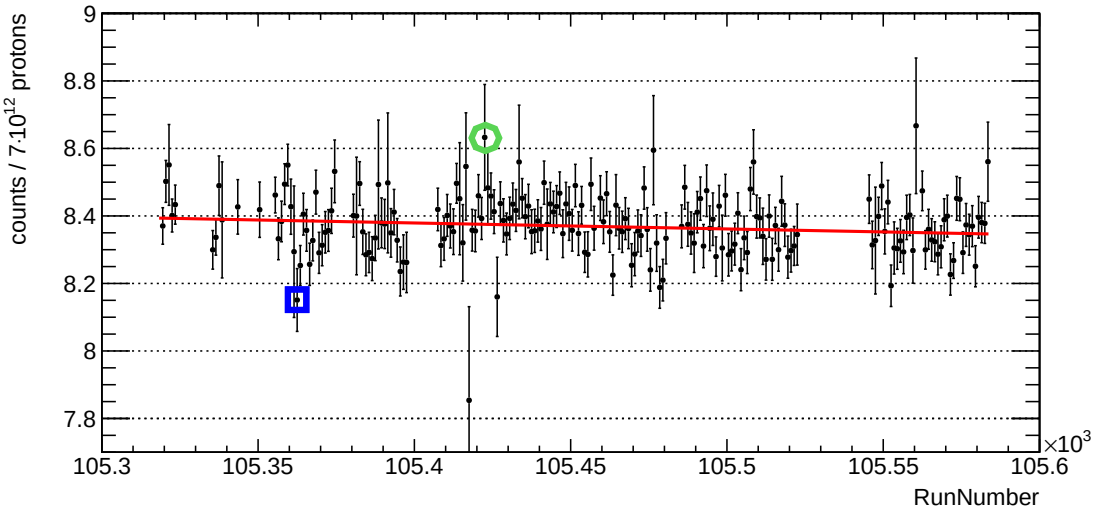

Figure 4.24: Gain drift over time: number of events with $amp > 3500$ adc units per protons per Run - typically 4 hours make a Run. The red line is a linear fit to the data points, with $p_0 = 27.0097$ and $p_1 = -1.77E - 4$.

gain can be observed with increasing time, indicated by the red linear fit and the calculated gain drift between the beginning and the end of the experiment is less than 1 %.

To ensure and to cross-check that the metric used to measure the gain drift is valid, the pulse height spectra of two runs, indicated by the blue rectangle and green circle in Figure 4.24, are shown in Figure 4.25. The only observable differences are related to statistical fluctuations.

Another method to monitor the gain can be used with this fission chamber. As explained before, the properties of the FICH allow to select fission fragments emitted perpendicular to the samples by gating on certain rise times of the signals. The results are two nicely distinguishable peaks, the light and the heavy fission fragment peak. For each of the two peaks a gaussian fit can be performed and its centroid can be monitored over time, see left

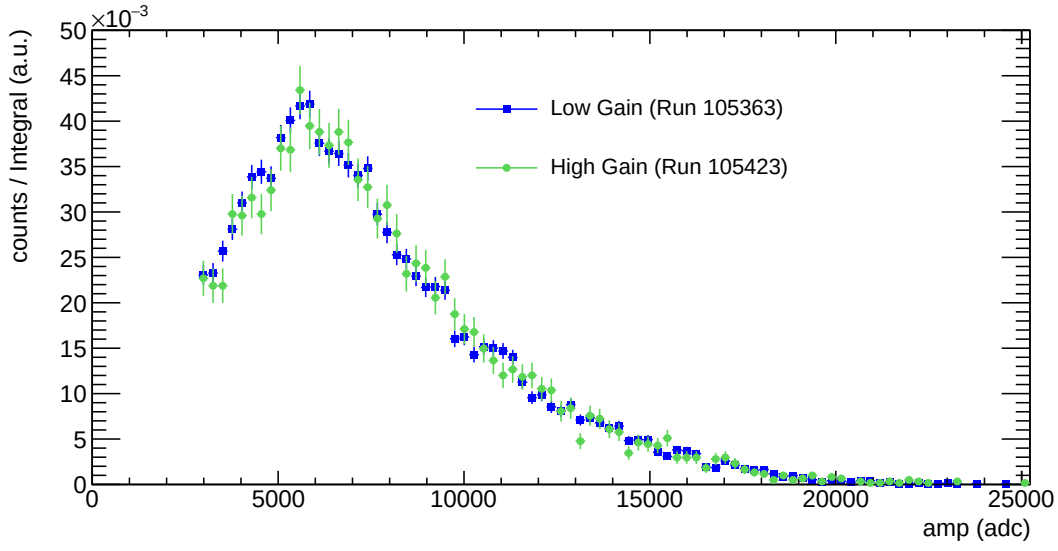

Figure 4.25: Pulse-height spectra of fission events for two different gains.

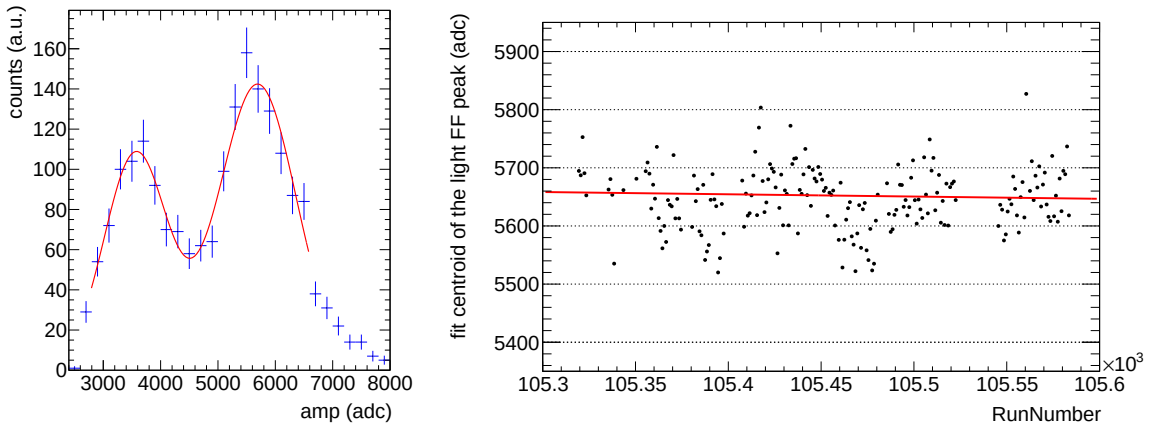

Figure 4.26: Using the rise time gates from Table 4.3 the heavy and the light fission fragment peaks can be fitted with gaussians (left). The centroid of the fit to the light FF peak in FICH channel 4 during all runs of the ^{233}U α-ratio campaign. The red line is a linear fit to the data points, with $p_0 = 9751.77$ and $p_1 = -3.887E-2$. (right).

and right panel of Figure 4.26 respectively. A similar trend as with the other method is observed. The variation in the gain is below 1 % over the full duration of the experiment and can be explained by statistical fluctuations and uncertainties in the fits. The conclusion is that the gas regulation system worked as intended and no gain correction has to be applied to the data.

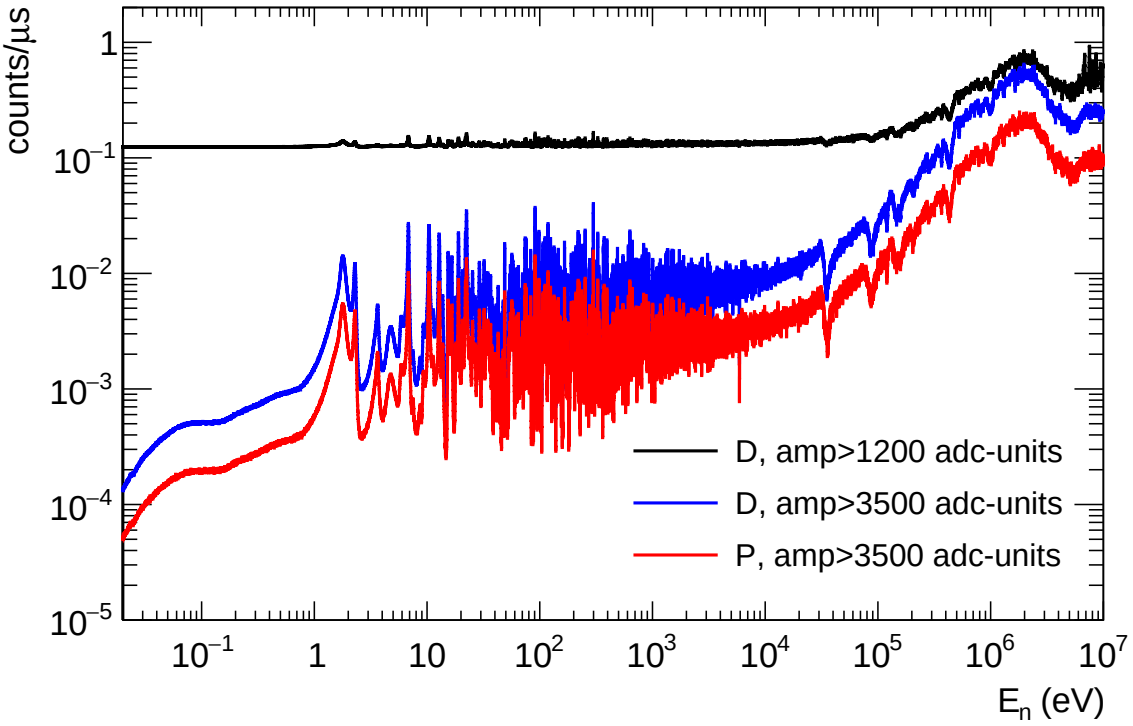

Figure 4.27: Count rate in the FICH for dedicated and parasitic beam types and different amplitude cuts.

4.2.3 Count rate and comparison of the ^{233}U(n,f) cross-section with evaluated libraries

The count rate in all read out channels is dominated by the α-activity of the ^{233}U samples by far. Gating on higher signal amplitudes allows to filter α particles as can be seen in Figure 4.27 where the count rate is given for a low and high amplitude cut as well as for dedicated and parasitic beams. The count rate including α particles in Figure 4.27 is not the true count rate in the detectors, as an amplitude cut ($amp > 1200$ adc units) has been applied, filtering most of the α particle related counts already. With the described pulse shape parameters, especially the FWHM of the order of 30 ns, count rates of several MBq should be sustainable without having to correct for pile-up effects in fission fragments detection which can also be seen in Figure 4.28 where the dedicated and parasitic pulse types are compared and no difference can be observed.

To verify the satisfactory behaviour of the fission detector the shape of the ^{233}U(n,f) cross-section has been calculated from the FICH events and the shape of the neutron flux taken from the *SiMon* monitor. This shape has then been normalized to evaluated libraries in the neutron energy range from 8.1 eV to 17.6 eV because this region is well separated avoiding interference from neighbouring resonances as has been suggested in [94]. Figure 4.29 and Table 4.4 show a comparison of the scaled ^{233}U(n,f) cross-section obtained from the experiment and evaluated libraries, ENDF/B-VII.1 [95], ENDF/B-VIII.0 [9], JEFF-3.3 [10] and JENDL-4.0u2 [11], from 0.1 eV up to 10 keV. A reasonable agreement is reached within ± 4 % up to a neutron energy of 300 eV. The results above 300 eV seem to suggest that the evaluated libraries underestimate the ^{233}U(n,f) cross-section by as much as 10 %, specifically

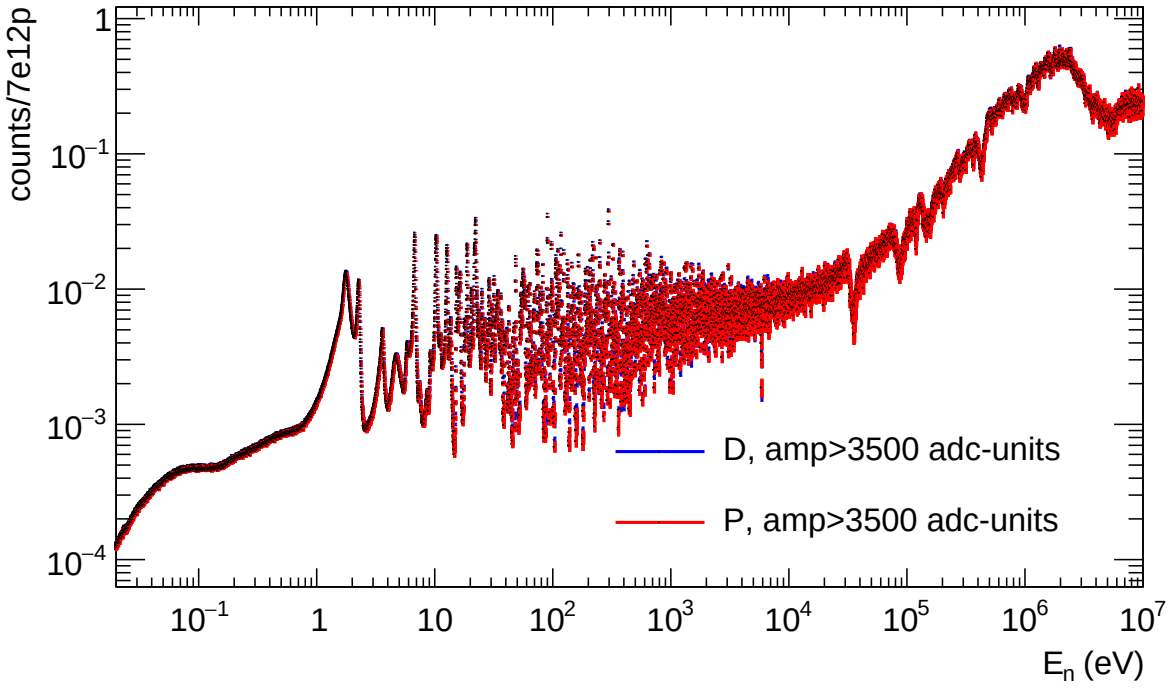

Figure 4.28: Count rate in the FICH normalized to a standard proton pulse for dedicated and parasitic beam types.

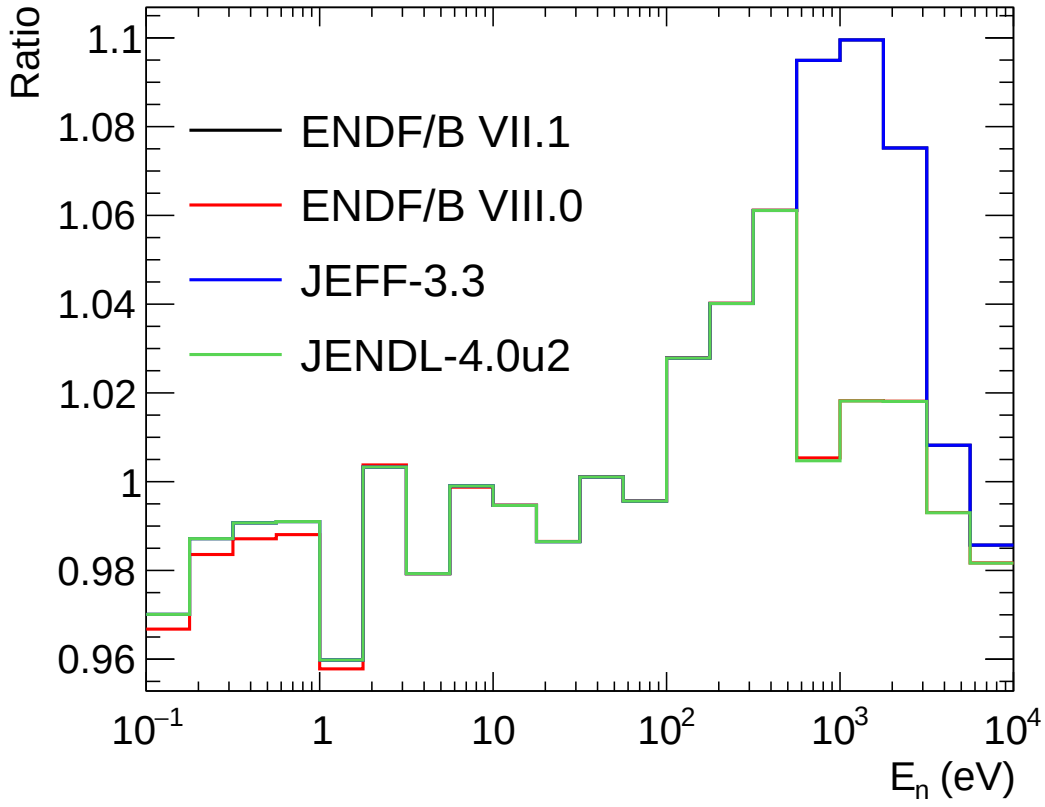

Figure 4.29: Ratio between the experimentally determined cross-section, scaled to the evaluated library in the neutron energy range from 8.1 eV to 17.6 eV, and the evaluated library.

the JEFF-3.3 (= ENDF/B-VII.1) evaluation shows a lower average cross section after the resolved resonance region ending at 600 eV.

It can be concluded that the fission chamber is working satisfactorily in the neutron energy range of this measurement. An accurate prompt fission background subtraction for the calculation of the ^{233}U α-ratio can be assured.

Table 4.4: Ratio between the experimentally obtained ^{233}U(n,f) cross-section and the evaluated libraries for different neutron energy bins.

E_n (eV)	ENDF/B-VII.1	ENDF/B-VIII.0	JEFF-3.3	JENDL-4.0u2
0.1 - 1	0.983 ± 0.004	0.980 ± 0.001	0.983 ± 0.004	0.983 ± 0.004
1 - 10	0.982 ± 0.004	0.981 ± 0.001	0.982 ± 0.004	0.982 ± 0.004
10 - 100	0.993 ± 0.004	0.993 ± 0.002	0.993 ± 0.004	0.993 ± 0.004
100 - 1000	1.049 ± 0.005	1.034 ± 0.003	1.049 ± 0.005	1.034 ± 0.005
1000 - 10000	1.055 ± 0.006	1.007 ± 0.004	1.055 ± 0.006	1.007 ± 0.005

4.3 Fission Tagging

This section describes the procedure and analysis carried out regarding the event reconstruction of coincidences between the TAC and the FICH. Prompt fission events are characterized with high γ-multiplicity [96], as was observed and suggested in previous works [59, 60]. Hence, the prompt fission events will be detected as high crystal multiplicity events with a high probability.

4.3.1 Event reconstruction

4.3.1.1 Time calibration and coincidence window

The coincidence algorithm is again based on the use of a coincidence window between TAC and FICH $T_{coinc}^{TAC-FICH}$. The only differences compared to the TAC event reconstruction algorithm is that multiple tagging is allowed and will occur depending on the maximum coincidence window $T_{coinc}^{TAC-FICH}$. Furthermore, the event reconstruction algorithm for prompt fission events also considers and allows negative time differences. If $T_{coinc}^{TAC-FICH}$ is larger than the coincidence window for TAC events T_{coinc}^{TAC} multiple taggings can happen, meaning there can be two TAC events for a single FICH event. The process of selecting which event is being assigned as the prompt fission event is described in section 4.3.1.2.
The time calibration is done in a similar way as for the BaF_2 crystals only now between events from the FICH and the already reconstructed TAC events. Therefore a second coincidence window $\delta T^{TAC-FICH}$ is necessary. Correcting for the time offset and choosing this time window follows the same methodology as for the coincidences built in the TAC in section 4.1.3. Figure 4.30 shows the time differences $\delta T = TOF_{TAC} - TOF_{FICH}$ between the TAC and the

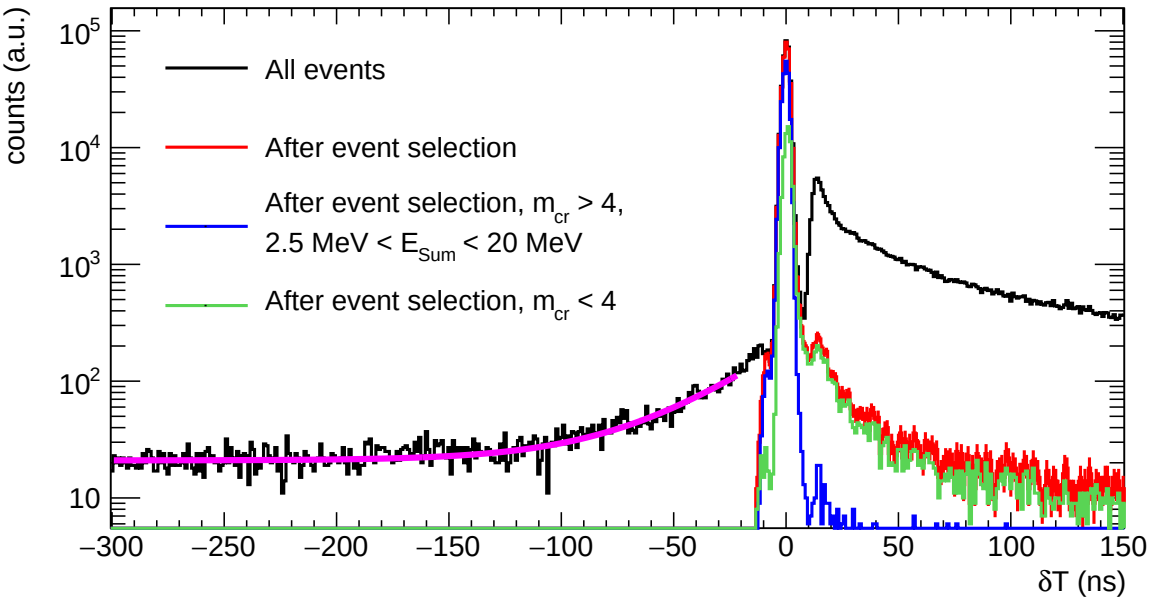

Figure 4.30: Time difference distribution between TAC and FICH events for a maximum allowed coincidence window $T_{coinc}^{TAC-FICH} = 1\,\mu s$. The features of the distribution are explained in the text.

FICH event for all found coincidences for a maximum allowed $\delta T^{TAC-FICH}$ of 1000 ns. The time offset correction has already been applied and distribution can be explained as follows:

- Events with $\delta T < -200$ ns show a flat distribution and correspond to random coincidences similar as in the TAC event reconstruction.
- The shape for $-200\,\text{ns} < \delta T < -20$ ns can be described by an exponential sitting on top of the constant background. The exponential increase corresponds to events where a γ-ray is emitted before the nucleus fissions. These events can be explained by the existence of the (n,γf) process (fission isomers) and are discussed below in section 4.3.1.2.
- A main peak for $-10\,\text{ns} < \delta T < 10$ ns corresponding to the prompt fission events as suggested by the characteristics of those events with high E_{sum} and m_{cr}, indicated by the blue data points.
- Another sharp structure or side peak for $10\,\text{ns} < \delta T < 20$ ns which is an artifact of the event reconstruction process. Essentially, the coincidence window in the TAC blocks another TAC event from opening for 12 ns which corresponds exactly to the time difference between the main peak and this side peak. The position of the side peak will shift with the coincidence window of the TAC.
- Events with $\delta T > 20$ ns, the exponential tail, correspond to events induced by fission neutrons being captured in the experimental setup and emitting γ-ray cascades on their own or isomeric states of the fission products that have a delayed de-excitation via γ-ray cascades.

4.3.1.2 Event selection

For reasons of causality the coincidence window between TAC and FICH ($T^{TAC-FICH}_{coinc}$) cannot be smaller than the coincidence window in the TAC (T^{TAC}_{coinc}), otherwise there is the possibility to lose coincidences. An optimal coincidence window can be determined due to the time resolution of both detection systems but the same compromise between pile-up and efficient tagging has to be made.
As already mentioned $T^{TAC-FICH}_{coinc} > T^{TAC}_{coinc}$ can lead to multiple coincidences found for a single FICH event. The different coincidences will be characterized by different TAC events, hence different E_{sum}, m_{cr} and $\delta T^{TAC-FICH}$. If two or more TAC events are assigned to the same FICH event a selection has to be made. The selection is made by selecting the TAC event with the highest crystal multiplicity m_{cr} as the *correct* prompt fission event. If the TAC events happen to have the same crystal multiplicity then the event with higher E_{sum} is selected as the *correct* prompt fission event. In principle these criteria are arbitrary and the performance of the different event selection algorithms is illustrated in Figure 4.31. It shows the E_{sum} spectra of the *correct* prompt fission events selected with different algorithms. It is evident that no matter which algorithm is chosen the difference is negligible.
The left panel of Figure 4.32 shows the effect of different coincidence windows $T^{TAC-FICH}_{coinc}$ on the total number of found coincidences normalized to the total number of fission events with

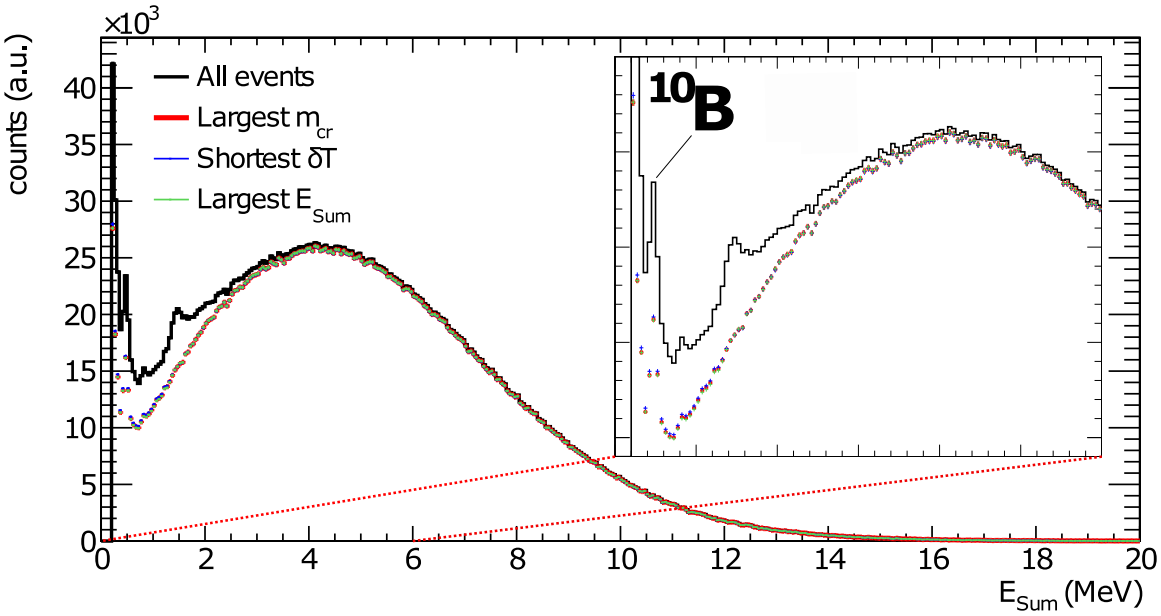

Figure 4.31: Comparison of the different event selection algorithms using either largest E_{sum}, largest m_{cr} or smallest $\delta T^{TAC-FICH}$ as primary criteria. In the zoom in the region for $E_{Sum} < 6$ MeV the suppression of the 480 keV γ-ray emitted in the ^{10}B(n,α) reaction and the 1435 keV γ-ray from inelastic scattering of fission neutrons on ^{138}Ba can be observed.

$amp > 3000$ adc units and 1.6 eV$< E_n <$ 1.9 eV. A steady increase can be seen with increasing $T_{coinc}^{TAC-FICH}$ which is understandable although those TAC events are not necessarily related to the FICH event but correspond to random coincidences. On the other hand the right panel of Figure 4.32 shows the number of coincidences where exactly one TAC event is found for one FICH event, again for events with $amp > 3000$ adc units and 1.6 eV$< E_n <$ 1.9 eV. With increasing coincidence window $T_{coinc}^{TAC-FICH}$ the number of one to one coincidences

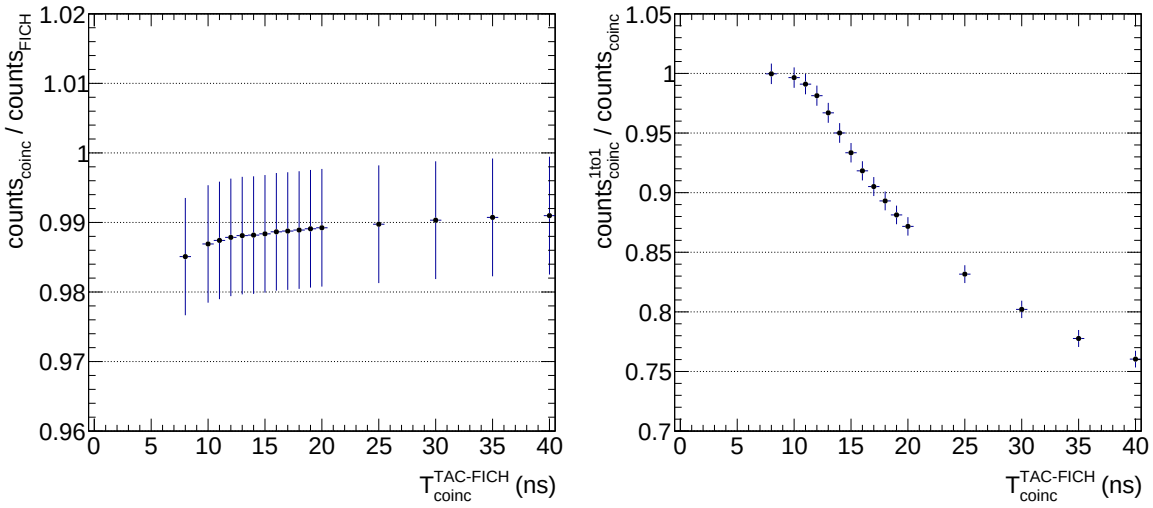

Figure 4.32: Fraction of found coincidences with respect to the total number of fission events in the FICH for different TAC-FICH coincidence windows $T_{coinc}^{TAC-FICH}$(left). Fraction of events where exactly one TAC event is found for one FICH event with respect to all found coincidences (right). Both for events with $amp > 3000$ adc units and 1.6 eV$< E_n <$ 1.9 eV.

drastically decreases. A coincidence window $T_{coinc}^{TAC-FICH}$ slightly larger than the T_{coinc}^{TAC} is already sufficient to tag close to 99 % of the FICH events while a window too large might result in an uncertain assignment of multiple TAC events to a FICH event. To reduce this uncertainty the $T_{coinc}^{TAC-FICH}$ coincidence window is set to 14 ns in the further analysis.

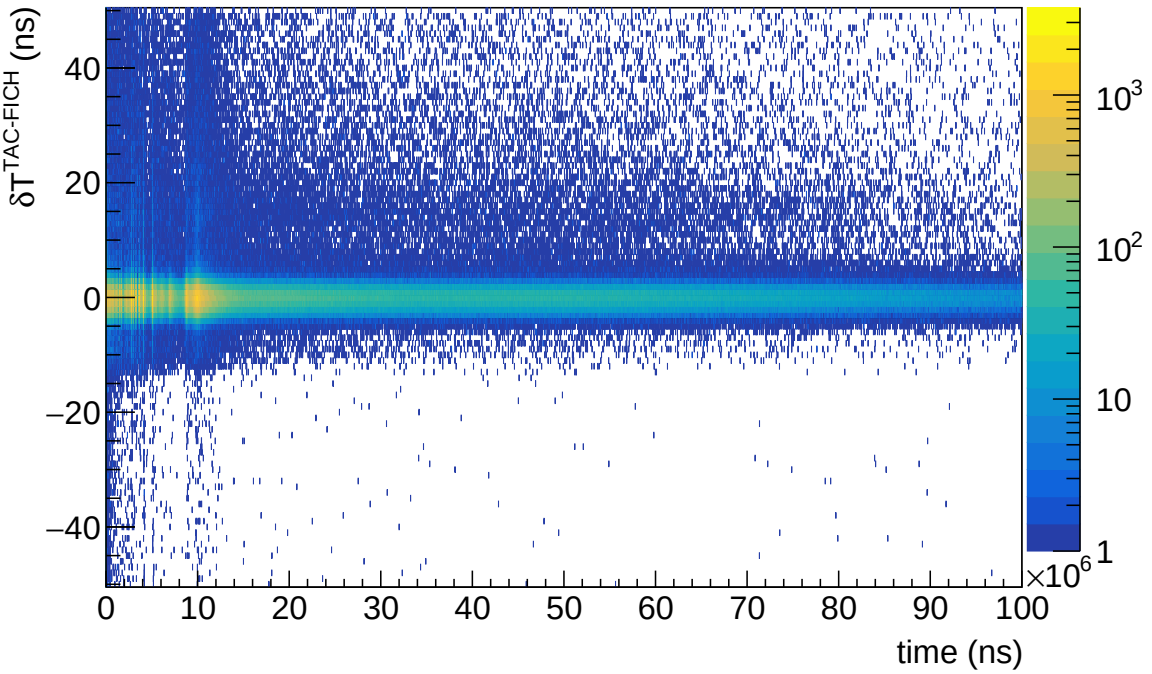

Figure 4.33: Stability of the time differences $\delta T^{TAC-FICH}$ for fission events in coincidence with TAC events with time. No drift can be observed.

For the same reasons like in the TAC event reconstruction the stability of the time window with respect to the time-of-flight has to be checked and is shown in Figure 4.33. No drift of the $\delta T^{TAC-FICH}$ with time can be observed making a further correction unnecessary, thanks to the perfectly working n_TOF DAQ.

The (n,γf) process

In the (n,γf) process [97, 98] the configuration of the compound nucleus (deformation) can be situated energetically in the second minima of the fission barrier and thus fissioning or decay to the first minimum by tunnel effect emitting a γ-ray cascade along the decay path may occur. The tunnel effect is not instantaneous, hence the meta-stable state has a half-life that depends on the excitation energy and the height and width of the fission barrier. It has been suggested [97] that for the fissile isotopes, ^{233}U, ^{235}U and ^{239}Pu, the average values of radiation width $\overline{\Gamma}_\gamma$ and fission width $\overline{\Gamma}_f$ coupled with the small $\overline{\Gamma}_n$ in neutron resonances lead to an appreciable probability of fission after primary emission of a γ-ray and thus be important in the actinide region for low neutron energy resonances [99, 100]. In Figure 4.30 the coincidence distribution for events with −950 ns to −22 ns is fitted with the following

function:

$$f(t) = a_0 + a_1 e^{a_2 t}, \tag{4.4}$$

where a_0, a_1, a_2 are the parameters describing the random coincidences, the intensity of the (n,γf) process and the half-life of the fission isomer respectively. Three fission resonances at 1.6-1.9 eV, 2.2-2.4 eV and 4.2-5.3 eV have been investigated. The fit in the neutron energy region of 1.6-1.9 eV is shown in Figure 4.30 and the parameters of all fits are summarized in Table 4.5, where only statistical uncertainties are considered. From these values the fission isomer half-life $t_{1/2}$ and the ratio between (n,γf) and (n,f) events has been calculated and can also be found in Table 4.5.

Table 4.5: Fit parameters for the (n,γf) process in different neutron energy intervals and calculated values of the half-life of the meta-stable fission isomer and the contribution of the (n,γf) process to the total fission events. The uncertainties of the half lives $t_{1/2} = ln(2)/|a_2|$ only contain statistical contributions from the fits.

En (eV)	a_0 (counts)	a_1 (counts)	a_2 ($\cdot 10^{-2}$ ns^{-1})	$t_{1/2}$ (ns)	(n,γf)/(n,f) (%)
1.6 - 1.9	19.7 ± 0.16	4.92 ± 0.11	2.78 ± 0.11	24.9 ± 1.0	0.057 ± 0.002
2.2 - 2.4	5.79 ± 0.09	3.85 ± 0.14	2.69 ± 0.16	25.8 ± 2.3	0.139 ± 0.009
4.2 - 5.3	2.96 ± 0.06	3.45 ± 0.17	2.73 ± 0.18	25.3 ± 2.8	0.209 ± 0.015

The half-life obtained by the calculation in all neutron energy regions are consistent with themselves, and compatible with values from literature [52, 53] of 30.4(49) ns for the fission isomer. The probability of (n,γf) is of the order of 0.1 % with respect to the (n,f) process for the selected resonances. The (n,γf) process does not present a problem in the further analysis as it accounts only for about 0.1 % of all fission events and furthermore those are strongly suppressed by the conditions applied to the TAC for the analysis of the ^{233}U α-ratio .

4.3.2 Pulse-height spectra

A better separation between fission fragments and α-particles allows to lower the amplitude threshold in the FICH for characterizing the prompt fission γ-ray spectra. Fission tagging improves the separation of fragments and *alpha*-particles in the pulse-height spectrum as the probability to tag an α-particle is smaller compared to a fission fragment. In Figure 4.34 the tagged fission amplitude spectra for different TOF/E_n regions is compared to the best achievable separation solely using the FICH. The improvement is obvious and it allows to investigate the shape of the fission fragment energy deposition in the fission chamber below what was possible with the FICH alone.

4.3.2.1 Monte Carlo simulations of the FICH response to fission fragments

Understanding the response of the FICH to the fission fragments is relevant for the ^{233}U α-ratio analysis with respect to understanding angular correlations between the fission axis and the emitted prompt fission γ-rays observed in the experiment, discussed later. For

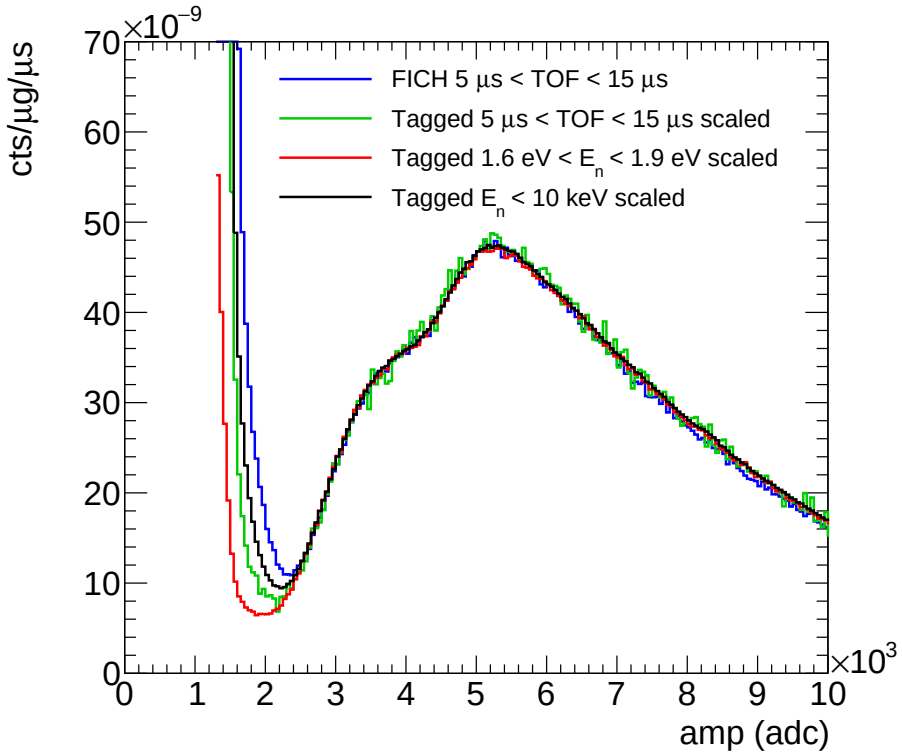

Figure 4.34: Pulse-height spectra of the events in the fission chamber for 5 µs $< TOF <$ 15 µs compared to tagged events for different TOF/E_n regions.

this purpose the detector's response to fission events has been calculated via Monte Carlo simulations, divided in two steps:

- Generation of the fission events used in the calculation such as the neutron-induced fission fragment mass, charge and total kinetic energies, excitation energies, prompt neutrons and γ-ray cascades emitted from the fission fragments. The fragment masses and their total kinetic energy have been obtained event by event using the Monte Carlo GEF code [96]. It can describe fission of a compound nucleus from any entrance channel with a given excitation energy and angular momentum, for example thermal neutron induced fission. It is based on a general approach to nuclear fission explaining a large part of the observables on the basis of fundamental laws of physics and general properties of microscopic systems. The description reproduces a number of peculiar observed features of the prompt neutron multiplicities and of the even-odd effect in fission fragment Z distributions.

- The Monte Carlo simulation of the FICH response to the fission fragments (ions) generated by the GEF code in the previous step. The output of GEF code, namely the fission fragment distribution, is used as input for simulating the detector response based on the GEANT4 toolkit. The details are given below.

The output of the GEF code is shown in the left panel of Figure 4.35 illustrating the fission fragment distribution of thermal neutron induced fission of ^{233}U. As expected in asymmetric

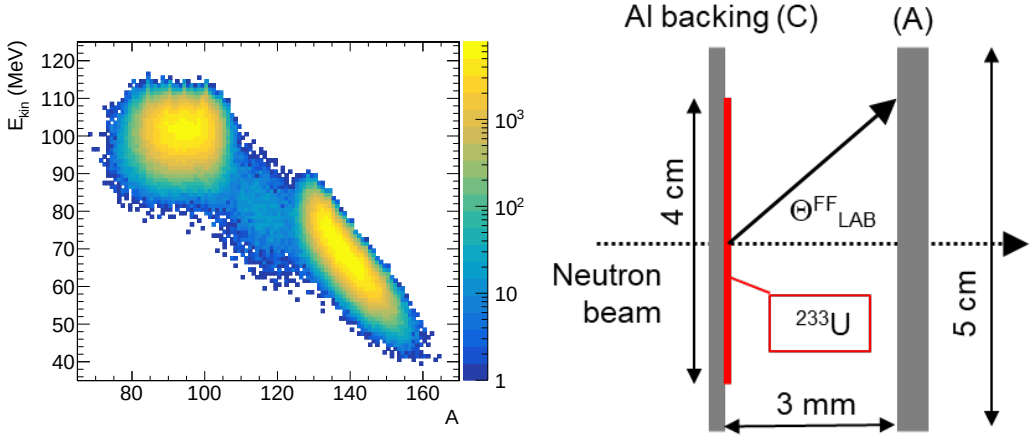

Figure 4.35: Fission fragment distribution for thermal fission of ^{233}U according to the GEF code (left). Schematic illustration of the ionization cell geometry used in GEANT4 simulations (right).

fission two mass peaks, corresponding to the light and heavy fission fragment, can be observed. In the GEANT4 simulations it is assumed that the prompt fission neutrons have been emitted instantaneously after the scission point, i.e. at very short times. Hence, the mass of the fission fragments and the total kinetic energy TKE given after the prompt neutron emission has been used to calculate the fission fragment's kinetic energies and momenta neglecting the incident neutron's momentum and energy applying the conservation laws of the kinetic energy and momentum:

$$TKE = E^{kin}_{A_1} + E^{kin}_{A_2} \tag{4.5}$$

$$\vec{0} = \vec{P}_{A_1} + \vec{P}_{A_2} \tag{4.6}$$

where A1 and A2 are the masses of the fission fragments after prompt fission neutron emission. Thus the kinetic energy of each fragment can be calculated to:

$$E^{kin}_{1,2} = TKE \frac{A_{2,1}}{A_1 + A_2} \tag{4.7}$$

and the direction of both fission fragments is fully determined by the conservation of the momenta to

$$\vec{P}_{A_1} = -\vec{P}_{A_2} \tag{4.8}$$

namely a back to back emission. According to the GEF code, see left panel of Figure 4.35, the heavy fragments exhibit kinetic energies ranging from as low as 40 MeV up to 90 MeV while the light ones posses kinetic energies from 80 MeV up to 115 MeV.

A schematic illustration of the geometry of a single ionization cell of the FICH is shown in the right panel of Figure 4.35, indicating also the emission angle Θ^{FF}_{LAB} of the fission fragment with respect to the neutron beam or the normal vector of the ^{233}U samples. The polar angle is

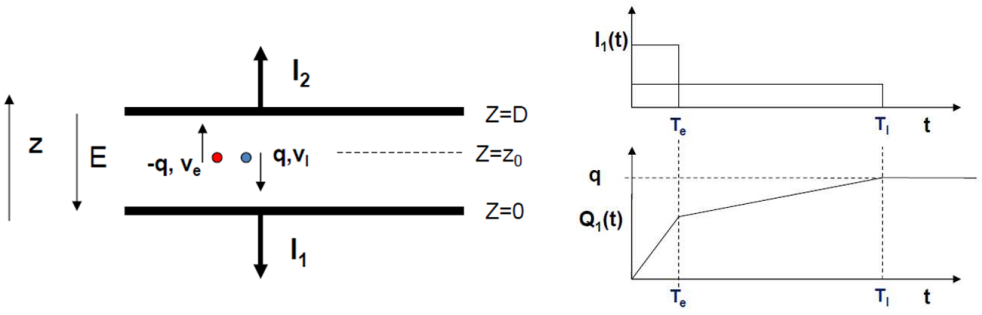

Figure 4.36: Definition of a parallel plate geometry, like the FICH ionization cells, and relevant quantities for the Shockley-Ramo theorem (left). Induced currents in a parallel plate geometry (right).

not shown but is considered in the simulations and both angles are assumed to follow isotropic distributions. Particles with an emission angle $\Theta_{LAB}^{FF} = 0$ exhibit a direction parallel to the neutron beam, while $\Theta_{LAB}^{FF} = \pi/2$ corresponds to the direction perpendicular to the neutron beam. The coordinate system is placed so that the x-y plane corresponds to the plane of the ^{233}U sample while z is the depth in the sample or detector. The thickness of the ^{233}U samples is calculated from the areal density of the ^{233}U samples using the bulk mass density of U_3O_8 of 8.2 g/cm^3. The z coordinate (depth in the sample) of the point of emission is uniformly chosen within the thickness of the sample while the planar (x-y) coordinates or radius are sampled using a Gaussian distribution, centered at 0, with a width of $\sigma = 0.7$ cm mimicking the spatial neutron beam profile. Both fission fragments are emitted back to back with initial directions corresponding to the isotropically sampled Θ_{LAB}^{FF} and polar angles. Their kinetic energies are calculated as described in Eq. (4.7) from the output of the GEF code.

The simulation intends to understand the detector response, hence a simplified geometry has been used, which is shown in the right panel of Figure 4.35. The geometry consist of a cylindrical gas volume which is touching the aluminium backing of the ^{233}U deposits on one side with a thickness of 10 μm. The surrounding plastic spacers of the stacks and the aluminium and copper rings of the electrodes at the edge of the sample backing have not been included in the simplified geometry.

For the calculation of the amplitude in the FICH produced by a fission fragment the correct signal formation has to be taken into account. Using the Shockley-Ramo theorem [101, 102] allows to easily calculate the instantaneous electric current i induced by a charge q moving in the vicinity of an electrode. For a parallel plate geometry, see Figure 4.36 and associated definitions, the derivation is as follows. The Shockley-Ramo theorem says that the induced current on an electrode is proportional to the product of the charge, a weighting field E_w at the position of the charge and the velocity of the charge v_q:

$$i = -\frac{dQ}{dt} = qE_w v_q. \tag{4.9}$$

With the weighting field E_w for a parallel plate geometry with a distance between the electrodes D and an applied potential difference V_0

$$E_w = E_1/V_0 = -E_2/V_0 = 1/D \tag{4.10}$$

the induced current on the electrodes 1 and 2, can be calculated as

$$I_1 = -I_2 = qv_e/D + qv_I/D. \tag{4.11}$$

As $v_e >> v_I$, due to the lower mobility for ions compared to electrons in gas, the induced current of the ion can be neglected and the induced charge caused by this current is simply the integral over time

$$\begin{aligned} Q_1^{tot} &= \int_0^{T_i} I_1 dt = qv_e/D \cdot T_e \\ &= qv_e/D \cdot (D - z_0)/v_e \\ &= q(D - z_0)/D. \end{aligned} \tag{4.12}$$

For the simulation of the signal amplitude caused by the production of ionization pairs proportional to the deposited energy in a parallel plate detector the deposited energy has to be weighted by the factor $(D - z_0)/D$, in a first approximation. Therefor a step limitation is introduced in GEANT4, limiting the maximum step size to 1 μm in the gas, and weighting the deposited energy in each step by the respective factor as described above. The output of the simulations essentially contains the deposited energy, the amplitude, calculated from the position weighted energy deposition, and the angle of emission for the light and heavy fragments.

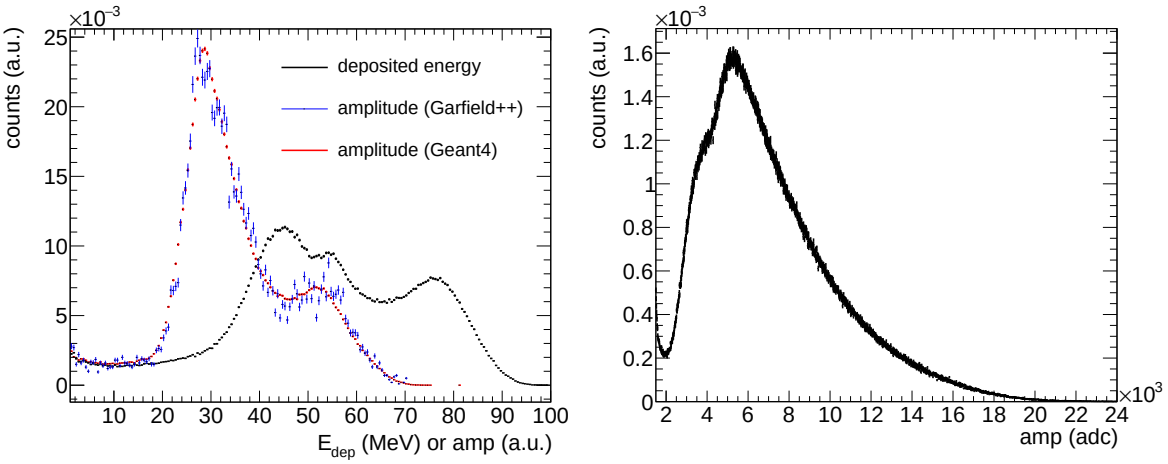

Figure 4.37: Deposited energy and calculated amplitude of fission fragments from a U_3O_8 layer with a density of 8.2 g/cm^3 and an areal density of $\sigma = 305\,\mu$g/cm^2 ^{233}U (left). Experimental amplitude spectra of FICH channel 4 with an areal density of $\sigma = 305\,\mu$g/cm^2 ^{233}U (right).

For a given ^{233}U areal density, or mass, the thickness of the layer can be calculated if the density is known. Due to the process of electro-deposition of the sample material the exact layer composition or density is unknown. What is known, is the base material, uranium oxide, most likely in the form of U_3O_8, exhibiting a bulk density of 8.2 g/cm^3. The thickness of a U_3O_8 layer with an areal density $\sigma = 305\,\mu$g/cm^2 ^{233}U (FICH channel 4) calculates to 432 nm, containing 84.5 mass % ^{233}U and 15.5 mass % oxygen. The deposited energy spectrum and the calculated amplitude for such a layer are shown in the left panel of Figure 4.37. It is

evident that the simulated amplitude spectrum does not match the experimental amplitude distribution shown in the right panel of Figure 4.37 even though the conversion from amplitude to adc units is missing. When looking at the amplitude region between 2000 adc units and 7000 adc units the shoulder at 3500 adc units is missing in the simulations, which might be for the following reasons:

- The approximation in the calculation of the amplitude in GEANT4 is wrong
- The thickness and/or the composition of the layer will influence the energy loss for the fission fragments in the sample, hence the deposited energy in the gas

Addressing the first point requires the simulation of the drift of individual electrons inside the gas, which can be done using GARFIELD++. Therefor the deposited energy in each step is stored together with the distance to the electrode and used as an input to GARFIELD++ putting a number of electrons corresponding to the deposited energy and the work function of CF_4 of 33.8 eV [103] at the recorded positions from GEANT4. The known transfer function of the electronics is convoluted with the current induced by the electron drift to calculate the shape of the signals and extract their amplitudes, see left panel of Figure 4.37. There is no difference between the amplitude spectra produced by GEANT4 and GARFIELD++ hence the additional step in GARFIELD++ is unnecessary. Furthermore, the calculations with GARFIELD++ simulating the drift of millions of electrons is time consuming and hence only limited statistics was achieved in the comparison. It shall be noted that a shift between the GEANT4 and GARFIELD++ amplitude calculation of 15 % is observed which has been corrected for in the left panel of Figure 4.37.

The thickness and the composition of the deposited layer greatly influences the energy loss in the layer. The surface of a typical sample and an analysis of the elemental composition has been shown in Figure 3.20 taken from Ref. [86]. In this picture a wide distribution of oxygen, carbon and aluminium was found as well as a significant roughness or surface inhomogeneity has been observed, see the maze like structure in Figure 3.20. Those factors make a simulation rather complicated due to the large amount of free parameters: the density, thickness and elemental composition of the layer as well as its roughness, and how to model the roughness. Several approaches have been performed:

- Variation of the thickness of a U_3O_8 deposit with constant density
- Modification of the mass fractions of the layer to match results obtained in [86]
- Geometry splitting of the deposit in several layers and adjustment of the elemental composition
- Different physics models in the simulations
- Any combinations of the above

Several physics lists (containing the physics models used in the simulations with GEANT4), namely QGSP_BERT_HP, QGSP_BIC_HP, QGSP_INCLXX_HP, Shielding as well as custom built lists based on the hadron therapy physics list in GEANT4 including high precision low energy EM models as well as the G4BraggIonGasModel and G4BetheBlochIonGasModel physics models, have been tested but no noticeable difference is observed.

Modifying the thickness and density of the layer separately have similar effects because the energy loss is related to the product of the thickness and density. The results of the thickness variation of a U_3O_8 layer are shown in Figure 4.38 where the multiplication factor M describes how much thicker the corresponding layer is with respect to the standard layer ($M \equiv 1$). With increasing multiplication factor M the thickness increases and the fragments lose more energy in the sample. The heavy fragments lose more energy compared to the light ones and the low amplitude shoulder starts to emerge out of the central peak, see the blue curve in the left panel of Figure 4.38. This effect grows until the two peaks can be separated completely at high multiplication factors M (i.e. thicker layers), see the green curve in the left panel of Figure 4.38. In the right panel of Figure 4.38 the amplitudes are converted to ADC channels using a linear function. While the positions of the central peak and the low amplitude shoulder can be matched, the relative peak heights cannot be matched. Furthermore, the remaining third peak in the simulated spectra between 6000 adc units and 12 000 adc units does not show up in the experimental spectra. The third peak can merge into the central peak when the thickness is increased further and this might also result in better relative peak heights. Nevertheless, this results in unrealistically thick layers and the fraction of fission fragments lost in the samples increases drastically from 8 % to 16 % and 20 % corresponding to $M = 1$, $M = 2.$ and $M = 2.6$ respectively. The real efficiency for similar applied amplitude cuts is of the order of 10 %, hence a large modification of the sample thickness can be ruled

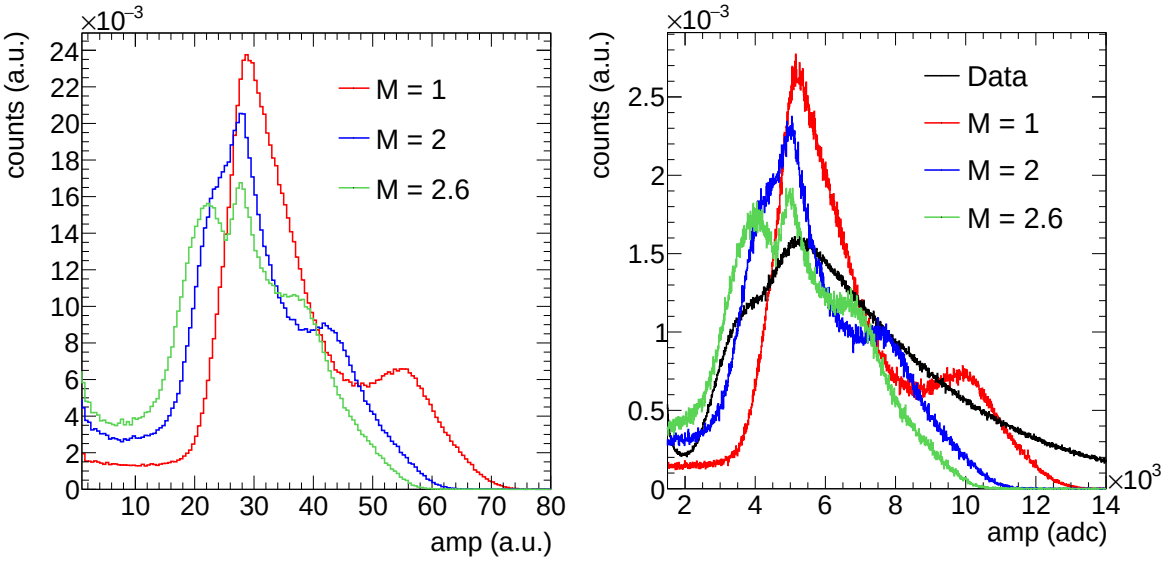

Figure 4.38: Calculated amplitude of fission fragments in the FICH for different thicknesses: a factor of 2 means that the thickness of the layer was multiplied by 2 (left). Conversion of the calculated amplitude into ADC channels based on a linear conversion (right).

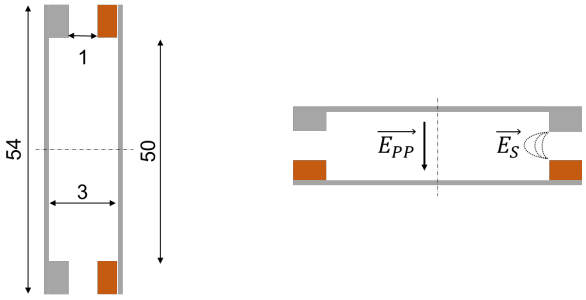

Figure 4.39: Geometry of one ionization cell including the rings that supply the electrical connections (left) - measures in mm. Schematic illustration of the electric fields caused by the parallel plates $\vec{E_{PP}}$ and the stray field of the electrical connection rings $\vec{E_S}$ (right).

out.

The layer can be split into several smaller layers where thickness and material composition can be modified individually, creating a depth profile of the stopping power of the material layer. The difficulty with this approach is that there is no measurement to give a hint on this profile. In general it can be assumed that the layer closest to the aluminium backing will contain some aluminium due to the roughness of the backing itself while the last layer in contact with the gas has been exposed to air, thus oxidation might lead to a higher oxygen content in this layer. In both cases the stopping power per unit length would decrease compared to the standard U_3O_8 layer as uranium is replaced by lighter elements.

None of the attempts lead to a satisfying agreement between the simulations and the experimental spectra as the simulations were not able to properly reproduce either the central peak and its low amplitude shoulder or the higher amplitude tail. Furthermore, the more complicated the model the more free parameters are available for variation, resulting in a large parameter space that has to be investigated. A problem in the simulation cannot be excluded but it should also be reminded that inhomogeneities in the electric field can also lead to significant deviations from the experimental spectra.

Indeed, one potential explanation has not been mentioned yet - a distortion of the electric field due to the geometry of the ionization cells. Previously a pure parallel plate geometry was assumed and especially the edges of the gas volume have been neglected. The geometry of an ionization cell is shown in the left panel of Figure 4.39 including the electrical contacts for the electrodes. Those contacts themselves are rings with 50 mm and 54 mm inner and outer diameters respectively and are made out of aluminium on the deposit side and aluminum or copper on the anode side depending on which side of the electrode. Those rings have a height of 1 mm which might be significant for a gap of only 3 mm between the electrodes. It is possible that the electric field produced by the rings has a significant effect on the electron drift in the outer radial region of the ionization cell, see right panel of Figure 4.39. This would affect signals from fission events with large emission angles more than signals with small angles of emission as the tracks of such signals are likely to reach the edges of the ionization cell. Effectively, this might distort the whole amplitude spectrum and entails a simulation of the electric field and the individual electron drift inside this field. Such simulations have not been performed.

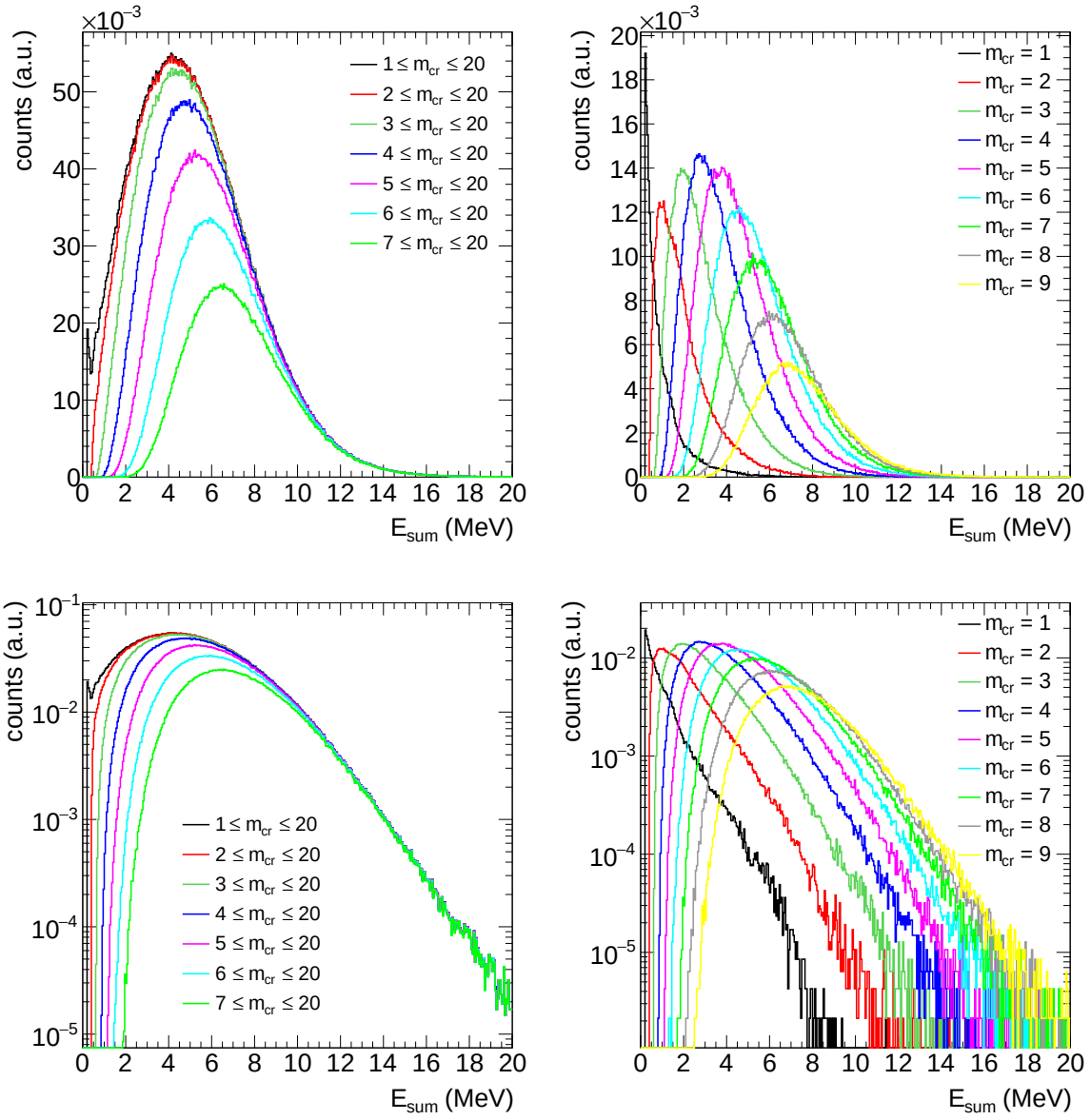

Figure 4.40: PFG spectra for events with $amp > 3000$ adc units and $1.6\,\text{eV} < E_n < 1.9\,\text{eV}$.

4.3.3 Prompt fission γ-ray spectra

The prompt fission γ-rays (PFG) emitted during fission events are fission tagged and can be selected. The experimentally obtained PFG spectra are shown in Figure 4.40 and the mean sum energy is given together with its respective standard deviations in Table 4.6 for various conditions in crystal multiplicity m_{cr}.

4.3.3.1 Comparison with Monte Carlo simulations

The simulations of the prompt fission γ-rays have been carried out in GEANT4. The geometry of the TAC and FICH is implemented in GEANT4 as described in section 3.5 and the events are generated from the probability distribution given by the respective models. The PFG cascade generator has been introduced according to three different models:

Table 4.6: Mean sum energy E_{Sum} and $\sigma(E_{Sum})$ of the measured prompt fission γ-ray spectrum, using a low energy γ-ray threshold $E_{thresh} = 200$ keV for events with $amp > 2500$ adc units.

	$<E_{Sum}>$ (MeV)	$\sigma(E_{Sum})$ (MeV)		$<E_{Sum}>$ (MeV)	$\sigma(E_{Sum})$ (MeV)
$1 \leq m_{cr} \leq 20$	5.12	2.76	$m_{cr} = 1$	1.08	0.995
$2 \leq m_{cr} \leq 20$	5.27	2.69	$m_{cr} = 2$	2.04	1.31
$3 \leq m_{cr} \leq 20$	5.53	2.6	$m_{cr} = 3$	2.95	1.51
$4 \leq m_{cr} \leq 20$	5.88	2.52	$m_{cr} = 4$	3.81	1.66
$5 \leq m_{cr} \leq 20$	6.32	2.45	$m_{cr} = 5$	4.62	1.77
$6 \leq m_{cr} \leq 20$	6.81	2.4	$m_{cr} = 6$	5.39	1.86
$7 \leq m_{cr} \leq 20$	7.34	2.37	$m_{cr} = 7$	6.13	1.93
			$m_{cr} = 8$	6.85	1.98
			$m_{cr} = 9$	7.56	2.03

- A PFG model developed by Valentine [104] and a slightly modified version of the model [105]
- The GEF code [96] was used to generate fission fragments in thermal fission of ^{233}U and the respective PFG distributions
- A model developed by M. Jandel at Los Alamos [106]

For the comparison the simulated and experimental data have been normalized to 1 for $m_{cr} > 0$.

In the original model of Valentine [104] no correlation between the number and the energy of the γ-rays emitted in a fission event is assumed. In the modified version such a correlation was introduced [105]. The results from the simulations of the original model of Valentine [104] and

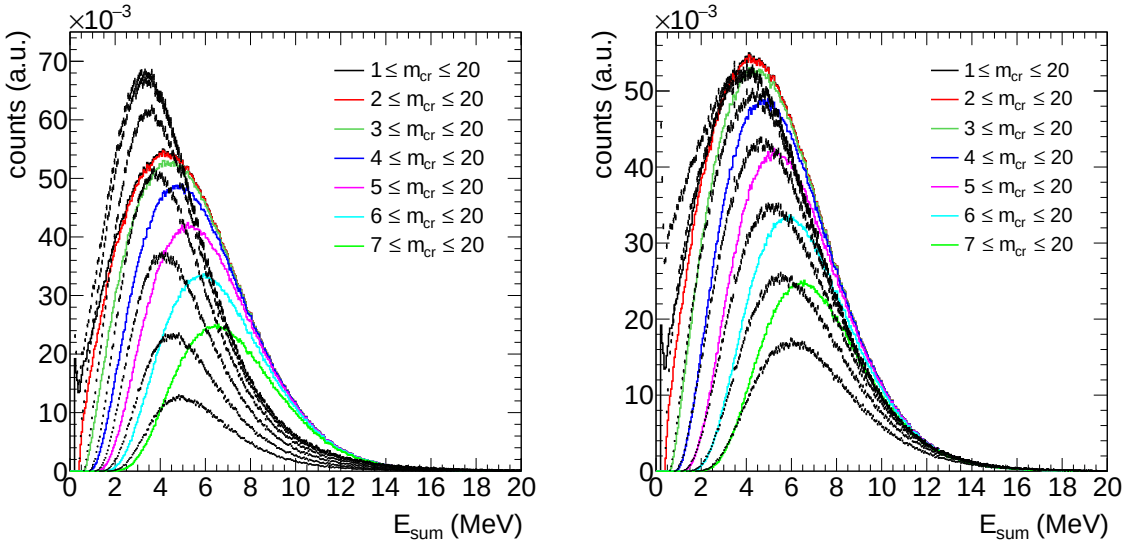

Figure 4.41: PFG spectra (dashed lines) using the model of Valentine [104] (left) and a modified model based on Valentine with modified parameters [105] used in a previous ^{233}U(n,γ) measurement at n_TOF (right) compared to the experimental data (solid lines).

Table 4.7: Comparison of the PFG spectra properties for the evaluated library ENDF/B-VIII.0, various tested models including DANCE optimized which fit the experimental data very well.

	$<M_\gamma>$	$\sigma(M_\gamma)$	$<E_{tot}>$ (MeV)	$\sigma(E_{tot})$ (MeV)	$<E_\gamma>$ (MeV)	$\sigma(E_\gamma)$ (MeV)
ENDF/B-VIII.0	7.95		7.74			
Valentine [104]	6.31	3.01	6.69	3.16	1.05	1.316
Valentine modified [105]	7.21		7.6			
GEF [96]	6.18	2.28	7.92	4.36	1.28	1.30
GEF [96] mass dependent	6.33	2.20	8.11	4.32	1.28	1.30
DANCE [106]	6.74	3.18	7.23	3.33	1.073	0.832
DANCE optimized	6.94	3.22	7.61	3.45	1.097	0.852

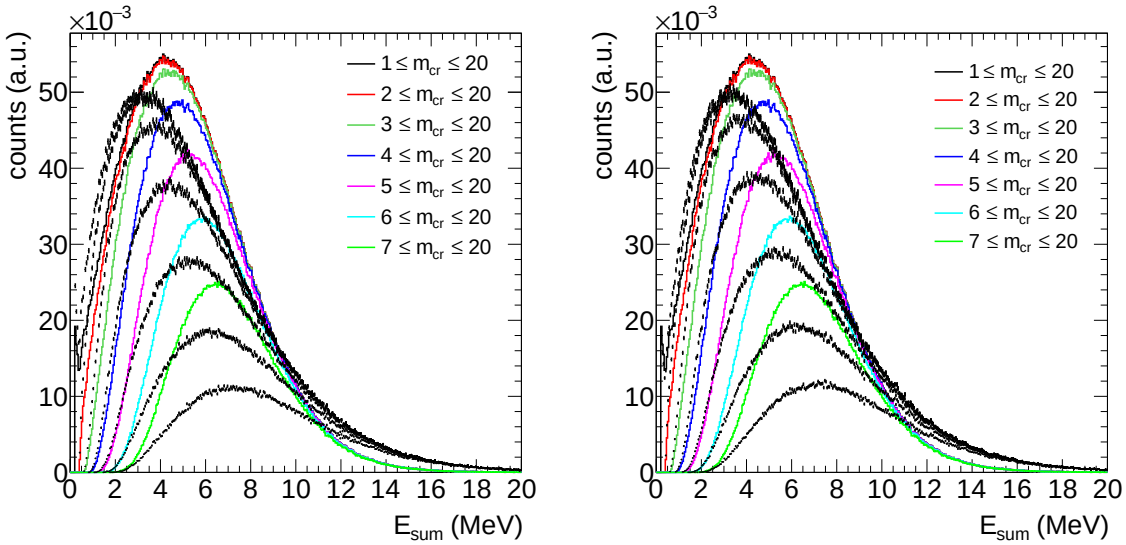

Figure 4.42: PFG spectra using the GEF code without (left) and with (right) fragment mass dependence (dashed lines) compared to the experimental data (solid lines).

after modification are shown in Figure 4.41. It is obvious that none of these models reproduce the experimental data in this experiment. The parameters are summarized in Table 4.7.

The GEF code [96] offers two distributions for sampling the prompt γ-ray multiplicity, with and without fragment mass dependence. It shall be emphasized that both distributions are originating from the same models and thus should produce the same spectra. Both models have been implemented, and the fragment mass dependent version has been coupled with the fission fragment yield distribution from GEF for thermal fission of ^{233}U. The comparison with the experimental data can be seen in Figure 4.42 but no satisfying agreement is achieved and both implementations show the almost the same sum energy spectra. The parameters are summarized in Table 4.7 but in general it can be said that the GEF code probably misses a correlation between the number of emitted γ-rays in fission and their energy, indicated by the wide distributions.

Table 4.8: Parameters used in the simulations of the PFGs using the DANCE model. The only changed parameter is c2.

	a1	a2	b1	b2	c1	c2	l1	l2
original	3.376	1.575	0.0449	0.0461	6.53	2.22	2	3
optimized	3.376	1.575	0.0449	0.0461	6.53	2.44	2	3

The model developed by M. Jandel [106] at Los Alamos correlates the emitted γ-ray energy E_γ and the number of emitted γ-rays M_γ per fission. Using the suggested parameters [106] the model shows a fair agreement between the simulations and the experimental data, as can be seen in Figure 4.43. Note that the model's original parameters were adapted to fission reactions for neutron energies in the range of 4 eV to 500 keV, while the shown experimental data are for 1.6-1.9 eV. It might well be that the fast neutrons add energy and angular momentum to the reaction which could affect the sum spectra and explain the remaining difference between the simulated and the experimental PFG spectra.
Nevertheless, a minor modification of the parameters leads to a satisfying agreement with the experimental data, as can be seen in Figure 4.44 where the simulated and experimental sum energy spectra are shown with the optimized set of parameters. The parameters suggested by [106] for ^{233}U and the modified parameters matching the experimental data well are given in Table 4.8. The agreement in E_{Sum} for all multiplicities is excellent and a fair agreement is also reached in the multiplicity spectra and the individual γ-ray energies E_γ, as shown in the left and right panel of Figure 4.45 respectively.

While the model by Valentine fails to reproduce the measured data, the GEF code offers a fair

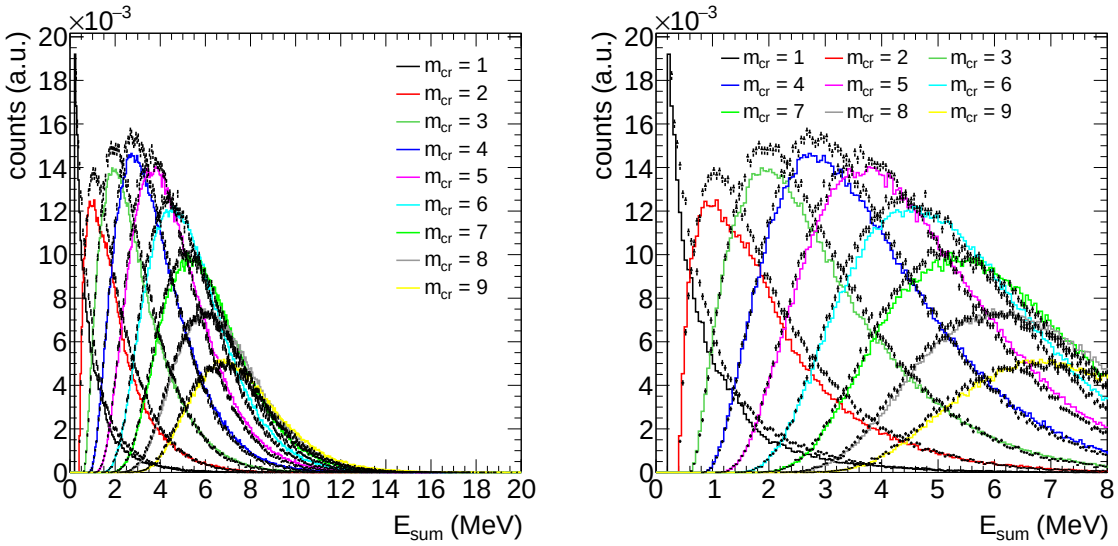

Figure 4.43: Comparison of the DANCE model using its original parameters [106] (dashed lines) and the experimental data (solid lines). A fair agreement is achieved.

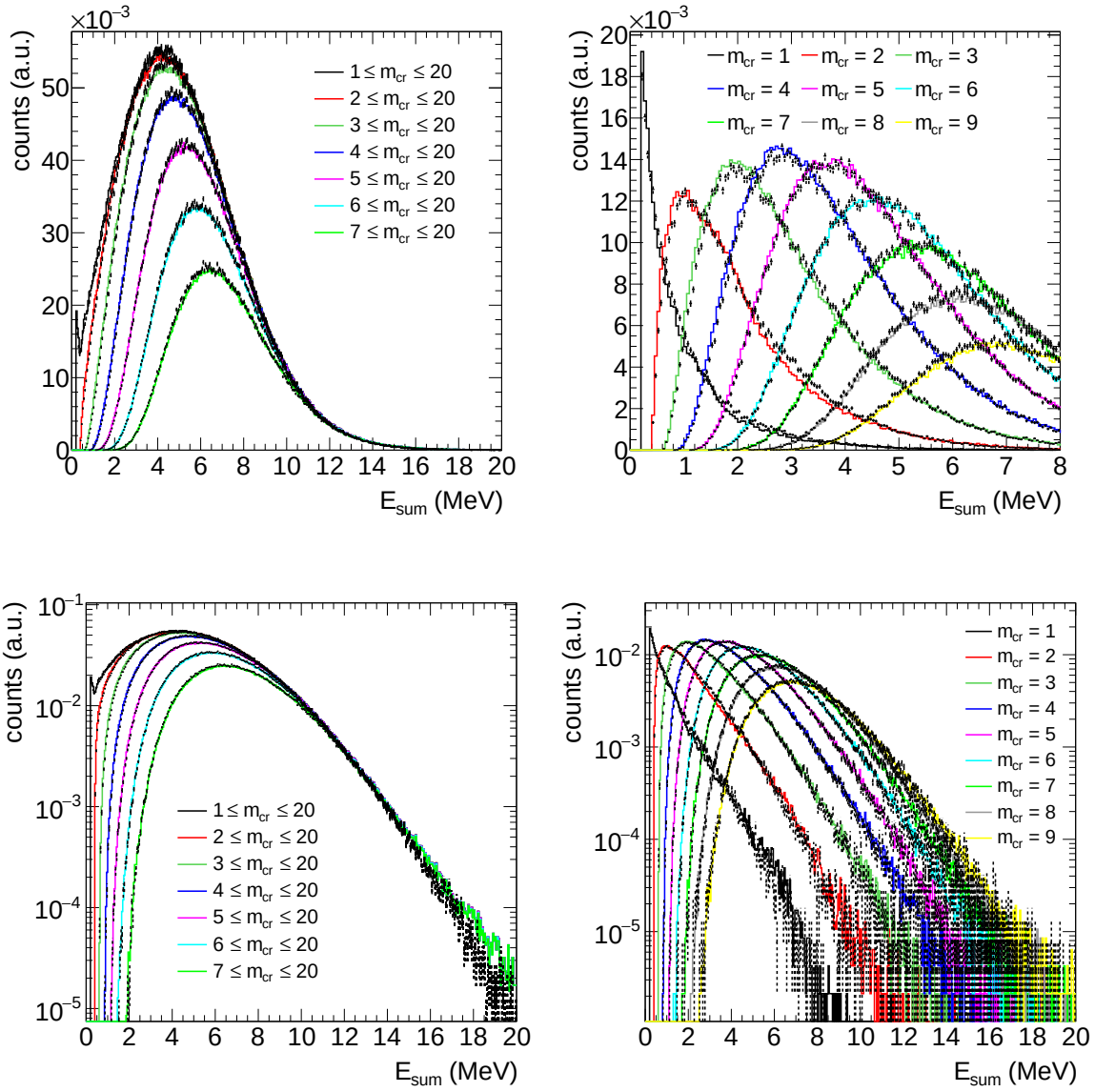

Figure 4.44: Comparison of the experimental (colored/solid lines) and simulated (dashed lines) total deposited energy E_{Sum} spectra in the TAC from prompt fission γ-rays for various conditions in crystal multiplicity m_{cr}. The DANCE PFG cascade generator was used with optimized parameters.

reproduction of the mean total released energy from γ-rays $<E_{tot}>$. Overall, the experimental data agree very well with the model of DANCE, using optimized parameters, compared to the other models. The experimental mean total released energy by γ-rays is close to the ENDF/B-VIII.0 evaluated library while the mean multiplicity $<M_\gamma>$ seems to be lower in the experimental data as well as in the DANCE data/model compared to ENDF/B-VIII.0.

An additional effect has to be taken into account that correlates the signals from the FICH and the deposited energy in the TAC, namely the anisotropic emission of γ-rays from fission fragments. This angular correlation has been observed and can be described [107] by expressing the angular distribution $W(\Theta^{\gamma}_{FF}, \phi^{\gamma}_{FF})$ of the γ-rays for a given polar angle ϕ^{γ}_{FF} in the

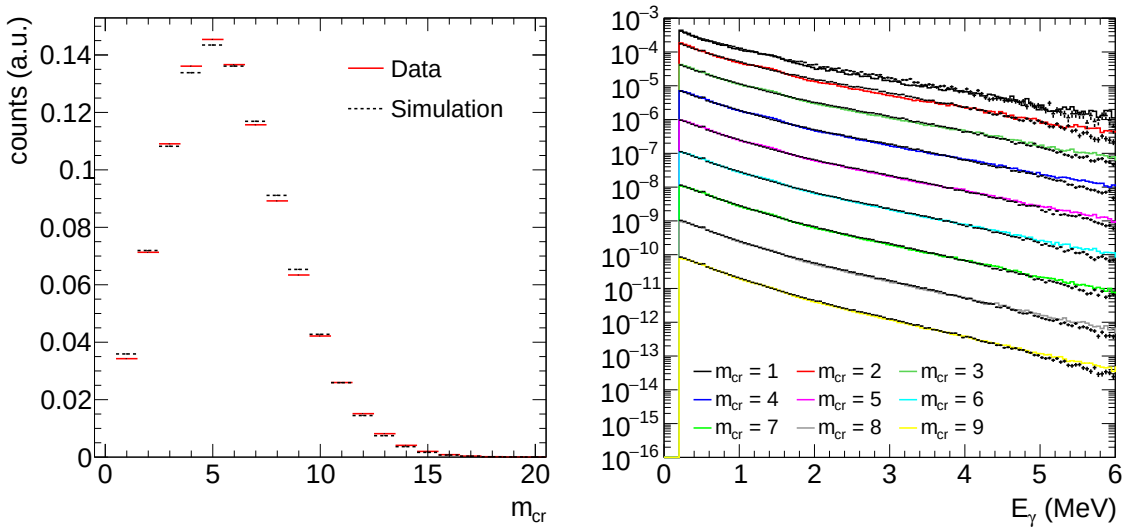

Figure 4.45: Comparison of the experimental (colored/solid lines) and simulated (dashed lines) PFG crystal multiplicity m_{cr} spectra (left) and the individual γ-ray energy E_γ spectra (right). The E_γ spectra have arbitrary scaling factors for better visualization. The DANCE PFG cascade generator was used with optimized parameters.

following way

$$W(\Theta^{\gamma}_{FF}, \phi^{\gamma}_{FF}) = a_0 + a_1 cos^2\Theta^{\gamma}_{FF} + a_2 cos^4\Theta^{\gamma}_{FF}, \tag{4.13}$$

where Θ^{γ}_{FF} and ϕ^{γ}_{FF} are the emission angles in the fission fragment reference system while a_0, a_1 and a_2 describe the isotropic, dipole and quadrupole components respectively. In general, a_0, a_1 and a_2 are non-zero and can be calculated from quantum mechanical considerations. The distribution has been reproduced and implemented in the simulations for the prompt fission γ-rays, as can be seen in the left panel of Figure 4.46. As the emission angles of

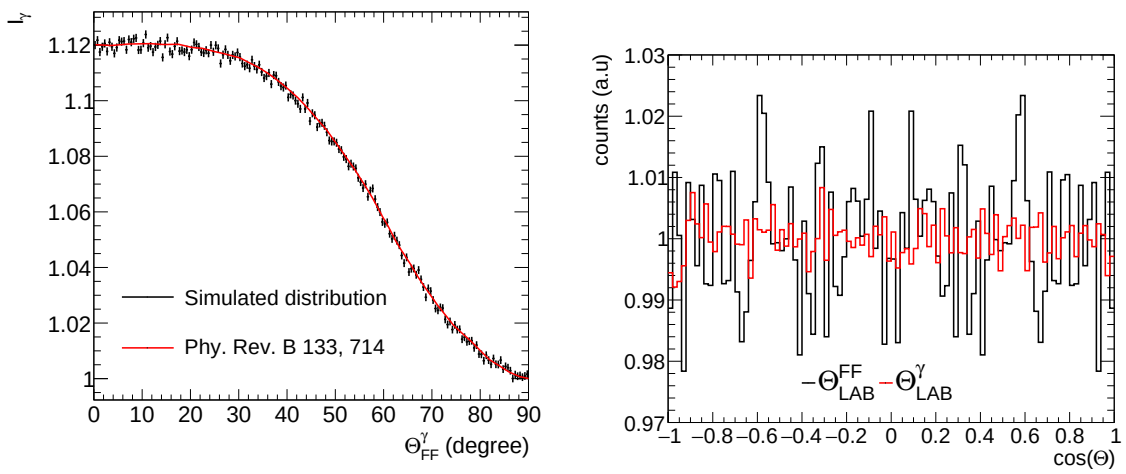

Figure 4.46: Simulated distributions of the emission angles for γ-rays of the PFG cascade in the fission fragment frame of reference [107] (left) and the γ-ray and fission fragment emission angle in the laboratory system.

the fission fragments Θ^{FF}_{LAB} and ϕ^{FF}_{LAB} are sampled isotropically in the laboratory system, the Θ^{γ}_{LAB} and ϕ^{γ}_{LAB} (see left panel of Figure 4.47 for the definition) also exhibit isotropic distributions in the laboratory system as can be seen in the right panel of Figure 4.46. The relevant angles and their relation between each other is illustrated in the left panel of Figure 4.47.

In Figure 4.48 the comparison of simulations with angular biased γ-ray emission with the experimental data is shown with the same optimized parameters as in Figures 4.44 and 4.45. The agreement is slightly worse and a better agreement would need readjustment of the parameters but requires extensive simulations and trials, as the correlation of the parameters is not easy to interpret. The biased spectra are shifted towards lower crystal multiplicities as can be seen in the bottom right panel of Figure 4.48 where both types of simulations are compared to each other and the experimental data.

This can be understood easily due the geometry of the TAC. As the TAC does not have a 100 % geometrical efficiency for individual γ-rays, the angular anisotropy introduces an effect on the total deposited energy in the TAC and will lead to a reduction of the mean sum energy $<E_{Sum}>$ for fission fragments emitted parallel to the neutron beam. The right panel in Figure 4.47 illustrates the different regions in the experimental setup with different detection efficiencies in the TAC and the FICH. The red colored region corresponds to a region with a high detection efficiency for the FICH as all fission fragments will deposit an appreciable amount of energy in the gas. However, part of the prompt fission γ-rays will escape through the entrance and exit holes for the neutron beam and cannot be detected by the TAC. On the other hand, the blue colored region corresponds to a region where the TAC exhibits a high geometrical detection efficiency but at such angles there is a higher chance for fission fragments to be lost in the sample due to self-absorption, hence the FICH detection efficiency decreases. The simulations clearly show this effect as can be seen in the bottom left panel of Figure 4.49 where the mean sum energy is shown as a function of the fragment emission angle. The mean sum energy for near parallel-to-beam emission of fission fragments

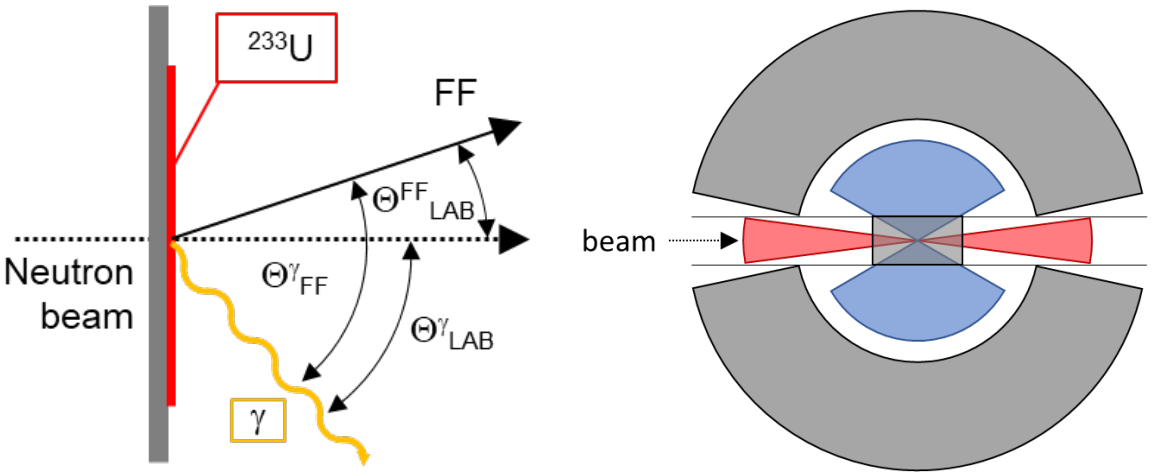

Figure 4.47: Definition of the angles in the simulations (left). Illustration of the TAC and FICH detection efficiencies - ε_{TAC} is high (low) in the blue (red) region; ε_{FICH} is high (low) in the red (blue) region (right).

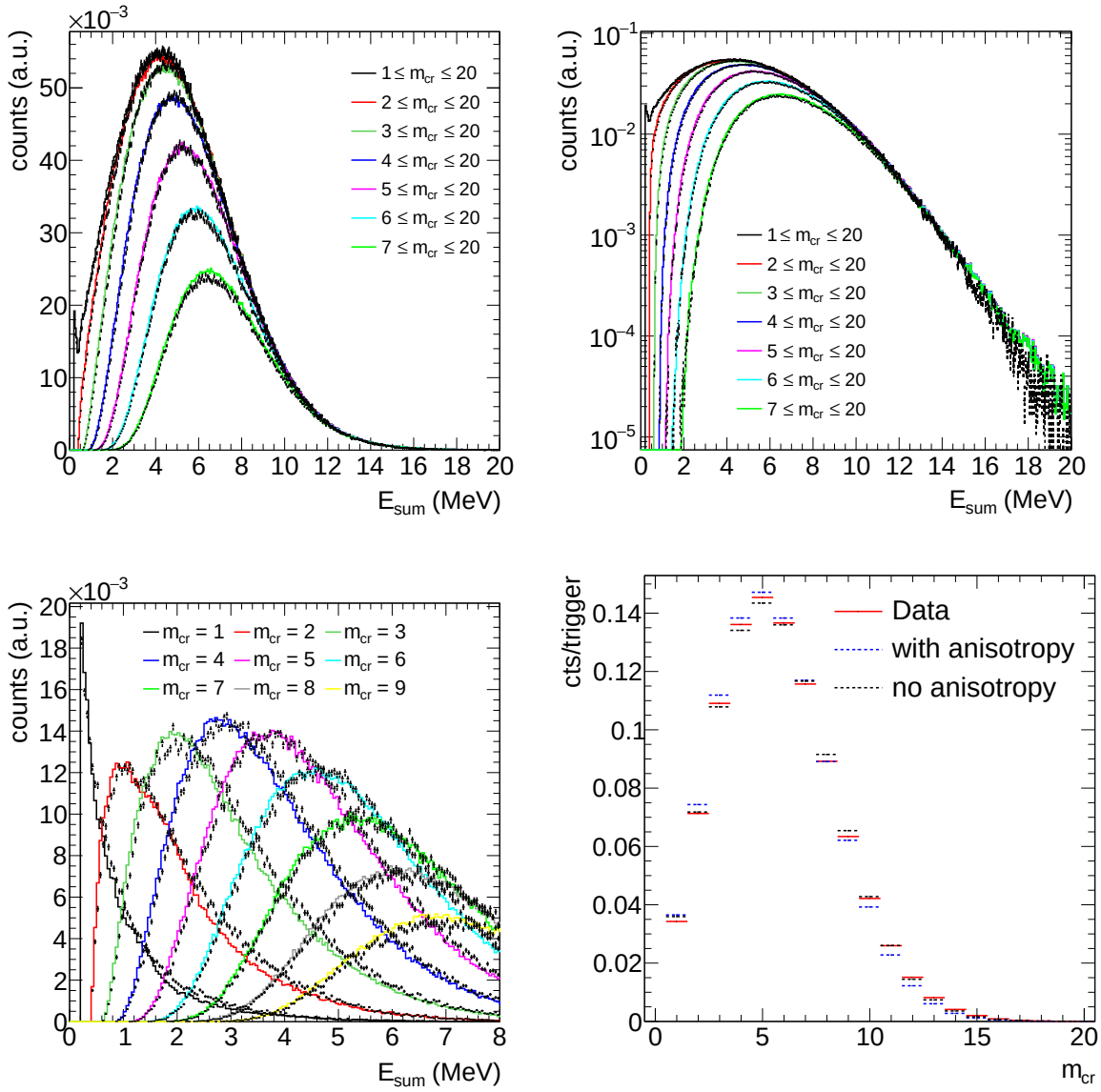

Figure 4.48: Comparison of the experimental (colored/solid lines) and simulated (dashed lines) PFG spectra with angular biased emission of the PFGs (top left, right and bottom left). Comparison of the experimental and simulated m_{cr} distributions (bottom right). The DANCE PFG cascade generator was used with optimized parameters.

drops by approximately 10 % compared to other angles in the angular biased spectra. But it is also worth noting, that in the biased spectra the mean deposited energy in the TAC for large emission angles is higher than in the unbiased spectra, which can also be explained by the anisotropy now *focusing* the γ-rays into the detectors rather than allowing the γ-rays escape through the beam entrance and exit holes of the TAC.

This effect can also be observed experimentally in the sum energy spectra. Due to the shape of the amplitude spectrum the amplitude itself cannot be used to gate on the angle of emission. But as has been described before, see section 4.2.1, the FICH signal rise time should be correlated with the angle of emission, thus calculating the mean sum energy $<E_{Sum}>$ for different rise time intervals should make this effect visible. In general, short rise times are

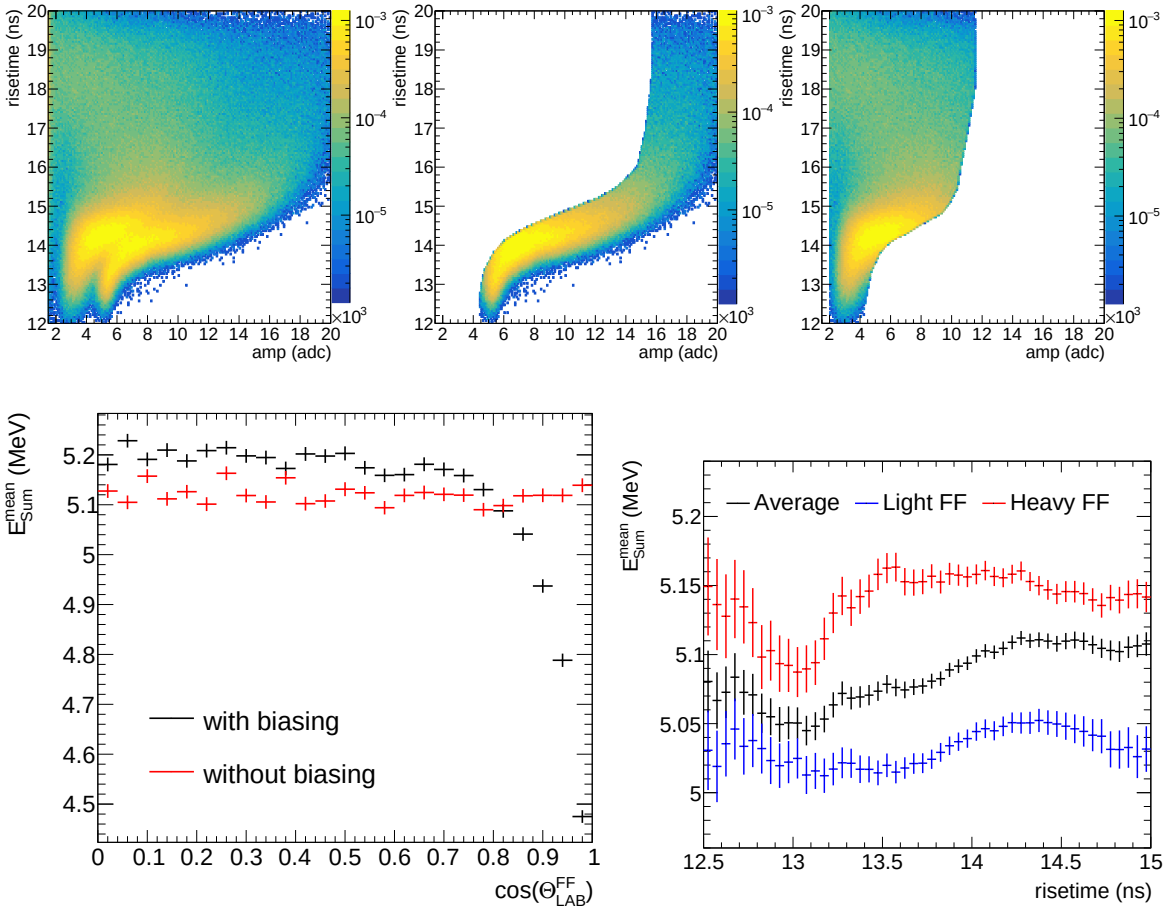

Figure 4.49: Amplitude versus rise time of the FICH signals for FICH channel 4 (top) - total (left), light fragment cut (middle), heavy fragment cut (right). Mean sum energy in the TAC as a function of the angle of emission of the fission fragment with and without angular biasing of the prompt fission γ-rays from simulations (bottom left). Mean sum energy of the prompt fission γ-rays in the experimental data depending on the rise time of the corresponding FICH signal (bottom right).

supposed to correspond to signals with $cos\Theta^{FF}_{LAB} \approx 1$ and therefore a smaller mean sum energy can be expected compared to fission events with large rise times. In the bottom right panel of Figure 4.49 the experimentally obtained mean sum energy in the TAC is shown as a function of the rise time of the corresponding FICH signals for FICH channel 4. First it has to be noted that the rise time spectra for the light and heavy fragments are shifted and the same rise times for light and heavy fragments do not necessarily correspond to the same angle. This is also visible in the top panels of Figure 4.49 where the two peaks for the fission fragments are shifted in rise time. Furthermore, the cuts shown in the top panels of Figure 4.49 for the heavy and light fragments bias those spectra for larger rise times which also leads to a distortion. However, in general the expected behaviour is visible. For short rise times a lower mean sum energy can be observed for both fragment types and with increasing rise time the mean sum energy in the TAC increases as well. The observed difference in sum energies in the experimental data is about 2 % maximum and definitely not as clearly visible as in the simulated spectra where the difference has been calculated to about 10 %. This discrepancy can be explained due the rise time spectra not being clean enough, the angle of emission being

not the only parameter influencing the rise time or differences in the alignment of the two detection systems in the experimental setup with respect to the simulations. Nevertheless, the effect is visible and shows once more that the rise time is correlated with the angle of emission. Furthermore it shall be noted that the mean sum energy of the heavy fragments in the data, see bottom right panel of Figure 4.49, is systematically higher compared to the light fragments. No physical explanation for this can be given yet.
This effect is small but needs to be taken into consideration when calculating the efficiency of the fission chamber which will be discussed in detail later.

Chapter 5

Data reduction for the determination of the experimental ^{233}U α-ratio

This chapter focuses on the extraction and calculation of the necessary quantities required to calculate the ^{233}U α-ratio from the experimental data. The experimental α-ratio can be written as

$$\alpha(E_n) = \frac{\varepsilon_{FICH}}{\varepsilon^{\gamma}_{TAC}} \frac{c_{tot}(E_n) - b(E_n)}{c_f(E_n) - b_f(E_n)}. \tag{5.1}$$

as has been explained in section 2.2.2. The background contributions to be subtracted from the total γ-spectra c_{tot} can be written as

$$b(E_n) = b_{const} + b_{Beam}(E_n) + b_{Fiss}(E_n) + b_{other}(E_n) \tag{5.2}$$

and shall be swiftly discussed:

- Time independent background b_{const}: related to the internal radioactivity of the BaF_2 crystals, environmental background and natural radioactivity of the ^{233}U samples. This component is determined by dedicated measurements without the neutron beam while retaining the same experimental conditions.
- Beam background not related to ^{233}U samples $b_{Beam}(E_n)$: originates from reactions of the neutron beam and accompanying γ-rays with the materials intercepting the beam. This component has been determined by dedicated measurements replacing the fission chamber containing the ^{233}U samples with an identical dummy fission chamber without ^{233}U samples.
- Prompt fission component $b_{Fiss}(E_n)$: The prompt fission γ-rays and neutrons emitted from the highly excited fission fragments and detected by the TAC within a few nanoseconds. This component is determined with the fission tagging method.
- Other components related to the ^{233}U samples $b_{other}(E_n)$ different to $b_{Fiss}(E_n)$: background caused by the interaction of the neutron beam with the targets, i.e. elastic

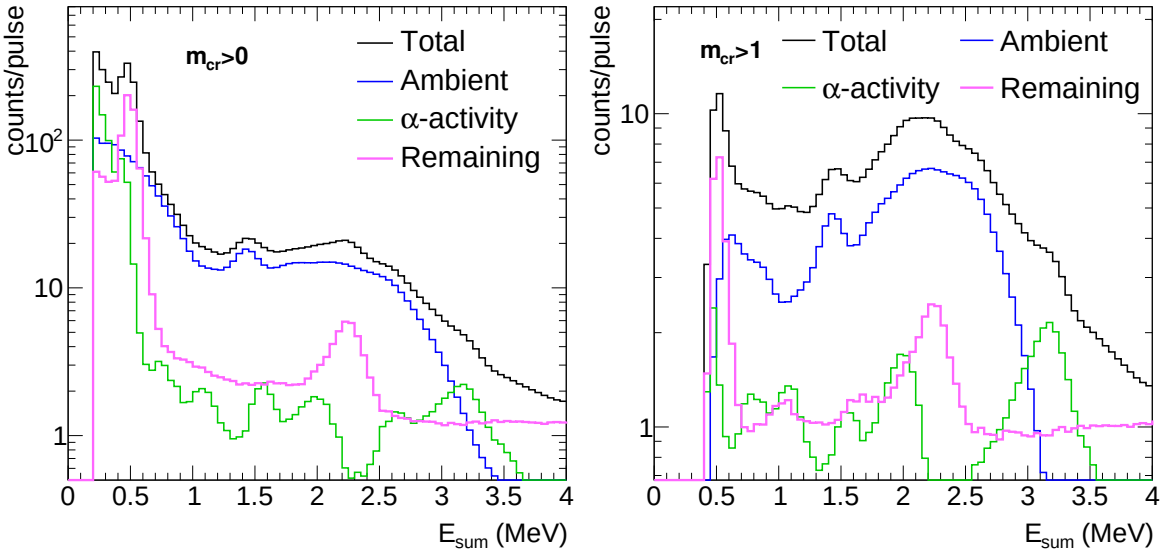

Figure 5.1: Comparison of the sum energy spectra in the TAC of the time independent background components and the total measured response in the neutron energy range from 0.02 eV up to 10 keV for $m_{cr} > 0$ (left) and $m_{cr} > 1$ (right).

scattering, delayed detection of the prompt fission neutrons and γ-ray decay of the fission fragments. Those components can be extracted partially from the data or rely on Monte Carlo simulations.

In the next sections the background will be subtracted from the total measured TAC response step by step. The fission tagging efficiency will be calculated from the experimental data and the TAC efficiency $\varepsilon^{\gamma}_{TAC}$ to capture cascades of ^{233}U will be calculated from Monte Carlo simulations.

5.1 Time independent background

The ambient background related to the internal radioactive decay of the BaF_2 crystals and environmental (including cosmic) radioactivity and the background related to the natural radioactivity of the ^{233}U samples is obtained in dedicated measurements without the neutron beam. The internal radioactive decay of the BaF_2 crystals originates from radio-chemical contaminants in the crystals and produces isotopes along the decay chain of Ra isotopes. Furthermore, the ambient spectrum shows the ^{40}K γ-line at 1505 keV. In Figure 5.1 both components, the ambient background and the natural ^{233}U activity are shown and compared to the total measured response for two different crystal multiplicity m_{cr} thresholds, illustrating that most of the time independent background events exhibit $m_{cr} = 1$ and demonstrates the discriminatory power of using a segmented calorimeter like the TAC. The TAC is unable to resolve the peaks in the natural decay of ^{233}U (α-activity) spectrum but those must be related to the decay of ^{233}U and its daughters. It can also be seen that the ^{233}U decay dominates the low sum energy part of the spectra for $m_{cr} > 0$, which can be explained due to the high activity.

5.2 Neutron beam induced background unrelated to the ^{233}U samples

The material of and in the fission chamber, all vacuum/chamber windows and the rest gas intercept the beam and produce reactions visible in the TAC. This background component is determined directly via dedicated measurement by replacing the chamber containing the samples with an identical dummy chamber without samples. The calculation of this component is straightforward and is shown in Figure 5.2 for several neutron energy ranges and crystal multiplicities. To illustrate the signal to background ratio depending on the neutron

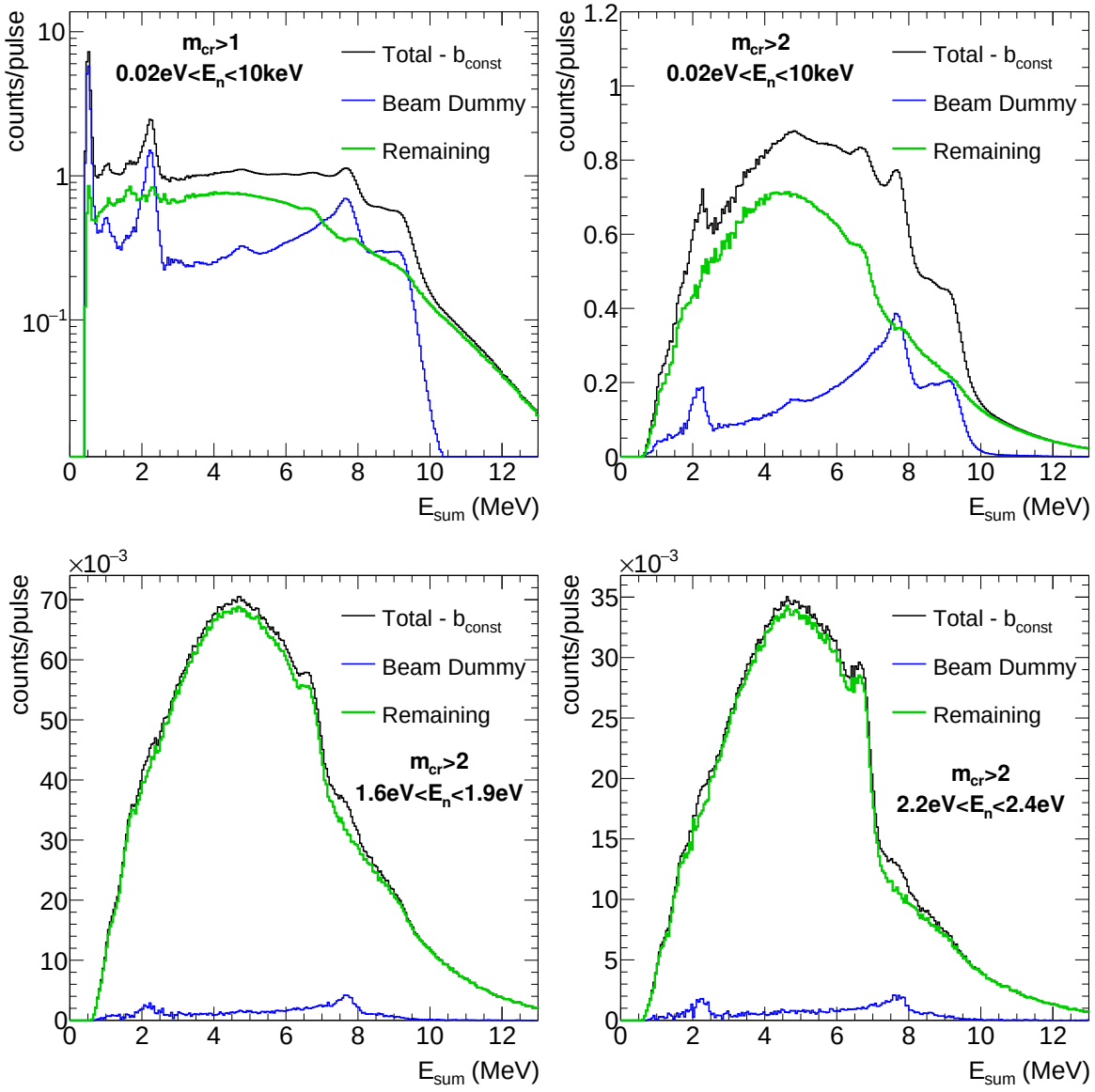

Figure 5.2: Comparison of the sum energy spectra of the neutron beam related background component to the time independent subtracted response for several neutron energy regions and several crystal multiplicities.

energy range the whole neutron energy range of interest shown in the top panels is compared to the two largest resonances - one fission dominated resonance (1.6-1.9 eV) and one capture dominated resonance (2.2-2.4 eV) - in the bottom panels. Comparing the spectra in the top panels showing different multiplicity thresholds it becomes evident that a multiplicity threshold of $m_{cr} > 2$ offers a nice discrimination of the background components, especially for small deposited energies. Hence, the comparison in the bottom panels are only given for a multiplicity threshold of $m_{cr} > 2$. The final analysis conditions are discussed in section 6.1.

5.3 Neutron beam induced background related to the ^{233}U samples

5.3.1 Elastic scattering

The neutron sensitivity ε_n can be understood as the probability of detecting a scattered neutron with a kinetic energy E_n by the TAC. This probability depends on the applied analysis conditions, E_{Sum} and m_{cr}. To study this effect Monte Carlo simulations have been performed using the GEANT4 toolkit, emitting neutrons with different kinetic energies from the ^{233}U samples. The ^{233}U samples in the simulations contain 0.21 m% oxygen and 0.10 m% carbon corresponding to the values of the investigation performed for similar samples [86]. The data reconstruction is performed analogously to the treatment of the experimental data. In Figure 5.3 the neutron sensitivity is shown as a function of the crystal multiplicity for 2.5 MeV $< E_{Sum} <$ 7 MeV, conditions applied in the analysis of the ^{233}U α-ratio .
This component of the background can be accounted for determining the following quantity

$$R(E_n; E_{Sum}, m_{cr}) = \frac{\varepsilon_n \sigma_n(E_n)}{\varepsilon_\gamma \sigma_\gamma(E_n)} \tag{5.3}$$

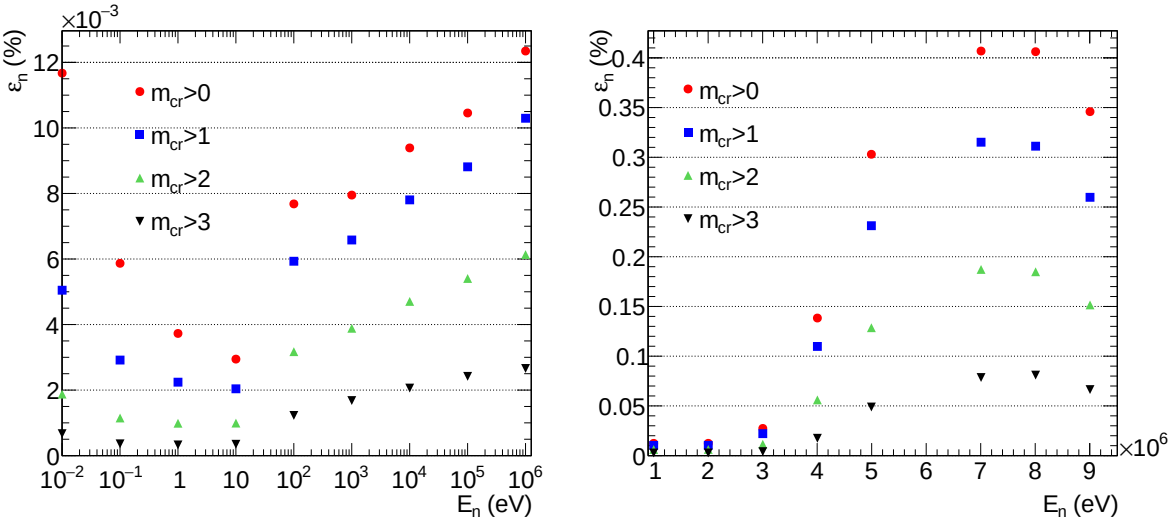

Figure 5.3: Neutron sensitivity $\varepsilon_n(E_n; E_{Sum}, m_{cr})$ as a function of the neutron energy and crystal multiplicity for events with 2.5 MeV $< E_{Sum} <$ 7 MeV for different neutron energy ranges.

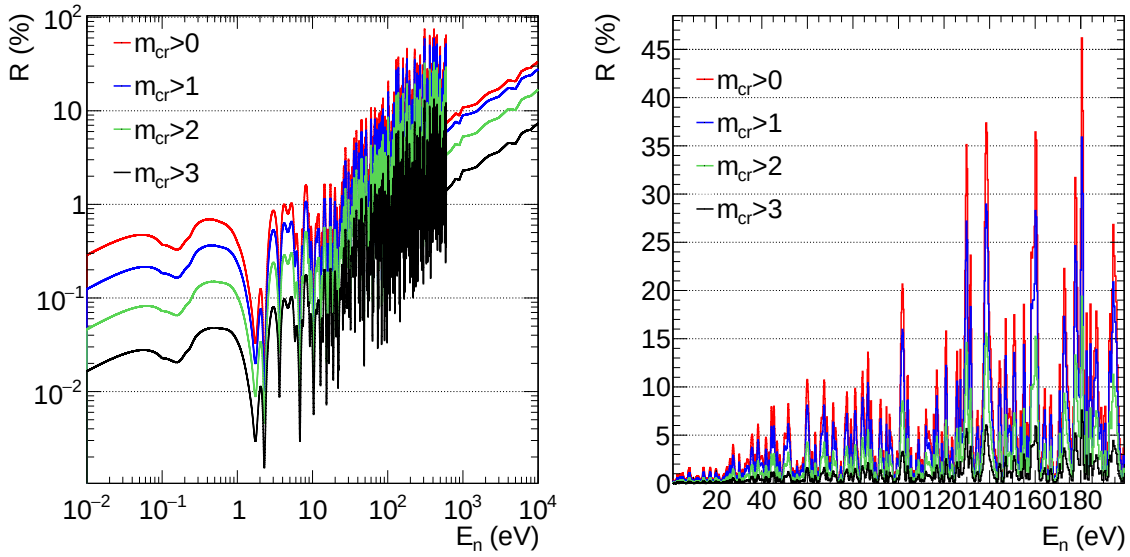

Figure 5.4: Ratio of expected scattered neutron and ^{233}U(n,γ) events depending on the neutron energy and crystal multiplicity for events with 2.5 MeV $< E_{Sum} <$ 7 MeV.

where σ_γ and σ_n are the neutron capture and elastic cross-sections and ε_γ and ε_n are the TAC detection efficiency for ^{233}U(n,γ) events and the TAC neutron sensitivity respectively. This essentially compares the background induced by neutron scattering in the samples with the expected number of ^{233}U(n,γ) events. This ratio is shown in Figure 5.4 as a function of the neutron energy and crystal multiplicity for applied analysis conditions of 2.5 MeV $< E_{Sum} <$ 7 MeV. The observed peaks correspond to valleys between resonances in the ^{233}U(n,γ) cross section and regions of small $R(E_n)$ to the capture resonances. The contribution of this background decreases with increasing multiplicity condition. For $m_{cr} > 2$ and neutron energies up to 200 eV the largest contribution is about 20 % between neutron resonances where the ^{233}U(n,γ) cross section is almost zero. Compared to the background induced by the fission chamber (elastic scattering or capture in beam intercepting material) this component is negligible and was not taken into account in the further analysis.

5.3.2 Delayed γ-rays from the decay of the fission products

The delayed γ-rays from the decay of the fission products has been simulated using GEANT4. The fission products generated in thermal fission of ^{233}U from the GEF code [96] were used as input for the simulation. The decay of the products was simulated using the specific decay functions in the GEANT4 toolkit. In the left panel of Figure 5.5 the E_{Sum} distribution is shown as a function of the decay time from the simulations. The projected time distribution of decay events with $m_{cr} > 2$ and 2.5 MeV $< E_{Sum} <$ 7 MeV is shown in the right panel of Figure 5.5. The fraction of events with such characteristics amounts to about 7 % of all events. The typical half lives of the unstable fission products range from several milliseconds to hours, making a time correlation difficult because of how the n_TOF DAQ works. Assuming a constant operation of the n_TOF facility, i.e. a long duration with a constant average rate of proton pulses, this component can be estimated in a first approximation as follows. The

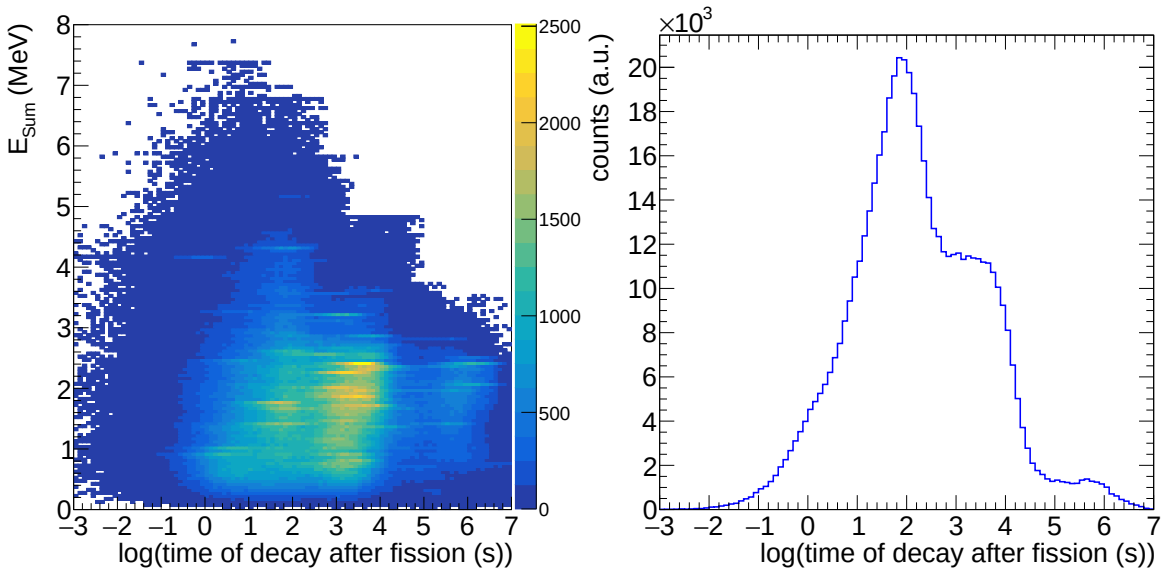

Figure 5.5: Sum energy and time distribution of the decay of fission products simulated with GEANT4 (left). Time distribution of fission product decay events with $m_{cr} > 2$ and $2.5\,\text{MeV} < E_{Sum} < 7\,\text{MeV}$.

n_TOF DAQ only opens a time window of 100 ms when a proton pulse hits the spallation target every 3.6 s on average, which leads to a duty cycle of about 2.8 %. This results in the probability of detecting a decay event with $m_{cr} > 2$ and $2.5\,\text{MeV} < E_{Sum} < 7\,\text{MeV}$ of about 0.2 %. As this component scales with the amount of fission reactions, or the fission cross section, the contribution of those events to the capture response can be estimated with the ^{233}U α-ratio and will therefore depend on the neutron energy region. As the resonance region covers only about 1-2 ms of the total DAQ acquisition window ($\approx TOF$) the contribution to the resonance region, even in the valley between the resonances, can be neglected. The remaining 98-99 ms of the DAQ acquisition window correspond to neutron energies below 1 eV where the ^{233}U α-ratio is in the order of 0.1, thus a contribution of 2 % in the capture response can be estimated. Compared to the background induced by the fission chamber (elastic scattering or capture in beam intercepting material) this component is negligible and is not considered in the analysis.

5.3.3 Prompt fission background

The prompt fission background component b_{fiss} is determined by coincidences between the FICH and the TAC within a time window of 14 ns, explained in section 4.3.3, scaled by the fission tagging efficiency ε^f_{TAC}

$$b_{fiss}(E_n; E_{Sum}, m_{cr}) = \frac{1}{\varepsilon^f_{TAC}} c_{tagg}(E_n; E_{Sum}, m_{cr}) \tag{5.4}$$

Under the condition that the probability of detecting a fission reaction in one of the detection systems does not depend on whether it is detected in the other one, the fission tagging efficiency ε^f_{TAC} equals the fission chamber efficiency ε_{FICH}. However, as has been shown

in section 4.3.3.1, this is not true for this experimental setup, due to a small degree of correlation between the TAC and the FICH detection systems as will be shown in section 5.3.5.1.

The experimental sum energy spectra and crystal multiplicity spectra are shown in the left and right panels of Figure 5.6 respectively. The mean released energy in the prompt cascades is 7.61 MeV by an average of 6.94 γ-rays according to simulations, see section 4.3.3. As expected the prompt response is characterized by events with large deposited energies and high crystal multiplicities. The mean deposited energy of those cascades for different crystal multiplicities is summarized in Table 4.6 in section 4.3.3 and can be reproduced by simulations as shown in section 4.3.3. The prompt fission response does not change depending on the incident neutron energy, as shown in Figure 5.7 for different crystal multiplicities.
The subtraction of the prompt fission background is shown in Figure 5.8 for several neutron energy intervals. After subtracting the prompt fission background a peak at 6.85 MeV shows up corresponding to the neutron separation energy of ^{234}U and representing $^{233}U(n,\gamma)$ cascades depositing their full energy in the TAC. Below the sum energy peak a smooth continuum can be seen corresponding to $^{233}U(n,\gamma)$ cascades that were not completely captured.
The remaining response is identical within statistical uncertainties in several neutron energy resonances, as indicated in Figure 5.9 where the sum energy spectra for several neutron energy intervals are shown normalized to each other. The shapes agree very well in the region from 2.5 MeV to 7 MeV. Below 2.5 MeV the spectra become less smooth and deviate from each other. The fluctuations indicate a remaining background component that has not been subtracted yet. Large uncertainties in this region can be excluded as all spectra show the same shape below sum energies of 2.5 MeV as is also shown in Figure 5.9. Above 7.3 MeV, corresponding to the neutron separation energy of ^{234}U and taking the energy resolution into account, no residual background is expected but is clearly visible in all spectra in Figures 5.8

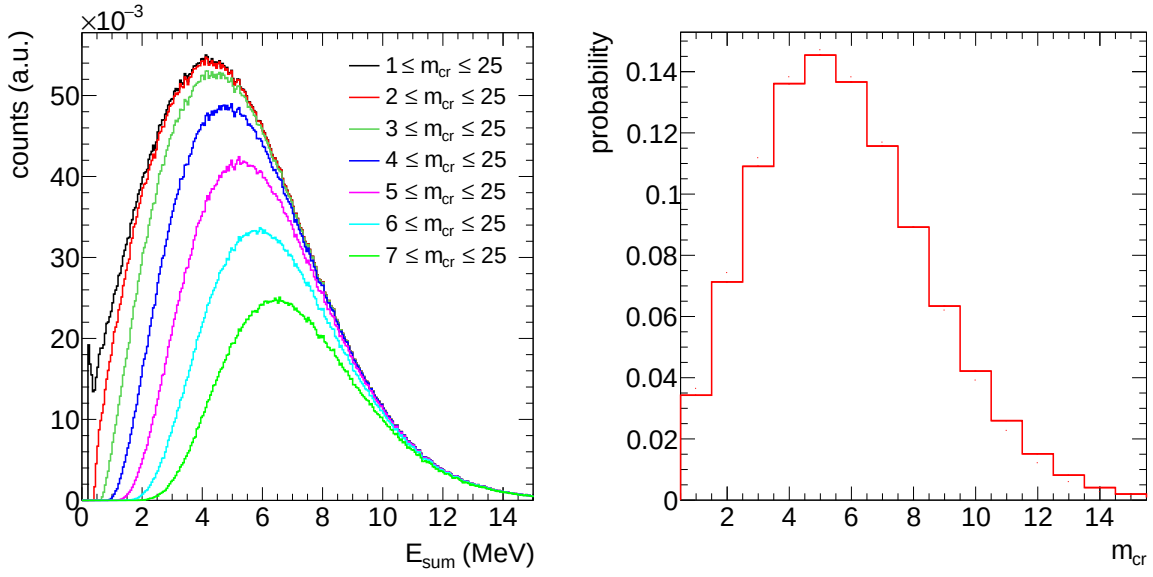

Figure 5.6: Experimental sum energy (left) and crystal multiplicity spectra (right) of the prompt fission response obtained with fission tagging.

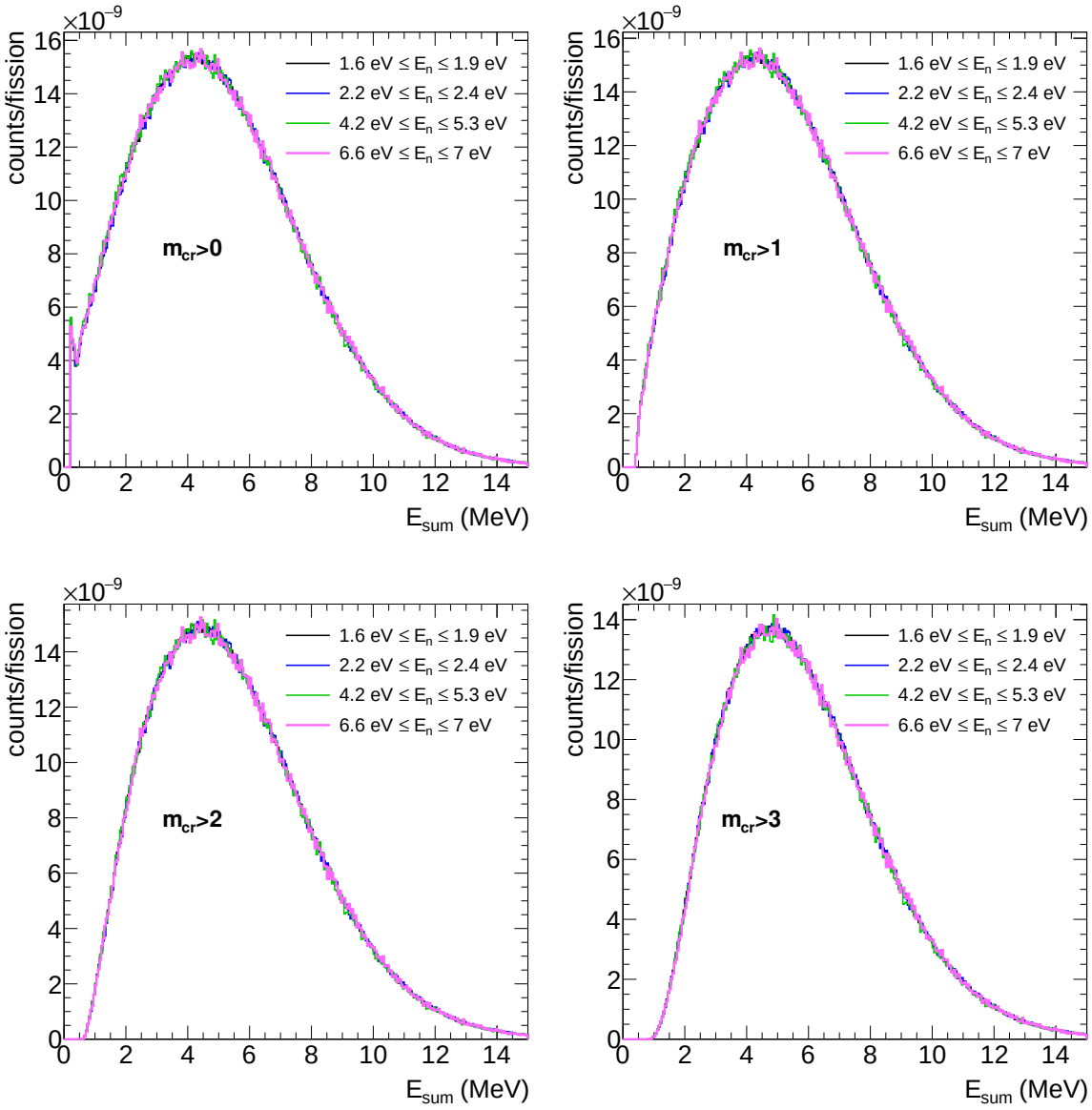

Figure 5.7: Comparison of the sum energy spectra of the prompt fission response for different multiplicity conditions. No difference is observed with the incident neutron energy.

and 5.9. Despite the normalization of the sum energy spectra shown in Figure 5.9, both background components, below 2.5 MeV and above 7.3 MeV, show a different scaling behaviour. Both components seem to be scaling with the α-ratio or fission cross section, i.e. the background components are much smaller with respect to the capture component in the capture dominated resonance from 2.2 eV to 2.4 eV compared to the fission dominated resonance from 1.6 eV to 1.9 eV. A smaller capture resonance at 6.6 eV to 7.0 eV remains between the two as also its α-ratio is in between the two. Thus, the background below 2.5 MeV might be linked to delayed background induced by fission neutrons, isomeric decay of isomeric states in the fission fragments (i.e. a peak is visible at approximately 1.65 MeV which could correspond to the isomeric level in ^{134m}Te, see section 5.3.4.) or delayed γ-rays from the fission products, see section 5.3.2. This component can be easily removed by applying a lower threshold for

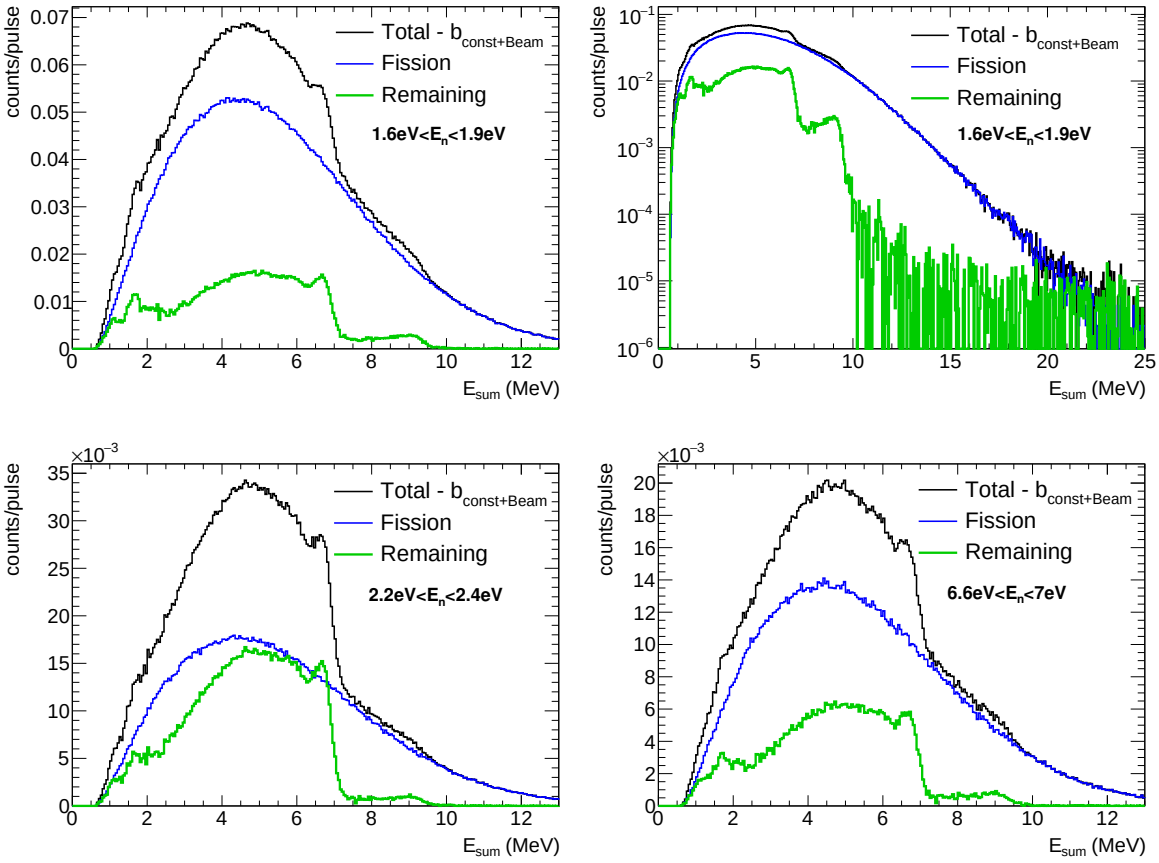

Figure 5.8: Sum energy spectra for TAC events with $m_{cr} > 2$ in several neutron energy intervals. The remaining background components below 2.5 MeV and above 7 MeV are discussed in the text.

the sum energy in the final analysis, i.e. $E_{Sum} > 2.5$ MeV. The background above 7.3 MeV is most likely caused by fission neutrons captured in the experimental setup, but ^{233}U. The treatment of this background component will be discussed in section 5.3.4.

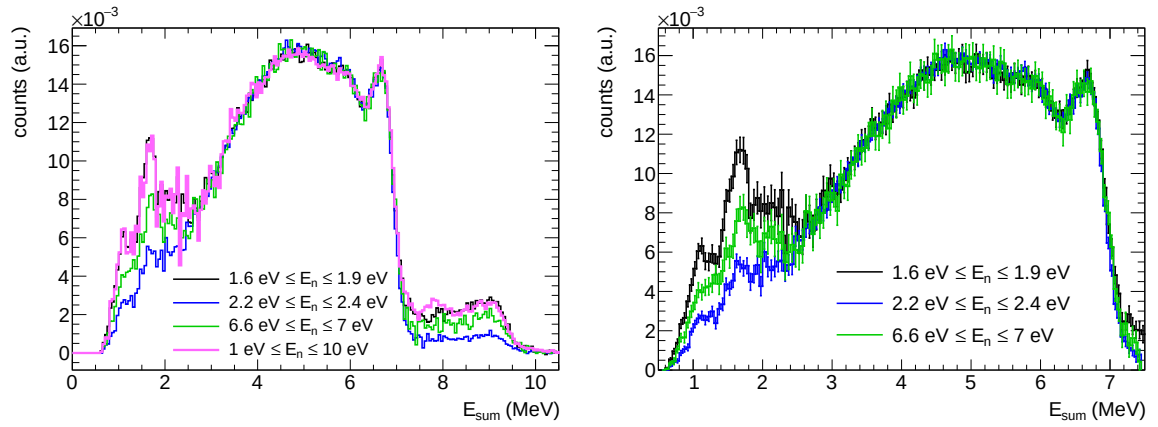

Figure 5.9: Sum energy spectra for TAC events with $m_{cr} > 2$ in several neutron energy intervals without (left) and with (right) statistical errors displayed. The spectra have been normalized in the region 3.5 MeV $< E_{Sum} <$ 7 MeV to compare the shapes.

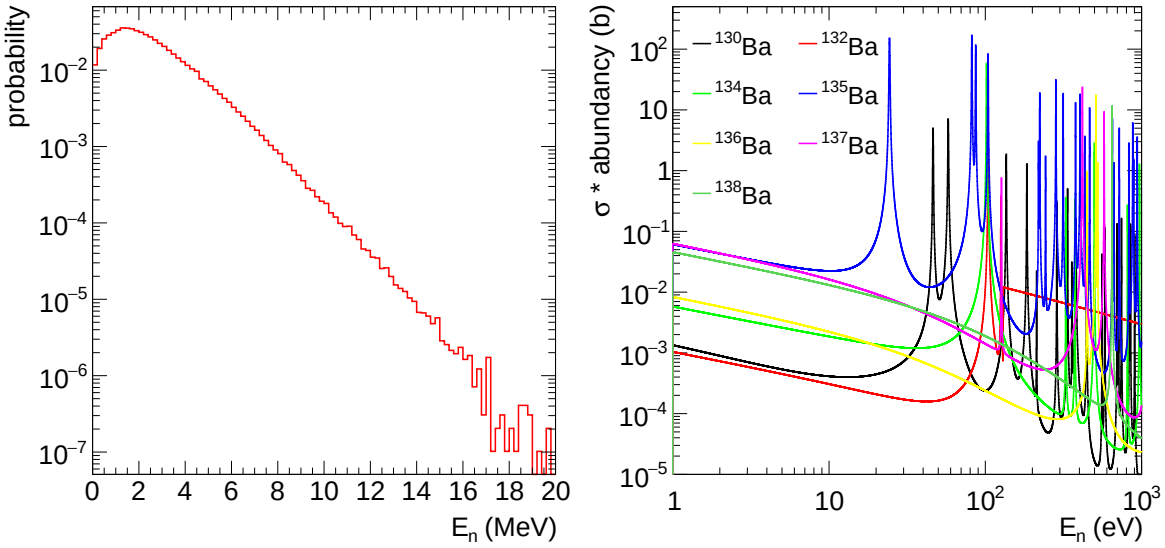

Figure 5.10: Fission neutron energy spectrum of ^{233}U taken from ENDF/B-VIII.0 (left). Capture cross sections of all stable barium isotopes weighted by their natural abundance (right).

5.3.4 Background induced by prompt fission neutrons

The remaining background in the range 7.3-10 MeV and the perturbations of a smooth shape for lower sum energies, i.e. $E_{Sum} < 2.5$ MeV most likely originate from fission neutrons (FN). Fission neutrons are emitted with energies in the MeV range, see left panel of Figure 5.10, from the excited fission fragments and are scattered and moderated inside the experimental setup leading to two features visible in the TAC:

- Direct reactions of the MeV neutrons can cause signals in the TAC, i.e. (n,n'γ) on ^{138}Ba of the BaF_2 crystals leads to a γ-ray with an energy of 1435 keV which can be easily discriminated by applying a threshold in the sum energy.

- Due to the moderation, especially in the absorber, the neutrons can reach thermal energies and in the process being captured. Most of them will be captured inside the absorber or the borated carbon fiber shell encapsulating the BaF_2 crystals and produce a single γ-ray with an energy of 2.2 MeV or 0.48 MeV respectively. Those γ-rays can be easily discriminated with conditions on multiplicity and sum energy in the TAC. A fraction of the neutrons can also escape the absorber and reach the BaF_2 crystals and be captured in barium.

Barium is a good candidate for the remaining background at 8-10 MeV because of the neutron separation energies of some of the barium isotopes perfectly fitting this range and the available material. There are 7 stable isotopes of barium which have different neutron separation energies as listed in Table 5.1 together with their natural abundance. Depending on the isotope, barium has a significantly high neutron capture cross-section as can be seen in the right panel of Figure 5.10 where the capture cross section for various barium isotopes is weighted by their natural abundance. In general it can be said that the shape of the

Table 5.1: Natural abundance and neutron separation energy S_n of all stable barium isotopes.

Isotope	Abundance (%)	S_n for ^{x}Ba + n (MeV)
^{130}Ba	0.106	7.494
^{132}Ba	0.101	7.190
^{134}Ba	2.417	6.972
^{135}Ba	6.592	9.108
^{136}Ba	7.854	6.906
^{137}Ba	11.23	8.612
^{138}Ba	71.7	4.723

total capture cross-section of natural barium is strongly dependent on the neutron energy. The resonant shape of the barium capture cross-section and the different neutron separation energies of the different barium isotopes lead to a neutron energy dependent shape of the background in the TAC. This is important for neutron scattering, as different neutron energies lead to different shapes in the TAC which have to be corrected for.

However, fission neutrons have to be moderated in order to be efficiently captured by any nucleus as the capture cross sections tend to become rather small for fast neutrons. On average the moderation process is the same for every emitted fission neutron. Thus the shape of the background will not depend on the time-of-flight and an average shape can be used for a correction, contrary to the case of neutron scattering induced by beam intercepting materials. Furthermore, this contribution scales with the fission cross section, or counts in the fission chamber c_f and the average number of emitted neutrons $\bar{\nu}(E_n)$, thus this contribution can be calculated to

$$b_{FN}(E_n) = \frac{\bar{\nu}(E_n)}{\varepsilon_{FICH}} c_f(E_n) \cdot P_{Prompt-n}(m_{cr}, E_{Sum}, \delta T > 14ns) \tag{5.5}$$

with $P_{Prompt-n}$ being the probability of detecting an event caused by a fission neutron with a given multiplicity and sum energy after the prompt response ($\delta T > 14$ ns). The moderation and capture of the fission neutrons was simulated using GEANT4 and the distribution of the events with $m_{cr} > 2$ as a function of the time after the neutron is emitted is shown in the left panel of Figure 5.11. The moderation process can take up to a few 100s of milliseconds but most of the captured fission neutrons are captured rather quickly after they are emitted, i.e. approximately 75 % of the captured neutrons are captured in the first microsecond. Capture of fission neutrons predominately happens in the barium isotopes and hydrogen of the absorber as can be seen in the left panel of Figure 5.11, where the various contributions are shown. The sum energy signature that fission neutrons show in the TAC has been simulated using GEANT4 and is shown in the right panel of Figure 5.11 for events with $m_{cr} > 2$ and 14 ns $< \delta T <$ 1 μs. The signature below 2.5 MeV in the spectrum corresponds to direct reactions such as (n,n') as well as capture on hydrogen, which are both suppressed by the applied multiplicity condition. Above 2.5 MeV capture reactions on barium isotopes dominate the sum energy distribution. This shows that captured fission neutrons are a good candidate for the contribution above 8 MeV.

The fact that most of the fission neutrons are captured within the first microsecond after

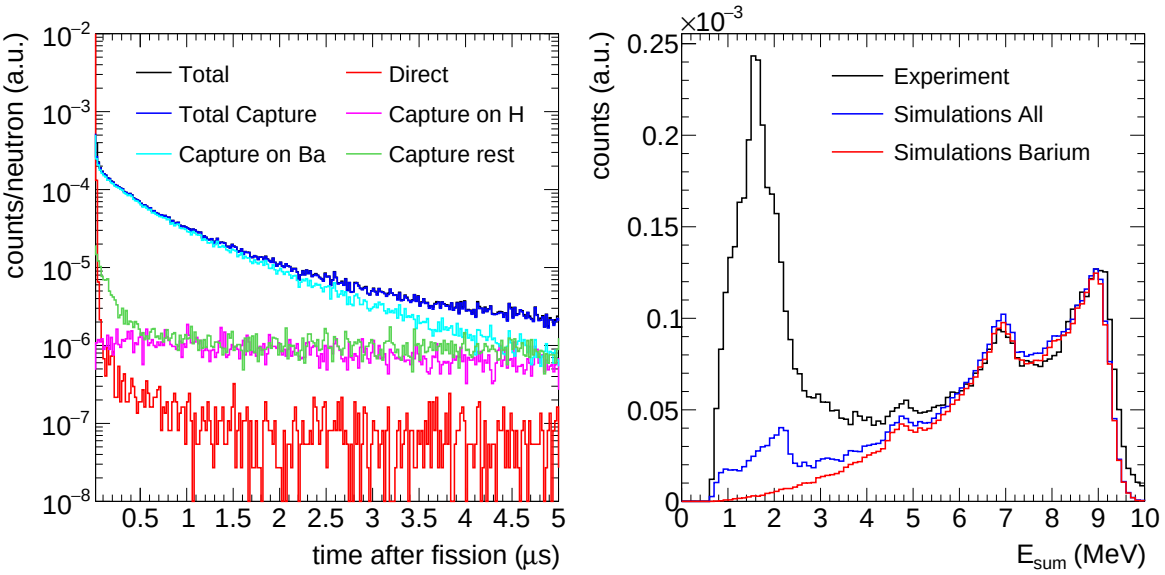

Figure 5.11: Distribution of events with $m_{cr} > 2$ registered in the TAC (simulated) as a function of the time after neutron emission (left). Comparison of the simulated and experimental sum energy response of the TAC to fission neutrons for events with $m_{cr} > 2$ and 14 ns $< \delta T <$ 1 μs (right).

fission, see left panel of Figure 5.11, allows to investigate the fission neutron signature in the TAC by exploiting this time correlation and determine the sum energy spectra within the first microsecond after a fission event, excluding the prompt fission γ-rays. The experimental TAC response to events with $m_{cr} > 2$ and a maximum time after fission of $\delta T < 1\,\mu$s is compared to the simulated spectra in the right panel of Figure 5.11. A reasonable agreement with the simulations for the barium sum energy peaks is achieved, indicating again the effect of fission neutron capture in barium dominating the region above $E_{sum} = 6$ MeV. A comparison of the FN response in the TAC for several neutron energy regions is shown in the upper left panel of Figure 5.12. The responses have been normalized to the number of fission reactions in the FICH in their respective neutron energy intervals and exhibit a perfect agreement in the region above 7 MeV sum energy. This already indicates that this part of the spectrum must scale with the fission cross section. The explanation of the region below 2.5 MeV is rather complex because in addition to direct reactions, i.e. the 1435 keV from inelastic scattering on ^{138}Ba, and capture on hydrogen it also involves decay of isomeric states in the fission fragments. For example ^{134m}Te with a half life of 164 ns almost completely decays within the first microsecond after fission. The energy of the isomeric level in ^{134m}Te is 1691 keV which decays via 3 γ-rays to the ground state, so it can be well inside the applied multiplicity condition. Note that no background subtraction has been performed for those spectra.
In the region between 2.5 MeV and 7 MeV differences can be observed in the spectra from the different resonances. These differences are most likely related to a different amount of capture reactions contained in those spectra. For example, in the fission dominated resonance at 4.2-5.3 eV the fission to capture ratio is much larger compared to the capture dominated resonance at 2.2-2.4 eV, meaning there is a much smaller contribution from potential capture reactions to the time gated fission neutron spectra in the fission dominated resonance. Hence,

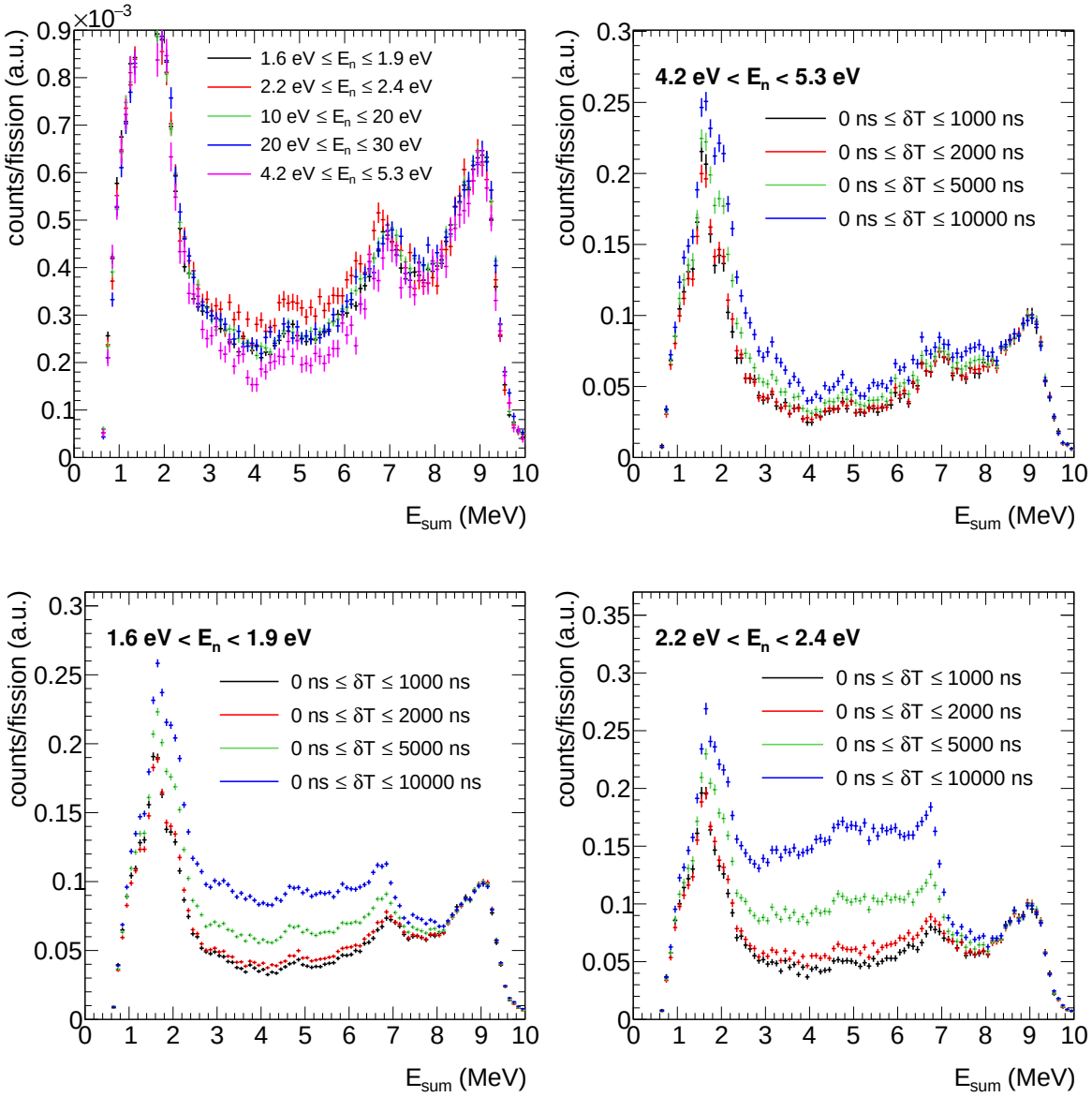

Figure 5.12: Comparison of the FN sum energy spectra for events with $m_{cr} > 2$: in different neutron energy intervals (top left), for various time windows δT after fission (others).

in the intermediate region between 2.5 MeV and 7 MeV more counts can be expected in strong capture resonances as is the case. This effect can be enhanced if the allowed time window is increased, as is shown in the top right and bottom panels of Figure 5.12 where the FN sum energy spectra are shown for several neutron resonances and time windows δT. Those spectra are additionally normalized in the E_{Sum} from 8.3 MeV to 9.5 MeV to better illustrate the effect of the different time windows. For the fission dominated resonance at 4.2-5.3 eV there is little effect on the region from 2.5 MeV to 7 MeV even if the time window is increased by a factor 10 to 10 μs. However, for the strongest capture resonance at 2.2-2.4 eV a significant increase in the intermediate region is observed with a sharp cut off at the neutron separation energy of ^{234}U of 6.85 MeV indicating that the additional counts are indeed originating from ^{233}U(n,γ) events. For another large resonance at 1.6-1.9 eV the effect is visible but not as

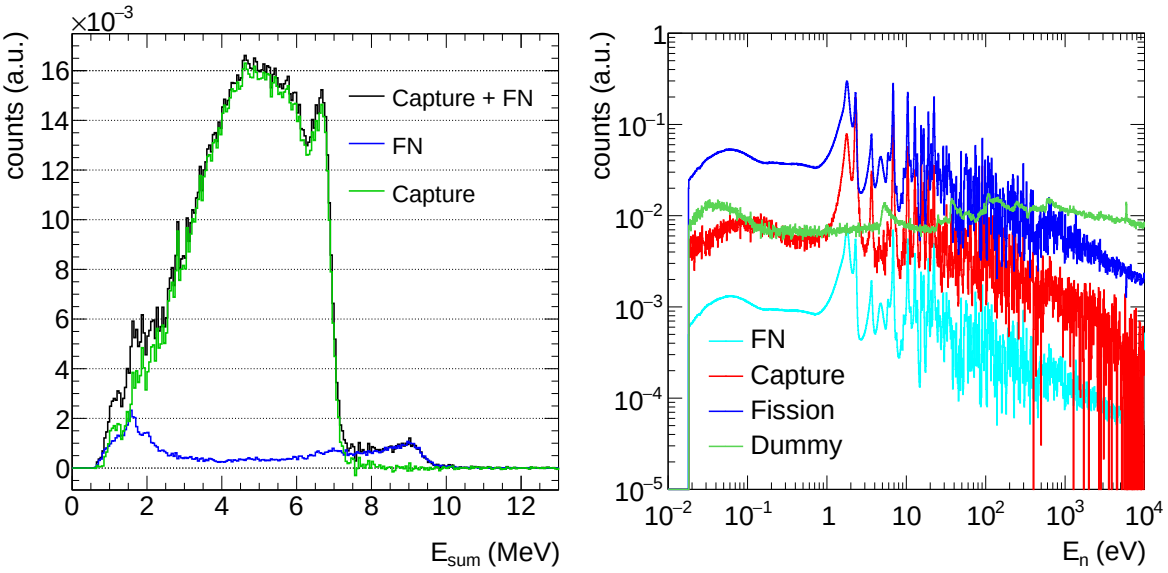

Figure 5.13: The shape of the fission neutron spectra is scaled to the remaining background contribution above 7 MeV in the capture response for the strong capture resonance at 2.2-2.4 eV and $m_{cr} > 2$ (left). The contributions to the TAC response as a function of the neutron energy (right).

strong compared to the strongest capture resonance at 2.2-2.4 eV which is consistent. This tendency can be observed for several resonances and seems to give a good explanation of the differences. This explains why the spectra of all resonances agree very well in the range 7.3 10MeV in the top left panel of Figure 5.12 considering that due to the neutron separation energy of ^{234}U of 6.85 MeV, and taking into account the energy resolution, no counts above 7.3 MeV need to be expected from ^{233}U(n,γ) .

If the FN spectrum for $\delta T < 1\,\mu$s in the fission dominated resonance at 4.2-5.3 eV is assumed to contain a minimal amount of neutron capture events, due to the small ^{233}U α-ratio , then the fission neutron induced component of the background can be estimated using the shape of this resonance. Furthermore, the shape is in excellent agreement with the residual background in the capture response above 8 MeV as shown in the left panel of Figure 5.13 where the FN response is scaled to the residual background. The scaling factor that has to be applied to the experimentally obtained shape of the fission neutrons, obtained within the first microsecond after fission, to properly subtract the background is reported in Table 5.2

Table 5.2: Scaling factors for the FN response taken in the first microsecond after fission (excluding the prompt fission γ-rays) obtained by fitting the FN response to the residual background above 7 MeV in the capture response.

E_n range (eV)	scaling factor for FN background
1.6-1.9	1.31
2.2-2.4	1.31
6.6-7.0	1.33
1-10	1.35
10-20	1.33
20-30	1.32

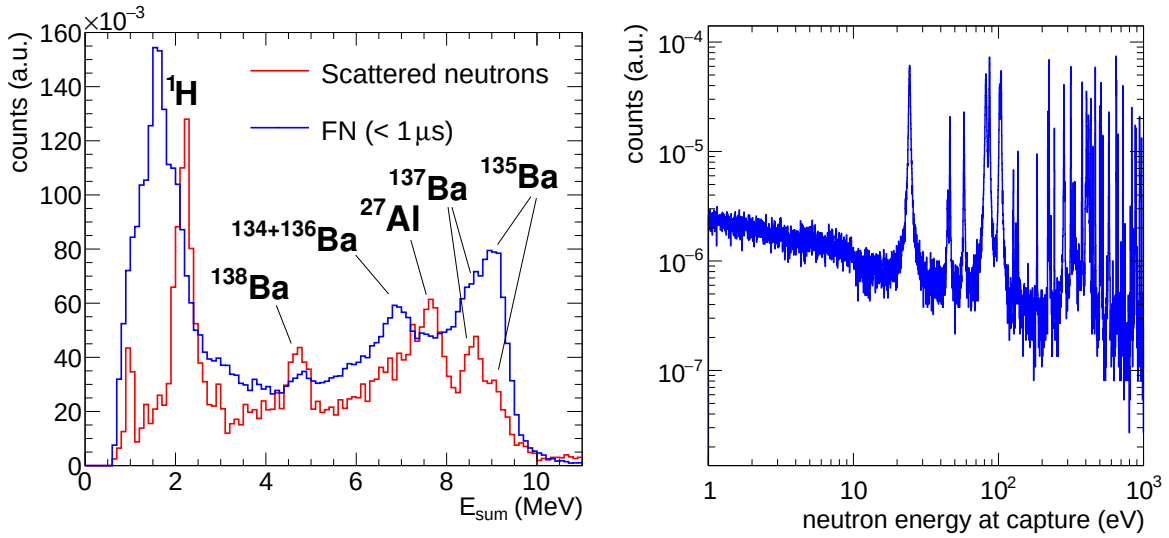

Figure 5.14: Comparison of the sum energy spectra of FN and elastic neutron scattering, obtained by using a carbon sample, for events with $m_{cr} > 2$. The sum-energy peaks, labeled with nucleus ^{A}Z, correspond to the neutron separation energy of the compound nucleus ^{A+1}Z after capture ^{A}Z+n (left). Neutron energy spectrum at capture during moderation of fission neutrons from simulations (right).

for several resonances. The average value of 1.32 is very close to the simulated probability of detecting a fission neutron for the applied multiplicity condition of $m_{cr} > 2$ of $1/0.75 \approx 1.33$, thus giving a good indication that those counts are indeed related to fission neutrons. This fitting procedure can not be done for individual neutron energy bins, but the excellent agreement with the data, the stable scaling factor for several neutron energy intervals and the confirmation from the simulations allow to use a constant scaling factor of 1.32 and the integral of the experimental FN spectra with $m_{cr} > 2$ and $2.5\,\text{MeV} < E_{Sum} < 7\,\text{MeV}$ from the resonance at 4.2-5.3 eV for the neutron energy bin by bin correction of the FN background component. The result is shown in the right panel of Figure 5.13.

The scaling factor depends slightly on the range the FN shapes is fitted to the residual background. To estimate the uncertainty of the subtraction the fitting range has been varied within reasonable bounds leading to an uncertainty of 2.5 % in the FN subtraction.

5.3.4.1 Fission neutrons and neutron scattering

Elastic neutron scattering could also be responsible for neutron capture in the BaF_2 crystals. Carbon is considered to be a pure scatterer, thus a carbon sample was used in order to investigate the effect of neutron scattering versus fission neutrons. The corresponding sum energy spectra for FN and scattered neutrons are compared in the left panel of Figure 5.14 for the same incident neutron energy interval of 1.6-1.9 eV. The same sum energy peaks appear corresponding to the same isotopes, i.e. barium, hydrogen and aluminium, which is understandable as fission and scattered neutrons are captured in the surrounding materials, namely the absorber, the BaF_2 crystals and/or the aluminium from the supporting structure

of the TAC or the fission chamber. Although the two spectra show the same sum energy peaks their intensities are very different. This can again be explained by the barium cross sections as well as the spectrum of neutrons emitted or scattered from the beam. While in elastic scattering the neutron is scattered with the same energy as the incoming beam, for example 1.6-1.9 eV, fission neutrons from fission reactions corresponding to the same incident neutron energy interval exhibit an average moderated spectrum given by the material around the fission samples, most importantly the absorber. Simulations show that fission neutrons can very well be captured in the resonances of the barium isotopes. The simulation of the moderated fission neutron spectrum at neutron capture from simulations is shown in the right panel of Figure 5.14 where resonances correspond to the abundance weighted barium cross sections in the right panel of Figure 5.10.

5.3.5 Determination of the fission tagging efficiency

The fission tagging efficiency ε^{f}_{TAC} and the fission detection efficiency ε_{FICH} are closely related and independent of the incident neutron energy for the neutron energy region of interest and defined as follows:

- The fission detection efficiency $\varepsilon_{FICH}(A_{th})$ is the probability of detecting a fission reaction by the FICH detector and depends only on the amplitude threshold A_{th} applied to the FICH events.
- The fission tagging efficiency $\varepsilon^{f}_{TAC}(A_{th}; E_{Sum}, m_{cr})$ describes the probability of detecting a fission event in the TAC. It is defined as the ratio between the tagged fission events $c_{tagg}(A_{th}; E_{Sum}, m_{cr})$ and the total fission counts detected by the TAC $c_{Fiss-TAC}(E_{Sum}, m_{cr})$. The tagged fission spectra have to be scaled by this factor.

$$\varepsilon^{f}_{TAC}(A_{th}; E_{Sum}, m_{cr}) = \frac{c_{tagg}(A_{th}; E_{Sum}, m_{cr})}{c_{Fiss-TAC}(E_{Sum}, m_{cr})} \tag{5.6}$$

Under the assumption that the probability of detecting a fission event in one of the detectors does not depend on whether it was detected in the other one:

1. The fission tagging efficiency ε^{f}_{TAC} and the fission detection efficiency ε_{FICH} are the same quantity.
2. The fission tagging efficiency depends only on A_{th}

$$\varepsilon^{f}_{TAC}(A_{th}; E_{Sum}, m_{cr}) = \varepsilon^{f}_{TAC}(A_{th}) \tag{5.7}$$

The first point can be shown easily by expressing the fission events detected in the TAC $c_{Fiss-TAC}(E_{Sum}, m_{cr})$ as a function of the TAC fission detection efficiency $\varepsilon^{f\gamma}_{TAC}$ and the total number of occurring fission reactions N_{fiss}

$$c_{Fiss-TAC}(E_{Sum}, m_{cr}) = \varepsilon^{f\gamma}_{TAC}(E_{Sum}, m_{cr}) \cdot N_{fiss}. \tag{5.8}$$

Furthermore, the tagged fission counts $c_{tagg}(A_{th}; E_{Sum}, m_{cr})$ can be written as a function of the fission detection efficiency $\varepsilon_{FICH}(A_{th})$, the TAC fission detection efficiency $\varepsilon^{f\gamma}_{TAC}$ and the total number of occurring fission reactions N_{fiss}

$$c_{tagg}(A_{th}; E_{Sum}, m_{cr}) = \varepsilon_{FICH}(A_{th}) \cdot \varepsilon^{f\gamma}_{TAC}(E_{Sum}, m_{cr}) \cdot N_{fiss}. \tag{5.9}$$

Dividing both quantities results in the proof of the first conclusion above:

$$\begin{aligned} \varepsilon^{f}_{TAC}(A_{th}; E_{Sum}, m_{cr}) &= \frac{c_{tagg}(A_{th}; E_{Sum}, m_{cr})}{c_{Fiss-TAC}(E_{Sum}, m_{cr})} \\ &= \frac{\varepsilon_{FICH}(A_{th}) \cdot \varepsilon^{f\gamma}_{TAC}(E_{Sum}, m_{cr}) \cdot N_{fiss}}{\varepsilon^{f\gamma}_{TAC}(E_{Sum}, m_{cr}) \cdot N_{fiss}} = \varepsilon_{FICH}(A_{th}). \end{aligned} \tag{5.10}$$

If equation (5.9) is not strictly fulfilled the detection probabilities are not independent, thus $\varepsilon^{f}_{TAC} \neq \varepsilon_{FICH}$. In this measurement, the detection probabilities are assumed to be independent in a first step. The efficiencies $\varepsilon^{f}_{TAC} = \varepsilon_{FICH}$ are calculated ignoring any correlation between the detectors and are corrected afterwards.
The method used for calculating the efficiency from the experimental data is based on equation (5.6) and is described below:

- The prompt tagged fission events are obtained by the coincidence of the TAC and FICH as has been explained before.
- For the calculation of the efficiencies all events that are not corresponding to the prompt fission events are considered background. Apart from the ^{233}U(n,γ) reaction, such events are discussed in the other sections of this chapter. The total spectra of the TAC can be cleaned from all background components by subtracting the corresponding spectra but this is prone to uncertainties and normalization errors and still the ^{233}U(n,γ) events would remain in the spectra. Another way to clean the total TAC spectra is to gate on large multiplicities and sum energies effectively removing all background components.
- If all background is removed the efficiency can be calculated from equation (5.6).

The sum energy and multiplicity spectra for the total and tagged TAC response with the full experimental setup as well as the two main components of the background, obtained by dedicated measurements, are shown in Figure 5.15. From those plots it can be easily imagined that calculating the fission tagging efficiency is less prone to uncertainties introduced by the background subtraction for events with $m_{cr} > 5$ and $E_{Sum} > 10\,\text{MeV}$ because there is little background for such conditions. Nevertheless, the sensitivity with respect to the applied conditions in crystal multiplicity and sum energy has to be investigated and is shown for two different amplitude thresholds A_{th} in the left panel of Figure 5.16. Even though the residual backgrounds were subtracted there is a significant trend for lower multiplicities that decreases with increasing multiplicities. One potential explanation could be background

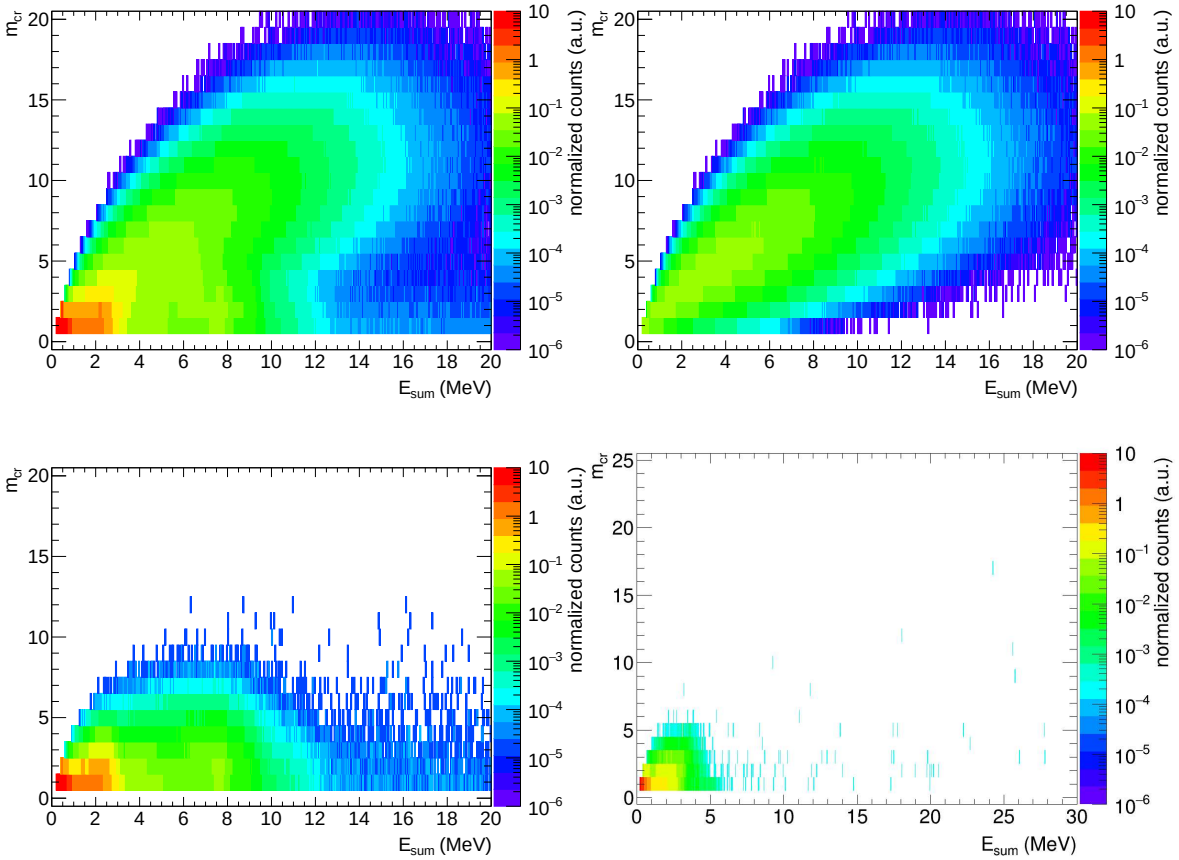

Figure 5.15: TAC event sum energy as a function of the crystal multiplicity for the full experimental setup (top left), the fission tagged counts (top right), the background component introduced by the dummy FICH (bottom left) and the α-activity (bottom right) for neutron energies in the interval from 1 eV to 10 eV.

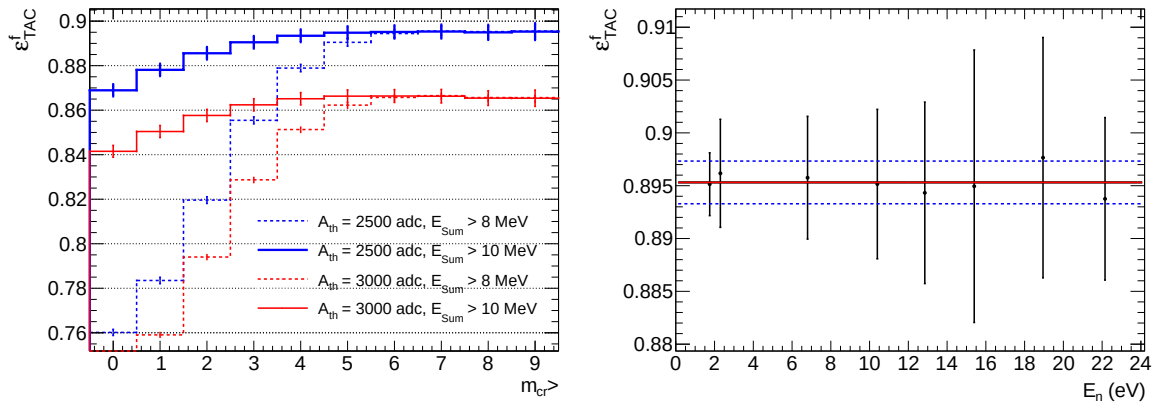

Figure 5.16: Fission tagging efficiency ε^f_{TAC} as a function of the crystal multiplicity and sum energy for two different amplitude thresholds A_{th} in the neutron energy interval from 1.6 eV to 1.9 eV (left). Fission tagging efficiency calculated in several neutron resonances for $A_{th} = 2500$ adc units, $m_{cr} > 6$ and $E_{Sum} > 10$ MeV, their average (red line) and the associated error of the average (blue dashed lines) (right).

Table 5.3: Fission tagging efficiency calculated for $A_{th} = 2500$ adc units in several neutron resonances for different sets of conditions: (1) $m_{cr} > 6$ and $E_{Sum} > 8$ MeV; (2) $m_{cr} > 6$ and $E_{Sum} > 10$ MeV; (3) $m_{cr} > 7$ and $E_{Sum} > 8$ MeV; (4) $m_{cr} > 7$ and $E_{Sum} > 10$ MeV.

E_n (eV)	ε^f_{TAC} (1)	ε^f_{TAC} (2)	ε^f_{TAC} (3)	ε^f_{TAC} (4)
1.6-1.9	0.8944(18)	0.8951(30)	0.8955(20)	0.8953(31)
2.2-2.4	0.8933(31)	0.8961(51)	0.8947(34)	0.8962(54)
6.6-7.0	0.8939(36)	0.8957(58)	0.8954(39)	0.8956(61)
10.2-10.6	0.8944(44)	0.8951(70)	0.8958(48)	0.8952(74)
12.6-13.1	0.8959(53)	0.8943(86)	0.8964(58)	0.8925(90)
15.2-15.6	0.8936(80)	0.895(13)	0.8964(87)	0.897(14)
18.7-19.2	0.8936(70)	0.898(11)	0.8945(77)	0.900(12)
21.7-22.6	0.8928(48)	0.8937(77)	0.8940(52)	0.8932(81)
Total	0.8941(12)	0.89531(20)	0.8953(14)	0.8954(21)

components i.e. fission neutrons - see section 5.3.4, that cannot be subtracted before removing the prompt background. This might also explain why the calculated efficiency in the left panel of Figure 5.16 show a strong dependence on the multiplicity for $E_{Sum} > 8$ MeV compared to the more restrictive conditions $E_{Sum} > 10$ MeV, as the fission neutron induced background should not exceed 10 MeV sum energy as can be seen for example in the left panel of Figure 5.8. The left panel of Figure 5.16 shows that for $m_{cr} > 6$ the sensitivity to the background is reduced within error bars as both conditions in E_{Sum} coincide. Using only events with $m_{cr} > 6$ and $E_{Sum} > 10$ MeV the efficiency is calculated in several neutron resonances and the results are shown in the right panel of Figure 5.16 for $A_{th} = 2500$ adc units together with the average to the points (red line) and the related error (blue dashed lines). The calculated efficiency versus the amplitude in the fission chamber is shown in Figure 5.17 and calculated with different sets of conditions in Table 5.3.

5.3.5.1 Correlations between TAC and FICH event detection

In the previous section ε^f_{TAC} and ε_{FICH} have been calculated assuming no correlation between the two detection systems. However, there are correlations that have to been considered:

- Kinematic boost of the γ-rays emitted from the fission fragments. This effect has been investigated in a previous work [108] but was found negligible and can also be expected to be negligible for this work as ^{233}U and ^{235}U do not show sizable differences in the kinetic energies of the fission fragments.

- The fission fragment detection efficiency depending on the mass of the fragment. This effect was shown in a previous work [108] using fission tagging at n_TOF . This effect has not been investigated in this work as it is only accessible with Monte Carlo simulation of the FICH amplitude spectrum which was not successful, thus prohibiting to draw conclusions. Nevertheless, the effect can be easily explained: Light and heavy fission fragments show different average amplitudes, hence a constant amplitude threshold will affect one fragment more than the other. As only one fragment is used

to tag the prompt fission γ-rays the constant amplitude threshold affects the efficiency. This component is not neglected and is attempted to be corrected for experimentally in section 5.3.5.2.

- Angular correlation of the prompt fission γ-rays and the fission fragments. Such a correlation has already been discussed in section 4.3.3.1 with respect to the reconstruction of the prompt fission response by Monte Carlo simulations.

The relation between the amplitude of the FICH signal and the deposited energy in the TAC is shown in both panels of Figure 5.18. The difference between the left and right panels is the normalization. The sum energy spectra in the left panels are normalized to their total integral in the range 0-20 MeV and it can be observed that for larger amplitudes the spectrum is slightly shifted towards lower sum energies. In the bottom left panel the differences of the sum energy spectra between the different amplitude intervals and the amplitude interval 1800-2500 adc units are shown, confirming that there is a systematic dependency on the amplitude indicated by the bump in the sum energy region 3-5 MeV growing the larger the amplitudes become. In the right panel the normalization is done in the tail of the sum energy, i.e. for $E_{sum} > 10$ MeV. A significant deviation is observed depending on the amplitude cut and confirmed in the respective bottom panel. This indicates that the sum energy in the TAC correlates with the FICH amplitude. This correlation acts like a selection of the FICH amplitude for restrictive conditions in the sum energy. Due to the very restrictive conditions when calculating the fission tagging efficiency the amplitude spectra of the FICH gets deformed. As the FICH amplitude spectrum could not be reproduced a simulation of the effects is not possible thus in the following section 5.3.5.2 it is explained how this correlation can be corrected for.

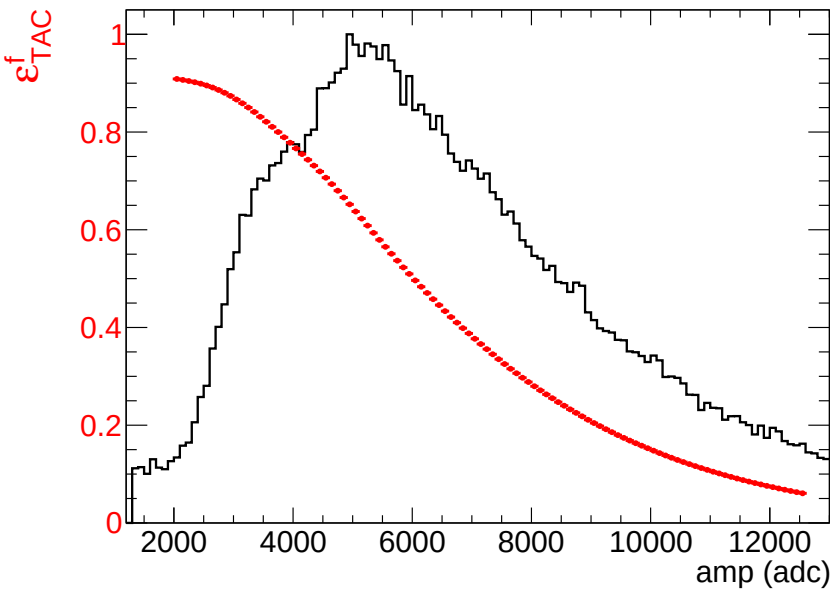

Figure 5.17: Fission tagging efficiency ε^f_{TAC} as a function of the FICH amplitude. The FICH amplitude spectrum in coincidence with the TAC for events with $m_{cr} > 6$ and $E_{Sum} > 10$ MeV is shown as well.

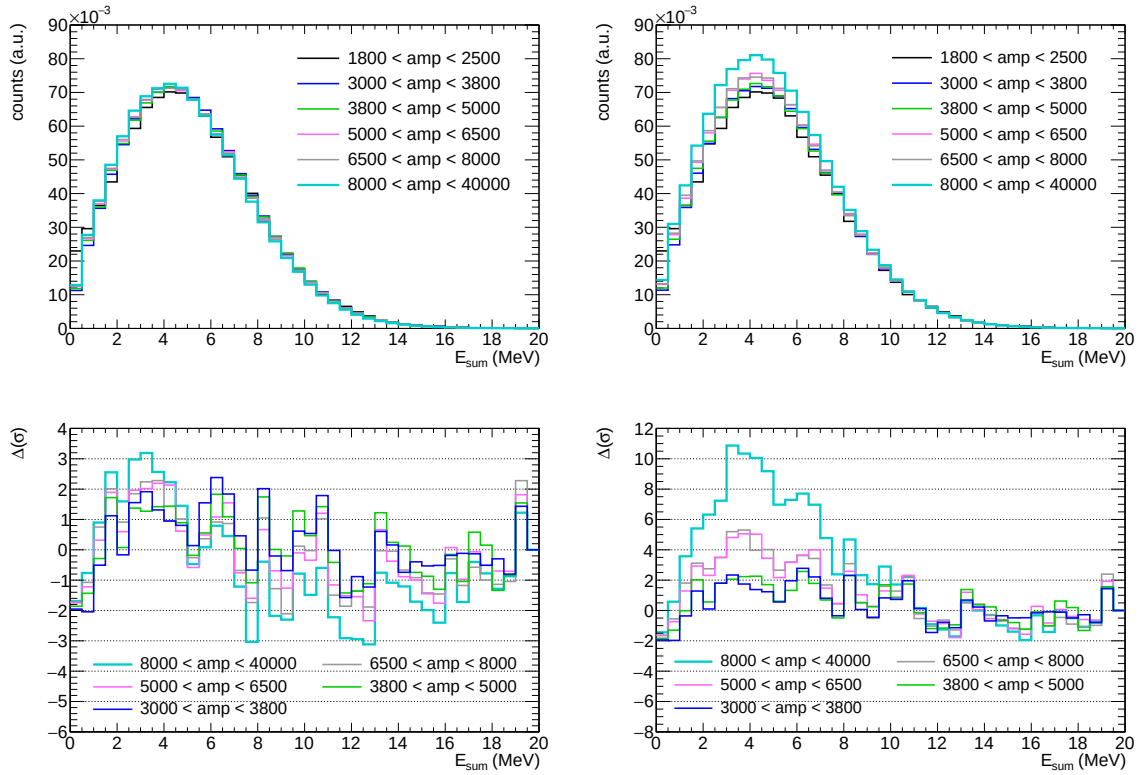

Figure 5.18: Sum energy spectra for different amplitude cuts normalized to the total integral (left) and normalized in the tail of the distribution ($E_{sum} > 10\,\text{MeV}$) (right). In the bottom panels the ratios of the corresponding amplitude regions to the region $1800 < amp(adcunits) < 2500$ are shown.

5.3.5.2 Experimental correction to the FICH efficiency

Due to a correlation observed in the experimental data a correction should be applied to the calculated values of the efficiencies. Certain restrictive conditions for m_{cr} and E_{Sum} have been applied for the calculation of ε^{f}_{TAC} and in the case of (n,f) reactions being detected independently by the TAC and the FICH the obtained value can be used for the calculation of the ^{233}U α-ratio with less restrictive conditions in m_{cr} and E_{Sum}. Due to the observed correlation:

- The fission tagging detection efficiency depends slightly on the conditions applied to the TAC, thus it must be determined for the final analysis conditions of the ^{233}U α-ratio : $3 \leq m_{cr} \leq 7$ and $2.5\,\text{MeV} < E_{sum} < 7\,\text{MeV}$.
- The fission detection efficiency has to be calculated, as $\varepsilon^{f}_{TAC} \neq \varepsilon_{FICH}$.

As suggested by a previous work [108] this is done by calculating a scaling factor to the obtained uncorrelated efficiency. For this purpose, the ratio between the fission tagging efficiency

$\varepsilon^f_{TAC}(A_{th}, E^x_{Sum}, m^x_{cr})$ for *restrictive* ($x = 1$, E^1_{Sum}, m^1_{cr}) and *relaxed* ($x = 2$, E^2_{Sum}, m^2_{cr})) conditions is calculated:

$$\begin{aligned}\frac{\varepsilon^f_{TAC}(A_{th}, E^1_{Sum}, m^1_{cr})}{\varepsilon^f_{TAC}(A_{th}, E^2_{Sum}, m^2_{cr})} &= \frac{c_{Tagg}(A_{th}, E^1_{Sum}, m^1_{cr})}{c_{Tagg}(A_{th}, E^2_{Sum}, m^2_{cr})} \cdot \frac{c_{Fiss-TAC}(E^2_{Sum}, m^2_{cr})}{c_{Fiss-TAC}(E^1_{Sum}, m^1_{cr})} \\ &= f(A_{th}) \cdot \frac{c_{Fiss-TAC}(E^2_{Sum}, m^2_{cr})}{c_{Fiss-TAC}(E^1_{Sum}, m^1_{cr})}\end{aligned} \tag{5.11}$$

where $f(A_{th})$ is defined as the ratio between the tagged fission counts for restrictive and relaxed conditions:

$$f(A_{th}) = \frac{c_{Tagg}(A_{th}, E^1_{Sum}, m^1_{cr})}{c_{Tagg}(A_{th}, E^2_{Sum}, m^2_{cr})}. \tag{5.12}$$

In this way the fission tagging detection efficiency can be calculated for relaxed conditions $\varepsilon^f_{TAC}(A_{th}, E^2_{Sum}, m^2_{cr})$ using equation (5.11) as the fission tagging efficiency as well as the fission counts in the TAC $c_{Fiss-TAC}$ are known for restrictive conditions and $f(A_{th})$ can be easily calculated. The missing value that has to be estimated is the number of fissions for relaxed conditions $c_{Fiss-TAC}(E^2_{Sum}, m^2_{cr})$. In the case where the FICH has an efficiency of 100 % corresponding to $A_{th} = 0$, including fission fragments stopped in the sample, the ^{233}U(n,f) events are detected independently by both detection systems. Thus $\varepsilon^f_{TAC}(0, E^1_{Sum}, m^1_{cr}) = \varepsilon^f_{TAC}(0, E^2_{Sum}, m^2_{cr})$ and equation (5.11) can be solved for $c_{Fiss-TAC}(E^2_{Sum}, m^2_{cr})$:

$$c_{Fiss-TAC}(E^2_{Sum}, m^2_{cr}) = \frac{c_{Fiss-TAC}(E^1_{Sum}, m^1_{cr})}{f(0)}. \tag{5.13}$$

Substituting equation (5.13) back into equation (5.11)

$$\frac{\varepsilon^f_{TAC}(A_{th}, E^1_{Sum}, m^1_{cr})}{\varepsilon^f_{TAC}(A_{th}, E^2_{Sum}, m^2_{cr})} = \frac{f(A_{th})}{f(0)} \tag{5.14}$$

and the tagging efficiency for the relaxed conditions is given by

$$\varepsilon^f_{TAC}(A_{th}, E^2_{Sum}, m^2_{cr}) = \frac{f(0)}{f(A_{th})} \varepsilon^f_{TAC}(A_{th}, E^1_{Sum}, m^1_{cr}). \tag{5.15}$$

For the calculation of $f(0)$ some assumptions have to be made:

- The FICH has an efficiency of about 90 %, as was shown in section 5.3.5.
- The fission events for the residual 10 % show similar characteristics as the ones obtained for low amplitudes (A_{th}), thus their ratio of the tagged to untagged counts will be similar as the one for low amplitudes.

The ratio of the tagged counts with restrictive (1) and relaxed (2) conditions is shown in Figure 5.19 where each region represents about 10 % of the fission reactions detected by the TAC with the respective conditions. The ratio $f(A_{th})$ is calculated for each amplitude interval. Under the assumption that the lowest 10 % of the fission events that fall below the analysis threshold have similar characteristics an artificial interval below the threshold

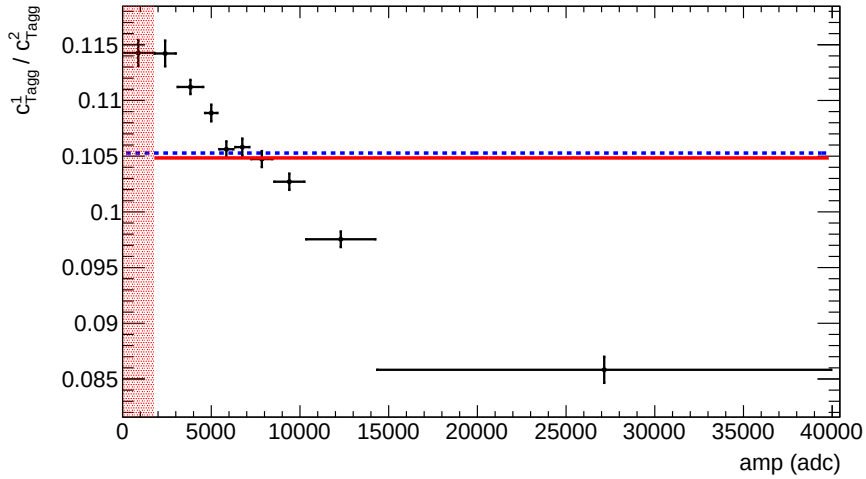

Figure 5.19: Ratio between the number of tagged fission counts with restrictive (1, $E_{Sum} > 10\,\text{MeV}$ and $m_{cr} > 6$) and relaxed conditions (2, $2.5\,\text{MeV} < E_{Sum} < 7\,\text{MeV}$ and $3 \leq m_{cr} \leq 7$) as a function of the FICH signal amplitude. The red and blue lines indicate the averages of the points in their respective intervals.

is included with the same ratio as the neighbouring interval (see red shaded region). To determine $f(0)$ the average of the amplitude intervals is computed without t (red line) and with the artificially added tagged counts (blue line). For the conditions used in the calculation of the efficiencies and the conditions applied to determine the ^{233}U α-ratio the correction is estimated to:

$$\frac{f(0)}{f(A_{th} = 2500)} = 0.994. \tag{5.16}$$

Thus the fission tagging detection efficiency obtained in section 5.3.5 has to be lowered by 0.6 % and the related systematic uncertainty is estimated to 15 %. As the correction is rather small and the second assumption regarding the similarity of the TAC response to fission events with the neighbouring amplitude intervals is not clearly fulfilled this correction has not been applied. It is estimated that the maximum effect is below 2 % by varying the amplitude intervals.

5.4 Simulated response to ^{233}U(n,γ) events

After the subtraction of all background components the shape of the TAC response to the EM cascades emitted in the ^{233}U(n,γ) reactions is summarized in Figure 5.20. The remaining parameter that has to be determined is the efficiency of the TAC $\varepsilon^{\gamma}_{TAC}$ to capture those EM cascades which will be done by Monte Carlo Simulations described in this section. The process of determining the efficiency is done in two steps:

1. Generation of the cascades with the Monte Carlo code DICEBOX
2. Transport of the γ-rays of the cascade in GEANT4 to calculate the deposited energy in the TAC

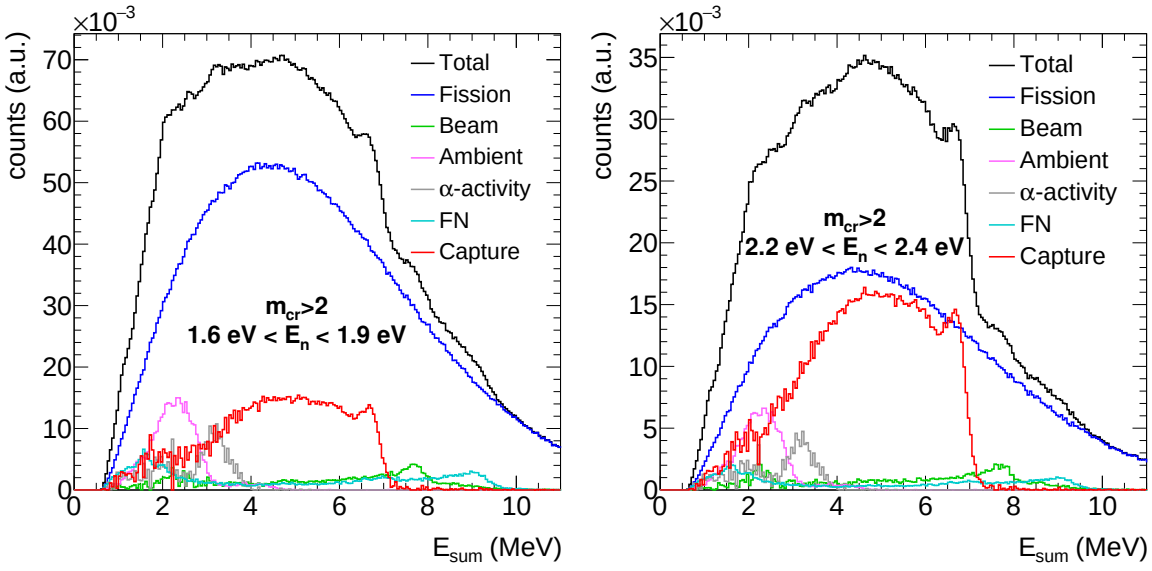

Figure 5.20: Sum energy response of the TAC in two neutron resonances to the different components obtained either by direct measurement or subtraction of components from the total response.

5.4.1 The ^{233}U(n,γ) cascade generator

The event generator used to generate the ^{233}U(n,γ) cascades is the Monte Carlo DICEBOX code [45]. Neglecting the energy added to the compound nucleus by the incident neutron in the capture process, the excitation energy of the compound nucleus equals the neutron separation energy $S_n(^{234}U) = 6.85\,\text{MeV}$. From this excitation energy the (n,γ) cascades can generally decay via many intermediate levels to the ground state. The number of estimated intermediate levels in ^{234}U, is of the order of 10^5 to 10^7, depending on the level density model. DICEBOX uses the following approach to calculate the individual decays from all those levels and transitions:

- Below a certain excitation energy E_{cr} the properties of the nuclear levels are known with respect to their energy E, spin J, parities π and all branching ratios for the transitions between levels. These data are compiled in the Evaluated Nuclear Structure Data File (ENSDF) [109].
- Above the critical energy E_{cr} the levels are generated randomly according to a chosen level density model $\rho(E, J^\pi)$
- The transition probability between nuclear levels a and b above E_{cr} is given by the radiation widths $\Gamma_{a\gamma b}$ which can be calculated by

$$\Gamma_{a\gamma b} = \sum_{X,L} y_{XL}^2 (E_a - E_b)^{2L+1} \frac{S_\gamma^{(XL)}(E_a - E_b)}{\rho(E_a, J_a^{\pi_a})}) \tag{5.17}$$

where $S_\gamma^{(XL)}(E_\gamma)$ is the photon strength function for a given type X (electric or magnetic) and multipolarity L and Porter-Thomas fluctuations are included by the random values y_{XL} sampled from a standard normal distribution.

- Each cascade starts from a well defined initial level with known energy, spin and parity.

The procedure of generating the de-excitation from the initial level to the final state can be described as follows:

1. Discretization of the level density $\rho(E, J^\pi)$ to yield energies E_a, spins J_a and parities π_a of individual levels above E_{cr}, where $a = 0$ and $a = n$ correspond to the initial level and the ground state respectively.

2. Each level with $E_a > E_{cr}$ is assigned a generator seed α_a

3. Generation of the partial widths $\Gamma_{a\gamma a'}$ for a full set of transitions $a \longrightarrow a'$ from the initial level a to all accessible final levels a'

4. The total radiation width $\Gamma_{a\gamma}$ is calculated for the initial level a

$$\Gamma_{a\gamma} = \sum_{a'>a} \Gamma_{a\gamma a'} \tag{5.18}$$

5. A full set of branching intensities $I_{aa'}$ for transitions from the initial level a are determined following

$$I_{aa'} = \Gamma_{a\gamma a'}/\Gamma_{a\gamma} \tag{5.19}$$

6. A level a_1, to which the initial level a decays, is determined by a random number s_1 fulfilling the requirement

$$\sum_{a'=a+1}^{a_1-1} I_{aa'} \leq s_1 < \sum_{a'=a+1}^{a_1} I_{aa'} \tag{5.20}$$

   resulting in a known level a_1 reached by a step of the cascade.

7. If $E_{a_1} < E_{cr}$ the branching intensities $I_{a_1 a'}$ are deduced from the evaluated ENSDF data exclusively and the decay is computed from these data until a final level of a cascade is reached. If $E_{a_1} \geq E_{cr}$ the substitution $a_1 \longrightarrow a$ is performed and the items 3-6 are repeated until a level a_k with $E_{a_k} < E_{cr}$ or a final level of a cascade is reached. The final level of a cascade is either the ground state or an isomer with a half life on the level of the experimental time window.

The cascades are characterized by the γ-ray energies E_γ and the γ-multiplicity m_γ. The nuclear level density (NLD) and the photon strength function (PSF) are obtained from physical models. The parameters of those models are adjusted [110] to fit the experimental data obtained from the deposited energy spectra of the TAC for different conditions applied to the crystal multiplicity m_{cr}.
In the simulations the constant temperature formula (CTF) model was used for the NLD with the temperature $T = 0.45\,\text{MeV}$ and the energy offset $E_0 = -0.38\,\text{MeV}$, together with the standard form of spin dependence with constant spin cut-off parameter and no parity dependence [112]. The chosen model is compared to experimental data from the Oslo group

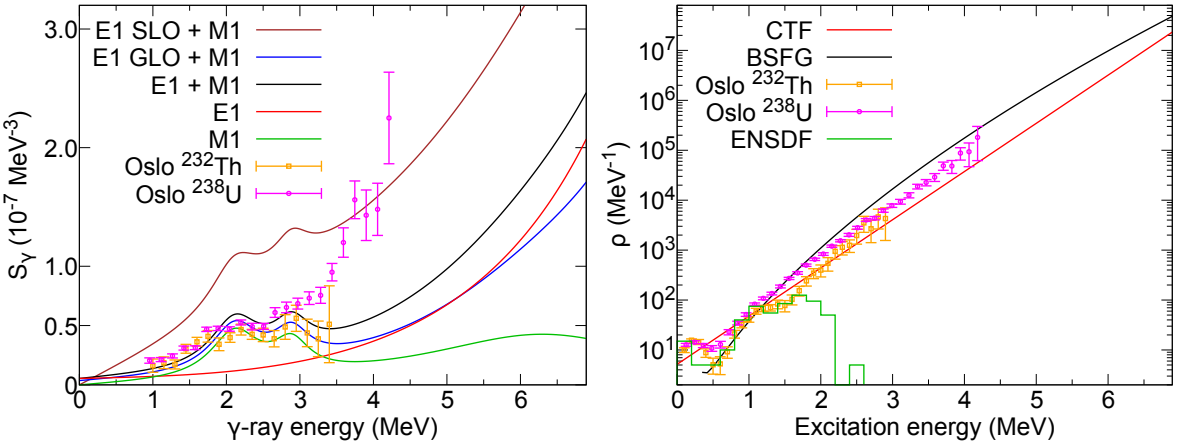

Figure 5.21: Photon strength function used to reproduce the experimental ^{234}U γ-ray decay (black, red, green) [110] compared to suggested model as defined in the RIPL-3 data base [111] (brown and blue lines, SLO/GLO in the legend) and other data sets from the Oslo group (left). Two level density models compared to experimental data from the Oslo group and experimental level counting from ENSDF (right), for detailed explanation see section 5.4.1.

as well as the back-shifted Fermi-gas (BSFG) model in the right panel of Figure 5.21. Typically the levels and transitions for low excitation energies can be taken from data bases like ENSDF [109] but choosing a critical energy lies with the experimenter. For this measurement the critical energy was chosen to be 1560 keV to include an isomeric level of ^{234}U at 1421.3 keV with a half life of 33.5 μs and $J^{\pi} = 6^{-}$ and its feeding from doorway states. The number of nuclear levels of ^{234}U taken from the ENSDF data base is also shown in the right panel of Figure 5.21 and shows a reasonable agreement with the chosen level density (CTF) up to 1.56 MeV.

The γ-ray cascades for the determination of $\varepsilon^{\gamma}_{TAC}$ were adjusted similarly as in previous analysis (with TAC-type detector DANCE) [113]. The starting parameters of the photon strength functions were based on the data from the Oslo nuclear physics group [114, 115], which showed evidence of considerable $M1$ scissors-mode (SM) resonances in the PSF in similar nuclei. The conclusions of recent work [116] regarding the constraints on the PSFs in actinides were taken into account. The $E1$ PSF was taken in the form of a modified general Lorentzian (MGLO) prescription [117] (with $k = 1.8$) of the tail of the giant electric dipole resonance (GEDR), the $M1$ PSF consisted of double-humped SM and single spin-flip (SF) mode described by Lorentzian resonances and the $E2$ PSF, which has negligible influence on

Table 5.4: PSF parameters used to reproduce the experimental data.

	E_{G_1} (MeV)	σ_{G_1} (mb)	Γ_{G_1} (MeV)	E_{G_2} (MeV)	σ_{G_2} (mb)	Γ_{G_2} (MeV)
$E1$ (MGLO)	11.28	325	2.48	13.73	384	4.25

	E_{SM_1} (MeV)	σ_{SM_1} (mb)	Γ_{SM_1} (MeV)	E_{SM_2} (MeV)	σ_{SM_2} (mb)	Γ_{SM_2} (MeV)	E_{SF} (MeV)	σ_{SF} (mb)	Γ_{SF} (MeV)
$M1$ (SM + SF)	2.15	0.95	0.80	2.9	0.87	0.60	6.61	3.15	4.00

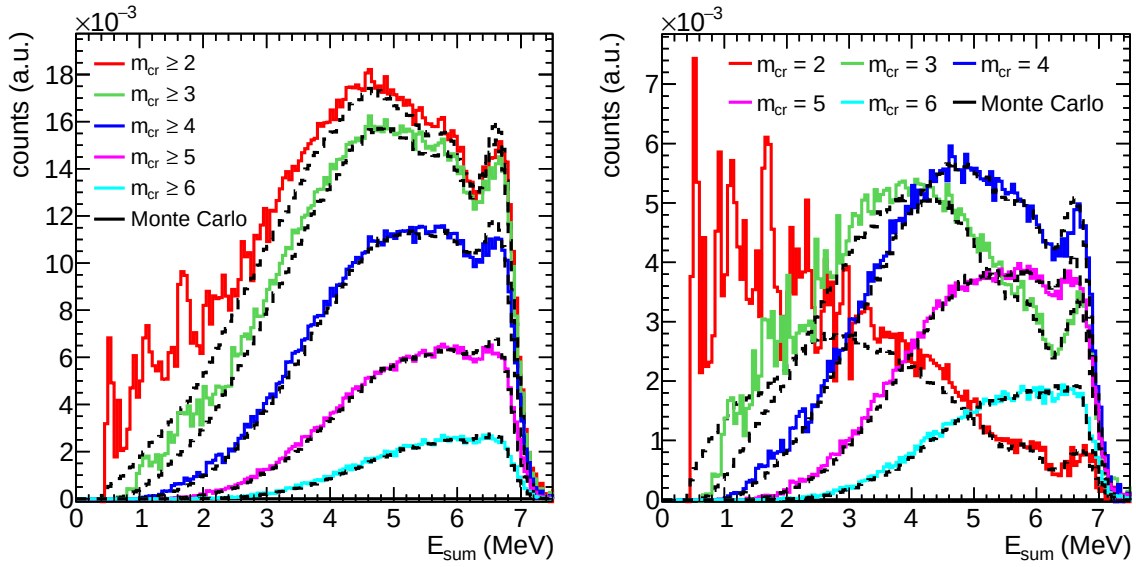

Figure 5.22: Comparison of the experimental and simulated sum energy spectra for capture events and various crystal multiplicity conditions. For multiplicities larger than 2 a good agreement is achieved.

the results, was approximated by single Lorentzian description of the giant electric quadrupole resonance (GEQR). The parameters of the $M1$ PSF, namely the σ_r of all three components, were adjusted to best describe the experimental spectra and are summarized in Table 5.4 together with the $E1$ parameters. In the left panel of Figure 5.21 the total photon strength function used to reproduce the experimental ^{233}U(n,γ) γ-ray cascades is shown together with its $E1$ and $M1$ components and compared to suggested values from the RIPL-3 data base [111] as well as data from the Oslo group for ^{232}Th and ^{238}U [118, 119].
DICEBOX explicitly accounts for the internal electron conversion using the α coefficients from the BRICC database [120].

5.4.2 Simulated response to the ^{233}U capture cascades

A detailed geometry of the TAC, containing the detector modules and all the supporting and structural materials was implemented in previous works. The FICH, including the PCB structures, pre-amplifiers and chamber windows as well as the absorber were added to this geometry according to the technical drawings of each piece. The validation of the implementation has been performed as described in section 3.5. The γ-ray cascades generated by DICEBOX were used as input for the GEANT4 simulation utilizing the TAC geometry and taking into account particle interactions and geometrical effects. The time stamps, the deposited energy in the BaF_2 crystals and the corresponding detector numbers were recorded. The event reconstruction from the simulated data has been performed analogous to the reconstruction process of the experimental data and was described in section 3.5.1.
The results for the sum energy spectra are shown in Figure 5.22 for various crystal multiplicity conditions. A good agreement between experimental and simulated spectra is achieved for $m_{cr} \geq 3$. For smaller crystal multiplicities the spectra are still dominated by background or

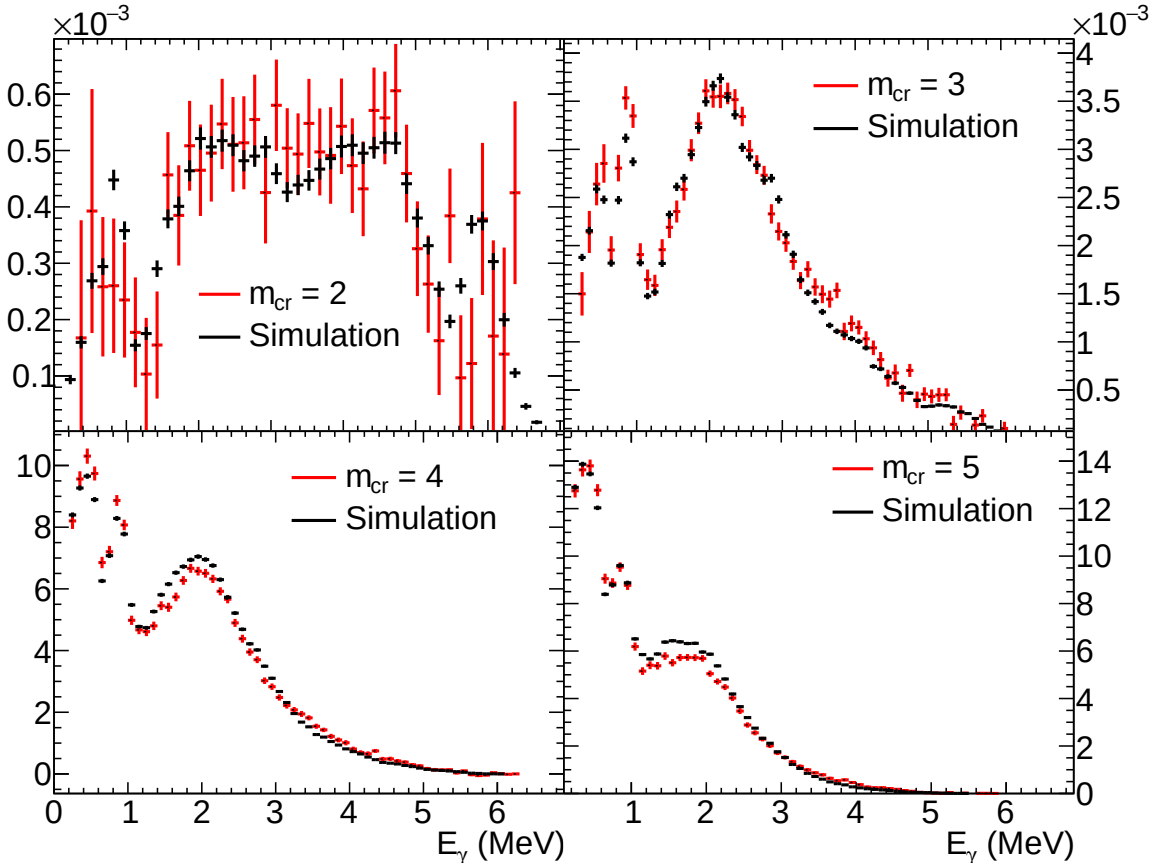

Figure 5.23: Comparison of the experimental and simulated γ-ray energies E_γ for capture events with $6.4\,\text{MeV} < E_{sum} < 7\,\text{MeV}$.

suffer from statistical fluctuations especially in the sum energy region below 2.5 MeV. Thus the ^{233}U α-ratio is calculated from events with $2.5\,\text{MeV} < E_{Sum} < 7\,\text{MeV}$ and $m_{cr} \geq 3$.

The validity of the chosen photon strength function can be checked when looking at fully captured EM cascades. In the experimental data it can be assumed that a cascade has been fully captured when the sum energy in the TAC is approximately the neutron separation energy of ^{234}U, namely 6.85 MeV. Gating on the sum energy peak allows to investigate the transitions in the ^{234}U nucleus by looking at individual multiplicities. This is called multistep cascade spectra (MSC) and those spectra are shown in Figure 5.23 for several multiplicities. Essentially those spectra correspond to the individual γ-rays emitted in their respective multistep cascade. The low energies are governed by the levels and transitions from the data library (ENSDF) while the smoother shapes are driven by the statistical model and the photon strength functions. Overall, a good agreement is achieved showing that the chosen PSF is adequate for the analysis and do not only reproduce the sum energy spectra, dominated by the geometrical model of the TAC, but is also able to reproduce the physics of the ^{234}U decay. Furthermore, the sum energy peak also offers to check the multiplicity distribution of the simulated spectra. This comparison is done in Figure 5.24 and shows a reasonable agreement as well.

The efficiency is easily obtained from the simulations as the ratio of the cascades registered for the applied analysis conditions ($m_{cr} > 2$, $2.5\,\text{MeV} < E_{Sum} < 7\,\text{MeV}$) and the total number

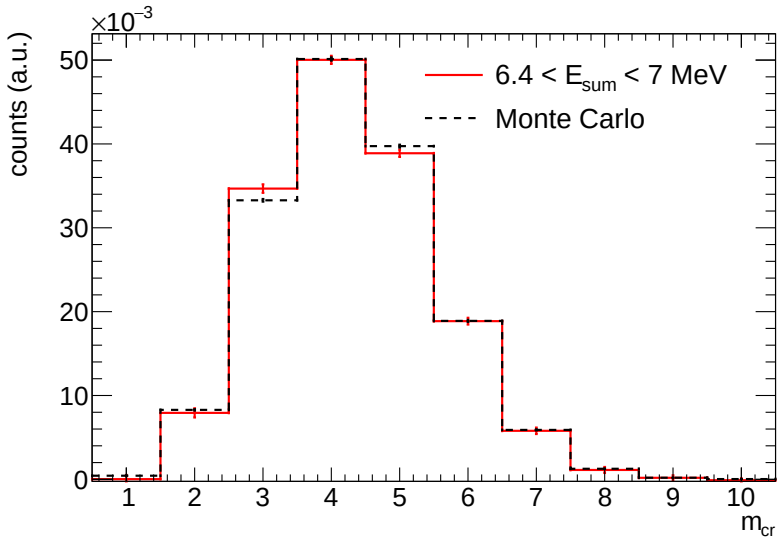

Figure 5.24: Comparison of the experimental and simulated crystal multiplicity distribution for capture events with 6.4 MeV $< E_{sum} <$ 7 MeV.

of cascades. The efficiency is summarized for several conditions in Table 5.5.

Table 5.5: TAC efficiency $\varepsilon^{\gamma}_{TAC}$ for ^{233}U(n,γ) cascades for different multiplicity conditions.

$m_{cr} >$	E_{Sum} (MeV)	$\varepsilon^{\gamma}_{TAC}$
0	2.5 - 7.0	87.2
1	2.5 - 7.0	86.1
2	2.5 - 7.0	75.8
3	2.5 - 7.0	52.3
4	2.5 - 7.0	25.6
5	2.5 - 7.0	8.8
6	2.5 - 7.0	2.1

5.4.3 Final TAC efficiency and uncertainty estimation

The uncertainty in the TAC efficiency to the ^{233}U(n,γ) cascades are governed by two main sources:

- The uncertainty related to the geometry model Δ_G: It has been observed that the parameter with the greatest impact on $\varepsilon^{\gamma}_{TAC}$ is the TAC inner radius R_{TAC}. An uncertainty in this parameter $\Delta R_{TAC} = \pm 1$ mm has been assumed, as for larger variations the deposited energy spectra from calibration sources shown in Figure 3.22 are not reproduced by the Monte Carlo Simulations. The density of the absorber was also varied by ± 10 %. From the simulated efficiencies for various analysis conditions the impact is calculated as the difference between the maximum and minimum value divided by two and is summarized in Table 5.6.

  Considering realistic analysis conditions the systematic uncertainty associated with the geometry model implemented in the GEANT4 simulations is up to 1.1 %

Table 5.6: Sensitivity of the TAC efficiency $\varepsilon^{\gamma}_{TAC}$ to variation of the model used in the GEANT4 simulations. In all simulations the TAC radius has been varied by ± 1 mm to obtain the values of $\Delta_G(\varepsilon^{\gamma}_{TAC})$. Where indicated the density of the absorber has been varied with respect to the nominal value of $1.06\,\mathrm{g/cm^3}$.

$m_{cr} >$	E_{Sum} (MeV)	absorber density (%)	$\Delta_G(\varepsilon^{\gamma}_{TAC})$ (%)
2	2.5 - 7.0	100	1.0
2	2.5 - 7.0	90	1.0
2	2.5 - 7.0	110	1.0
2	2.5 - 7.5	100	1.0
2	3.0 - 7.0	100	1.1
3	2.0 - 7.0	100	0.9

- The uncertainty Δ_{CM} related to the ^{233}U(n,γ) cascade model used is estimated from the ratio between the integrals I_x of the experimental and simulated deposited energy spectra for different crystal multiplicities and summarized in Table 5.7.

Table 5.7: Ratio between the experimental and simulated deposited energy spectra integral for $2.5\,\mathrm{MeV} < E_{sum} < 7\,\mathrm{MeV}$ and different crystal multiplicities. The normalization is done for $m_{cr} > 2$.

$m_{cr} >$	E_{Sum} (MeV)	I_{exp}/I_{sim}
0	2.5 - 7.0	1.011
1	2.5 - 7.0	1.010
2	2.5 - 7.0	1.000
3	2.5 - 7.0	0.989
4	2.5 - 7.0	0.992
5	2.5 - 7.0	1.008

The good reproduction of the experimental sum energy spectra in the simulations leads to an uncertainty related to the ^{233}U(n,γ) cascade model, calculated as the difference of the maximum and minimum ratios, to

$$\Delta_{CM}(\varepsilon^{\gamma}_{TAC}) = 2.2\% \tag{5.21}$$

Thus the uncertainty of the TAC detection efficieny to ^{233}U(n,γ) cascades is calculated to

$$\Delta(\varepsilon^{\gamma}_{TAC}) = \sqrt{\Delta^2_G + \Delta^2_{CM}} \approx 2.5\% \tag{5.22}$$

and the final TAC efficiency to ^{233}U(n,γ) cascades is

$$\varepsilon^{\gamma}_{TAC} = (75.8 \pm 2.5)\%. \tag{5.23}$$

5.5 Summary

In this chapter the TAC response to the ^{233}U(n,γ) reaction was determined by subtracting the following contributions from the total response which shall be briefly summarized:

- Time independent background (section 5.1): corresponds to the environmental natural radioactivity and the α-activity of the ^{233}U samples. It is dominated by low multiplicity and low sum energy and is easily removed by conditions on those parameters.

- Background related to the neutron beam but not to the ^{233}U samples (section 5.2): corresponds to reactions (scattering, neutron capture) of the neutron beam with materials intercepting it. Dedicated measurements have been performed with a dummy chamber, identical to the fission chamber but without the deposits inside. This background component depends on the neutron energy and consists of events that are similar to the ^{233}U response, thus a careful subtraction was performed.

- Elastic scattering by the ^{233}U deposits (section 5.3.1): can be neglected in the neutron energy region of interest.

- Delayed γ-rays from the decay of fission products (section 5.3.2): Decay of the fission products leads to emission of γ-rays with a large delay, thus only showing a weak time correlation with the fission events. In the valleys between the resonances, where the ^{233}U α-ratio is minimum (i.e., worst case), this component is estimated by simulations to be negligible while contributing up to maximum 2 % to the capture response below 1 eV. As the background related to the fission chamber, fission neutrons and the prompt fission components is much more significant this contribution was neglected.

- Prompt fission background: was determined using the fission tagging method (section 5.3.3). The fission tagging and fission chamber efficiency has been calculated (section 5.3.5) to
$$\varepsilon^{f}_{TAC} = (89.53 \pm 0.20)\%.$$

- Fission neutron component (section 5.3.4): fission neutrons emitted in the ^{233}U(n,f) reaction are moderated and captured in the experimental setup, mostly in the BaF_2 crystals. The shape of the FN spectra is constant with respect of the incident neutron's energy, hence the shape has been determined from a fission dominated resonance at 4.2-5.3 eV. The integral in the region of interest is scaled with a constant scaling factor, determined from the experimental data and confirmed with simulations, and the counts of the fission chamber in order to subtract this component from the total response. The scaling factor slightly depends on the fitting region which leads to a 3 % uncertainty in the value that is subtracted from the total response.

After the subtraction of the background components the response to the ^{233}U(n,γ) has been compared with simulations of the EM cascades from the ^{233}U(n,γ) reaction using DICEBOX and calculating the deposited energy with simulations in GEANT4 in order to determine the detection efficiency of the TAC to ^{233}U(n,γ) cascades, see section 5.4. The TAC detection efficiency for ^{233}U(n,γ) cascades is calculated to

$$\varepsilon^{\gamma}_{TAC} = (75.8 \pm 0.25)\%.$$

Chapter 6

The experimental ^{233}U α-ratio

In this chapter the choice of the analysis conditions and the obtained results of the capture response are presented. From those results the ^{233}U α-ratio is calculated and compared to evaluated libraries and other experimental data.

6.1 Analysis conditions

In order to improve the signal to background ratio in the determination of the capture response, specific conditions can be applied to the TAC, namely the crystal multiplicity m_{cr} and the sum energy E_{Sum}. The more restrictive the conditions the better the signal to background ratio but the lower the efficiency, therefore counting statistics, and the higher the sensitivity of the ^{233}U α-ratio to the applied corrections and background subtraction. Thus a compromise must be found. In the left and right panel of Figure 6.1 the signature in crystal multiplicity and sum energy for the different components as well as the total measured spectra are shown respectively. For small crystal multiplicities the background (beam, FN, ambient and α-activity) dominates the spectrum while the fission related prompt background

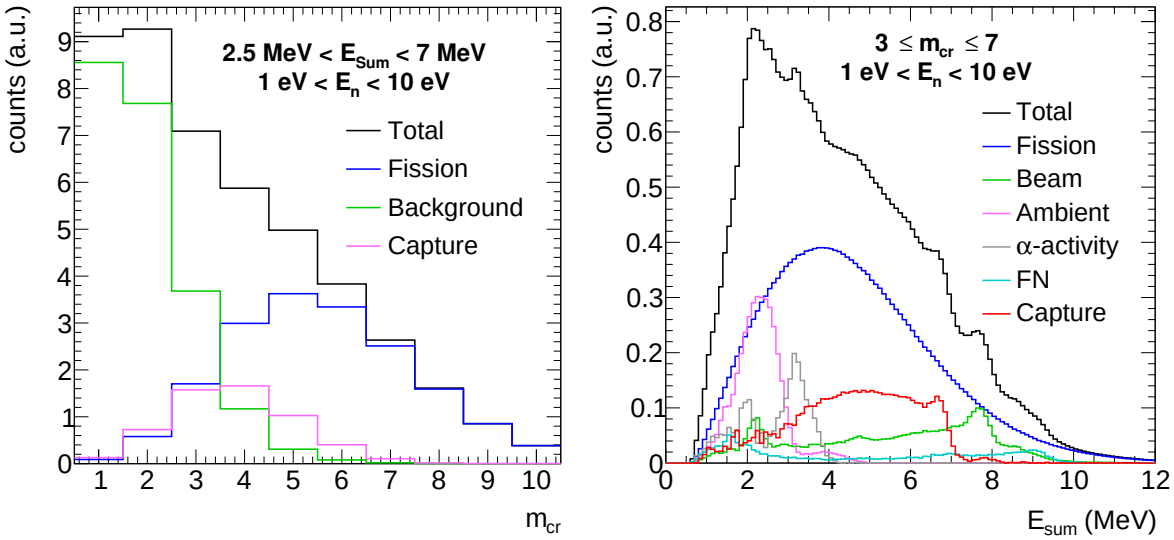

Figure 6.1: Crystal multiplicity distribution of TAC events with 2.5 MeV $< E_{sum} <$ 7 MeV for the different contributions to the total measured spectrum (left). Sum energy distribution in the TAC corresponding to their source for events with $3 \leq m_{cr} \leq 7$ (right).

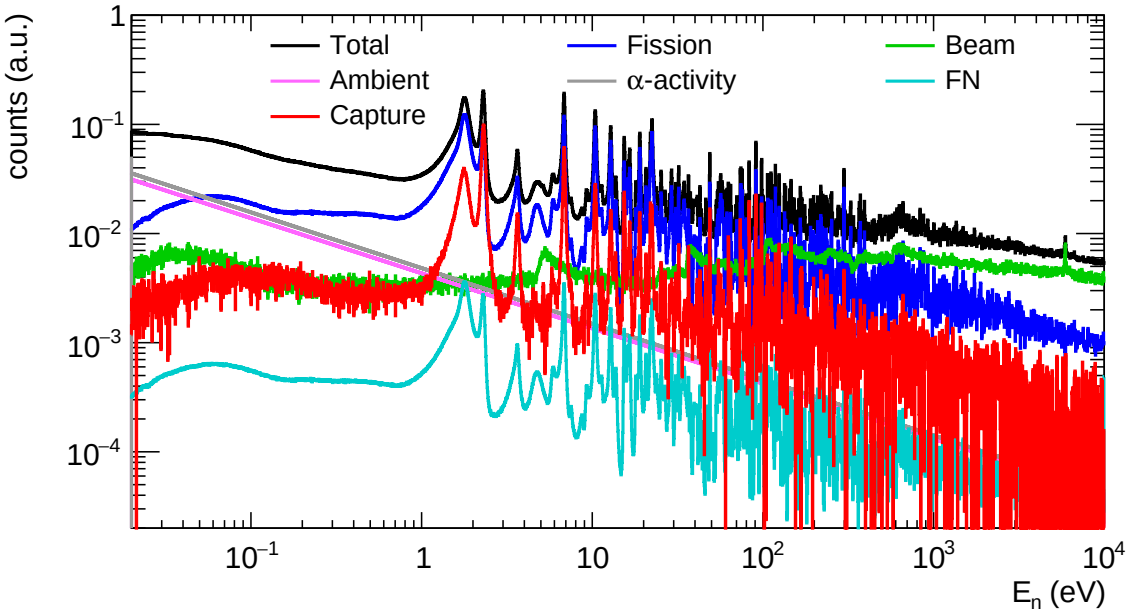

Figure 6.2: Experimental response of the TAC to the different components obtained either by direct measurement or subtraction of components from the total response for events with $3 \leq m_{cr} \leq 7$ and $2.5\,\text{MeV} < E_{sum} < 7\,\text{MeV}$.

is responsible for essentially all counts with $m_{cr} > 7$ as expected. In the sum energy spectra events with $3 \leq m_{cr} \leq 7$ and sum energies above 7 MeV are mainly due to the fission reaction and the beam background induced by the material of the fission chamber as expected. Below 2.5 MeV the capture component exhibits strong fluctuations as the ambient and prompt fission background are the dominant components. Therefore the following compromise on the final analysis conditions is chosen to improve the signal to background ratio:

- **Conditions applied to m_{cr}:** The background unrelated to the ^{233}U samples is strongly discriminated for $m_{cr} \geq 3$. The prompt fission γ-rays are suppressed for $m_{cr} \leq 7$ and there are almost no ^{233}U(n,γ) events above. Thus, the best conditions for the crystal multiplicity is $3 \leq m_{cr} \leq 7$.

- **Conditions applied to E_{Sum}:** Background not related to the prompt fission component is strongly suppressed for $E_{Sum} > 2.5\,\text{MeV}$. In addition due to the separation energy of ^{234}U of 6.85 MeV there is no ^{233}U(n,γ) reaction detected above 7.0-7.3 MeV. Excluding this region thus improves the signal to background ratio. Therefore the best conditions applied to E_{Sum} to improve the signal to background ratio are $2.5\,\text{MeV} < E_{sum} < 7\,\text{MeV}$ and/or $2.5\,\text{MeV} < E_{sum} < 7.3\,\text{MeV}$.

Finally the analysis conditions for the TAC events to extract the capture response are $2.5\,\text{MeV} < E_{sum} < 7\,\text{MeV}$ and $3 \leq m_{cr} \leq 7$, giving a satisfactory compromise between the TAC detection efficiency and the improved signal to background ratio. In Figure 6.2 the experimentally obtained ^{233}U(n,γ) response together with the total response and various background components for events with $3 \leq m_{cr} \leq 7$ and $2.5\,\text{MeV} < E_{sum} < 7\,\text{MeV}$ is shown.

6.2 Dead time corrections

For the moment no dead time corrections have been applied to the experimental ^{233}U α-ratio. In section 4.2.3 it has been shown that dead time corrections can be neglected for the FICH data due to the fast response of the detector. In principle the dead time models for measurements with the TAC are well established [61, 92, 108] but require a certain effort to be carried out properly. The dead time corrections for the TAC response is ongoing work but a brief outlook on the method shall be given in the following. Note that the wave forms of the BaF_2 signals are digitized every 2 ns thus the dead time correction can be done by artificially producing wave forms which are then analyzed by the pulse shape routine again to characterize differences from the original parameters and a proposed method derived from the original works shall be briefly explained:

- The digitized BaF_2 signals from the background (with the dummy chamber) are analyzed individually for low neutron energies in the range 1.6-1.9 eV and if a γ-ray signal with a deposited energy in the region of interest is detected the waveform is stored together with the reconstructed parameters, i.e. deposited energy, for further studies of the routine's performance.
- The waveform is copied into digitized buffers at times corresponding to higher neutron energies for reconstruction by the pulse shape analysis routine.
- This combined buffer, original and signal under study, are analyzed by the routine and the total detection probability $P_{E_\gamma}(E_n)$, describing the probability the signal is not detected at all due to dead time, and the probability $P_{E_\gamma,E'_\gamma}(E_n)$, describing the probability of detecting an incident signal with an energy E_γ with a different energy E'_γ is calculated.
- This procedure is repeated for all BaF_2 detectors, hence a full description of the dead time effects is obtained as a function of the neutron energy.

To give an indication of the effect the individual γ-ray energies from the prompt fission cascades are shown in the left panel of Figure 6.3 for several neutron energy intervals. Assuming no dead time in the region 0.1-1 eV the effect for small γ-ray energies is clearly visible for neutron energies higher than 10 eV.
For a similar experiment, the ^{235}U(n,γ) cross section measurement [61, 108] applying the fission tagging technique at n_TOF the dead time effects were studied in detail and have been corrected for. The effects of the dead time correction in both experiments can be expected to be similar above 20 eV due to the similar mass and capture cross sections, see left panel of Figure 6.4, and a similar ratio to the beam induced background, compare right panel of Figure 6.4 and Figure 6.2, thus the corrections for the ^{235}U(n,γ) cross section measurement is shown in the right panel of Figure 6.3.

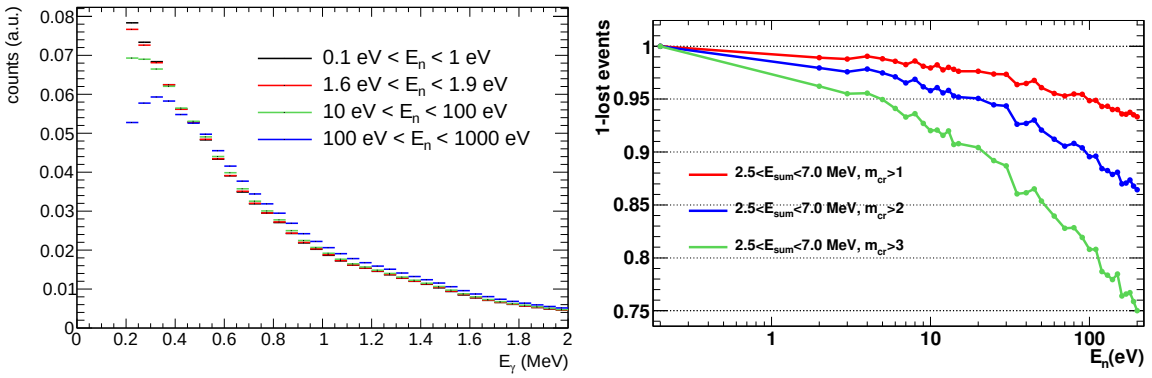

Figure 6.3: Individual γ-ray energies in the prompt fission cascades for different neutron energy intervals from this work (left). Decrease of the efficiency with neutron energy in the ^{235}U(n,γ) cross section measurement [61, 108] performed at n_TOF applying the fission tagging technique taken from [108] (right).

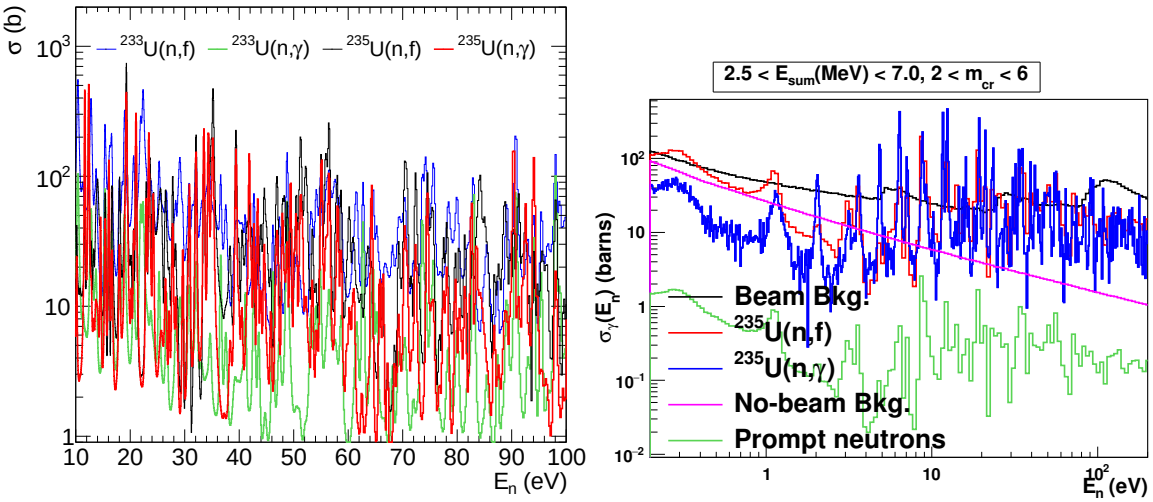

Figure 6.4: Capture and fission cross sections for ^{233}U and ^{235}U taken from ENDF/B-VIII.0(left). Background conditions in the ^{235}U(n,γ) cross section measurement [61, 108] performed at n_TOF applying the fission tagging technique taken from [108] (right).

6.3 Comparison with evaluated libraries and other experimental data

The capture response of the TAC and the fission counts from the FICH are shown in the top panel of Figure 6.5 and by division of the capture by the fission counts the ^{233}U α-ratio is obtained and shown in the bottom panel of Figure 6.5. In the following the experimentally obtained ^{233}U α-ratio is compared to the ^{233}U α-ratio calculated from two evaluated libraries (ENDF/B-VIII.0 and JEFF-3.3=ENDF/B-VII.1) as well as the two available data sets from Weston [32] and Berthoumieux [33]. Note that there is no experimental data below 18 meV corresponding to the maximum length of the acquisition window of the new n_TOF DAQ of 100 ms and the flight path length of about 185 m. In the following comparison it is important to note that the experimental data from this work lack a correction due to pileup and dead time effects in the TAC. Previous works [88, 108] show that such corrections can be significant

above 20 eV.

6.3.1 Comparison with evaluated libraries

The experimentally obtained ^{233}U α-ratio is compared to the ^{233}U α-ratio obtained from the ENDF/B-VIII.0 and JEFF-3.3 (=ENDF/B-VII.1) libraries in Figures 6.6, 6.7, 6.8, 6.9, 6.10, 6.11 and 6.12 for different neutron energy regions, while a comparison for JENDL-4.0u2 is

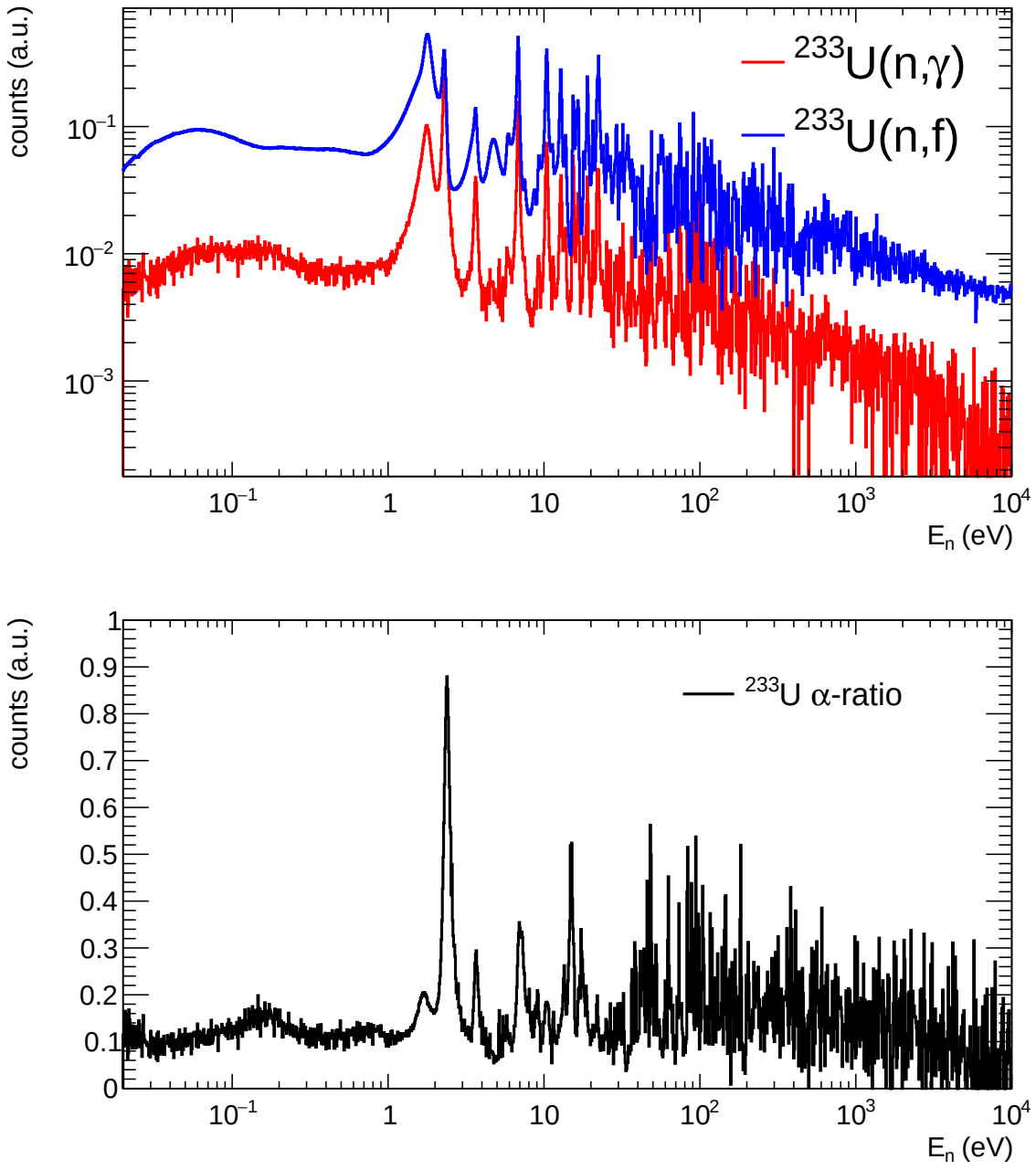

Figure 6.5: Comparison of the experimentally obtained counts for the ^{233}U(n,γ) reaction from the TAC and for the ^{233}U(n,f) reaction from FICH (top) for events with $3 \leq m_{cr} \leq 7$ and 2.5 MeV $< E_{sum} <$ 7 MeV and $A_{th} = 2500$ adc units. Experimental ^{233}U α-ratio calculated from the spectra in the top panel (bottom). No dead time corrections have been applied.

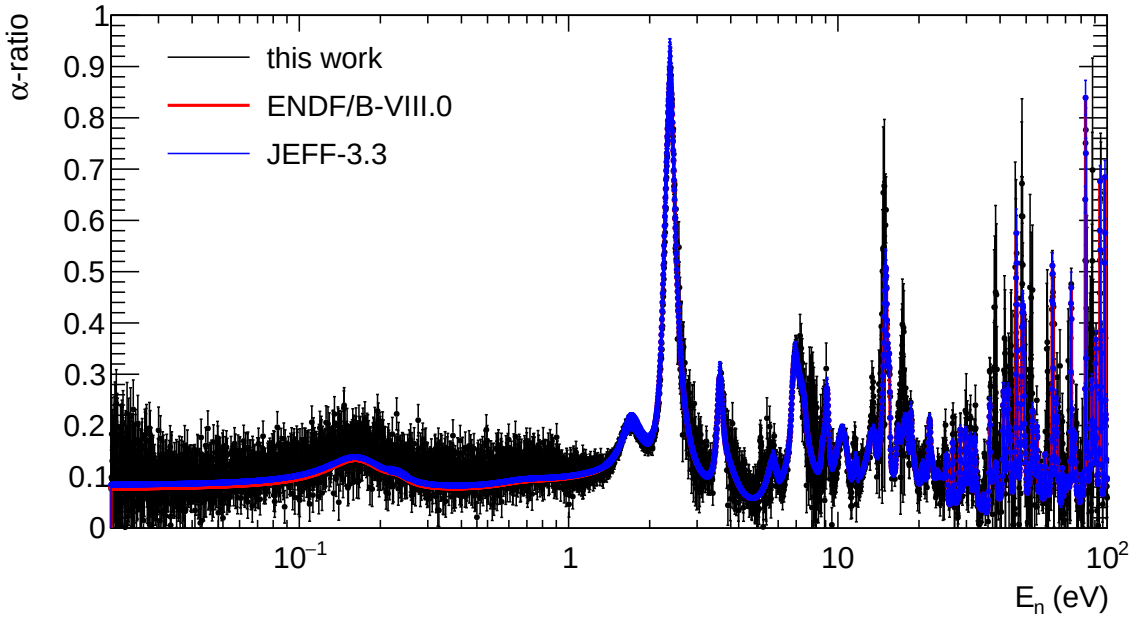

Figure 6.6: Experimental ^{233}U α-ratio calculated from events with $3 \leq m_{cr} \leq 7$ and $2.5\,\text{MeV} < E_{sum} < 7\,\text{MeV}$ compared to the ^{233}U α-ratio from ENDF/B-VIII.0 and JEFF-3.3 up to 100 eV. No dead time corrections have been applied.

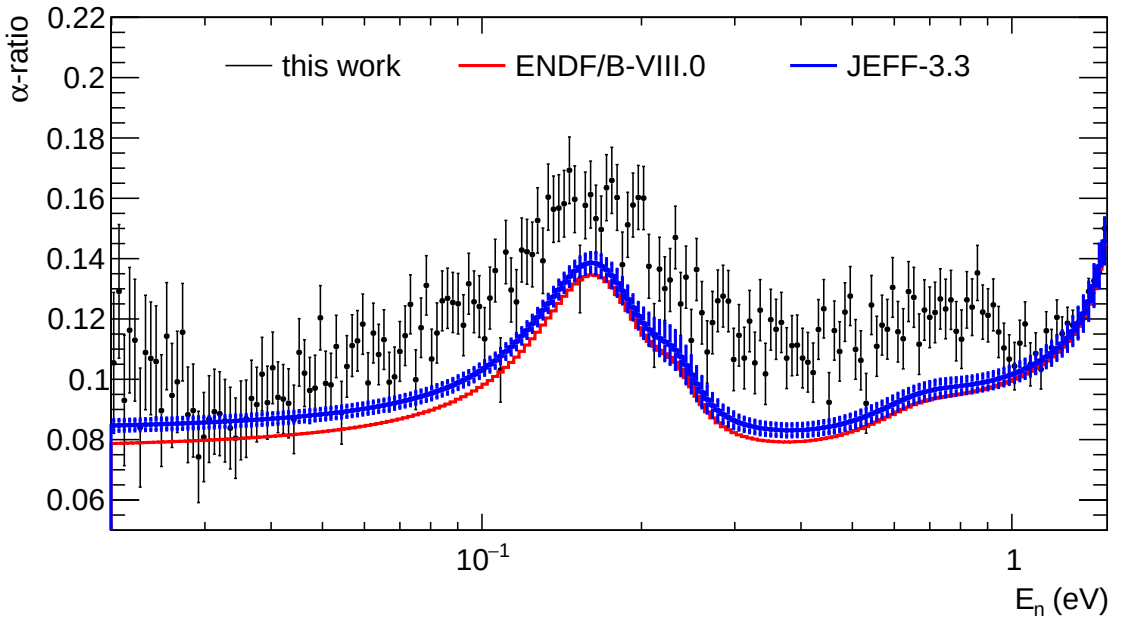

Figure 6.7: Comparison of the point wise experimental ^{233}U α-ratio compared to the ^{233}U α-ratio from ENDF/B-VIII.0 and JEFF-3.3 for the low energy region from 0.02 eV to 1.5 eV.

omitted as it is identical to ENDF/B-VIII.0. In Figure 6.6 a good overall agreement is achieved while local deviations can be observed.

In the low neutron energy region, shown in Figure 6.7, the comparison shows a significantly higher ^{233}U α-ratio for the experimental data from 0.04 eV to 1.0 eV.

The neutron energy region from $0.5\,\text{eV} < E_n < 4\,\text{eV}$ contains the largest resonances of the fission and capture cross sections and the corresponding comparison of the ^{233}U α-ratio is

shown in Figure 6.8. The absolute values in the strongest resonance in the capture reaction at approximately 2.4 eV seem to agree very well. Furthermore, a slight shift on the rising flanks of the structures at 2.1 eV and 2.4 eV as well as 3.5 eV and 2.65 eV towards lower neutron energies can be observed for the libraries compared to the experimental results.
A structure shows up in the experimental data at 5.15 eV, shown in Figure 6.9, which can be expected due to the 0.0496 % ^{234}U contamination of the samples. The position of this structure fits the largest resonance in the ^{234}U(n,γ) cross section very well. The same shift in the neutron energy as in the region from 0.5 eV $< E_n <$ 4 eV can be observed.
For neutron energies from 10 eV to 30 eV shown in Figure 6.10 deviations from the libraries are observed at 13.5 eV, 14.5 eV, 17 eV and 27.3 eV.
A few more local deviations from the libraries can be observed for neutron energies higher than 30 eV, shown in Figures 6.11 and 6.12. In addition to the point wise comparison the average ^{233}U α-ratio is computed for different energy regions:

- Neutron energy decades: shown in the left panel of Figure 6.13 and a summary in Table 6.1. It shall be noted here that the energy decade from 0.01 eV to 0.1 eV is not fully covered by the experimental data which only starts at around 0.018 eV.
- Neutron energy intervals according to the 33 group energy structure of the WPEC Subgroup 33 (SG33) [121] shown in the right panel of Figure 6.13 and summarized in Table 6.2.

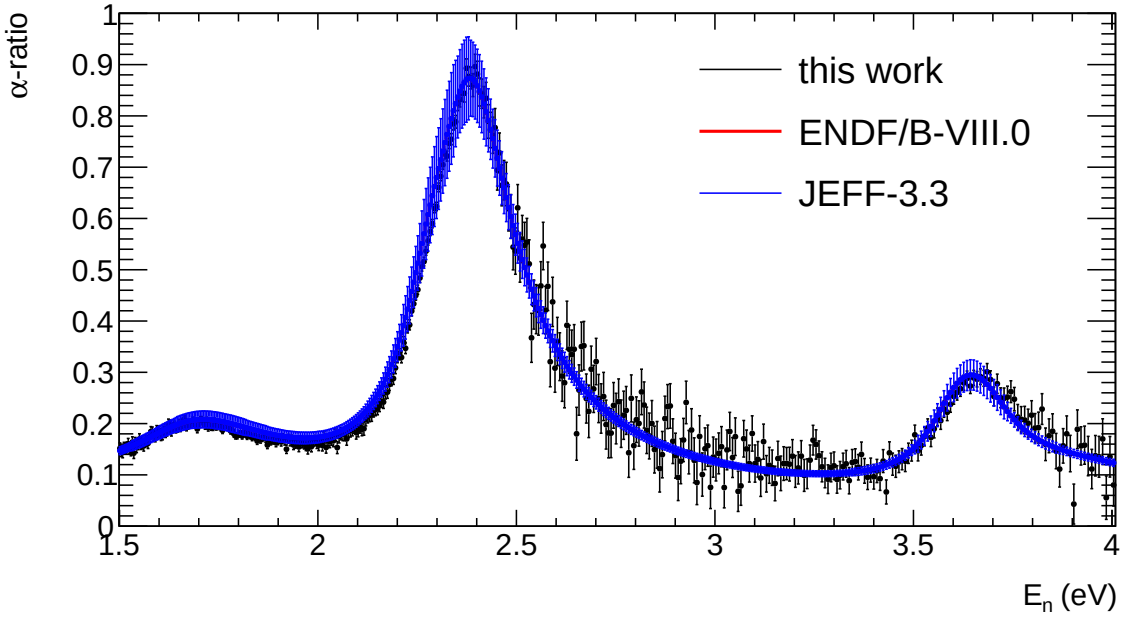

Figure 6.8: Comparison of the point wise experimental ^{233}U α-ratio compared to the ^{233}U α-ratio from ENDF/B-VIII.0 and JEFF-3.3 for the two big resonances from 0.5 eV $< E_n <$ 4 eV.

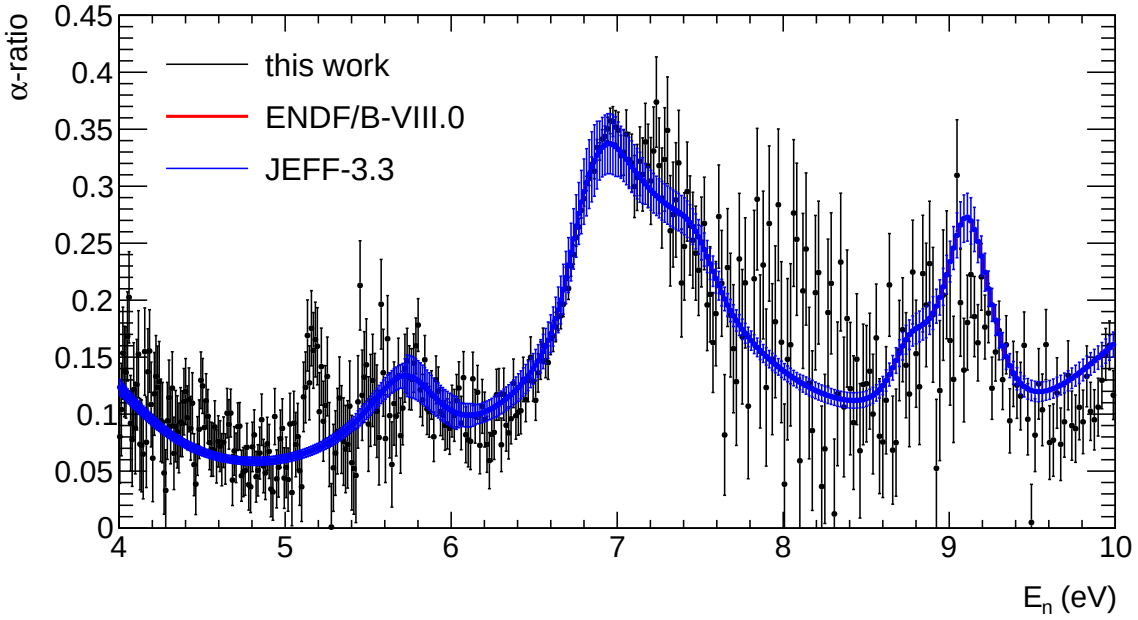

Figure 6.9: Comparison of the point wise experimental ^{233}U α-ratio compared to the ^{233}U α-ratio from ENDF/B-VIII.0 and JEFF-3.3 in the neutron energy region 4 eV $< E_n <$ 10 eV. The experimental data from this work shows a structure at 5.15 eV as expected due to the 0.0496 % ^{234}U contamination of the samples, see section 3.4.

6.3.2 Comparison with other experimental data

The experimentally obtained ^{233}U α-ratio is compared to the ^{233}U α-ratio obtained from other two TOF experiments from Weston and Berthoumieux in Figure 6.14, 6.15, 6.16, 6.17,

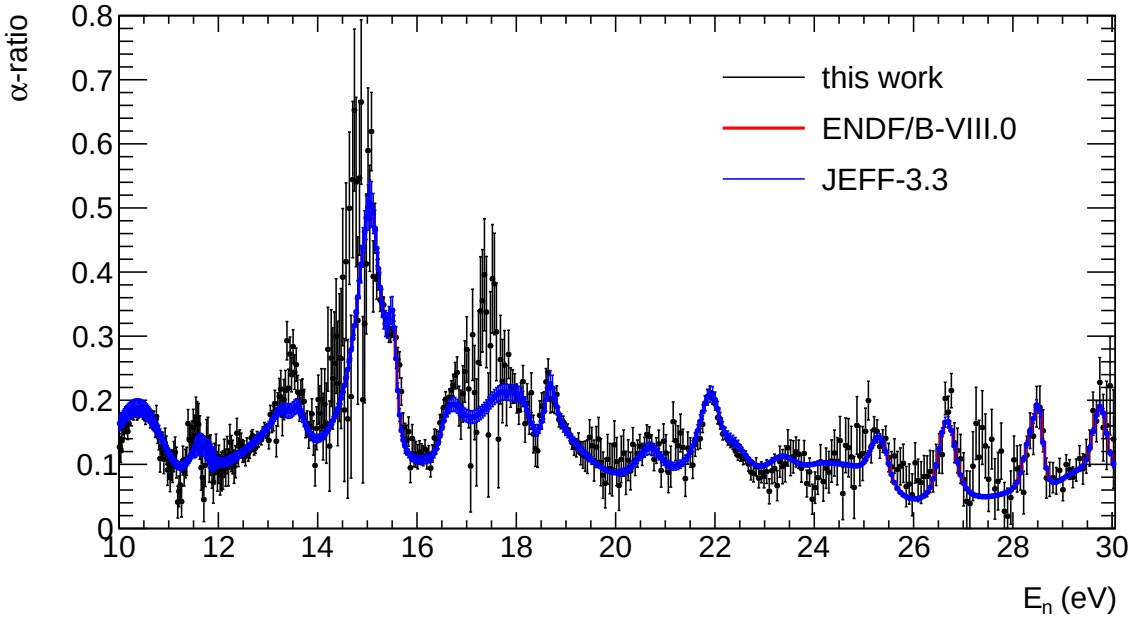

Figure 6.10: Comparison of the point wise experimental ^{233}U α-ratio to the ^{233}U α-ratio from ENDF/B-VIII.0 and JEFF-3.3 in the neutron energy region from 10 eV to 30 eV. No dead time corrections have been applied.

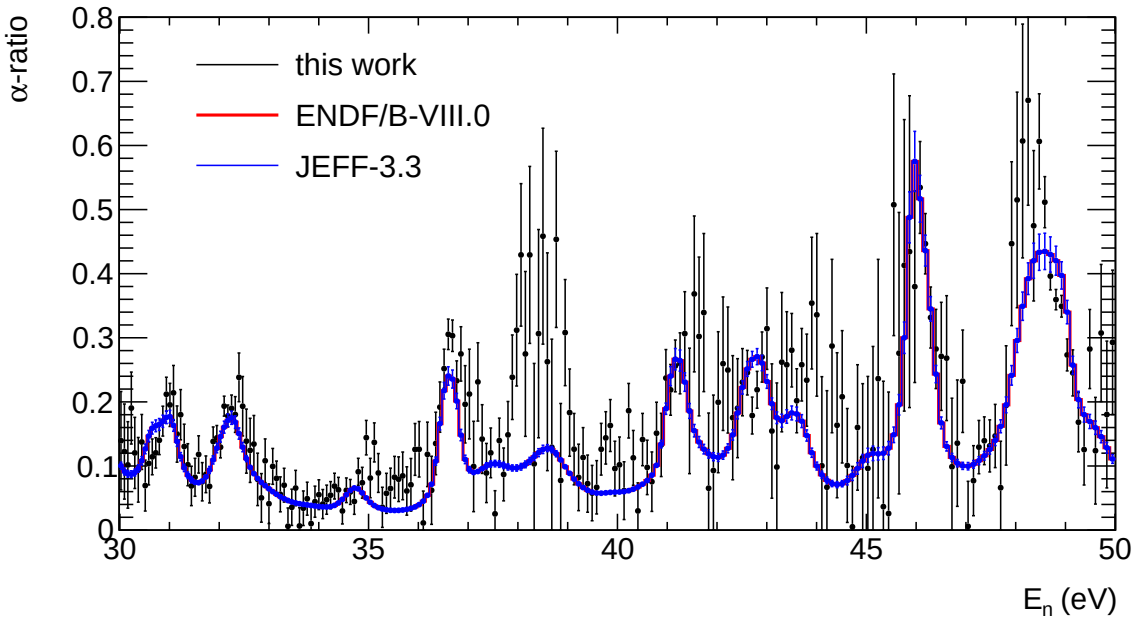

Figure 6.11: Comparison of the point wise experimental ^{233}U α-ratio to the ^{233}U α-ratio from ENDF/B-VIII.0 and JEFF-3.3 in the neutron energy region from 30 eV to 50 eV. No dead time corrections have been applied.

6.18 and 6.19 for different neutron energy regions. The other experimental data sets are limited in neutron energy range, listed in Table 6.3, so it has to be kept in mind that the comparison, especially for the average values, only makes sense when the full neutron energy bin is available in each corresponding data set. In Figure 6.14 a good overall agreement can be observed between the data sets but the comparison also shows local deviations.

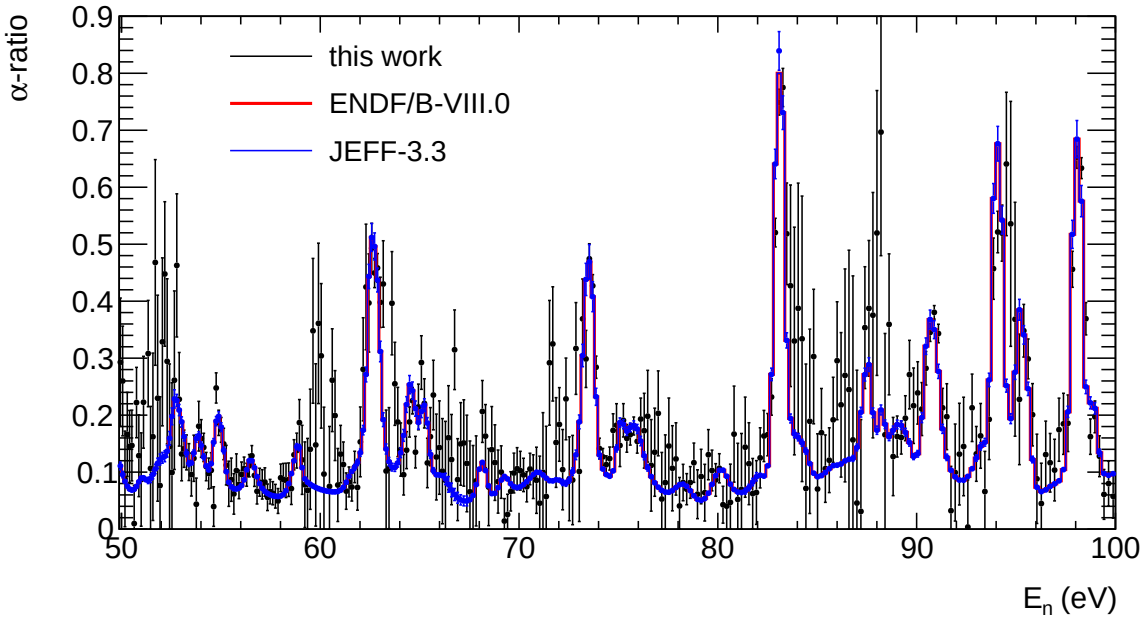

Figure 6.12: Comparison of the point wise experimental ^{233}U α-ratio to the ^{233}U α-ratio from ENDF/B-VIII.0 and JEFF-3.3 in the neutron energy region from 50 eV to 100 eV. No dead time corrections have been applied.

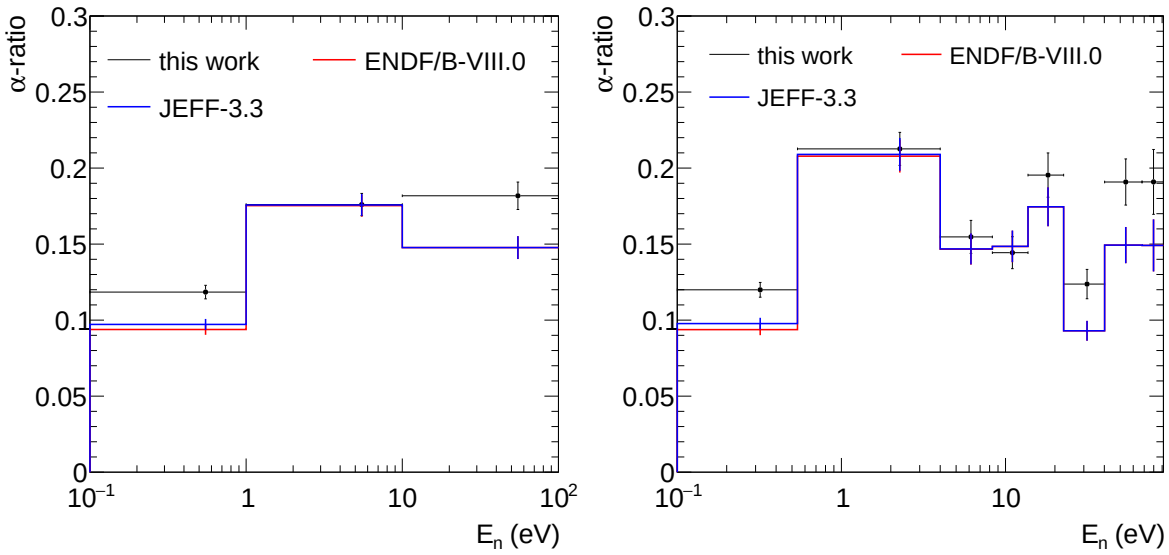

Figure 6.13: Comparison of the average values of the experimental, ENDF/B-VIII.0 and JEFF-3.3 ^{233}U α-ratio for neutron energy decades (left) and neutron energy intervals according to the 33 group energy structure of the WPEC Subgroup 33 (SG33) [121] (right) The corresponding values are summarized in Table 6.2. No dead time corrections have been applied.

Table 6.1: Comparison of the average ^{233}U α-ratio and related uncertainties of the experimental data with ENDF/B-VIII.0 and JEFF-3.3 libraries per neutron energy decade. No dead time corrections have been applied. Both statistical and systematic uncertainties are included for the experimental data.

E_n	Experimental data		ENDF/B-VIII.0		JEFF-3.3	
(eV)	α-ratio	uncertainty	α-ratio	uncertainty	α-ratio	uncertainty
0.01 - 0.1	0.0992	0.004	0.085	0	0.091	0.004
0.1 - 1	0.118	0.004	0.094	0	0.097	0.004
1 - 10	0.176	0.007	0.175	0	0.176	0.007
10 - 100	0.182	0.009	0.148	0	0.148	0.008

Table 6.2: Average ^{233}U α-ratio and related uncertainties of the experimental data, ENDF/B-VIII.0 and JEFF-3.3 in neutron energy intervals according to the 33 group energy structure of the WPEC Subgroup 33 (SG33) [121]. No dead time corrections have been applied. Uncertainties in the data contain statistical and systematic uncertainties.

E_n (eV)	Experimental data		ENDF/B-VIII.0		JEFF-3.3	
	α-ratio	uncertainty	α-ratio	uncertainty	α-ratio	uncertainty
0.10 - 0.54	0.121	0.005	0.094	0.004	0.098	0.004
0.54 - 4.00	0.214	0.011	0.208	0.011	0.209	0.011
4.00 - 8.32	0.156	0.011	0.147	0.010	0.147	0.010
8.32 - 13.71	0.145	0.011	0.148	0.010	0.149	0.010
13.71 - 22.60	0.196	0.015	0.174	0.013	0.175	0.013
22.60 - 40.17	0.125	0.010	0.093	0.007	0.093	0.007
40.17 - 67.90	0.192	0.015	0.149	0.012	0.149	0.012
67.90 - 91.66	0.192	0.021	0.149	0.017	0.149	0.017

In Figure 6.15 the neutron energy region from 0.5 eV to 4 eV shows that below 1.5 eV the ratios start to deviate and the experimental data of this work are on average higher. With respect to Weston there seems to be a shift of the ^{233}U α-ratio towards higher neutron energies in this work as well as in Berthoumieux's data which can be very well observed in the rising flank of the ^{233}U α-ratio between 2.1 eV and 2.4 eV.

In the neutron energy range from 4 eV to 10 eV, shown in Figure 6.16, a structure at 5.15 eV can be observed in the experimental data which fits the resonance of ^{234}U(n,γ) and is expected due to the 0.0496 % ^{234}U contamination of the samples, see section 3.4. Furthermore, the shift in neutron energy is observed again with the same trend of Weston's data being shifted

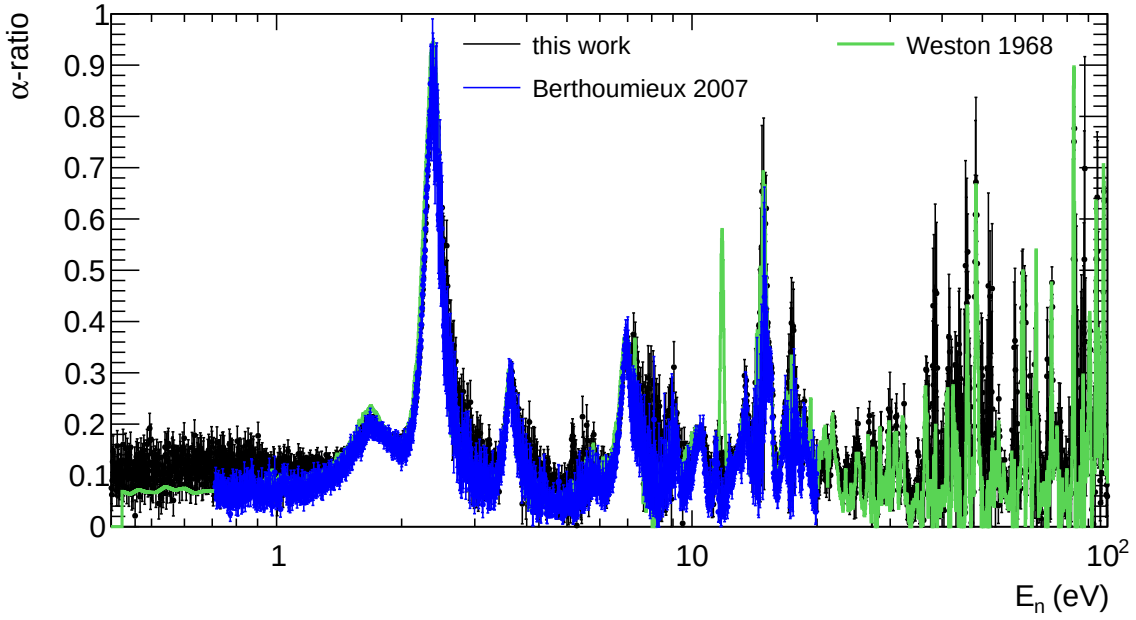

Figure 6.14: Comparison of the point wise experimental ^{233}U α-ratio from this work and from the experimental data sets from Weston and Berthoumieux up to 100 eV. No dead time corrections have been applied.

Table 6.3: Energy range for the other available experimental data sets for the ^{233}U(n,γ) or ^{233}U α-ratio .

	E_n (eV)	number of points
Weston (1968) [32]	0.405 - 2050	3423
Berthoumieux (2007) [33]	0.708 - 20	1451

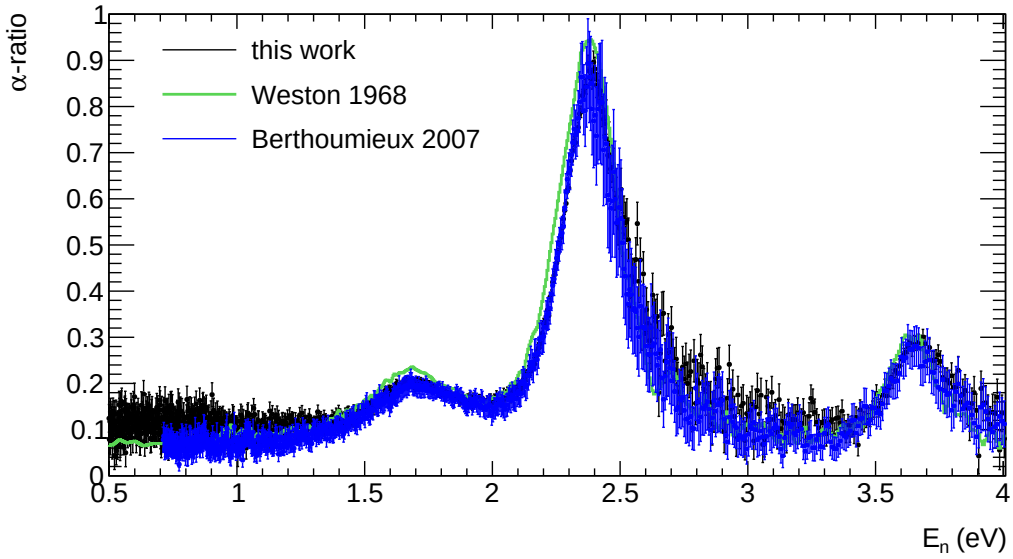

Figure 6.15: Comparison of the point wise experimental ^{233}U α-ratio from this work and from the experimental data sets from Weston and Berthoumieux for the two largest resonances from 0.5 eV $< E_n <$ 4 eV.

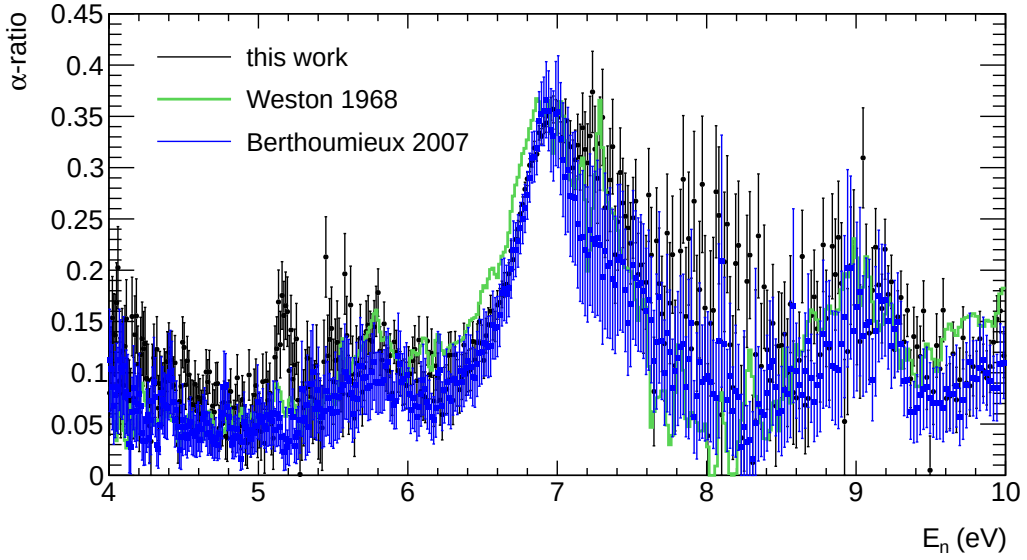

Figure 6.16: Comparison of the point wise experimental ^{233}U α-ratio from this work and from the experimental data sets from Weston and Berthoumieux in the neutron energy region from 4 eV $< E_n <$ 10 eV. The experimental data from this work shows a structure at 5.15 eV as expected due to the 0.0496 % ^{234}U contamination of the samples, see section 3.4.

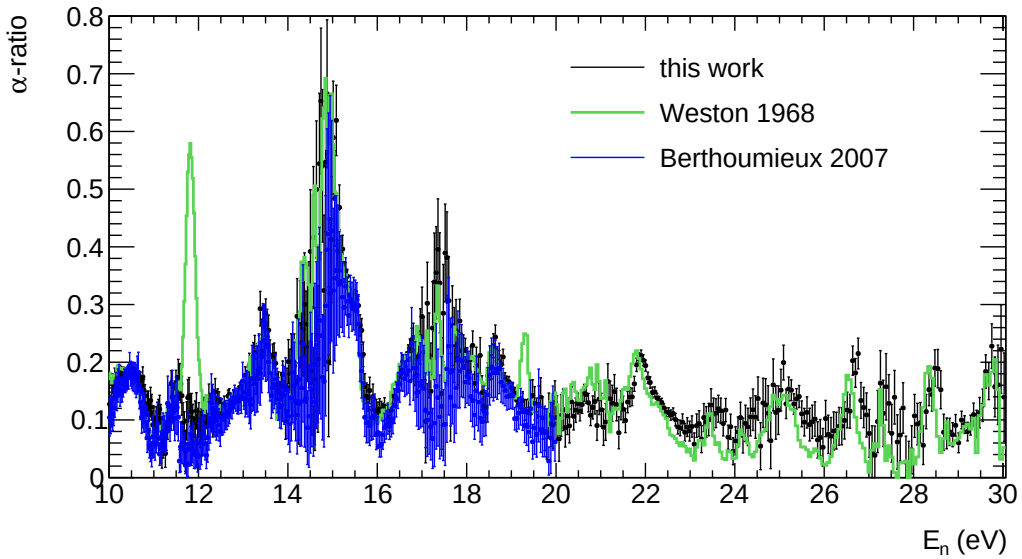

Figure 6.17: Comparison of the point wise experimental ^{233}U α-ratio from this work and from the experimental data sets from Weston and Berthoumieux in the neutron energy region from 10 eV $< E_n <$ 30 eV. Berhtoumieux's data stops at 20 eV. The data from Weston show structures at 11.8 eV and 19.3 eV which are not present in the experimental data from this work and Berthoumieux and are probably related to impurities in Weston's samples. No dead time corrections have been applied.

towards lower neutron energies as can be nicely seen for the rising flank of the ^{233}U α-ratio between 6 eV and 7 eV.

For neutron energies from 10 eV to 30 eV, shown in Figure 6.17, two structures at 11.8 eV and 19.3 eV can be observed in Weston's data but not in the other data sets (nor in the evaluated data, see Figure 6.10). This suggests that there were impurities in the samples used by Weston. For neutron energies above 30 eV and up to 100 eV the comparison is shown in Figures 6.18 and 6.19 but above 40 eV the statistical fluctuations in the experimental data do not allow a conclusive point wise comparison.

In addition to the point wise comparison the average ^{233}U α-ratio is computed for different energy regions:

- Neutron energy decades: the values are summarized in Table 6.4.
- Neutron energy intervals according to the 33 group energy structure of the WPEC Subgroup 33 (SG33) [121] shown in Figure 6.20 and summarized in Table 6.5

Table 6.4: Comparison of the average ^{233}U α-ratio and related uncertainties of this work and Weston data per neutron energy decade. No dead time corrections have been applied.

E_n (eV)	Experimental data		Weston	
	α-ratio	uncertainty	α-ratio	uncertainty
1 - 10	0.176	0.007	0.160	0
10 - 100	0.182	0.009	0.132	0

Table 6.5: Comparison of the average ^{233}U α-ratio and related uncertainties of the experimental, Weston and Berthoumieux data in neutron energy intervals according to the 33 group energy structure of the WPEC Subgroup 33 (SG33) [121]. Note that Berthoumieux's data only covers the range from 0.7 eV to 20 eV and Weston only starts at 0.4 eV, thus the values for neutron energies outside those ranges do not make sense for a comparison and are given only for completeness. No dead time corrections have been applied. Uncertainties in the data contain statistical and systematic uncertainties.

E_n	Experimental data		Weston		Berthoumieux	
(eV)	α-ratio	uncertainty	α-ratio	uncertainty	α-ratio	uncertainty
0.10 - 0.54	0.121	0.005	0.018	0.002	0	0
0.54 - 4.00	0.214	0.011	0.201	0.011	0.180	0.010
4.00 - 8.32	0.156	0.011	0.127	0.010	0.116	0.009
8.32 - 13.71	0.145	0.011	0.163	0.013	0.114	0.009
13.71 - 22.60	0.196	0.015	0.201	0.015	0.112	0.010
22.60 - 40.17	0.125	0.010	0.075	0.006	0	0
40.17 - 67.90	0.192	0.015	0.119	0.013	0	0
67.90 - 91.66	0.192	0.021	0.113	0.019	0	0

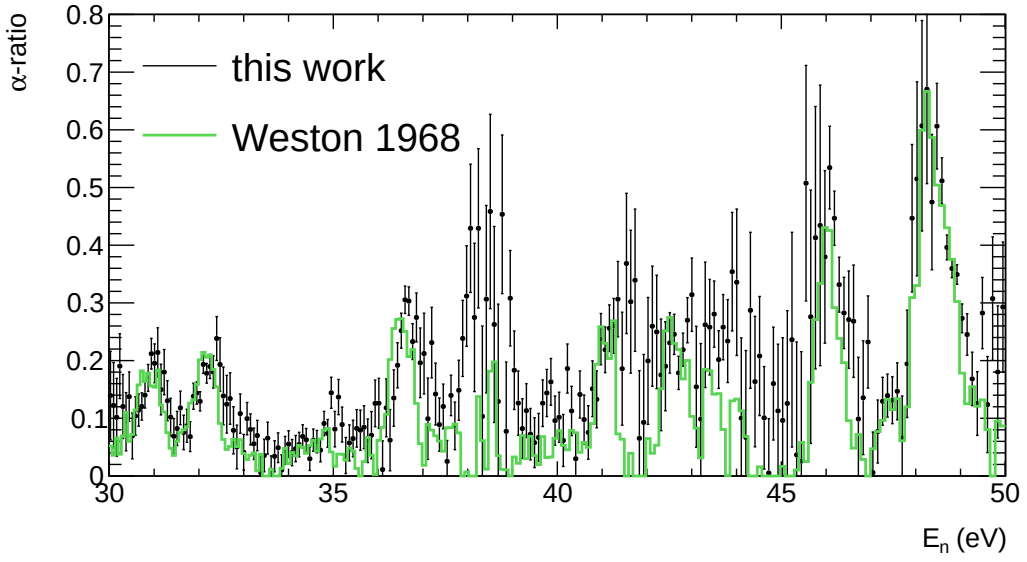

Figure 6.18: Comparison of the point wise experimental ^{233}U α-ratio from this work and from the experimental data sets from Weston in the neutron energy region from 30 eV $< E_n <$ 50 eV. No dead time corrections have been applied.

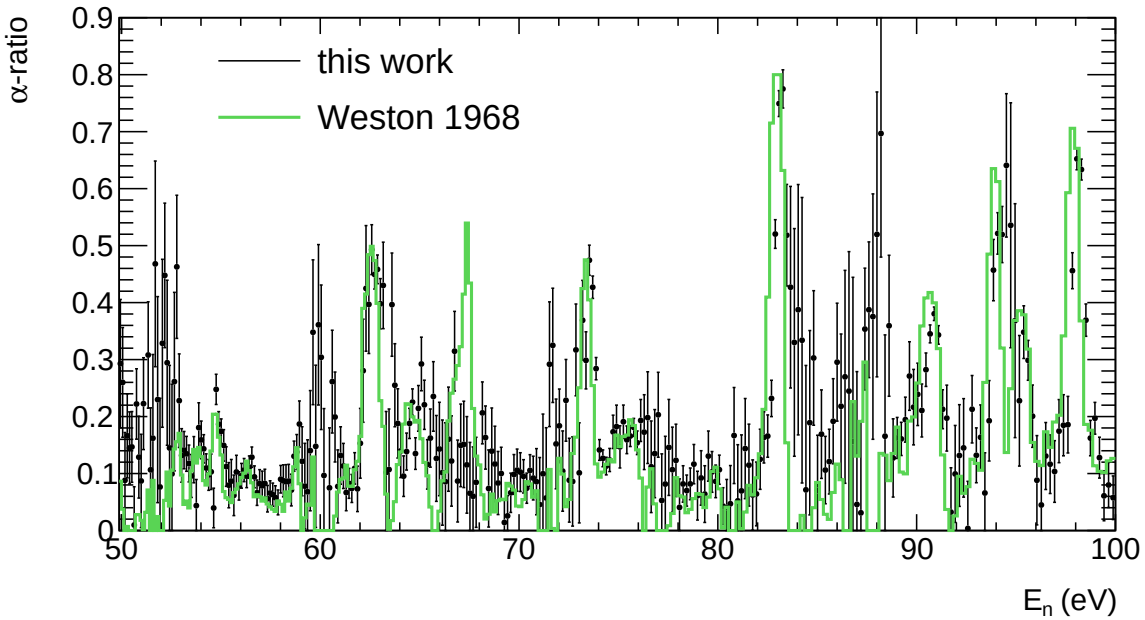

Figure 6.19: Comparison of the point wise experimental ^{233}U α-ratio from this work and from the experimental data sets from Weston in the neutron energy region from 50 eV $< E_n <$ 100 eV. No dead time corrections have been applied.

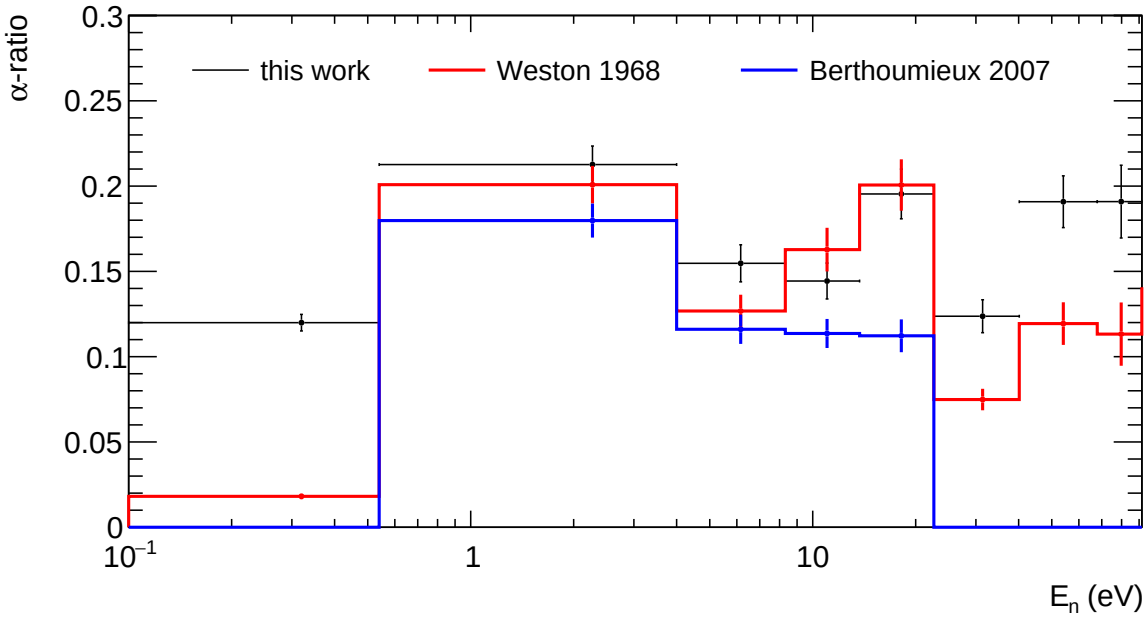

Figure 6.20: Comparison of the average values of the experimental, Weston and Berthoumieux ^{233}U α-ratio for neutron energy intervals according to the 33 group energy structure of the WPEC Subgroup 33 (SG33) [121] The corresponding values are summarized in Table 6.5.

Chapter 7

Summary and Conclusions

This PhD thesis describes the experimental setup and analysis of the measurement of the ^{233}U α-ratio at the CERN n_TOF facility performed in 2016. A novel fission chamber was developed and has been employed together with the n_TOF Total Absorption Calorimeter using the fission tagging technique to accurately determine the prompt background induced by the ^{233}U(n,f) reaction. The main idea of the fission tagging technique is the simultaneous measurement of the fission and capture reactions with the fission chamber and the γ-ray detector respectively and removing the prompt fission γ-rays from the fission reaction from the total measured spectra in the γ-ray detector by applying a time coincidence method between the two detection systems. Some inherent difficulties of the method are:

- The necessity of thin samples for the fission detector limits the achievable counting statistics, thus the signal to background ratio will be smaller compared to thick samples usually used in capture measurements.
- The large amount of material intercepting and surrounding the neutron beam due to the fission chamber decreases the signal to background ratio further compared to standard capture measurements.
- The accurate determination of the fission chamber efficiency is crucial and can lead to large systematic uncertainties.

From the experimental spectra an optimal set of conditions for the analysis of the ^{233}U α-ratio has been deduced and the background components have been carefully subtracted with the aim of providing to the nuclear data community a set of accurate experimental data. The data analysis involves the data reduction of complex experimental data from two detection systems and a large number of individual data acquisition channels and their correlations. The critical parts of the analysis can be summarized as follows:

- Coincidence analysis between the TAC and the FICH detection systems: The coincidence time distribution is shown in Figure 7.1 for different conditions applied to the TAC events. The optimal coincidence time window was chosen as a compromise between two opposite criteria: the maximum tagging efficiency and the minimal amount of random coincidences with background events. A time window of ± 14 ns contains close to 99 % of the distribution. Furthermore, the tail of the distribution corresponds to the

Table 7.1: Fission isomer(s) observed in the coincidence analysis with their respective half lives and fission probabilities including statistical uncertainties only.

En (eV)	$t_{1/2}$ (ns)	(n,γf)/(n,f) (%)
1.6 - 1.9	25(1)	0.057(2)
2.2 - 2.4	26(2)	0.139(9)
4.2 - 5.3	25(3)	0.209(15)

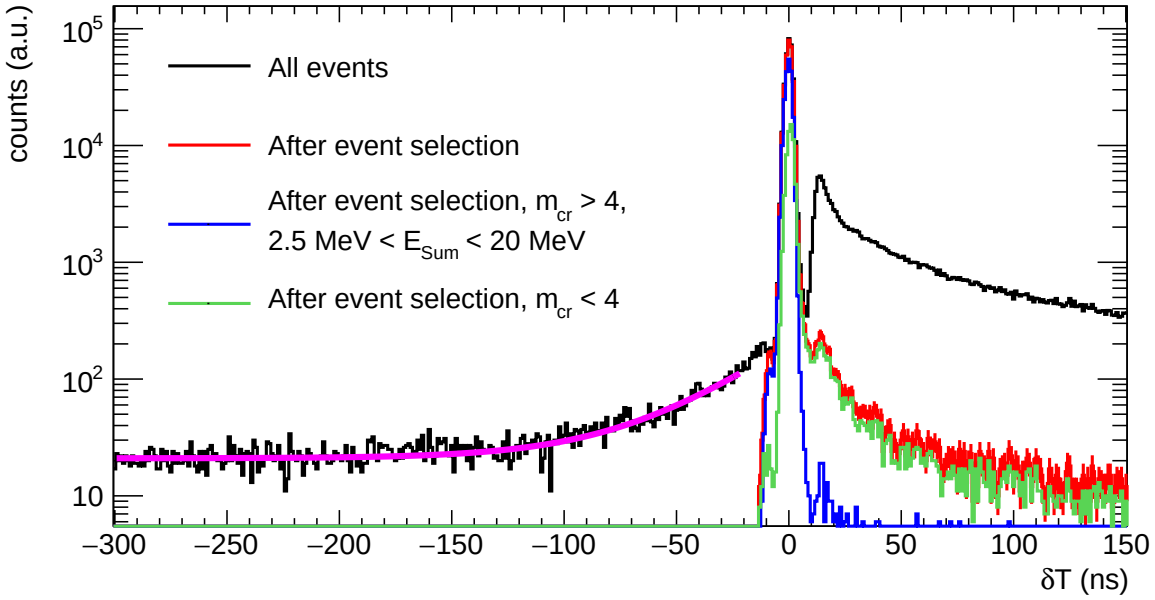

Figure 7.1: Time difference distribution between TAC and FICH events for a maximum allowed coincidence window $T_{coinc}^{TAC-FICH} = 1\,\mu s$ and with different conditions applied to the TAC signals. Same Figure as 4.30.

(n,γf) process which indicates the existence of long lived fission isomer(s) summarized in Table 7.1.

- Determination of the fission detection efficiency $\varepsilon_{FICH}(A_{th})$, describing the probability to detect a fission event in the FICH, and fission tagging efficiency $\varepsilon_{TAC}^{f}(A_{th}, E_{Sum}, m_{cr})$ which corresponds to the probability to detect a fission event in the TAC with the given conditions applied to the TAC. In case the probability of detecting a fission event in one or the other detector is independent (i) both quantities are the same and (ii) as a consequence the fission tagging efficiency only depends on the amplitude threshold A_{th}. Although a correlation between the two systems has been observed the efficiencies are calculated neglecting this correlation in a first approximation and it is attempted to correct for this correlation experimentally. The obtained efficiencies are

$$\varepsilon_{TAC}^{f}(2500) = \varepsilon_{FICH}(2500) = (89.53 \pm 0.20)\%. \tag{7.1}$$

- TAC detection efficiency $\varepsilon_{TAC}^{\gamma}$ and the ^{233}U(n,γ) cascades: The γ-de-excitation of the ^{234}U nucleus has been simulated using the Monte Carlo code DICEBOX, requiring the description of the nuclear level scheme on a statistical basis via nuclear level density and

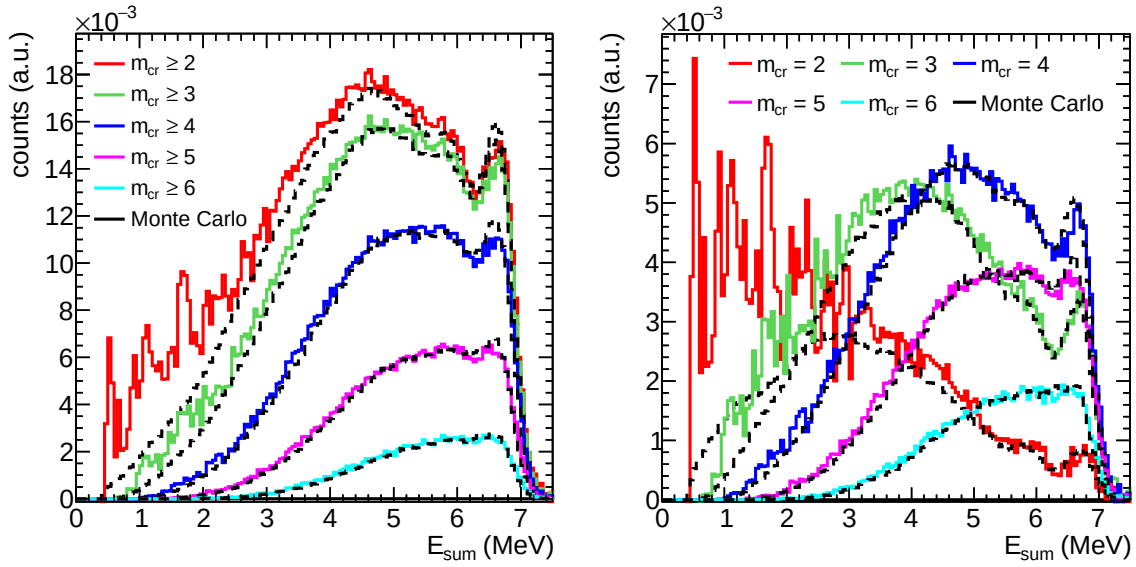

Figure 7.2: Comparison of the experimental and simulated sum energy spectra of ^{233}U(n,γ) events for various crystal multiplicity conditions. For multiplicities larger than 2 a good agreement is achieved. Same Figure as 5.22.

photon strength function models. Those cascades were transported in the geometrical model of the experimental setup with the help of the GEANT4 toolkit and the experimental data could be reproduced satisfactory as is shown in Figure 7.2, leading to an efficiency of the TAC to detect the ^{233}U(n,γ) events within the analysis conditions of

$$\varepsilon^{\gamma}_{TAC} = (75.8 \pm 2.5)\%. \tag{7.2}$$

Up to this point the point wise ^{233}U α-ratio has been extracted from the experimental data, as shown in Figure 7.3 but two additional steps have to be carried out in order to finalize the ^{233}U α-ratio measurement described in this manuscript:

- Investigate further a potential correction to the fission tagging and fission chamber efficiency due to correlations of the experimental setup and the fission fragments amplitude or angle of emission.
- Include dead time corrections for the TAC to correct for lost counts above 10 eV.

7.1 Improvements for future measurements

Due to upgrades of the n_TOF DAQ in 2015, a very stable behaviour with respect to the drift of the timing properties of individual data buffers was observed compared to previous measurements [61, 108]. To further enhance the quality of neutron capture cross section measurements in fissile isotopes several improvements can be implemented:

- Improve the signal to background ratio: The prompt background seems to be very well under control with the applied fission tagging method. A different setup could help

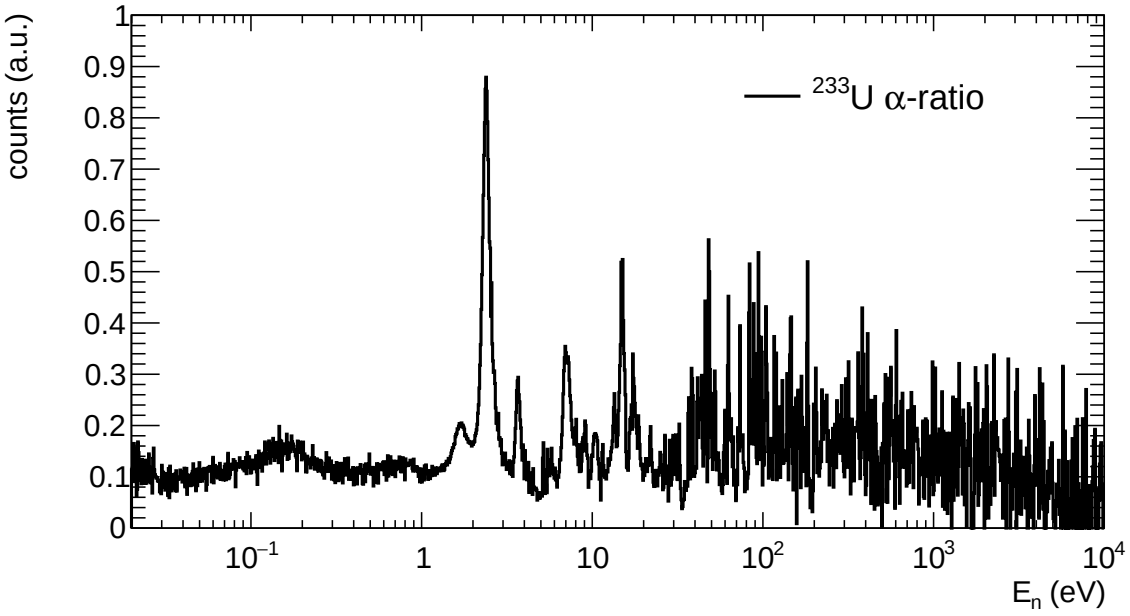

Figure 7.3: Experimentally obtained ^{233}U α-ratio . Same Figure as 6.5 bottom panel.

to improve the signal to background ratio by only partially tagging the prompt fission γ-rays from few very thin samples with high efficiency while several thicker samples, without fission tagging, can be used in parallel in the same setup to improve the capture statistics. Furthermore, this would reduce the amount of material intercepting the beam as less electrodes and electronics would be necessary, thus reducing the background which dominates the counting spectra especially in the valleys between resonances and the neutron energy region above a few 100s of eV.

- The sample quality: evaporated samples show a smoother surface and less contamination with materials other than the base material in the deposited layers compared to electro-deposited samples. A change to evaporated samples could minimize the amount of fission fragments absorbed in the sample, thus increasing the fission chamber efficiency and decreasing related uncertainties.

- Reduce the correlation between the TAC and the FICH: The angular correlation between the fission efficiency and the emitted prompt fission cascade could potentially be minimized by tilting the samples by 45° which should reduce the correlation between the fission fragment signal amplitudes and the deposited energy in the calorimeter. Tilting of samples by 45° with respect to the neutron beam to reduce angular effects on the efficiency is applied already with PPAC detectors at n_TOF .

- Comparing the results of the ^{233}U α-ratio and the ^{235}U(n,γ) cross section measurement it seems that the effect of the fission neutrons is smaller in the latter. This can be attributed to the larger average α-ratio in ^{235}U but also the dimensions of the absorber definitely has an influence on the neutron sensitivity. Thus, moving the electronics outside the TAC and avoiding structures like flanges (beam pipe/chamber) inside the

TAC in order to increase the thickness of the absorber shell definitely helps to reduce the neutron sensitivity.

- Replacing the passive absorber with an active one, i.e. a plastic scintillator coupled with a silicon photomultiplier read out, could help to clearly distinguish signals from (fission) neutrons in the TAC while at the same time open the possibility to measure the average emitted neutron per fission.

Those improvements can be considered for future measurements of the α-ratio or capture cross section in fissile isotopes applying the fission tagging technique.

Bibliography

[1] International Energy Agency. *World Energy Balances 2018*. (2018).

[2] International Energy Agency. *Electricity Information 2018*. (2018).

[3] International Atomic Energy Agency. *IAEA Annual Report 2017*. (2018).

[4] N.Holtkamp for the ITER Project Team. *An overview of the ITER project*. Fusion Engineering and Design **82**:427 (2007).

[5] N. A. Sepulveda et al. *The Role of Firm Low-Carbon Electricity Resources in Deep Decarbonization of Power Generation*. Joule **2**:2403-2420 (2018).

[6] C. Rubbia et al. *An energy amplifier for cleaner and inexhaustible nuclear energy production driven by a particle beam accelerator*. European Organization for Nuclear Research, Geneve, Tech. Rep. CERN CERN-LHC-98-02 (EET) (1998).

[7] Multi purpose hYbrid Research Reactor for High-tech Applications. URL: `http://myrrha.sckcen.be/` (July 23, 2019).

[8] The Generation IV International Forum. URL: `http://www.gen-4.org/` (July 23, 2019).

[9] D. A. Brown et al. *ENDF/B-VIII.0: The 8th Major Release of the Nuclear Reaction Data Library with CIELO-project Cross Sections, New Standards and Thermal Scattering Data*. Nuclear Data Sheets **148**:1-142 (2018).

[10] JEFF team. *JEFF-3.3: Evaluated nuclear data library*.

[11] K. Shibata et al. *JENDL-4.0: A New Library for Nuclear Science and Engineering*. Journal of Nuclear Science and Technology **48**:1-30 (2011).

[12] N. Otuka et al. *Towards a More Complete and Accurate Experimental Nuclear Reaction Data Library (EXFOR): International Collaboration Between Nuclear Reaction Data Centres (NRDC)*. Nuclear Data Sheets **120**:272–276 (2014).

[13] International Nuclear Data Committee. *Assessment of nuclear data needs for thorium and other advanced cycles*. IAEA, Tech. Rep. INDC(NDS)-**408** (1999).

[14] J. R. Lamarsh and A.J. Baratta. *Introduction to Nuclear Engineering*. Prentice Hall, Third Edition (2001).

[15] H. Hifenecker, O. Meplan, and S. David. *Accelerator Driven Subcritical Reactors*. Institute of Physics Publishing (2003).

[16] International Atomic Energy Agency. *Classification of Radioactive Waste*. IAEA Safety Standards Series No. GSG-1 (2009).

[17] International Atomic Energy Agency. *Clearance Levels for Radionuclides in Solid Materials: Application of Exemption Principles*. IAEA-TECDOC-855 (1996).

[18] A. Junghans et al. *Transmutation of high-level radioactive waste - Perspectives*. Proceedings of the ERINDA 2013 Worskhop in Proceedings of the ERINDA Workshop, CERN, Geneva, Switzerland, 1-3 October 2013, CERN-Proceedings-2014-002 (CERN, Geneva, 2014), pp. 175-182.

[19] The n_TOF Collaboration. *Measurements of Fission Cross Sections for the Isotopes relevant to the Thorium Fuel Cycle*. CERN-INTC-2001-025 (2001).

[20] S. Ganesan. *A review of the current status of nuclear data for major and minor isotopes of thorium fuel cycle*. International Topical Meeting on Advances in Reactor Physics and Mathematics and Computation into the Next Millennium, Pittsburgh, Pennsylvania, USA. (2000).

[21] European Technical Working Group on ADS. *A European Roadmap for Developing Accelerator Driven Systems (ADS) for Nuclear Waste Incineration*. ENEA, Rome (2001).

[22] J. Magill et al. *Impact limits of partitioning and transmutation scenarios on the radiotoxicity of actinides in radioactive waste*. Nucl. Energy **42**:263-277 (2003).

[23] International Atomic Energy Agency. *Implications of Partitioning and Transmutation in Radioactive Waste Management*. Technical Reports Series **435** (2004).

[24] Ansaldo Nucleare. *Energy Amplifier Demonstration Facility reference configuration: Summary Report*. EA-B0.000-1-200, Rev.0. Technical report, Ansaldo Nucleare, (1999).

[25] US Department of Energy Nuclear Energy Research Advisory Committee. *Technology Roadmap for Generation IV Nuclear Energy Systems*. US DOE (2002).

[26] Z. Zhang et al. URL: `www.neimagazine.com/features/featurehtr-pm-making-dreams-come-true-7009889/` (Aug. 31, 2019).

[27] W. M. Stacey. *Nuclear Reactor Physics*. Wiley Interscience (2001).

[28] F. Brooks et al. *Eta and Neutron Cross Sections of ^{239}Pu and ^{233}U*. United Kingdom Atomic Energy Research Establisment, Harwell, Berks., England, Tech. Rep. AERE-M-1709, (1966).

[29] T. A. Bredeweg et al. *Simultaneous measurement of (n, γ) and (n, fission) cross sections with the DANCE 4π BaF_2 array*. Nucl. Instr. Meth. B **261**:986-989 (2007).

[30] T. A. Bredeweg et al. *Recent actinide nuclear data efforts with the the DANCE 4π BaF_2 array*. International Conference on Nuclear Data for Science and Technology 2007, 161 (2008).

[31] I. Companis et al. *Measurement of neutron capture and fission cross sections of ^{233}U in the resonance region*. EPJ Web of Conf. textbf21, 10002 (2012).

[32] L. W. Weston et al. *Measurement of the Neutron Fission and Capture Cross Sections for ^{233}U in the Energy Region 0.4 to* 2000 eV. Nuc. Sci. Eng. **34**:1–12 (1968).

[33] E. Berthoumieux et al. *Simultaneous measurement of the neutron capture and fission yields of ^{233}U.* International Conference on Nuclear Data for Science and Technology 2007, 152 (2008).

[34] entry #23071 Experimental nuclear reaction database EXFOR. URL: `www-nds.iaea.org/exfor/exfor.htm` (July 25, 2019).

[35] The Nuclear Energy Agency: High Priority Request List. URL: `www.oecd-nea.org/dbdata/hprl` (July 25, 2019).

[36] K. H. Beckurts. *Neutron Physics.* Springer Verlag (1964).

[37] N. Bohr and J. A. Wheeler. *The mechanism of nuclear fission.* Phys. Rev. **56**:426-450 (1939).

[38] G. Breit et al. *Capture of slow Neutrons.* Phys. Rev. **49**:519-531 (1936).

[39] W. Heisenberg. *Über den anschaulichen Inhalt der quantentheoretischen Kinematik und Mechanik.* Zeitschrift für Physik **43**:172-198 (1927).

[40] E. P. Wigner. *Resonance Reactions.* Phys. Rev. **70**:606-618 (1946).

[41] E. P. Wigner and L. Eisenbud. *Higher Angular Momenta and Long Range Interaction in Resonance Reactions.* Phys. Rev. **72**:29-41 (1947).

[42] A. M. Lane and R. G. Thomas. *R-Matrix Theory of Nuclear Reactions.* Rev. Mod. Phys. **30**:257-353 (1958).

[43] F. H. Frohner. *Evaluation and Analysis of Nuclear Resonance Data.* JEFF Report18 (2000).

[44] J. L. Tain et al. *Accuracy of the Pulse Height Weighting Technique for Capture Cross Section Measurements.* Journal of Nuclear Science and Technology **39**:689-692 (2002).

[45] F. Becvar. *Simulation of γ cascades in complex nuclei with emphasis on assessment of uncertainties of cascade-related quantities.* Nuc. Inst. and Meth. A **417**:434-449 (1998).

[46] J. Kopecky and M. Uhl. *Test of gamma-ray strength functions in nuclear reaction model calculations.* Phys. Rev C **41**:1941-1955 (1990).

[47] C. H. Johnson. *Statistical model radiation widths for $75 < A < 130$ and the enhancement of P-wave neutron capture for $A \approx 90$.* Rev. Mod. Phys. **53**:385-479 (1981).

[48] J. C. Hardy. *The essential decay of pandemonium: β-delayed neutrons.* Nuclear Physics A **305**:15-28 (1978).

[49] P.O. Hansen et al. *Applications of statistical nuclear physics to nuclear spectroscopy.* Nuclear Physics A **518**:13-34 (1990).

[50] N. Bohr and J. A. Wheeler. *The mechanism of nuclear fission.* Phys. Rev. **56**:426-450 (1939).

[51] V. Strutinsky. *Shell effects in nuclear masses and deformation energies.* Nucl. Phys. A **95**:420-442 (1967).

[52] A. J. Elwyn and A. T. G. Ferguson. *Short-lived fission isomers from neutron studies.* Nuclear Physics A **148**:337-350 (1970).

[53] H. J. Specht. *Nuclear fission*. Rev. Mod. Phys. **46**:773-787 (1974).

[54] A. Tsinganis. *Measurement of the ^{242}Pu(n,f) reaction cross-section at the CERN n_TOF facility*. Tech. rep., CERN (2014).

[55] Jr. W. E. Lamb. *Capture of Neutrons by Atoms in a Crystal*. Phys. Rev. **55**, p 190 (1939).

[56] D. G. Naberejnev, C. Mounier, and R. Sanchez. *The Influence of Crystalline Binding on Resonant Absorption and Reaction Rates*. Nuc. Sci. Eng. **131**:222 (1999).

[57] G. de Saussure et al. Conference Proceedings Nuclear Data for Reactors **66**:233 (1966).

[58] R. B. Perez et al. *Simultaneous Measurements of the Neutron Fission and Capture Cross Sections for Uranium-235 for Neutron Energies from* 8 eV *to* 10 keV. Nuclear Science and Engineering **52**, 46 (1973).

[59] C. Guerrero et al. *Simultaneous measurement of neutron-induced capture and fission reactions at CERN*. Eur. Phys. J. A **48**, 29 (2012).

[60] M. Jandel et al. *New Precision Measurements of the ^{235}U(n,γ) Cross Section*. Phys. Rev. Lett. **109**, 202506 (2012).

[61] J. Balibrea-Correa et al. *Measurement of the neutron capture cross section of the fissile isotope ^{235}U with the CERN n_TOF total absorption calorimeter and a fission tagging based on micromegas detectors*. EPJ Web of Conferences **146**, 11021 (2017). DOI: 10.1051/epjconf/201714611021.

[62] C. Guerrero et al. *The n_TOF Total Absorption Calorimeter for neutron capture measurements at CERN*. Nucl. Instr. Meth. A **608**:424–433 (2009).

[63] M. Bacak et al. *A compact multi-plate fission chamber for the simultaneous measurement of ^{233}U capture and fission cross-section*. EPJ Web Conf. **146**, 03027 (2017).

[64] C. Rubbia et al. *A high resolution spallation driven facility at the CERN-PS to measure neutron cross sections in the interval from* 1 eV *to* 250 MeV. CERN/LHC/98-02 (1998).

[65] F. Mingrone et al. *Development of a neutron imaging station at the n_TOF facility of CERN and applications to beam intercepting devices*. Instruments **3(2)**, 32 (2019).

[66] C. Guerrero et al. *Performance of the neutron time-of-flight facility n_TOF at CERN*. Eur. Phys. J. A **49**, 27 (2013).

[67] Denis Gerard Cotte. *Private communication*. (2019).

[68] E. Chiaveri et al. *Proposal for the n_TOF Experimental Area2 (EAR-2)*. CERN INTC-2012-029/intc-o-015 (2012).

[69] M. Barbagallo et al. (n_TOF Collaboration). *^{7}Be(n,α)^{4}He Reaction and the Cosmological Lithium Problem: Measurement of the Cross Section in a Wide Energy Range at n_TOF at CERN*. Phys. Rev. Lett. **117**, 152701 (2016).

[70] Physikalisch-Technische Bundesanstalt (PTB). URL: www.ptb.de (Apr. 23, 2019).

[71] M. Barbagallo et al. *High-accuracy determination of the neutron flux at n_TOF*. Eur. Phys. J. A **49**, 156 (2013).

[72] FLUktuierende KAskade (FLUKA). URL: `www.fluka.org` (Apr. 23, 2019).

[73] Monte Carlo N-Particle code (MCNP). URL: `https://mcnp.lanl.gov/` (Apr. 23, 2019).

[74] J. Pancin et al. *Measurement of the n_TOF beam profile with a micromegas detector*. Nucl. Instr. Meth. A **524**:102–114 (2004).

[75] F. Belloni et al. *Neutron beam imaging with an XY-micromegas detector at n_TOF at CERN*. Physica Scripta **T150**, 014004 (2012).

[76] A. Masi et al. *The CERN n_TOF Facility Data Acquisition System*. Proceedings of ICALEPCS (2017). DOI: `10.18429/JACoW-ICALEPCS2017-THPHA195`.

[77] The SP Devices website. URL: `https://www.spdevices.com/` (Apr. 23, 2019).

[78] CERN Advanced STORage manager. URL: `castor.web.cern.ch` (Apr. 23, 2019).

[79] S. Marrone et al. *A low background neutron flux monitor for the n_TOF facility at CERN*. Nucl. Instr. and Meth. A **517**:389 (2004). DOI: `10.1016/j.nima.2003.09.060`.

[80] C. Guerrero. *Measurements of the ^{237}Np and ^{240}Pu neutron capture cross sections at the CERN n_TOF facility*. PhD thesis, Madrid (2008). URL: `https://cds.cern.ch/record/1263604/files/CERN-THESIS-2010-064.pdf`.

[81] K. Wisshak et al. *The Karlsruhe 4π barium fluoride detector*. Nucl. Instr. Meth. A **292**:595-618 (1990).

[82] E. Berthoumieux. *Preliminary report on BaF_2 Total Absorption Calorimeter test measurement*. Rap. Tech. CEA-Saclay/DAPNIA/SPhN (2004).

[83] GARFIELD: Simulation of Gaseous Detectors. URL: `http://garfield.web.cern.ch/garfield/` (Apr. 23, 2019).

[84] J. Taieb et al. *A new fission chamber dedicated to Prompt Fission Neutron Spectra measurements*. Nucl. Instr. and Meth. A **833**:1–7 (2016). DOI: `10.1016/j.nima.2016.06.137`.

[85] P. Zugec et al. *Pulse processing routines for neutron time-of-flight data*. Nucl. Instr. and Meth. A **812**:134–144 (2016). DOI: `10.1016/j.nima.2015.12.054`.

[86] G. Sibbens et al. *Morphological and compositional study of ^{238}U thin film targets for nuclear experiments*. AIP Conference Proceedings **1962**, 030007 (2018). DOI: `10.1063/1.5035524`.

[87] C. Guerrero et al. *Monte Carlo simulation of the n_TOF Total Absorption Calorimeter*. Nucl. Instr. Meth. A **671**:108–117 (2012).

[88] Emilio Mendoza Cembranos. *Measurement of the ^{243}Am capture cross section at the n_TOF facility*. PhD thesis, Madrid.

[89] S. Agostinell et al. GEANT4- *a simulation toolkit*. Nucl. Instr. Meth. A **506**:250–303 (2003).

[90] J. Allison et al. *Recent developemnts in* GEANT4. Nucl. Instr. Meth. A **835**:186-225 (2016).

[91] G. Knoll. *Radiation Detection and Measurement*. Wiley Third edition (2000).

[92] E. Mendoza et al. *Pulse pile-up and dead time corrections for digitized signals from a BaF_2 calorimeter*. Nuc. Inst. and Meth. A **768**:55-61 (2014).

[93] C. Guerrero et al. *Correction of dead-time and pile-up in a detector array for constant and rapidly varying counting rates*. Nuc. Inst. and Meth. A **777**:63-69 (2015).

[94] A. J. Deruytter and C. Wagemans. *Measurement and Normalization of the Relative Uranium-233 Fission Cross Section in the Low Resonance Region*. Nucl. Sci. Eng. **54**, 423 (1974).

[95] M. B. Chadwick et al. *ENDF/B-VII.1 Nuclear Data for Science and Technology: Cross Sections, Covariances, Fission Product Yields and Decay Data*. Nuclear Data Sheets **112**:2887-2996 (2011).

[96] K. H. Schmidt et al. *General Description of Fission Observables: GEF Model Code*. Nuclear Data Sheets **131**:107–221 (2016).

[97] V. Stavinsky and M.O. Shaker. *The (n,γf) proccess*. Nuclear Physics **62**:667–672 (1964).

[98] J. E. Lynn. *On the slow neutron, gamma-fission reaction*. Physics Letters **18**, 31 (1965).

[99] P. Talou et al. *Assessing the role of the (n,γf) process in the low-energy fission of actinides*. EPJ Web of Conferences **122**, 01013 (2016).

[100] J. E. Lynn et al. *Reexamining the role of the (n,γf) proccess process in the low-energy fission of ^{235}U and ^{239}Pu*. Phys. Rev. C **97**, 064601 (2018).

[101] W. Shockley. *Currents to Conductors Induced by a Moving Point Charge*. Journal of Applied Physics **9**, 635 (1938).

[102] S. Ramo. *Currents Induced by Electron Motion*. Proceedings of the IRE **27**, 9 (1939).

[103] I.C. Wolfe. *Measurement of work function in CF_4 gas*. Thesis, Massachusetts Institute of Technology, Dept. of Physics, 2010. URL: `https://dspace.mit.edu/handle/1721.1/61268`.

[104] T.E. Valentine. *Evaluation of prompt fission gamma rays for use in simulating nuclear safeguard measurements*. Annals of Nuclear Energy **777**, 3 (2001).

[105] C. Carrapico. *Measurement of the ^{233}U neutron capture cross sections at the n_TOF facility at CERN*. PhD thesis, Lisbon (2012). URL: `https://cds.cern.ch/record/1529714/files/CERN-THESIS-2012-283.pdf`.

[106] M. Jandel et al. *Prompt Fission Gamma-Ray Studies at DANCE*. Physics Procedia **59**:101-106 (2014).

[107] M.M. Hoffman. *Directional Correlation of Fission Fragments and Prompt Gamma Rays Associated With Thermal Neutron Fission*. Phys. Rev. B **133**, 714 (1964).

[108] J. Balibrea-Correa. *Measurement of the neutron capture cross section of Uran5 at the n_TOF facility*. PhD thesis, Madrid (2017). URL: `https://eprints.ucm.es/47661/1/T39925.pdf`.

[109] National Nuclear Data Center (NNDC) Evaluated Nuclear Structure Data File Search and Retrieval. URL: `/www.nndc.bnl.gov/ensdf` (Aug. 31, 2019).

[110] S. Valenta and M. Krtička. *Private communication*. (2019).

[111] R. Capote et al. *RIPL - Reference Input Parameter Library for Calculation of Nuclear Reactions and Nuclear Data Evaluations*. Nuclear Data Sheets **110**:3107-3214 (2009).

[112] T. Egidy and D. Bucurescu. *Systematics of nuclear level density parameters*. Phys. Rev. C **72**, 044311 (2005).

[113] J. L. Ullmann et al. *Constraining the calculation of ^{234,236,238}U(n,γ) cross sections with measurements of the γ-ray spectra at the DANCE facility*. Phys. Rev. C **96**, 024627 (2017).

[114] M. Guttormsen et al. *Observation of Large Scissors Resonance Strength in Actinides*. Phys. Rev. Lett. **109**, 162503 (2012).

[115] M. Guttormsen et al. *Scissors resonance in the quasicontinuum of Th, Pa, and U isotopes*. Phys. Rev. C **89**, 014302 (2014).

[116] M. Krtička et al. *Constraints on the dipole photon strength functions from experimental multistep cascade spectra*. Phys. Rev. C **99**, 044308 (2019).

[117] J. Kroll et al. *Systematics of nuclear level density parameters*. Phys. Rev. C **88**, 034317 (2013).

[118] M. Guttormsen et al. *Scissors resonance in the quasicontinuum of Th, Pa, and U isotopes*. Phys. Rev. C **89**, 014302 (2014).

[119] M. Guttormsen et al. *Constant-temperature level densities in the quasicontinuum of Th and U isotopes*. Phys. Rev. C **88**, 024307 (2013).

[120] T. Kibédi et al. *Simulation of gamma cascades in complex nuclei with emphasis on assessment of uncertainties of cascade-related quantities*. Nuc. Inst. and Meth. A **589**:202-229 (2008). URL: `bricc.anu.edu.au`.

[121] Nuclear Energy Agency. *Methods and Issues for the Combined Use of Integral Experiments and Covariance Data*. NEA/NSC/WPEC/DOC(2013)445.